Steam Generator Tube Integrity Program

Annual Report October 1998 — September 1999

Argonne National Laboratory

U.S. Nuclear Regulatory Commission
Office of Nuclear Regulatory Research
Washington, DC 20555-0001

AVAILABILITY OF REFERENCE MATERIALS
IN NRC PUBLICATIONS

Steam Generator Tube Integrity Program

Annual Report
October 1998 — September 1999

Prepared by
D. R. Diercks, S. Bakhtiari, K. E. Kasza, D. S. Kupperman,
S. Majumdar, J. Y. Park, W. J. Shack

Argonne National Laboratory
9700 South Cass Avenue
Argonne, IL 60439

J. Muscara, NRC Project Manager

Steam Generator Tube Integrity Program:
Annual Report October 1998-September 1999

by

D. R. Diercks, S. Bakhtiari, K. E. Kasza, D. S. Kupperman,
S. Majumdar, J. Y. Park, and W. J. Shack

Abstract

This report summarizes work performed by Argonne National Laboratory on the Steam Generator Tube Integrity Program during the period October 1998 through September 1999. The program is divided into five tasks: (1) Assessment of Inspection Reliability; (2) Research on In-Service-Inspection (ISI) Technology; (3) Research on Degradation Modes and Integrity; (4) Integration of Results, Methodology, and Technical Assessments for Current and Emerging Regulatory Issues; and (5) Program Management. Under Task 1, progress is reported on the assembly of the steam generator tube mock-up, the collection of data for the round robin exercise, and the review of these data. In addition, the effect of a corrosion product on the eddy current signal from a stress corrosion crack is being evaluated, and a technique for profiling cracks based on phase analysis is being developed. Under Task 2, research efforts were associated primarily with multiparameter analysis of eddy current NDE results. Two separate multifrequency mixing procedures are being evaluated, and the application of a signal restoration technique to enhance the spatial resolution of rotating probes is being studied. Under Task 3, laboratory-induced cracking has been produced in a total of ≈450 Alloy 600 tubes. Additional tests have been conducted using the Pressure and Leak-Rate Test Facility on EDM axial notch OD flaws of several different lengths and flaw depth, and the High-Pressure Test Facility has been completed and utilized in initial tests on tubes with OD axial EDM throughwall and part-throughwall notches. Models for predicting the onset of crack growth and for calculating crack opening area and leak rate from a throughwall circumferential crack in a steam generator tube have been developed. In addition, models for predicting the failure of Electrosleeved tubes have been developed. Under Task 4, eddy current and ultrasonic examinations were conducted on test sections with cracks grown at Argonne.

Contents

Figures

vii

Tables

Executive Summary

Assessment of Inspection Reliability

Assembly of the nine mock-up levels, each consisting of 400, 0.3-m (1-ft.)-long Alloy 600 test sections, has been completed. In addition to test sections with stress corrosion cracking (SCC), test sections with dents have been installed. Flawed test sections in the tube bundle have been examined with both bobbin coil and three-coil (including +Point) rotating probes before assembly. For each scan, the probe passes through the degraded test section, a standard with 18 notches, and an ASME standard. After assembly, the tube bundle was examined with a borescope. In addition to an eddy current examination, cracked test sections were examined with dye-penetrant before being incorporated into the mock-up tube bundle.

Simulation of magnetite in the tube support plate (TSP) crevice was accomplished by filling the crevice with magnetic tape or a ferromagnetic fluid. Sludge was simulated by a mixture of magnetite and copper. Sludge was placed above the tube sheet roll transition and above the TSP in some cases.

An indication that the cracks grown at Argonne are representative of field cracks comes from a comparison of bobbin coil voltages and phases for the field-degraded McGuire steam generator tubes with the bobbin coil voltages and phases for the Argonne laboratory-cracked tubes. A comparison for axial outer diameter (OD) SCC at tube support plates shows the two plots to be similar.

During June 1999, a three-person team from Zetec collected data from the mock-up as part of the data-acquisition exercise. The data acquisition team included persons qualified at QDA Level IIa and QDA Level IIIa. A 10-D pusher-puller, MIZ30 with 36-pin cables, and Eddynet software were used for data acquisition. Bobbin coil data from a mag-biased probe was collected from 3600 test sections of the mock-up. Calibration for the bobbin coil data was carried out before and after the four-hour interval required to collect the data. No change in voltage from the standard was detectable during this time period.

In addition, MRPC data was taken from all degraded test sections as well as many test sections with artifacts and many clean test sections. The three-coil mag-bias probe used consisted of a 2.92-mm (0.115-in.)-diameter pancake coil, a +Point coil, and a 2.03-mm (0.080-in.)-diameter high-frequency shielded coil. An ASME standard and as well as a standard with 18 ID and OD axial and circumferential EDM notches (20, 40, 60, 80 and 100% TW) were used for calibration.

Data have been collected to show equivalency of mag and non-mag-biased probes. Data have been analyzed from several mock-up flaws using all frequencies employed in the mock-up data acquisition exercise. In general, data from a mag-biased +Point coil and non-mag-biased coil are virtually the same. Nevertheless, problems do occur for a small number of test sections that have a heat different from the rest of the mock-up. For those cases, a phase rotation is observed when using the pancake coil. This problem does not appear for the +Point coil (i.e., the phase from a flaw is the same for both mag-biased and non-mag-biased +Point coils regardless of the heat of material). Data have also been analyzed to show equivalency

between an MRPC at 900 rpm (12.7 mm/s [0.5 in./s]) and an MRPC at 300 rpm (2.54 mm/s [0.1 in./s]). The signals are almost indistinguishable.

The mock-up data collected for the round robin exercise was reviewed by a recognized industry expert. The overall quality of the data was judged to be good and generally representative of field data. In addition, bobbin coil data from the mock-up were analyzed to show the distribution of voltages and distribution of crack depths based on pre-mock-up assembly data. The histograms show a good dynamic range of bobbin coil voltages and crack depths.

In preparation for the round robin exercise, several meetings were held with the NDE Task Group. Documents prepared by the NDE Task Group members provided technical direction for the eddy current (EC) examination. These documents include the Site-Specific Performance Demonstration, Analyst's Guideline, Examination Technique Specifications Sheets, and Training Manual. The documents were reviewed by the Task Group and by ANL leading to several revised versions.

The effect of a corrosion product (thin oxide film) on the eddy current signal from an SCC is under evaluation. Alloy 600 tubes with OD axial SCC were placed under pressurized water reactor (PWR) water chemistry conditions (300°C [572°F] and oxygen at the ppb level) for about two months. The cracks have been examined with both mag-bias bobbin and +Point coils before and after corrosion products developed. The voltages for the bobbin coil increased significantly with the creation of the thin oxide film. However, the general shape of the Lissajous figures remained unchanged. In contrast, the results for the +Point coil are inconclusive at this time. The creation of corrosion products in the crack could lead to a reduction in the number of electrically conducting paths from contacting crack faces. In that case, the EC signal would be expected to increase, as observed, while the depth remains essentially the same.

A technique for profiling cracks has been attempted. The phase angle from the Lissajous pattern generated by a +Point coil at 300 kHz was compared, at various deep points along the crack, to the phase angle of EDM notches of depths 40, 60, 80 and 100 percent throughwall (%TW). The estimate of % TW was made at intervals of 1 mm (0.040 in.) as long as reasonable signal-to-noise ratios were evident. For smaller signals and where phase analysis is not effective (depth less than 60-70% TW), a depth was established from the phase analysis at relatively deep points and then depth was correlated with signal amplitude using straight linear extrapolation to 0% TW. As a result, the entire eddy current profile of the crack could be made.

Numerous test sections with 80% TW laser-cut slots in various geometrical configurations were examined with a +Point coil. The purpose was to help establish the reliability of +Point phase analysis to estimate the maximum depth of cracks, especially segmented cracks. The results for 12 test sections is presented in this report. In all cases, the predicted depth of the 80% TW axially oriented laser-cut slots was less than the design depth, despite very high signal-to-noise ratios. The greatest deviation occurs when there is a ligament between the axial slots. The ligaments provide a current path between slots resulting in a phase shift of the Lissajous figure. For circumferentially oriented laser-cut slots, the estimate with the +Point coil is greater than the design depth. This discrepancy may be the result of lack of

contouring of the circumferentially oriented part of the +Point coil to the tube inner surface. The axially oriented part of the coil has a better fit to the inner surface of the tube.

Research on ISI Technology

Research efforts were associated primarily with multiparameter analysis of eddy current NDE results. Preliminary results are presented on two separate multifrequency mixing procedures that could help improve bobbin coil detection of flaw indications in presence of interfering artifacts at the same axial location along the tube axis. Both direct and indirect mixing techniques were evaluated. This investigation was initiated in part to assess alternate mixing methods that could help compensate for lack of similarity between simulated artifacts in tube standards and those in the field. To assess the validity of independent mix algorithms, bobbin coil readings on two tubes with laboratory-grown circumferential and axial stress-corrosion cracking (SCC) at tube sheet (TS) roll transition region were examined. The outcome of this on-going study suggests that improved detection with bobbin coil could be achieved through selective application of direct mixing methods.

A description of recent activities is provided on multiparameter data analysis of eddy current inspection results. Implementation of a rule-based computer-aided data analysis routine is initially discussed. The algorithm uses multiple frequency eddy current readings from rotating probes to estimate depth profile of indications in a tube. Preliminary results are also presented on the application of this multifrequency phase-based algorithm to various sets of experimental data acquired with conventional rotating probes. Results of the analysis are presented on a set of twenty tubes furnished by PNNL that contained laboratory-produced cracking morphologies that represent those that are incorporated into the ANL's SG mockup. Data analysis results are also presented for a single specimen with laboratory-produced cracking which exhibited reportable bobbin coil indications with no clear flaw signal from rotating probe inspections (pancake and +Point™ coils).

Estimated depth profiles are also provided for a set of 24 laser-cut specimens with single and multiple axial/circumferential notches (with and without ligament) that simulate complex cracking geometries. The NDE and nominal flaw size on this set of 24 tubes, originally constructed for high-pressure studies under Task 3 of this program, provide a useful mean for assessment of data analysis algorithms that are currently under investigation at ANL. Using inspection data from bobbin and rotating probes, preliminary analysis of data on the laser-cut specimens was performed. NDE data was initially analyzed using the Eddynet98™ analysis software. Subsequent multiparameter analysis of laser-cut specimens was carried out using the data from a 2.92-mm (0.115-in.)-diameter primary pancake coil of a three-coil rotating probe. Although all flaws were detected with all three techniques, the sizing estimates vary significantly between bobbin and RPC probes and to a lesser extent between the two RPC methods. Initial analysis of bobbin coil data indicates an overall underestimation of depth for all the available flaw types. Results from +Point™ coil inspections show improved sizing accuracy over bobbin for the majority of indications and in particular the ligamented flaws. The +Point™ results indicate some under-estimation of axial flaw depths, particularly for the ligamented notches and overestimation of depth for most circumferential flaws. The multiparameter sizing estimates, although closer to the single-frequency +Point™ estimates, show smaller overall scatter of the sizing results and better agreement with the nominal values for the notch depths.

Finally, results are presented from a recent study on the application of a signal restoration technique to enhance the spatial resolution of rotating probes. In particular, the application of pseudoinverse filters to the restoration of RPC indications is described. The primary purpose of this on-going investigation is to evaluate the effectiveness of real-time approximate deconvolution algorithms for improving spatial resolution and, in turn, sizing accuracy of rotating probes for crack-like indications. The collection of laser-cut notch specimens mentioned above was utilized for the initial benchmarking studies. So far, results of this investigation suggest that, in general, pseudoinverse filters, when applied discerningly, can help reduce EC signal background variations, improve spatial resolution, and, in turn, improve multiparameter sizing of crack-like indications. The pseudo-deconvolution scheme described here has been integrated as part of the multiparameter data analysis algorithm to further help improve characterization of complex SG tubing flaws. Further verification of the proposed signal processing scheme will be carried out by including laboratory-produced samples from the ANL steam generator mock-up facility.

Research on Degradation Modes and Integrity

Laboratory-induced cracking has been produced in a total of ≈450 22.2-mm (7/8-in.)-diameter Alloy 600 tubes under accelerated (chemically aggressive) conditions. These cracked tubes are being used for the evaluation of NDE equipment and techniques in the steam generator mockup and for pressure and leak-rate testing. The stress corrosion cracks produced in these tubes have six different basic configurations, namely circumferential cracks at the inner and outer (ID and OD) surfaces, axial cracks at the ID and OD, skewed cracks at the ID and OD. Cracking has also been produced in roll-expanded and dented tubes. In some cases, multiple and segmented cracks have been produced. The cracks are detected by visual inspection, dye penetrant techniques, and nondestructive eddy current inspection. Additional facilities for the production of cracked tubes are being constructed.

Additional tests have been conducted using the Pressure and Leak-Rate Test Facility on EDM axial notch OD flaws of several different lengths and flaw depth, including initial tests on multiple interacting flaws. An OD cracked tube produced by Westinghouse using doped steam has also been tested for comparison with results obtained earlier from four Argonne laboratory-degraded tubes. These tests addressed flaw leak stability behavior at constant temperature and pressure under normal operating and main-steam-line-break conditions. The tubes were tested at both room and elevated temperature to assess flaw behavior dependence on temperature. Testing of EDM and laser-cut axial and circumferential flaws with multiple interacting notches separated by various sized ligaments has also been initiated.

The tests conducted to date have yielded information on the influence of crack geometry, temperature, and pressure on flaw behavior, and pre- and posttest flaw characterization procedures. The results from these current tests may be summarized as follows:

1. Single axial throughwall and part-throughwall EDM notches of lengths 8.9, 12.7, and 25.4 mm were tested at room and elevated temperatures. The observed leak rates were well predicted by a circular hole orifice model after the flaw area was corrected for three dimensional curvature effects. For the two longest flaws as well as for the 38.1-mm-long flaws reported previously, the ligament rupture pressures and crack opening areas for the

part-throughwall flaws were well predicted by analytical methods. However, the 8.9-mm-long flaw exhibited a considerably larger ligament rupture pressure than predicted.

2. Tubes with two aligned axial EDM throughwall notches was tested to evaluate the influence of small ligaments on the link-up behavior of aligned axial flaws and on the resulting leak and flaw-opening pressures. The two aligned axial notches are each 6.35 mm long and 0.19 mm wide and were separated by a 0.25-mm-long ligament. Tests were conducted at both room temperature and 282°C. The flaw did not fail at pressures up to 17.2 MPa at room-temperature, and very little flaw distortion was observed, even though the ligament was calculated to tear at a pressure considerably less than 13.8 MPa. The observed leak rate through the flaw during the test was essentially identical to that calculated for the two individual notches using an orifice model. The companion tube tested at 282°C exhibited ligament tearing at 15.5 MPa, and the leak rate corresponded to that expected for a widened 12.7-mm-long notch. This ligament tearing appears to be the result of the somewhat reduced flow stress of Alloy 600 at 540°F.

3. A tube containing a nominally 12.7-mm-long axial OD crack produced by Westinghouse using doped steam was tested at both room temperature and 282°C. The flaw had a maximum depth of ≈90% throughwall, though local throughwall penetration of the crack was indicated by bubble testing. The tube was first tested at room temperature under extended hold times at 8.3 and 17.2 MPa. No leak was observed at the lower pressure. Likewise, no leak was initially observed at 17.2 MPa,, but a leak rate of ≈0.04 L/min was measured after a 3.25-h hold time and ≈0.068 L/min after an overnight hold time. Increasing the pressure to 18.6 MPa and holding for 5.5 h resulted in a leak rate of 0.12 L/min. The tube was then tested at 282°C and 18.6 MPa, and the leak rate increased from ≈0.30 L/min to 0.72 L/min during a 2-h hold. A posttest examination revealed that the flaw had opened slightly along its length. Thus, like three of four similar ANL laboratory-cracked tubes tested and reported previously, the Westinghouse tube exhibited a time-dependent increase in leak rate at constant pressure.

The design and construction of a room-temperature, high-pressure (0-51.7 MPa), low-flow-rate (0-48.4 L/min) High-Pressure Test Facility was completed, and shakedown and performance quantification testing were carried out. This facility complements the elevated-temperature Pressure and Leak-Rate Test Facility in that it permits the failure testing of tubes that cannot be failed at the 20.7 MPa maximum pressure of that facility. The continuous pressurized water supply in this facility also permits long-term crack stability and jet-impingement testing, since it is not limited by the 760-L blowdown vessel water inventory of the high-temperature Pressure and Leak-Rate Test Facility. In addition, the finite flow capacity of the High-Pressure Test Facility will permit testing of many leaking throughwall flaws without the use of internal bladders and foils.

Initial tests were conducted in the High-Pressure Test Facility using a tube with 0.79–mm (1/32-in.)-diameter sharp-edge circular orifice. Two test runs were made with the tube, the first with pressures plateaus up to 51.7 MPa (7500 psi) and the second with plateaus to 34.5 MPa (5000 psi). The pressurizer control operated very smoothly over the full range, and the pressure pulsations generated by the triplex pump, were small. The accuracy of the turbine flow meter readings was verified, and pump heating of the water was found to be controllable. The flawed tube was examined visually after each test, and interesting structural

changes were observed. Post-test examinations of the aluminum plate impacted by the jet from the specimen at a distance of ≈12.7 mm (5 in.) revealed two erosion craters, one for each test. The craters were nominally 1.6 to 3.2 mm (1/16 to 1/8-in.) deep and ≈3.2 to 6.4 mm (1/8 to 1/4-in.) wide. Additionally, some erosion of the circular orifice hole was detected after the first test, and the second test of this same tube yielded a higher flow rate than predicted by the circular hole orifice flow model. This suggests that the hole geometry/area was increased by jet erosion during the first test.

Following this, pressure tests on tubes with OD axial EDM throughwall and part-throughwall notches predicted to be unstable at <7500 psi were initiated. A total of 42 flawed specimens of several different designs have been fabricated, with some flaw geometries in triplicate for the assessment of test reproducibility. These notches are all 0.19 mm (0.0075-in.) wide and 6.35, 12.7, 19.1, or 25.4 mm (0.25, 0.5, 0.75, or 1.0-in.) long. The flaws are 60, 80, 90, or 100% TW. Upon completion of these tests, the facility will be used for testing tubes with SCC flaws or with complex segmented tight laser-cut notches.

Models for predicting the onset of crack growth and for calculating crack opening area and leak rate from a throughwall circumferential crack in a steam generator tube have been developed. It is shown that under normal operating and design-based accident conditions of PWRs, plasticity is confined to the plane of the crack. However, in failure tests conducted in the laboratory, plasticity spreads to sections away from the crack section. For typical steam generator tubes containing a circumferential throughwall crack at the top of tube sheet, any crack 180° or less in circumferential extent does not reduce the failure pressure from the burst pressure of an unflawed tube. Also, tubes with throughwall cracks ≥240° will behave as if they were fully constrained against bending and will have significantly greater failure pressures than the same tubes under free bending condition. For typical PWR steam generator properties, the longest throughwall circumferential cracks at the top of tube sheet that are predicted to experience onset of crack initiation during normal operation and design basis accident conditions are 310° and 340°, respectively. Crack opening areas during normal operation and design-basis accidents are small when compared with the tube cross-sectional area for a steam generator tube with ≤240°-throughwall crack at the top of the tube sheet. The driving force for crack instability, which is negligible as long as plasticity is confined to the crack plane, increases rapidly with plastic yielding away from the crack plane. However, failure by unstable tearing is more likely with short cracks (<180°) than with long cracks.

Failure pressures, leak rates, etc. depend on the mechanical properties (primarily the flow stress) of the tubing. The minimum ASME code requirements for yield and ultimate tensile strengths of Alloy 600 steam generator tube are 240 MPa (35 ksi) and 550 MPa (80 ksi), respectively, which correspond to a minimum flow stress of 400 MPa (58 ksi). Some of the older steam generators may have tubes with properties close to the code minima. The actual flow stress of steam generator tubes in most current plants can vary widely, depending on the age and heat of material used. In order to compare results on one material with results on a different material, the effect of variations in the mechanical properties must be accounted for, i.e., the results must be normalized in terms of the flow stress. The analyses of the pressure and leak rate tests have been used to develop procedures for accounting for flow stress effects.

Models for leak rate at room temperature and high temperature have been validated with leak rate tests on specimens with notched EDM slots. Simplified equations for calculating

crack opening area have been verified with finite-element calculations. The models for crack opening area and leak rate have been used to develop calibration curves for converting leak rate data from one material to a different material.

Detailed analyses of the tests on specimens with laboratory-grown SCC cracks show that if the pretest crack depth profile is reasonably uniform and deep (80-90%) as measured by eddy current +Point, a significant portion of the through-thickness crack tip ligament can rupture abruptly at a pressure that can be calculated by the ANL correlation. Post-test pictures of the OD surface did not reveal the presence of any surface ligaments in these specimens. Effective throughwall crack lengths estimated by the ligament rupture model using the eddy current plus point data are reasonably close to those estimated from the leak rate data and correspond closely to a segment of the crack that is >70% through wall thickness. In these specimens, the leak rate generally increased abruptly from 0 or ≤0.04 L/min to >19 L/min under increasing pressure loading, indicating sudden rupture of the ligament, and the leak rate did not increase under constant pressure hold subsequent to ligament rupture.

For specimens having highly non-uniform crack tip ligament thickness (as measured by eddy current +Point) with predicted ligament failure pressures that are greater than our system capability (i.e., 19.3 MPa), the ligaments can fail locally during constant pressure hold at a lower pressure than the predicted failure pressure. The effective throughwall crack lengths for these specimens can subsequently increase due to time-dependent ligament rupture both at room temperature as well as at 282°C. Based on very scant data, it appears that the time-dependent ligament rupture process occurs at a much slower rate (hours rather than minutes) in the higher strength Westinghouse tube than in the lower strength heat-treated ANL tubes. Also, the time-dependent rupture process occurs more rapidly at 282°C than at room temperature. A procedure for converting the constant pressure hold data on time-dependent leak rate from heat-treated tube to as-received tube has to be developed in the future.

In all the ANL specimens to date, the lengths of the throughwall segments of the cracks calculated from leak rate data are close to the lengths of the most open part of the cracks as evident visually from post-test pictures of the specimens. None of these pictures showed the presence of axial segments separated by ligaments. In one test, the post-test measured length of the throughwall segment of the crack (by a submerged bubble technique) is reasonably close to that calculated from the measured leak rate. In contrast to the ANL specimens, the calculated throughwall crack length for the Westinghouse specimen is much shorter than that observed visually. However, a post-test photograph of the OD surface of this specimen revealed at least three axial segments separated by ligaments showing that the effective throughwall crack length can be seriously underestimated from the measured leak rate if the effects of the ligaments on the crack opening area are not taken into account.

Under severe accident conditions, steam generator tubing can be subjected to very high temperatures. In some accident sequences, the temperatures of the tubing will be high enough (≈840°C) that even virgin, undegraded tubing can fail. If other primary system components fail prior to the time the steam generator tubing would reach the temperature at which it will fail, the system will vent inside the containment, the primary system will

depressurize, and the steam generator tubes will not fail. If the tubes reach failure conditions before another primary system component fails, a bypass event can occur.

Prediction of failure of a complex composite structure like Electrosleeved steam generator tube under severe accident transients is a difficult problem. The Electrosleeve material derives its strength from its nanocrystalline grain structure. At the high temperatures that are anticipated during severe accidents, rapid grain growth occurs, resulting in a loss of strength. When the review of the behavior of Electrosleeve repairs at high temperatures was initiated, only very limited data on the strength of the Electrosleeve material at high temperatures were available. Analytical models were developed to predict failure. The available data were used to determine the parameters of the models, but no confirmatory test results were available.

Two approaches for predicting failure of Electrosleeved tubes were developed. The first is an approximate analytical procedure based on a linear damage rule hypothesis analogous to that often used to analyze creep failures. The second is a more mechanistically based approach that accounts for the loss of flow stress due to grain growth. Initial studies showed the failure temperatures predicted by the two approaches were comparable, but the mechanistic model was used for most of the analyses.

After the initial development of the analytical model, FTI provided failure data from six tests on internally pressurized tubes that were subjected to a variety of temperature ramps simulating those expected during the most challenging severe accidents, namely "high–dry" sequences that can occur when the core melts, the primary side remains at high pressure, and the secondary side is depressurized. The initial comparison of the model with the actual tests on tubes showed that the predicted failure temperatures were within 35–70°C of those observed in the experiments. FTI also provided additional Electrosleeve specimens, and eleven tests were subsequently conducted at ANL. The results from these tests were used to refine the input parameters used in the analytical model. Using the refined model and more accurate data on the test geometries, the predicted temperatures in the FTI and ANL tests are within ±15°C of the observed temperatures.

The model predicts that Electrosleeved tubes with throughwall axial cracks ≤1 in. and throughwall 360° circumferential cracks in the parent tubes will survive "high–dry" transients based on the temperature histories for such sequences presented in NUREG–1570. Tubes with throughwall axial cracks of any length but crack depths ≤80% are also predicted to survive these transients. Electrosleeved tubes with throughwall axial cracks of any length or 360° circumferential cracks are predicted to survive severe accidents in which the primary system is depressurized significantly, such as SBO sequence with pump seal leakage.

Development of Methodology and Technical Requirements for Current and Emerging Regulatory Issues

Several test sections with cracks grown at Argonne were electrosleeved by FTI. Results of EC and ultrasonic (UT) examinations of two test sections are presented in this report. Although significant deterioration of the EC signal was observed after Electrosleeving, detection of relatively deep cracks (>40% TW) was found to be possible for both circumferential inner-diameter stress corrosion cracks (CIDSCC) and circumferential outer-diameter stress

corrosion cracks (CODSCC). For the CODSCC, CIDSCC and an EDM notch, the ultrasonic echoes have a very good signal-to-noise ratio. By using a frequency around 3–4 MHz, the distortion of the ultrasonic signal from the rough ID surface of the electrosleeve is minimized. By propagating waves nearly parallel to the tube axis, echoes can be generated from cracks that do not intersect either the ID or OD, a situation where the corner reflector, that can provide a strong echo for crack detection, has been eliminated.

Acknowledgments

Acronyms and Abbreviations

ABBCE	ASEA Brown-Boveri Combustion Engineering
ANL	Argonne National Laboratory
ASME	American Society of Mechanical Engineers
BC	bobbin coil
CIDSCC	circumferential inner-diameter stress corrosion crack/cracking
CODSCC	circumferential outer-diameter stress corrosion crack/cracking
DE	destructive examination
EC	eddy current
EDM	electrodischarge machining
EM	electromagnetic
EPRI	Electric Power Research Institute
ETSS	examination technique specification sheet
FEA	finite-element analysis
FS	free span
FSR	flow stress ratio
FTI	Framatome Technologies, Inc.
ID	inner diameter
IDSCC	inner diameter stress corrosion cracking
IGA	intergranular attack
IGSCC	intergranular stress corrosion cracking
ISG-TIP-2	International Steam Generator Tube Integrity Program—2
ISI	in-service inspection
LIDSCC	longitudinal inner-diameter stress corrosion crack/cracking
LODSCC	longitudinal outer-diameter stress corrosion crack/cracking
MP	multiparameter
MRPC	motorized rotating pancake coil
NDE	nondestructive evaluation
NRC	U.S. Nuclear Regulatory Commission
OD	outer diameter
ODSCC	outer-diameter stress corrosion crack/cracking
PNNL	Pacific Northwest National Laboratory
POD	probability of detection
PWR	pressurized water reactor
PWSCC	primary-water stress corrosion cracking
QDA	qualified data analyst
RR	round-robin
RT	room temperature
SBO	station blackout
SCC	stress corrosion cracking
SG	steam generator
S/N	signal-to-noise ratio
SS	stainless steel
SSPD	site-specific performance documentation
TGSCC	transgranular stress corrosion cracking
TS	tube sheet

TSP	tube support plate
TTS	top of tube sheet
TW	throughwall
UT	ultrasonic testing
VHN	Vickers hardness number

1 Introduction

The objective of this program is to provide the experimental data and predictive correlations and models needed to permit the U.S. Nuclear Regulatory Commission (NRC) to independently evaluate the integrity of steam generator (SG) tubes as plants age and degradation proceeds, new forms of degradation appear, and new defect-specific management schemes are implemented. The areas addressed by the program include assessment of procedures and equipment used for in-service inspection (ISI) of SG tubes, and recommendations for criteria and requirements to improve the reliability and accuracy of ISI; validation and improvement of correlations and models that are used to evaluate integrity and leakage of degraded SG tubes; and validation and improvement of correlations and models that predict the generation and progression of degradation in SG tubes.

The studies in this program focus primarily on Alloy 600 SG tubing in the mill–annealed condition, because this tubing material is (and will be) present in plants where SGs have not been replaced and because it is more susceptible to cracking than replacement materials such as thermally treated Alloy 600 or 690. Although most SGs that use mill–annealed Alloy 600 will probably require eventual replacement, the behavior of this material will be of concern for many more years.

The bulk of the materials used in the program will be exposed to simulated operating conditions and more aggressive environments representing accelerated conditions during laboratory testing. Because of the necessity to use accelerated conditions and because service degradation, tubing conditions, and in-service operating and inspection conditions cannot always be faithfully represented in laboratory conditions and specimens, this program has obtained and will use service-degraded tubing for correlation with and validation of experimental data, integrity and degradation predictive models, and inspection capability. Comparisons are being made with the morphology and character of service–degraded flaws to help ensure that the flaws produced in the laboratory and used for studies on inspection reliability, pressurization, and leak-rate testing will be as realistic as possible. The reliability of flaw detection and accuracy of flaw sizing data will be assessed by typical ISI personnel, procedures, and equipment.

This program is divided into four technical tasks and one management task:

1. Assessment of Inspection Reliability,

2. Research on ISI Technology,

3. Research on Degradation Modes and Integrity,

4. Integration of Results, Methodology, and Technical Assessments for Current and Emerging Regulatory Issues,

5. Program Management.

This annual report describes program activities and results from October 1998 through September 1999.

2 Assessment of Inspection Reliability (D. S. Kupperman and S. Bakhtiari)

The objective of the inspection task is to evaluate and quantify the reliability of current and emerging inspection technology for current-day flaws, i.e., establish the probability of detection (POD) and the capability to accurately size cracks. Both eddy current (EC) and ultrasonic testing (UT) techniques will be evaluated. The results of the NDE will be validated by inspection and destructive evaluation of service-degraded tubing.

A steam generator mock-up has been assembled for round-robin (RR) studies that will use currently practiced techniques and commercial teams. The mock-up will also be used as a test bed for evaluating emerging technologies for the ISI of SG tubes. The RR test will include both EC and UT methods. Teams will report the flaw types, sizes, and locations, as well as other commonly used parameters such as voltage responses, from the EC tests.

2.1 Steam Generator Tube Mock-up Facility

Assembly of the nine mock-up levels, each consisting of 400 0.3-m (1-ft.)-long Alloy 600 test sections, has been completed. Above the ninth level is a 0.91-m (3-ft.)-long run-out section (see Fig. 2.1 for tube bundle diagram). In addition to stress corrosion cracks (SCCs), test sections with dents (cracked and uncracked) have been installed in levels with tube support plate simulations. Flawed test sections in the tube bundle have been examined with both bobbin coil (BC) and three-coil (including +Point) rotating probes before assembly. After assembly, the tube bundle was examined with a borescope. This examination indicated some misalignment of test sections between level I and the three-foot runout sections. This misalignment was corrected by placing wooden spacers between the runout tubes and using a very long tapered rod that correctly aligns the test sections as the rod passes from level to level. In addition to a full EC examination, cracked test sections were examined with dye-penetrant before being incorporated into the mock-up tube bundle.

Simulation of magnetite in the tube support plate (TSP) crevice was accomplished by filling the crevice with magnetic tape or a ferromagnetic fluid. Sludge was simulated by a mixture of magnetite and copper. Sludge was placed above the tube sheet roll transition and above the TSP in some cases.

Magnetite-filled epoxy markers were placed on the ends of all test sections. These markers provide a reference for the angular locations of flaws when collecting data with a rotating pancake coil (RPC) or array probe. Figure 2.2 shows an isometric plot (c-scan) indicating the EC response from a 400-μm (0.016-in.)-wide x 250-μm (0.010-in.)-thick x 25-mm (1-in.)-long, axially oriented magnetite-filled epoxy marker located on the ID, at the end of a 22.2-mm (7/8-in.)-diameter Alloy 600 test section located in tube support plate simulation Level I. This test section also has an outer-diameter stress corrosion crack (ODSCC) at the TSP. These data were acquired at 400 kHz by using a 2.0-mm (0.080-in.)-diameter high-frequency shielded pancake coil rotating at 300 rpm with an axial speed of 5 mm/s. The epoxy marker can also be seen clearly with a 2.9-mm (0.115-in.)-diameter pancake coil at 300 kHz.

Back plate:
Carbon steel
(Drwng SGT17)

Carbon steel tubes,
914-mm (36-in.)-
long, 19.68-mm
(0.775-in.)-ID

Mechanical
slip fit
for Alloy 600
tubes

Polyethylene
plate

Alloy 600, 22.2-mm
(7/8-in.)-diameter
tube sections (3600)
are 305-mm(12-in.)
-long

Tube support plates:
Carbon steel
22.2-mm (3/4-in.)-
thick (Drwng SGT11)

Divider plates (9):
Polyethylene
22.2-mm (3/4-in.)-
thick (Drwng SGT13)

Simulated tube
sheet 152-mm
(6-in.)-
carbon-steel-
collar, over
Alloy 600 tube]

Eddy current
probe

Spacer plate: Aluminum
6.3-mm (1/4-in.)-thick (Drwng SGT18)

Tube bundle base plate: Carbon steel
12.7-mm(1/2-in.)-thick(Drwng SGT15)

Tube bundle support plate: Carbon steel
25.4-mm (1-in.)-thick

Fig. 2.1. *Schematic representation of steam generator mock-up tube bundle.*

A second type of circumferential reference marker has also been evaluated. Figure 2.3 shows the results using an epoxy-coated strip of 25-μm (0.001-in.)-thick magnetic tape. An isometric plot (c-scan) shows the EC response from a 100-μm (0.004-in.)-wide x 100-μm (0.001-in.)-thick x 20-mm (0.79-in.)-long, axially oriented epoxy-coated strip of magnetic tape located on the inner diameter (ID) at the end of a 22.2-mm (7/8-in.)-diameter Alloy 600 test section. These data were acquired at 300 kHz with a 2.9-mm (0.115-in.)-diameter standard pancake coil rotating at 300 rpm with an axial speed of 5 mm/s. This type of marker could

3
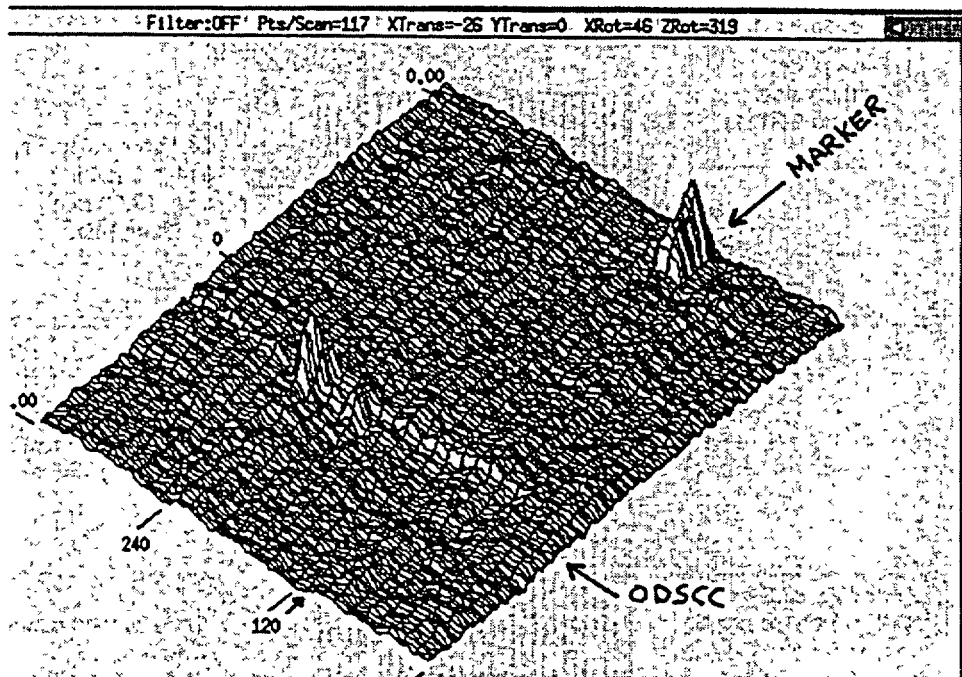
Fig. 2.2. *Isometric plot (c-scan) showing eddy current response from 400-μm (0.016-in.)-wide × 250-μm (0.010-in.)-thick × 25-mm (1-in.)-long, axially oriented magnetite-filled epoxy marker located on ID at end of 22.2-mm (7/8-in.)-diameter Alloy 600 tube. This type of marker is being used as a circumferential reference for location of flaws in mock-up test sections. Data were acquired at 400 kHz with a 2.0-mm (0.080-in.)-diameter high-frequency shielded pancake coil rotating at 300 rpm with axial speed of 5 mm/s. ODSCC in simulated tube support region can also be seen.*

also provide a circumferential reference for location of flaws in mock-up test sections but was not selected for the final assembly.

To ensure the uniformity of epoxy markers, a special tool was fabricated for quick removal of excessive epoxy without scratching the tube wall. All test sections of assembled levels were cleaned and checked for obstruction and alignment with both a bobbin coil (BC) and a motorized RPC (MRPC) probe.

A magnetically biased three-coil probe that includes a +Point, 2.9-mm (0.115-in.)-diameter pancake and high-frequency shielded coil has been used on sensitized tubes with flaws. A comparison of magnetically biased and unbiased coils shows that the biasing eliminates the voltage shift and noise in the EC signal resulting from the tube sensitization.

All of the EC files accumulated for Task 1 were entered into a spreadsheet (Excel 4.0). About 5000 scans of tubes with various combinations of flaws and artifacts from both rotating and bobbin coil probes have been accumulated and stored. The spreadsheet permits quick reference for locating the optical disk and file number for any scan of a test section. Each line in the spreadsheet has the tube identification number, type of probe used, flaw type, source of flaw, and nature of artifact if one was used in collecting the data. The spreadsheet allows an
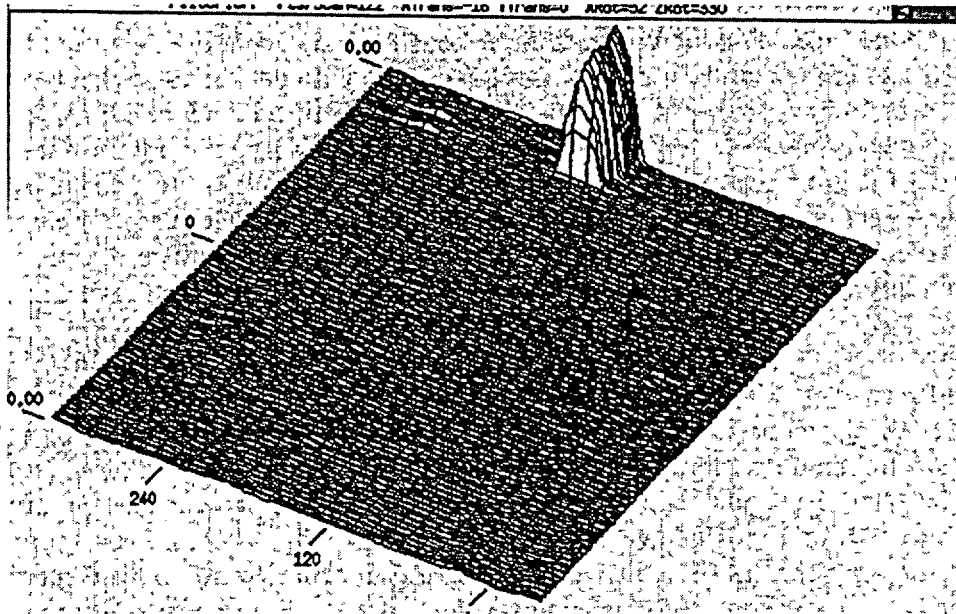
Fig. 2.3. *Isometric plot (c-scan) showing eddy current response from 100-μm (0.004-in.)-wide by 100-μm (0.004-in.)-thick by 20-mm (0.79-in.)-long, axially oriented epoxy-coated piece of magnetic tape located on ID at the end of 22.2-mm (7/8-in.)-diameter Alloy 600 tube. Data were acquired at 300 kHz with a 2.9-mm (0.115-in.)-diameter standard pancake coil rotating at 300 rpm with axial speed of 5 mm/s. This type of marker could provide a circumferential reference for location of flaws in mock-up test sections.*

easy search of the optical disk location and file number for any scan, given the tube identification number, acquisition date, artifact used, probe type, flaw type, or source of flaw. This spreadsheet is backed up on floppy disks and on an Argonne National Laboratory (ANL) computer backup system.

2.2 Round-Robin Protocol and Procedures

A comprehensive review of Task 1, including examination of EC signals from mock-up flaws, was made during the International Steam Generator Tube Integrity Program–2 (ISG-TIP-2) meeting held at ANL on October 19-23, 1998. Additional review was provided by the NDE Task Group. They provided suggestions related to (a) the selection of probes for the round robin, (b) the use of artifacts, and (c) the documentation of procedures for the mock-up assembly to ensure that flaws are correctly located, which have been incorporated into the planning for the conduct of the round robin testing.

A magneto-optical disk with eddy current (EC) data from 24 degraded mock-up test sections was prepared for review by the NDE Task Group. The data were previously examined by industry analysts to confirm that the EC signals from the test sections adequately simulate signals from field flaws. The disk contains 67 separate files for the 24 flaws. The flaws were scanned with a bobbin coil (BC) probe and a three-coil probe that includes a standard 2.9 mm (0.115-in.)-diameter pancake coil, +Point coil, and the 2.0-mm (0.080-in.)-diameter high-frequency shielded coil. All test sections scanned are Alloy 600, 22.2 mm (7/8 in.) in diameter

and 0.30 m (12 in.) long. For each scan, the probe passes through the degraded test section, a standard with 18 notches, and an ASME standard. To locate data files associated with a given test section, a table was prepared that shows (a) the type of flaw scanned; (b) location of the data file on the disk provided, and (c) whether the flaw is in a free span (FS), has a ring over it to simulate the tube support plate (TSP), or whether the tube has a steel collar over the lower half of the test section to simulate the tube sheet (TS). The table also indicates whether a simulated artifact (either a ring of sludge or a ring of magnetite) covers the area of the flaw. Other information indicates the test section identification number, location of the original data file at ANL, and which probe was used to generate the EC data.

A second review of EC data from mock-up flaws by members of the Task Group was held at the EPRI NDE Center in Charlotte, NC on May 12 and 13, 1999. More than 2000 scans were available for examination. EC signals from flaws with and without artifacts were compared. Suggestions made at the meeting with regard to improving the quality of the data that would be used for the RR have been implemented. The main improvements in the EC system were the replacement of cables and a slip ring in order to minimize electronic noise in the EC signals. Mag-biased MRPC will be used to eliminate noise problems resulting from sensitization of test sections in the crack-growing procedure in all but a few of the sensitized pieces. The problem associated with a few of the sensitized test sections when using a pancake coil (but not +Point), was addressed by modifying the test procedure.

Documents that provided technical direction for the EC examination, Site Specific Performance Demonstration, and Examination Technique Specifications Sheets were prepared based on input from NDE Task Group members on current industry practices. The documents were reviewed by the Task Group and by ANL personnel, leading to several suggested changes that have been incorporated into revised versions.

2.3 Data Acquisition from the Mock-up

Nine color-coded maps of each level of the mockup have been completed. In addition, 17 color-coded maps have been prepared to show each row. This format allows the status (flaw, artifact, etc.) of each test section in a tube to be easily verified by ANL staff during EC examination of the tube. Graphs and tables showing the distribution of flaws as a function of type have also been prepared.

During June 1999, a three-man team from Zetec collected data from the mock-up (Figs. 2.4 and 2.5). An observer from Westinghouse was also present. The data acquisition team included a QDA Level IIa and a QDA Level IIIa. Data were acquired with a 10-D pusher-puller, MIZ30 with 36-pin cables, and Eddynet software. Before data acquisition, misalignment of three test sections had to be corrected by using the same procedure developed for the mock-up before it was placed on its stand (moving the tube bundle from floor to stand probably was the cause of the additional tube misalignment). BC data from a mag-biased probe was collected from 3600 test sections of the mock-up. The BC data were calibrated before and after the 4-h interval required to collect the data. No change in voltage from the standard was detectable during this time period.

The BC data were taken at 0.53 m/s (21 in./s), maintaining a digitization rate of 37 samples per inch. Bobbin coil data were taken at 400, 200, 100, and 20 kHz (differential and
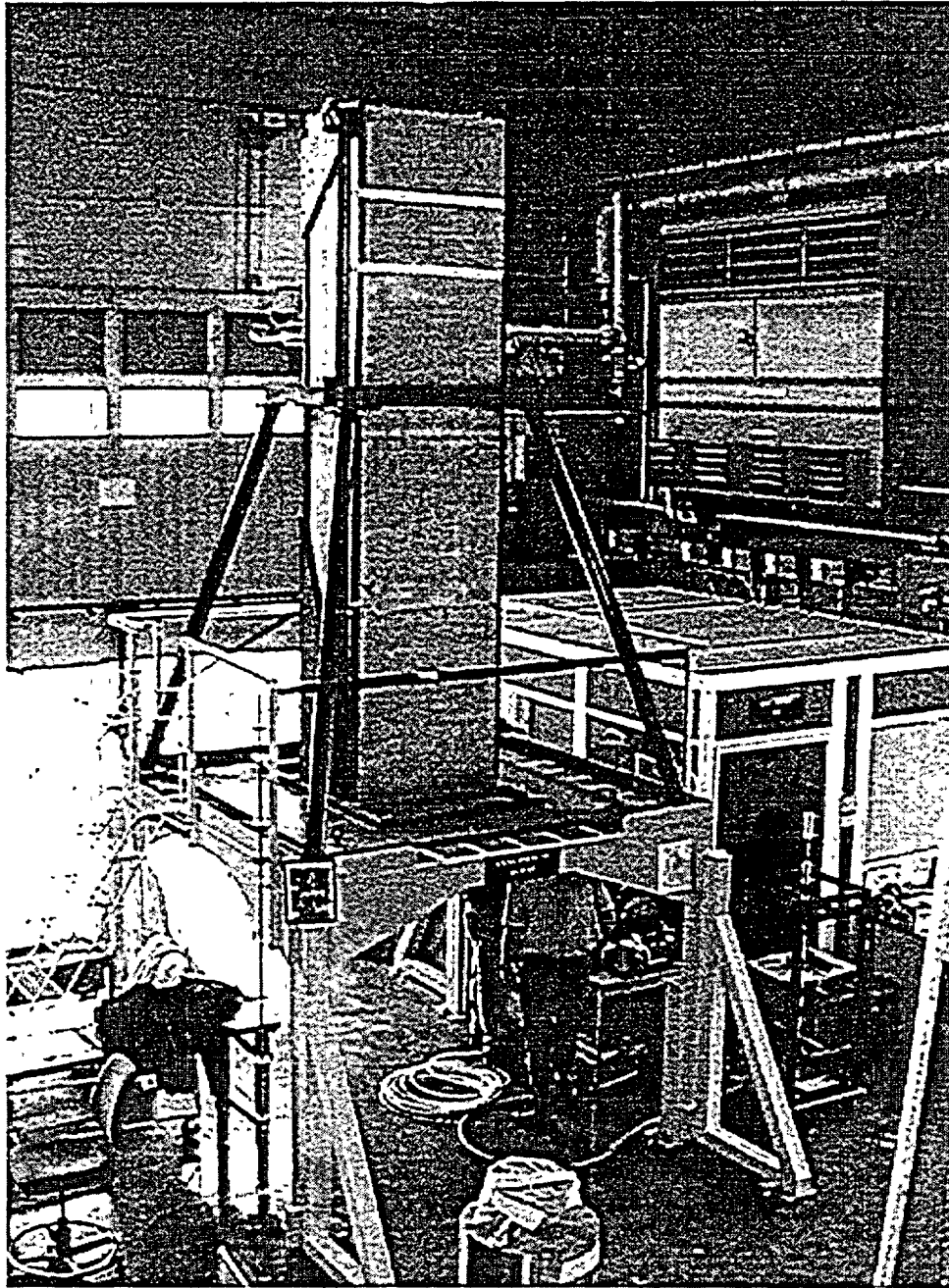
Fig. 2.4.   Photograph of activity during acquisition of eddy current data by Zetec team.

absolute). MRPC data was taken from all degraded test sections in addition to many test sections with artifacts and many clean test sections. The three-coil mag-bias probe used consisted of a 2.92-mm (0.115-in.) pancake, a +Point, and a 2.0-mm (0.080-in.) high-frequency shielded coil. An ASME standard and a standard with 18 ID and OD axial and circumferential EDM notches (20, 40, 60, 80, and 100% throughwall) were used for calibration. MRPC data were taken at 900 rpm and an axial speed of 12.7 mm/s (0.5 in./s) to maintain a digitization rate of 30 samples per inch in the circumferential direction and 30 in

7
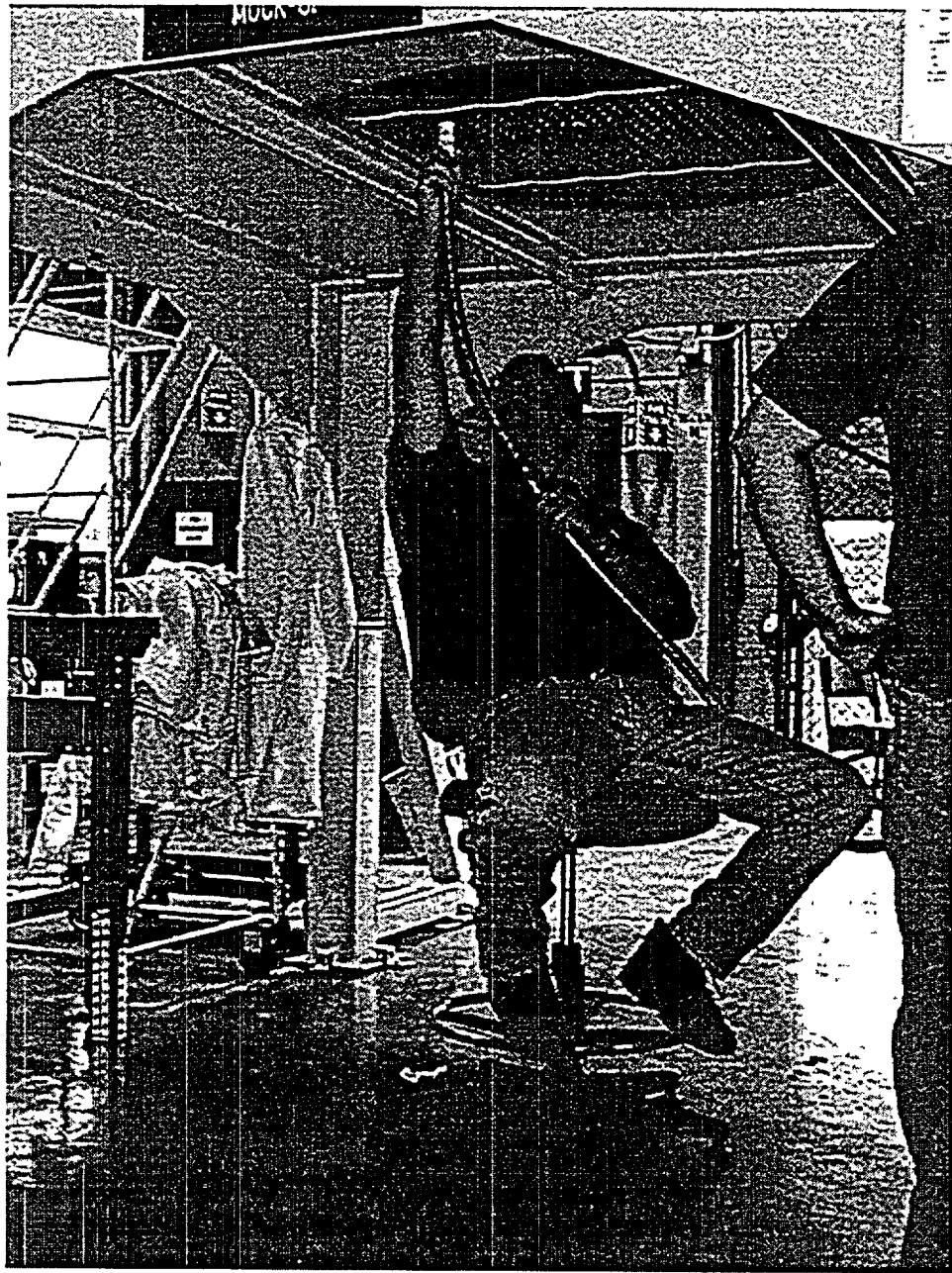
Fig. 2.5. *Photograph of underside of tube bundle. Conduit carrying the EC probe is shown being positioned under a tube.*

the axial direction. Data were taken at 600, 400, 300, 200, and 100 kHz. A total of nine MRPC probes containing the +Point, pancake, and high-frequency coils were used during this exercise because of probe wear. The probes were replaced when one of the channels could not be nulled. The MRPC probe wear rate exceeded expectations.

All data were collected on a 2.6-GB magneto-optical disk. Two copies of the master disk were made, and all the data were copied to an ANL archive computer back-up system. The quality of the data collected was judged to be good. The set-up for the bobbin coil and +Point

probe matches or exceeds the specifications of the examination technique specification sheets (ETSSs) qualified for the flaws in the tube bundle.

The mock-up data collected by Zetec was analyzed at ANL by ANL personnel with Eddynet98 software. The purpose was to review the BC signals and MRPC signals to confirm that they are similar to field data. In addition, the locations of the flaw signals were checked against the location data of the flaw map. Locations of possible dings due to assembly that could lead to significant EC signals were noted. These dings could be created if a test section were inadvertently pressed against the simulated TSP during assembly. A preliminary review shows about ten possible dings near the test-section ends.

During the week of August 9th, Cheryl Gortemiller of Moretech analyzed the ANL steam generator mock-up bobbin coil data and some of the MRPC data acquired by Zetec. Her review was much more comprehensive than of the NDE Task Group. The purpose was to an additional independent expert opinion on the representativeness of the mock-up EC indications. The overall quality of the data was judged to be good and to be generally representative of field data. Gortemiller commented that, in her opinion, the data from intergranular attack (IGA) did not look like data from field IGA (a similar opinion was expressed by many of the NDE Task Group). This comment ultimately resulted in a call to Westinghouse to discuss the differences between IGA specimens they fabricated for the mock-up and IGA of current field interest. The mock-up IGA is "pure" in that it is not mixed with other cracks. Westinghouse argued that the IGA they prepared for the mock-up simulates IGA found in the tube sheet crevice and is representative of the IGA at Cook, Point Beach, and San Onofre,.

EC signals from dings not previously known to exist in the mock-up were also observed by Gortemiller. Presumably, these dings were introduced inadvertently during the assembly of the mock-up tube bundle. As a result of this data review, important knowledge on how to prepare the site training document was acquired. An example of the IGA in the mockup was included in the "site" training sample set.

Gortemiller's review of the data was presented at an NDE Task Group meeting held August 24-26, 1999, at Argonne. The meeting was attended by S. Bakhtiari (ANL), C. Gortemiller (Moretech), G. Henry (EPRI), D. Kupperman (ANL), R. Maurer (ABBCE), D. Mayes (Duke), R. Miranda (FTI), S. Redner (Northern States Power), T. Richards (FTI), and B. Vollmer (Zetec). As a result of this meeting, the Degradation Assessment and Site Applicability documentation, ETSSs, Analysis Guidelines, and Data Acquisition documents were subsequently revised. In addition, opinions were expressed on how to handle "spin calls" (MRPC examination of test sections in which nonquantifiable or distorted indications were found by BC examination), how to handle the logistics of distributing EC data to the various teams, what should be in the training documentation, and what equivalency demonstrations need to be carried out. Following the meeting, for the purpose of demonstrating equivalencies, data were taken from notches, cracks, and dents at 900 rpm and 12.7 mm/s (0.5 in./s) and 300 rpm at 2.54 mm/s (0.1 in./s). In addition, data from mock-up flaws were taken with mag- and non-mag-biased rotating coils.

Other input from the NDE Task Group meeting included a suggestion to have a separate ETSS for sizing depth and length of axial and circumferential primary water stress corrosion cracking (PWSCC) based on the two qualified techniques. In addition, an opinion was

expressed that the round robin team should consist of five members. A five-member team would include a primary, a secondary, and two resolution analysts, and an independent qualified data analyst (QDA) from a utility. Names of possible independent QDAs were provided by the Task Group.

Following the Task Group meeting, BC data from the mock-up were analyzed to show the distribution of voltages and distribution of crack depths, based on pre-mock-up assembly data. The histograms show a good distribution of BC voltages and crack depths. In addition, prints of MRPC Lissajous figures and isometric plots were generated for each of the flaws in the tube bundle.

Following the August 24-26 NDE Task Group Meeting, an extensive effort was made to revise the RR documentation as a result of opinions and suggestions from Task Group members. The Analysis Guideline (ANL001) text was revised. The inspection teams were planned to include primary and secondary analysts, along with two resolution analysts and an independent QDA. The ETSSs 1 and 2 for bobbin and rotating coil probes, which are part of ANL001, were corrected and modified. Preparation of the ETSSs for sizing was started. They will be based on EPRI ETSSs 96702 and 96703, which have been developed for sizing PWSCC. Although qualified only for PWSCC, these ETSSs will form the basis for profiling both ODSCC and PWSCC. The document ANL002, ("Multi-Frequency Eddy Current Examination of Tubing within the ANL SG Mock-up"), was revised based on input from Todd Richards of FTI. The Steam Generator Mock-up Tubing Degradation Assessment and Technique Qualification (ANL003) was revised extensively by using new EC signal graphics that better represent the various types of flaws in the mock-up. The revised documentation was distributed to the Task Group. Further modifications are anticipated as additional comments are received following review of the revised documents.

Preparation of the Training Manual was begun. Flaws have been selected for the manual to provide an example of each type of degradation and potential artifact. The training manual will include an IGA example.

Tests have been performed to show equivalency of mag- and non-mag-biased probes. Data using both types of probes have been obtained for several mock-up flaws using all the frequencies employed in the mock-up data acquisition. Figure 2.6 shows data from a mag-biased +Point coil. Figure 2.7 shows data from the same flaw obtained with a non-mag-biased coil. The signals are virtually the same. Problems do occur for a small number of test sections that were fabricated from a heat of material different from those used for the rest of the mock-up specimens. For these test sections, using a mag-bias pancake coil could result in a phase shift, relative to a non-mag-biased coil of up to 90°. This problem does not occur with the +Point coil (i.e., the phase from a flaw is the same for both mag- and non-mag-biased +Point coils regardless of the heat of material). Tests have also been performed to show equivalency between an MRPC operating at 900 rpm [12.7 mm/s (0.5 in./s)] and an MRPC operating at 300 rpm [2.54 mm/s (0.1 in./s)]. Figure 2.8 shows a Lissajous figure from a mock-up flaw at 300 rpm (2.54 mm/s) using a +Point coil. Figure 2.9 shows a Lissajous figure from a mock-up flaw at 900 rpm (12.7 mm/s) using the same +Point coil as for data in Fig 2.8. The signals are almost indistinguishable. Similar results have also been seen for other frequencies and coils.
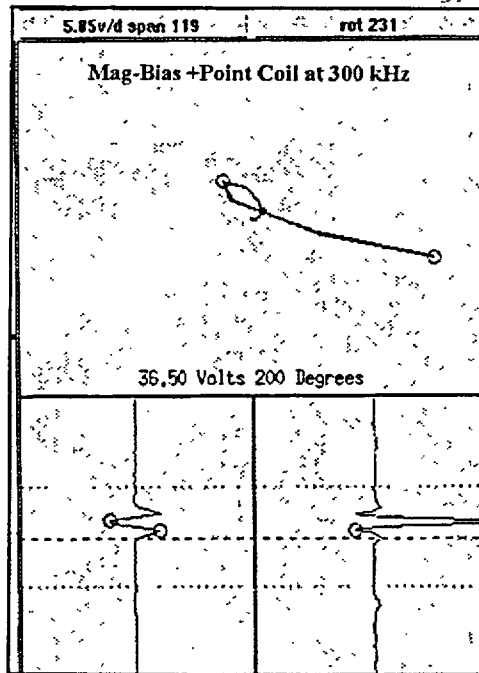
Fig. 2.6. Lissajous figure from mock-up flaw (in sensitized test section) obtained with mag-biased +Point coil at 300 kHz
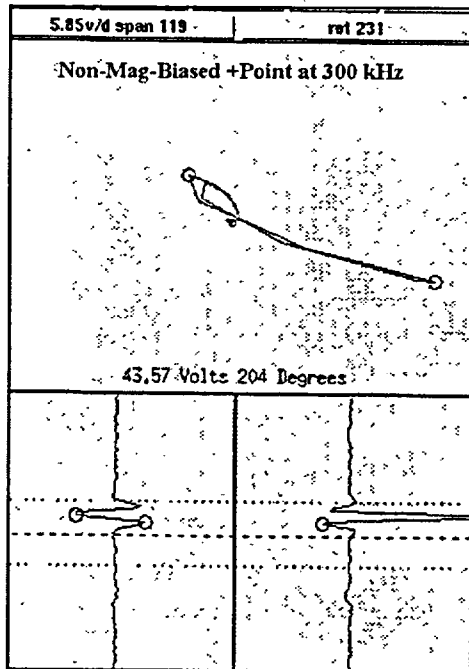
Fig. 2.7. Lissajous figure from same mock-up flaw as in Fig. 2.6 obtained with a non-mag-biased +Point coil at 300 kHz

11
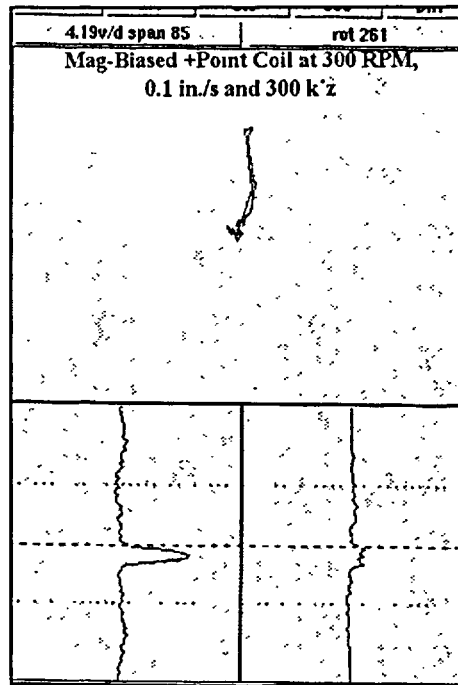
Fig. 2.8.   *Lissajous figure from mock-up flaw (in sensitized test section) obtained wtih a mag-biased +Point coil at 300 rpm, 2.54 mm/s (0.1 in./s) axial speed, and 300 kHz.*
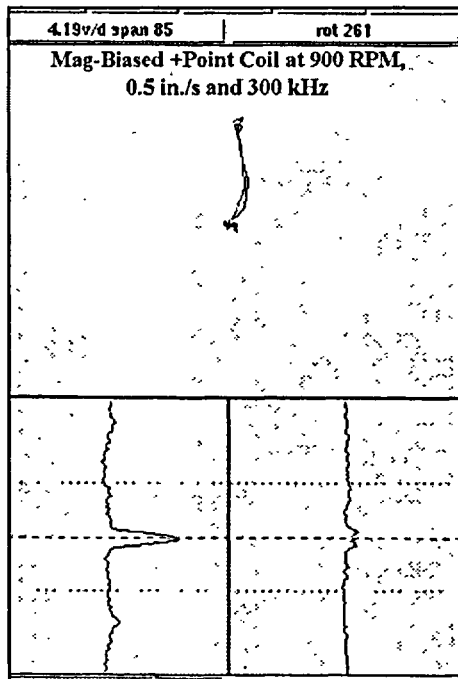
Fig. 2.9.   *Lissajous figure from mock-up flaw (in sensitized test section) obtained with a mag-biased +Point coil at 900 rpm, 12.7 mm/s (0.5 in./s) axial speed, and 300 kHz.*

2.4 Effect of Surface Oxide Films on Eddy Current Signals from SCC

The effect of corrosion products (thin oxide films) formed on crack faces on the EC signal from an SCC is under evaluation. Alloy 600 tubes with axial ODSCC were exposed under PWR water chemistry conditions (300°C and 3-8 ppb oxygen) for about two months. The cracks have been examined with both mag-bias bobbin coils (BCs) and a +Point coil before and after corrosion products were formed. The voltages for the BCs increased significantly with the creation of the thin oxide film. However, the general shape of the Lissajous figures remained unchanged. In contrast, the results for the +Point coil were inconclusive. In two cases, no change in +Point voltage was observed, while in a third, the voltage dropped significantly after the oxide film was formed. Figure 2.10 shows the BC Lissajous figure, along with voltage and phase information for one of the tubes. Table 2.1 summarizes the BC results for two tubes. While voltages increased significantly, the phase angle did not. The creation of corrosion products in the crack could lead to a reduction in the number of electrically conducting paths from contacting crack faces. In that case, the EC signal would be expected to increase, as observed, while the depth remains essentially the same.

2.5 Comparison of BC Voltages from Notches and ODSCC

The similarity of BC voltages for notches and cracks of comparable depth and length is illustrated in Table 2.2, which presents BC voltages for notches, four axial ODSCCs generated at ANL, and one ODSCC generated at Westinghouse.

For notches and cracks in the 80-90% TW range, the BC voltages appear comparable, with variations in voltages being attributed to profile variations. Variations in BC voltage for cracks, over the voltage range shown in Table 2.2, lead to relatively small changes in predicted failure pressure if the estimated failure pressure is from the alternate plugging criteria voltage-burst-pressure model for axial ODSCC at the TSP.

2.6 Comparison of Voltages from McGuire and ANL SCC

An indication that the cracks grown at ANL are representative of field cracks comes from a comparison of McGuire steam generator BC voltages and phases with-ANL SCC BC voltages and phase. Figure 2.11 shows McGuire voltages and phases from axial ODSCCs at TSPs, together with voltages and phases from the ANL-grown axial ODSCCs. The plots of voltage vs. phase are comparable.
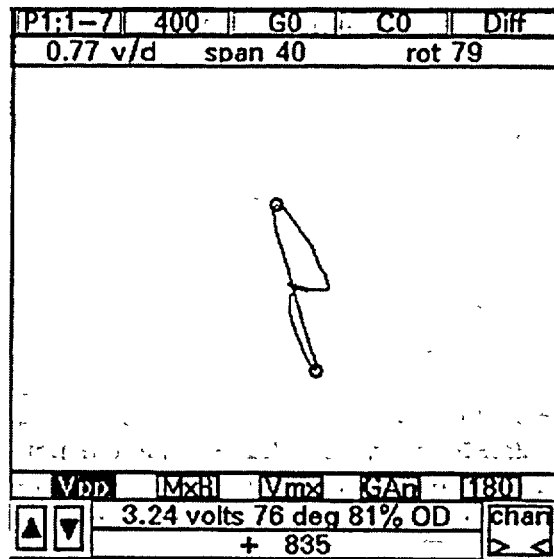
Fig. 2.10. *Mag-bias BC Lissajous figure after corrosion products (thin oxide film) were formed in a tube with axial ODSCC by exposing the tube to PWR conditions for ≈2 months. Voltage increased from 2.43 to 3.24 volts, suggesting less contact at crack faces. Estimated depth changed from 87 to 81% TW.*

Table 2.1. *Comparison of BC voltages and phase for two tubes before and after treatment to produce a surface oxide film. Each tube has an axial ODSCC ≈15 mm (0.60 in.) long.*

Tube #	BC Voltage	BC Phase Angle	BC % TW
SGL-197 (before)	2.43	66°	87
SGL-197 (after)	3.24	76°	81
SGL-149 (before)	3.27	87°	73
SGL-149 (after)	4.51	89°	72

14

Axial ODSCC
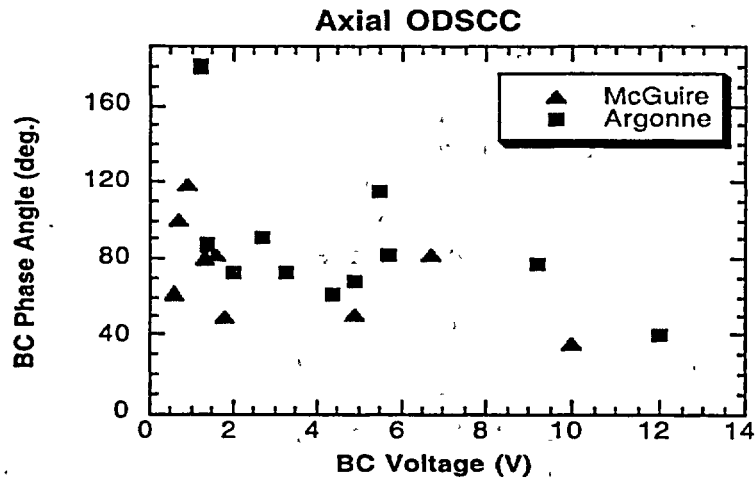
McGuire ▲
Argonne ■

Fig. 2.11. Comparison of McGuire steam generator D BC voltages and phase from axial ODSCCs at tube support plates to voltages and phase from ANL-produced axial ODSCC. Ranges of plots are comparable.

3 Research on ISI Technology (S. Bakhtiari and D. S. Kupperman)

The objective of this task is to evaluate advanced NDE and signal analysis techniques for the reliable in-service inspection (ISI) of original and repaired SG tubes. Improved correlations between EC probe response and flaw morphology, leak rate, and failure pressure will be developed and validated. In addition, the reliability of the voltage parameter and other EC parameters and techniques will be evaluated with respect to their ranges of applicability.

The present research on improved ISI of SG tubes focuses on four primary areas: (a) implementation of analytical methods for prediction of EC response as a function of probe design, flaw characteristics, and material properties; (b) development of effective signal analysis procedures; (c) development of flaw imaging and display methods for simple and accurate flaw characterization; and (d) evaluation of improved probe designs that may use directional arrays so that defects of arbitrary orientation can be examined simultaneously. The reliability and effectiveness of improved inspection techniques and the robustness of potential correlations will ultimately be substantiated through laboratory testing of the SG tube bundle mock-up and of SG tubes that contain various flaw morphologies. Final validation will also utilize in–service-degraded SG tubes.

Task 2 activities during the present reporting period are described here. Research efforts that are associated primarily with multiparameter analysis of EC NDE results are discussed. Representative test cases are presented in Sec. 3.1 for a study initiated to evaluate potential advantages of alternate multifrequency mixing techniques involving more than two frequencies over standard two-frequency mixes. These alternate techniques could help improve BC detection of flaw indications in the presence of interfering signals. Multiparameter data analysis is discussed in Sec. 3.2. Initial analysis of the results is provided on a set of 20 laboratory-grown specimens with various forms of cracking degradation. Flaw morphologies in these tubes are representative of those incorporated into ANL's tube bundle mock-up. Eddy current rotating probe readings on this set were analyzed by using an automated multifrequency data analysis algorithm that is currently under evaluation. Subsequently, analysis results are presented for a single laboratory-produced mockup specimen that exhibited a reportable BC signal without a clear rotating probe indication. Data analysis results are presented on a set of 24 laser-cut specimens with single and multiple axial/circumferential notches (with and without ligaments) that simulate complex cracking geometries. The NDE and nominal flaw size for this set of tubes, originally constructed for high-pressure studies under Task 3 of this program, provide a useful means for assessing data analysis algorithms currently under investigation at ANL. Finally, in Sec. 3.3, results are presented from a recent study on the application of a signal restoration technique to enhance the spatial resolution of rotating probes. The pseudo-deconvolution scheme described here has been integrated as part of the multiparameter data analysis algorithm to further help improve characterization of complex SG tubing flaws.

3.1 Multifrequency Mix for Improving Bobbin Coil Detection

Preliminary results are presented on two separate multifrequency mixing procedures that could possibly improve BC detection of flaw indications in the presence of interfering artifacts at the same axial location along the tube axis. This investigation was initiated in part to

evaluate alternate mixing methods that might help compensate for lack of similarity between simulated artifacts in tube standards and those in the field. All the data conversions and calibrations in this study were carried out automatically by using MATLAB-based graphical user interface (GUI) tools that have been developed at ANL and described previously.[1]

3.1.1 Direct and Indirect Mix Processes

Recovery of defect-induced signals in the presence of strong background interference is an important and often challenging NDE problem when analyzing NDE results for ISI of SG tubing. Data analysis is further complicated when degradations are accompanied by tube ID variations such as design-related tube diameter changes or the presence of significant denting. These difficulties are associated with such factors as low S/N ratio and small phase separation between ID and deep OD indications. Multifrequency mixing is routinely applied to improve detection of flaw signals that are obscured by tubing artifacts. However, the mix channel information should be analyzed discerningly, particularly when more than two frequencies are used in the process. Conventional two-frequency least-squares (LS)-based mix algorithms that are optimized primarily to suppress a single OD artifact generally provide consistent outcomes. On the other hand, processed channel information from mixing algorithms that incorporate more than two frequencies could be unreliable for the interpretation of signals outside the segment where the mix coefficients were calculated. This is due in part to uneven perturbation of the signal amplitude and phase information that is introduced by higher-order (nonlinear) mix models.

Two separate approaches, direct (independent) and indirect (dependent) mixing algorithms, to suppress multiple unwanted indications from a composite signal were considered in this study. In an indirect mix, regression coefficients are determined by using a data segment from a simulated artifact such as a TSP ring on a reference standard tube, which is expected to closely resemble those present in the actual SGs. The aim of the regression model is to best reproduce the primary/base frequency signal by combining signal components from auxiliary frequency channel(s). This is the conventional approach used for the analysis of EC ISI results. Alternatively, independent mix procedures have the potential to suppress unwanted signals by using multiple-frequency readings on the same tube. This approach, primarily suggested for suppression of dominant signal features, is of particular interest when tube standards with simulated artifacts that resemble field-induced signals are not readily available. Representative test case results are presented next on recent studies associated with direct and indirect mixing techniques.

To initially evaluate the direct mixing approach, a simulated composite BC signal was constructed by using normalized EC readings from an ASME tube standard. Individual signal components consisted of a simulated TSP ring and 10 and 20% ID circumferential grooves. The main objective was to develop a mixing procedure that would allow recovery of the shallow OD indication from the composite signal with minimal perturbation of the signal outside this region. A standard linear LS regression algorithm was initially utilized in this study. Various two- and three-frequency regression fits were implemented. Preliminary results indicated that two-frequency mixes are generally more consistent, so the approach was to sequentially apply two-frequency mixes for suppression of two unwanted indications at the same axial location. To improve the mix outcome, several modifications were made to our previously developed[1] standard mix algorithm. These consisted of energy-scaling each trace, resampling in

17

frequency domain, and phase-angle referencing. Frequency resampling was done to increase the number of available independent variables. Phase-angle tracking was done to help reduce phase ambiguity from multiple application of linear regression coefficients. Based on the small number of cases tested so far, the amplitude renormalization consistently exhibited improved quality of mix outputs. This is believed to be a result of the weighting introduced by the energy-scaling process. It is worth noting that this transformation does not significantly perturb the original phase information of original channels (i.e., the lissajous patterns remain nearly unchanged).

Figure 3.1 shows the horizontal and vertical differential signal components of the calibrated original (top) and renormalized (bottom) traces at f = 400 kHz. The drilled-hole signal was added to each trace to serve as the phase reference indication. Figure 3.2 shows intermediate results of the mix obtained by using a high- and low-frequency signal to suppress the TSP indication from each trace. Figure 3.3 displays the recovered differential and absolute channel signals for the shallow OD indication subsequent to combining the two intermediate mix outputs. In both cases, the 10% OD groove was recovered from the original composite trace. It should be noted that the three-frequency mix outputs shown in Fig. 3.3 do not contain the identical phase angle information as the original traces. Nevertheless, the results show significant improvement over standard three-frequency LS mixing procedures that were examined as part of this study.

To assess the validity of independent mix algorithms, BC readings on two tubes with laboratory-grown circumferential and axial SCC at tube sheet (TS) roll transition regions were utilized for analyses. Available metallography results indicate depths of 30% ID for the circumferential and 100% TW cracking for the axial flaw. The specimens used here were part of a 20-tube set of representative mock-up specimens furnished by Pacific Northwest National Laboratory (PNNL). With reference to Fig. 3.4, the indications from left to right consist of 100% TW hole and two roll transitions with ID circumferential and OD axial SCC flaws, respectively. Once again, a throughwall indication from the ASME standard was attached to the beginning of each trace to serve as the phase reference. Figure 3.4 displays both the calibrated original and the renormalized traces at f = 400 kHz. As in the case of direct mixing, regression coefficients were initially calculated for suppression of roll transition signals. The two intermediate mix outputs were once again produced by using the signal components from a high- and a low-frequency channel to suppress the strong signal from the tube diameter change. However, unlike the indirect mix, data from the first roll transition were used to suppress the artifacts. Subsequently, a final mix process was applied to recover the residual signal that is expected to contain information predominantly about the flaw.

Figure 3.5 displays the results of the independent mix for the differential and absolute channels, respectively. In both traces, the residuals at the roll transition regions (located approximately around data points 350 and 750) exhibit the presence of SCC flaws. A notable feature of the processed signal is the phase separation between the two indications and their relationship to the throughwall reference signal. This phase information cannot be recovered consistently with conventional multifrequency mixing techniques. Further evaluation of multifrequency mixing algorithms is currently being pursued under this program, and a more detailed discussion of the findings will be presented in future reports.
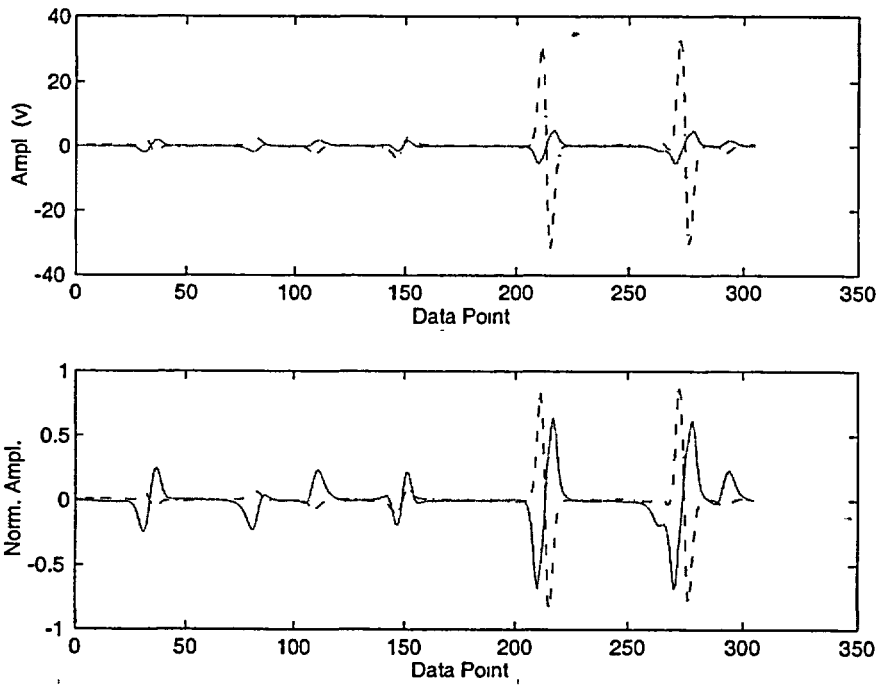
Fig. 3.1.   *Differential BC horizontal and vertical signal components of calibrated original (top) and renormalized (bottom) traces at f = 400 kHz. Simulated indications from left to right consist of throughwall drilled hole, TSP ring, 10% OD and 20% ID circumferential grooves, and composite (of last three indications) signal.*
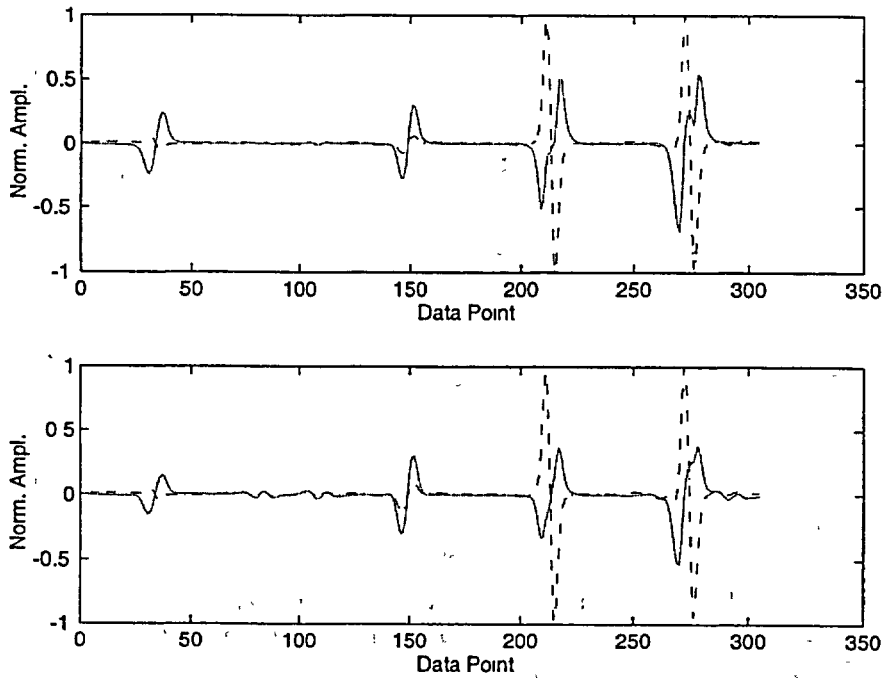
Fig. 3.2.   *Intermediate mix outputs using high- and low-frequency signals to suppress TSP indication from bottom trace shown in Fig. 3.1.*
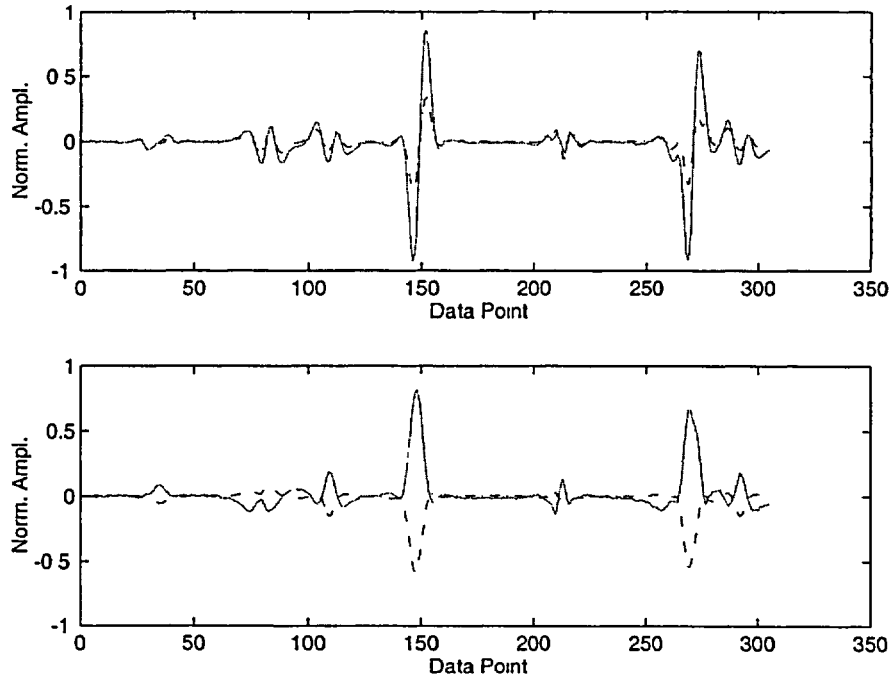
Fig. 3.3. Residual differential (top) and absolute (bottom) mix channel signals for shallow OD indication subsequent to combining intermediate mix outputs.
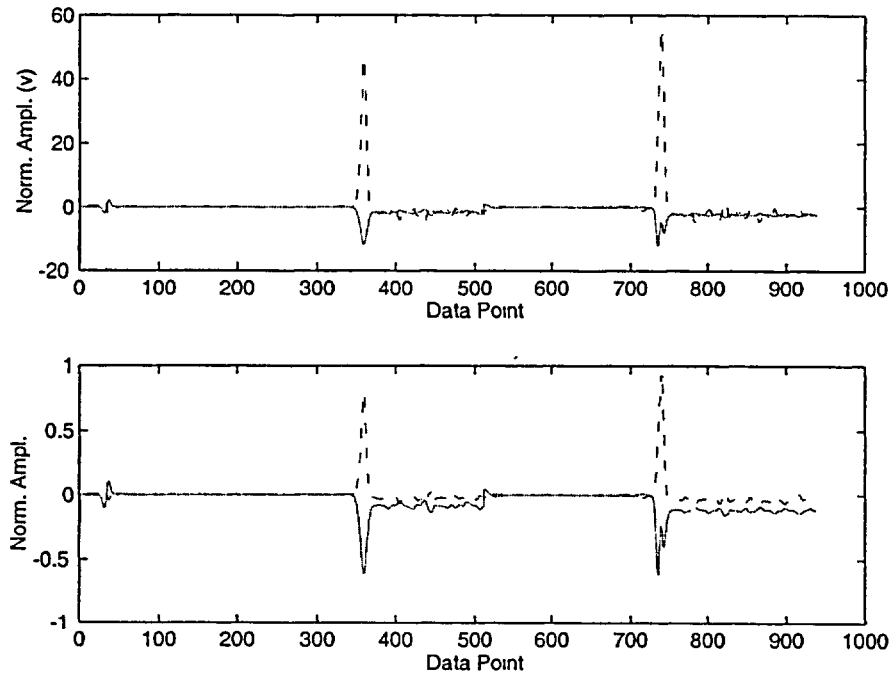
Fig. 3.4. Differential BC horizontal and vertical signal components of calibrated original (top) and renormalized (bottom) traces at f = 400 kHz. Indications from left to right consist of TW reference hole and two roll transition zones with 30% ID circumferential and TW OD axial SCC, respectively.
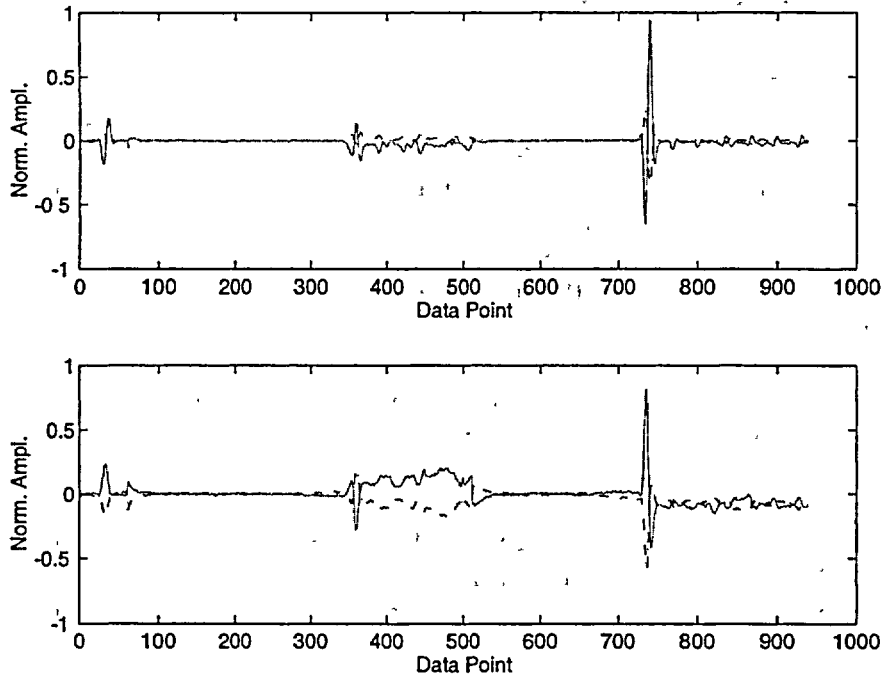
Fig. 3.5. *Independent mix output signal for differential (top) and absolute (bottom) channels of data shown in Fig. 3.4.*

3.2 Multiparameter Analysis of Rotating Probe Data

This section provides a description of recent activities associated with multiparameter data analysis of EC inspection results. Implementation of a rule-based computer-aided data analysis routine is discussed in Sec. 3.2.1. The algorithm uses multiple-frequency EC readings from rotating probes to estimate depth profile of indications in a tube. Preliminary results are presented on the application of this multifrequency phase-based algorithm to various sets of experimental data acquired with conventional rotating probes. Initial results of the analysis are presented in Sec. 3.2.2 on a set of 20 tubes furnished by PNNL that contained laboratory-produced cracking morphologies that represent some of those incorporated into the ANL's SG mockup. Data analysis results are presented in Sec. 3.2.3 for a single specimen with laboratory-produced cracking that exhibited reportable BC indications with no clear flaw signal from rotating-probe inspections (pancake and +Point™ coils). Finally, estimated depth profiles are provided for a set of 24 laser-cut specimens with single, multiple, and ligamented notches of axial and circumferential orientation.

Extensive studies are currently underway to analyze the NDE results from different coil configurations. Preliminary results in general suggest that EC readings from multiple coils could provide complementary information for more accurate sizing of difficult forms of degradations. Throughout this work, the rule-based algorithms that are described in this report will be refined as necessary to incorporate data analysis experiences acquired on new forms of degradation. More detailed descriptions of ongoing studies on multiparameter data analysis of EC NDE results will be provided in our future reports.

21

3.2.1 Computer-Aided Data Analysis

A series of algorithms have been implemented in MATLAB scripting language and are currently being refined to provide in real-time a profile of flaw depths in an SG tube from NDE results. The codes are integrated into a user interface tool to automatically process EC inspection results at multiple frequencies that are acquired with conventional bobbin and rotating probes. Figure 3.6 shows the main window of the GUI tool *ETProf*, which incorporates various independent algorithms for processing of NDE results. Pull-down menus, push buttons, and editable text areas on the display can be activated to perform the various stages of data analysis process.

Because estimates of flaw depth from phase angle information of multifrequency inspection data depend heavily on initial calibrations, it is expected that computer-aided data calibration routines will play an essential role in uniform and accurate normalization of raw EC data. Manual calibration of multifrequency rotating probe data is an especially time-consuming process and requires a great deal of effort. A series of GUI tools has been implemented at ANL to provide uniform and efficient calibration of raw EC inspection results. These codes, described in Ref. 1, were utilized in this study to carry out the initial calibration of raw EC readings.

The automated data analysis algorithm referred to in this work can be divided into three basic blocks. These blocks consist of various scripts that successively perform the calculation of S/N ratio for all channels, implement pre- and postprocessing filters, and ultimately combine multiple-frequency phase information from processed channels to provide an estimate of the depth profile for the entire length of the tube under examination. Initially, the S/N ratio is calculated from a user-defined approximate location along the trace baseline and minimum detectable amplitude from a calibration standard tube. Subsequently, this information is used to implement a set of filters that aid in suppressing signal background variations and in turn improve the S/N ratio. Filter characteristics are determined by taking into account both the coil configuration and the sampling frequency of the inspection data. Finally, the phase information at multiple frequencies is combined to calculate the depth profile for the entire tube in reference to known indications on a calibration standard tube. To reduce the ambiguity between OD (displayed as positive depth profile) and ID origin of an indication, the algorithm displays the depth information such that ID (and 100% TW) indications exhibit depth profiles with both positive and negative values along the depth axis. For ID indications, negative values provide the degradation extent. Currently, estimates of depth profile for each tube is made by direct comparison with known indications on a calibration standard tube. The algorithm is currently being refined to provide these values in a direct manner. This is done by fitting a polynomial to known flaw depths on the reference standard. Calculated coefficients of the regression fit would then be applied to the processed data channels to provide a continuous profile.

To verify the consistency of the outcomes, two calibration-standard tubes with different sets of machined flaw geometries were initially used for the analysis. With the EC response dependent on flaw geometry (i.e., length, depth, and width), the standards were selected to provide different flaw geometries with a similar range of depth variation. Figure 3.7 shows the original and processed channel traces for the two tube standards used in this study. The first
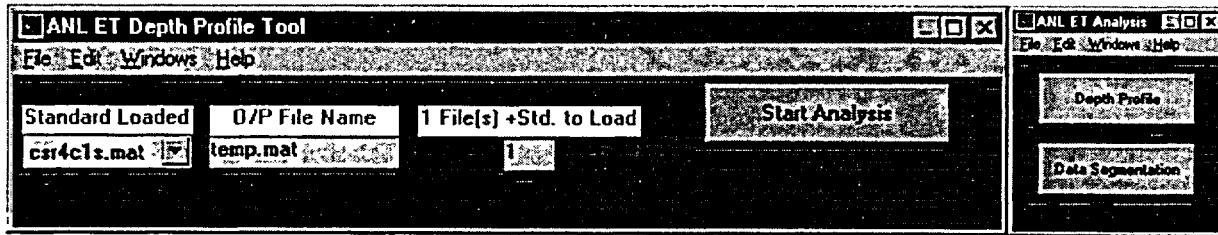
Fig. 3.6. A series of MATLAB-based Graphical User Interface (GUI) tools are currently under implementation to allow automated analysis of EC inspection results acquired with standard commercial instruments.

tube contained five circumferential OD notches of nominal length and width of 8 mm (0.315 in.) and 0.3 mm (0.012 in.), respectively, with depths ranging from 20 to 100% throughwall. The second tube selected is an ASME standard with drilled holes of similar depth. This standard also contains a TSP simulation ring, as well as 20% TW ID and 10% TW OD circumferential grooves. Figure 3.7(a) shows the calibrated amplitude traces at two frequencies. Examination of these data clearly indicates the presence of a nonlinear amplitude relationship that is dependent on both flaw geometry and operating frequency. Fig. 3.7(b) displays the estimated depth profiles for these tubes by combining the information from two and three channels, respectively. In all cases, the traces show similar depths for the entire range of OD indications. As mentioned earlier, the throughwall and ID indications have depth profiles that also extend in the negative direction. Although the results of analysis for the standards indicate similar results for two- and three-frequency depth profiles, studies so far have shown that for realistic flaws, more consistent estimates are generally achieved when three frequencies are used.

3.2.2 Analysis of 20 Lab-Produced Tube Specimens

The automated data analysis algorithm described in the previous section was utilized to estimate flaw sizes in a set of laboratory-grown specimens. Preliminary results on estimation of flaw depth profiles in this set of 20 tubes are presented next. The samples were furnished by PNNL and were originally manufactured by the Westinghouse Science and Technology Center (WSTC). Flaws in this set of 22.2-mm (0.875-in.)-diameter Alloy 600 tubing consisted mostly of longitudinal and circumferential ID/ODSCC, with a few samples containing shallow intergranular attack (IGA). The data set, which also contains metallography results, is currently being used to evaluate multiparameter sizing algorithms under study in this program.

The preliminary outcome of the assessments presented here pertains to the EC readings made with the primary 2.92 mm (0.115 in.) pancake coil of a three-coil rotating probe and at frequencies of 400, 300, and 200 kHz. The NDE results also contain information from several other probes that are also being evaluated as part of this study. Eddy current inspections were carried out by Zetec, with the frequency selection being limited to the range that is commonly used for ISI of 22.2-mm (0.875-in.)-diameter tubing. Attempts will be made throughout this study to evaluate potential improvement of the sizing capability by incorporating the inspection results from a wider range of frequencies.
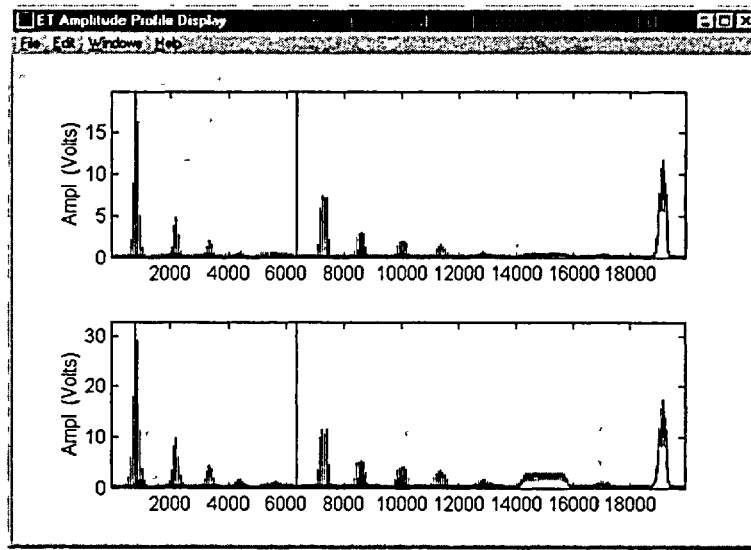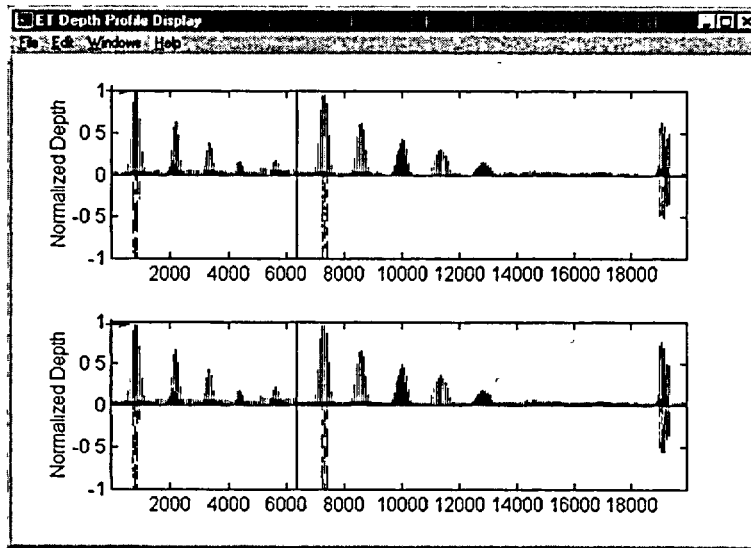
Fig. 3.7. Outputs of data analysis tool for estimation of defect depth profile for circumferential notch standard (left) containing five OD machined flaws ranging from 20 to 100% throughwall and an ASME standard (right) containing OD flat-bottom holes of same range, followed by TSP ring, 10% OD, and 20% ID grooves. Traces show (a) calibrated 400 kHz (top) and 200 kHz (bottom) amplitude (volts) and normalized depth profiles based on combining (b) two (upper), and three (lower) frequency channels. OD indications have positive trace and ID indications have both positive and negative traces. Eddy current readings are from 2.92 mm (0.115 in.) pancake of three-coil rotating probe.

24

Table 3.1 lists all the available information on the PNNL 20-tube subset of mock-up specimens, as well as the NDE depth estimates. For this initial investigation, NDE depth estimates are given at 20% intervals that cover the entire range of 0-100% of tube wall thickness. Figures 3.8-3.16 show selected test cases from the analysis of specimens in the data set. For all samples, both the calibrated amplitude trace at 400 kHz and the estimated three-frequency normalized depth profile are displayed. Each trace from left to right consists of the OD circumferential notch standard followed by the degraded test specimen, with a vertical line separating the two tubes. To reduce the size of the data, only the section of the tube that contains the NDE suggested flaw indication(s) is displayed. Because the EC reading at each measurement location is, in effect, an integration of the current distribution over the entire field of view of the coil, it is not expected that point-type defects, if detected, will produce EC responses proportional to the actual flaw depth. Also, because the NDE results are dependent on the S/N ratio, estimation of depth (particularly for shallow OD indications) should take into consideration the level of noise present in each trace.

3.2.3   Reanalysis of Lab-Produced Specimen SGL-432

NDE results from laboratory-produced specimen SGL-432, 22.2-mm (0.875-in.)-diameter Alloy 600 tubing, was also reanalyzed by using the multifrequency depth profile algorithm described earlier. This tube was reanalyzed because of the atypical nature of the original EC NDE results. Inspection results exhibited a BC indication with a relatively large flaw amplitude response, but without a discernible signal from midrange pancake and +Point coils. Figure 3.17(a) displays calibrated differential readings at 400 kHz primary and 100 kHz auxiliary frequencies that were acquired with an 18.3-mm (0.72-in.)-diameter magnetically biased bobbin probe. In the figure, the trace from an in-line ASME standard is shown on the left, and the response of the test specimen on the right. The lissajous patterns of the defected segment at the two frequencies are shown in Fig. 3.17(b). The bobbin results clearly suggest the presence of a shallow OD indication. The peak-to-peak signal amplitude and relative phase-angle for the flaw at 400 kHz were estimated to be 3.4 v and 160°, respectively. This rather large bobbin signal amplitude and phase are indicative of a shallow volumetric degradation. Figure 3.18 shows calibrated readings from 2.92-mm (0.115-in.) pancake and midrange +Point™ coils at the same two frequencies. For both coils, any signals are buried within the noise level. The noise level in this tube is relatively high for both bobbin and pancake coils and is presumably associated with permeability variations introduced by sensitization of the specimen.

The raw EC readings from specimen SGL-432 were analyzed off-line by using the multifrequency algorithm that was described earlier. Information from three frequencies is used to estimate the flaw depth. Figure 3.19 displays the processed data showing the calculated depth profiles at 400|300|200 and 300|200|100 kHz frequencies. Responses from an in-line EDM notch standard with 10 axial and circumferential OD indications are displayed on the left side of the trace; a comparison of the response from the indication with these responses provides an estimate of relative depth. In both cases, a shallow OD indication is visible just past data point No. 20,000, which is consistent with the location of the flaw based on the bobbin profile. The position of the flaw relative to the tube end was calculated by converting the number of measurement points to axial position along the tube using the locations of known markings on the standard. The phase-based flaw depth is estimated to be

Table 3.1. *Tabulated destructive examination and estimated EC NDE results by depth profile algorithm for PNNL 20-tube set of laboratory-grown specimens. Degradations were fabricated on 22.2-mm (0.875-in.)-diameter Alloy 600 tubes manufactured by Westinghouse Science and Technology Center. NDE results are given in 20% depth intervals from 0 to 100% TW.*

Tube ID #	Flaw Type[a]	Roll Expansion	Max Depth (% TW) (Destructive Exam)	Depth Range (% TW) (NDE Estimate)
1-03	CIDSCC	X	44	40-60
1-11	LIDSCC	X	100	>80
1-19	LIDSCC	X	100	>80
2-06	LODSCC		100	>80
2-11	LODSCC		95[b]	60-80
2-19	LODSCC		46	20-40
2-20	LODSCC		16	<20
2-21	LODSCC		30	20-40
3-05	CIDSCC	X	69	60-80
3-14	LIDSCC	X	NA[c]	20-40
4-01	CODSCC	X	83	60-80
4-04	CODSCC	X	64	20-40
4-06	CODSCC	X	100	>80
4-10	CODSCC	X	100	>80
5-02	IGA		4	NDD[d]
5-03	IGA		5	<20
5-04	IGA		24	20-40
5-09	IGA		43	20-40
5-25	IGA		66	20-40
B-10-07	LODSCC		28	20-40

[a] LIDSCC: longitudinal IDSCC; CIDCSS: circumferential IDSCC; LODSCC: longitudinal ODSCC; CODCSS: circumferential ODSCC.

[b] A single point is identified as having 95% degradation extent with flaws on both sides <20% TW. All other crack networks (105 marked locations) are <38% TW.

[c] Destructive results not available (NA). Target depth is 30%-60% TW.

[d] No detectable degradation (NDD).
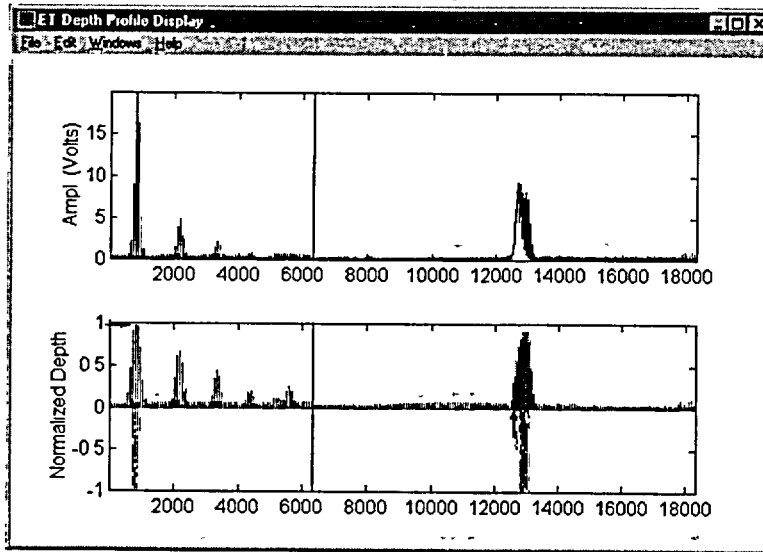
Fig. 3.8.   Output of data analysis tool for roll-expanded specimen #1-11 that was
destructively identified as having 100% (max. depth) LIDSCC degradation.
Traces show calibrated amplitude in volts (top), and normalized
multifrequency depth profile (bottom) of notch standard (left) followed by
sample tube, suggesting >80% degradation depth around scan location 1.3
x 10^4. Eddy current readings are from 2.92 mm (0.115 in.) pancake of
three-coil rotating probe.
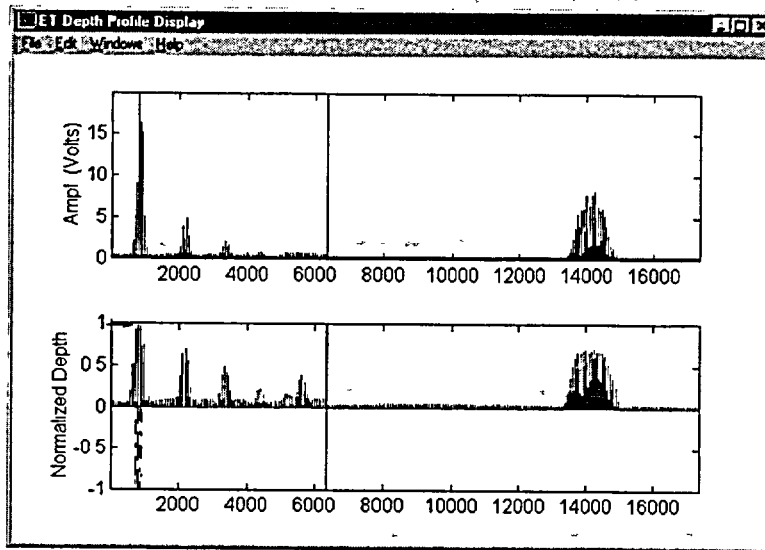
Fig. 3.9.   Output of data analysis tool for roll-expanded specimen #2-06 that was
destructively identified as having 100% (max. depth) LODSCC degradation.
Traces show calibrated amplitude in volts (top), and normalized
multifrequency depth profile (bottom) of notch standard (left) followed by
sample tube, suggesting >80% degradation depth around scan location 1.4 x
10^4. Eddy current readings are from 2.92 mm (0.115 in.) pancake of three-coil
rotating probe.

27
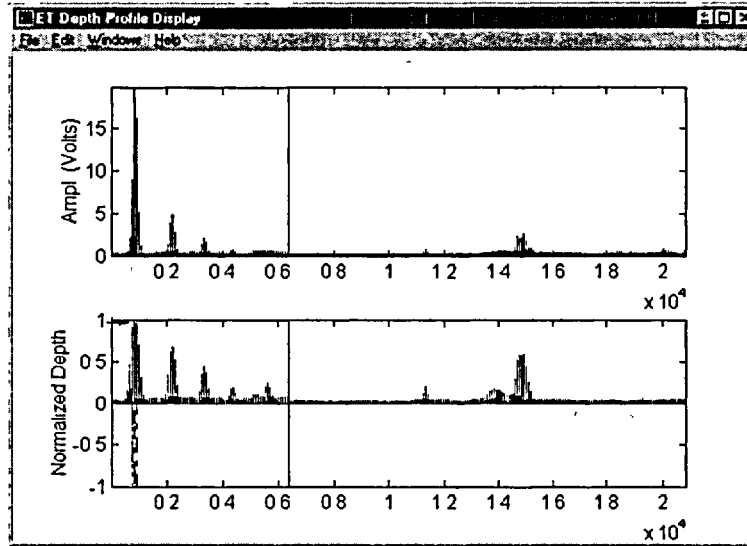
Fig. 3.10. Output of data analysis tool for specimen #2-11 that was destructively identified as having 95% (max. depth at a single point with all other indications marked <38%) LODSCC degradation. Traces show calibrated amplitude in volts (top), and normalized multifrequency depth profile (bottom) of notch standard (left) followed by sample tube, suggesting 60-80% degradation depth around scan location 1.5 x 10⁴. Eddy current readings are from 2.92 mm (0.115 in.) pancake of three-coil rotating probe.
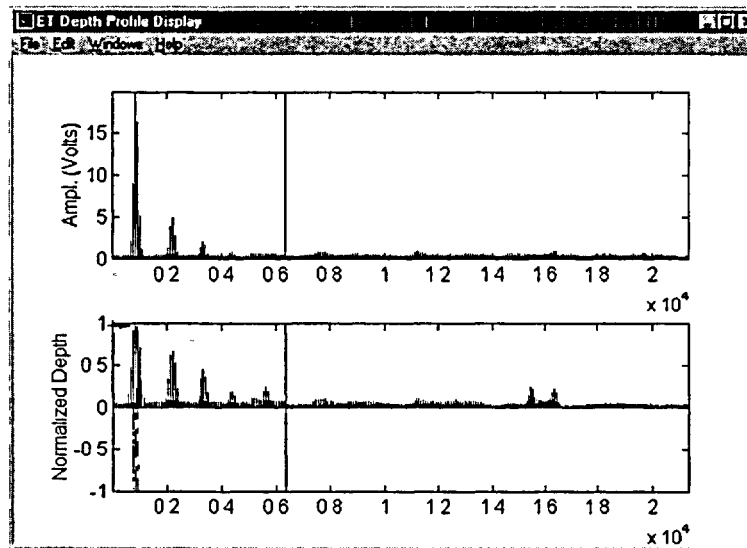
Fig. 3.11. Output of data analysis tool for specimen #2-19 that was destructively identified as having 46% (max. depth) LODSCC degradation. Traces show calibrated amplitude in volts (top), and normalized multifrequency depth profile (bottom) of notch standard (left) followed by sample tube, suggesting 20-40% degradation depth around scan location 1.6 x 10⁴. Eddy current readings are from 2.92 mm (0.115 in.) pancake of three-coil rotating probe.
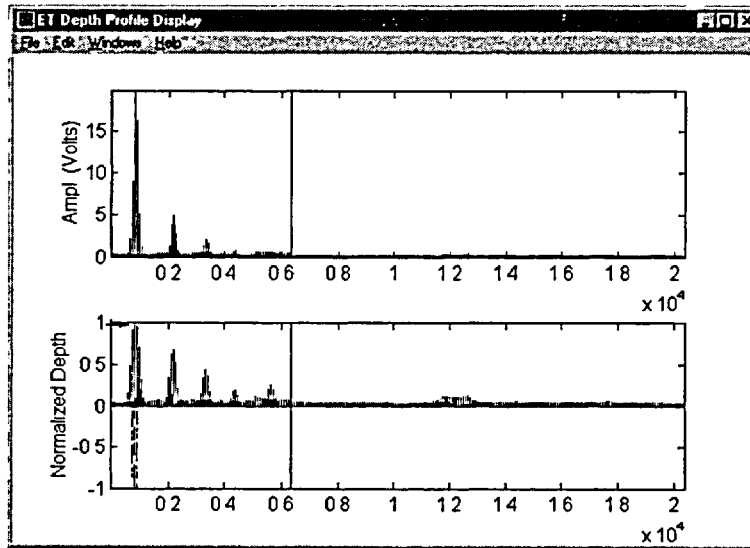
Fig. 3.12. Output of data analysis tool for specimen #2-20 that was destructively identified as having 16% (max. depth) LODSCC degradation. Traces show calibrated amplitude in volts (top), and normalized multifrequency depth profile (bottom) of notch standard (left) followed by sample tube, suggesting <20% degradation depth around scan location 1.2 x 10⁴. Eddy current readings are from 2.92 mm (0.115 in.) pancake of three-coil rotating probe.
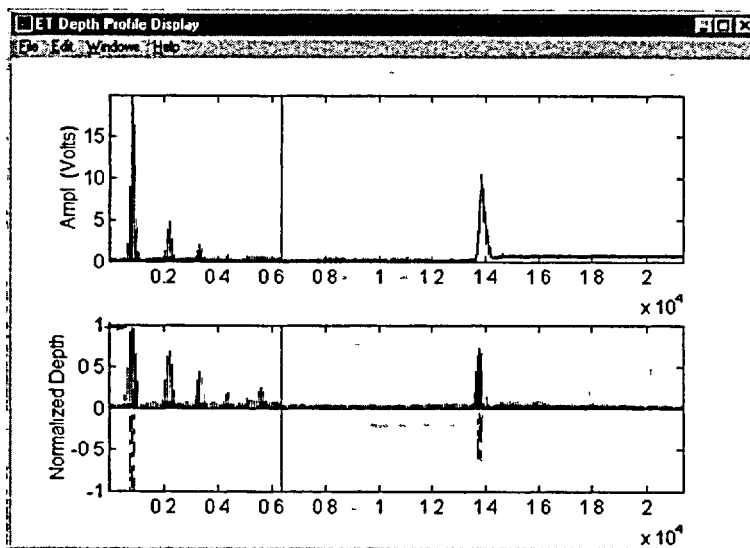
Fig. 3.13. Output of data analysis tool for roll-expanded specimen #3-14 LIDSCC degradation (no DE results available; target value 30%-60%). Traces show calibrated amplitude in volts (top), and normalized multifrequency depth profile (bottom) of notch standard (left) followed by sample tube, suggesting 40%-60% degradation depth around scan location 1.4 x 10⁴. Eddy current readings are from 2.92 mm (0.115 in.) pancake of three-coil rotating probe.

29
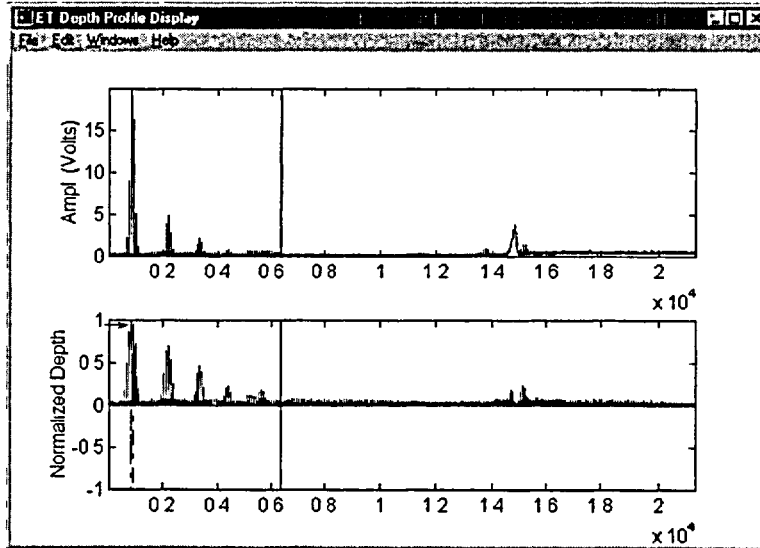
Fig. 3.14. *Output of data analysis tool for roll-expanded specimen #4-04 that was destructively identified as having 64% (max. depth) CODSCC degradation. Traces show calibrated amplitude in volts (top), and normalized multifrequency depth profile (bottom) of notch standard (left) followed by sample tube, suggesting >40% degradation depth around scan location 1.5 x 10^4. Eddy current readings are from 2.92 mm (0.115 in.) pancake of three-coil rotating probe.*
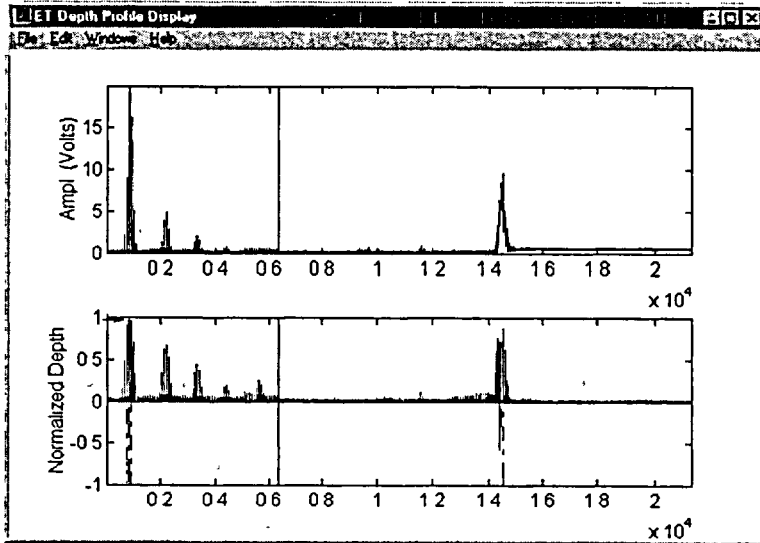
Fig. 3.15. *Output of data analysis tool for roll-expanded specimen #4-10 that was destructively identified as having 100% (max. depth) CODSCC degradation. Traces show calibrated amplitude in volts (top), and normalized multifrequency depth profile (bottom) of notch standard (left) followed by sample tube, suggesting >80% degradation depth around scan location 1.4 x 10^4. Eddy current readings are from 2.92 mm (0.115 in.) pancake of three-coil rotating probe.*

30
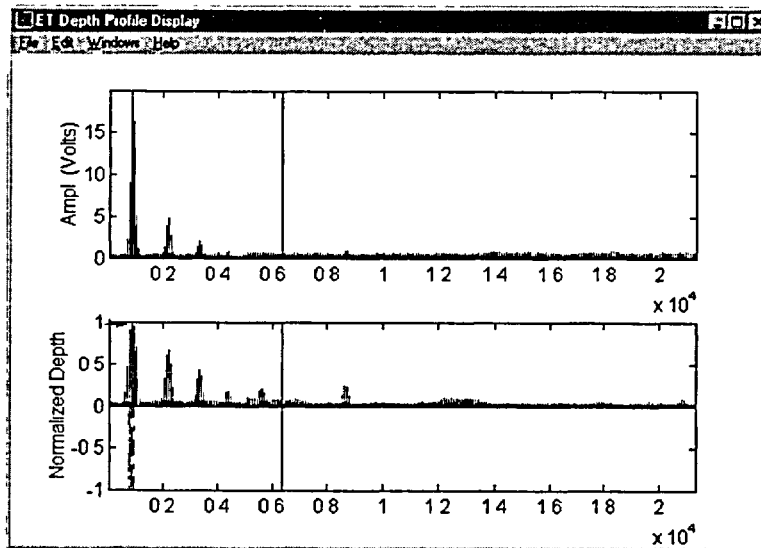
Fig. 3.16. *Output of data analysis tool for roll-expanded specimen #B10-07 that was destructively identified as having 28% (max. depth) LODSCC degradation. Traces show calibrated amplitude in volts (top), and normalized multifrequency depth profile (bottom) of notch standard (left) followed by sample tube, suggesting 20-40% degradation depth around scan locations 0.9 x 10⁴ and 1.3 x 10⁴. Eddy current readings are from 2.92 mm (0.115 in.) pancake of three-coil rotating probe.*

20-40% OD TW (relative to the level of noise). Slight improvement is achieved with the lower set of frequencies. This was expected because of the OD nature of the flaw. Although the bobbin response shows an axially long flaw profile, only the leading edge of the flaw is clearly discernible from the pancake coil results. This suggests a nonuniform depth profile of the degradation. Further testing of magnetically biased coils is planned to determine whether such probes can provide improved flaw depth estimates in sensitized tubing.

3.2.4 Analysis of Laser-Cut Specimens

Eddy current inspection results from a collection of 22.2-mm (0.875-in.)-diameter Alloy 600 tubes with laser-cut notches are currently being evaluated by conventional and alternate data analysis methods. Multiple-frequency EC inspection results were collected on all available specimens with bobbin and rotating probes. Manufactured defect geometries range from single axial/circumferential notches to multiple ligamented notches. Nominal OD flaw depth for the majority of tubes were specified to be 80% TW, with two samples having 40% TW depths. The geometry of all the available flaw types for laser-cut notch specimens is described in Table 3.2. Previous experience has shown that the nominal depths for such notches do not generally correspond to the actual depths, as suggested by the NDE depth estimates given in the table, and the actual laser-cut notch depths must be verified by fractography.

Raw EC readings for all specimens were converted, normalized, and reassembled in smaller segments for off-line analysis. Figures 3.20-3.23 display images of representative

31
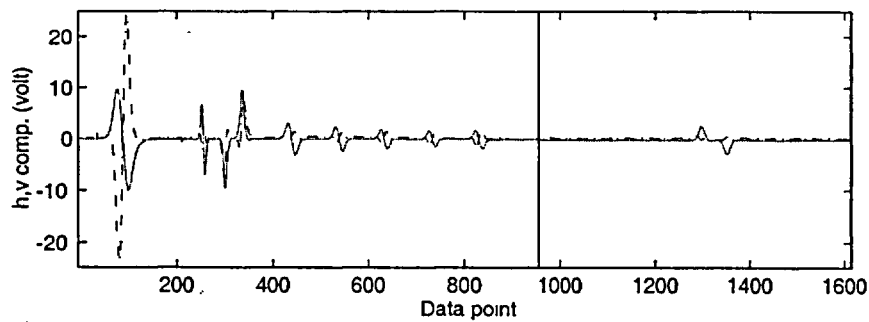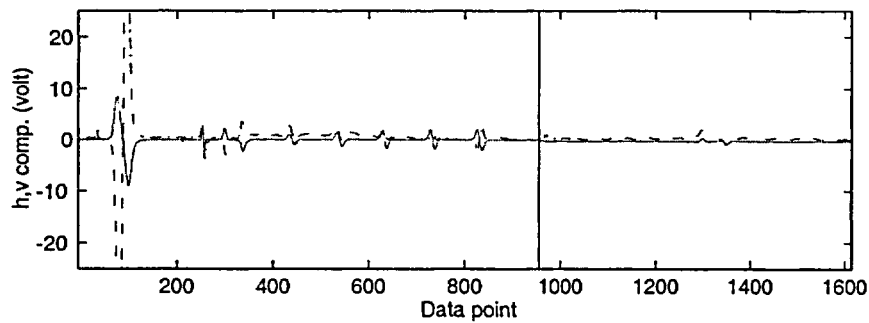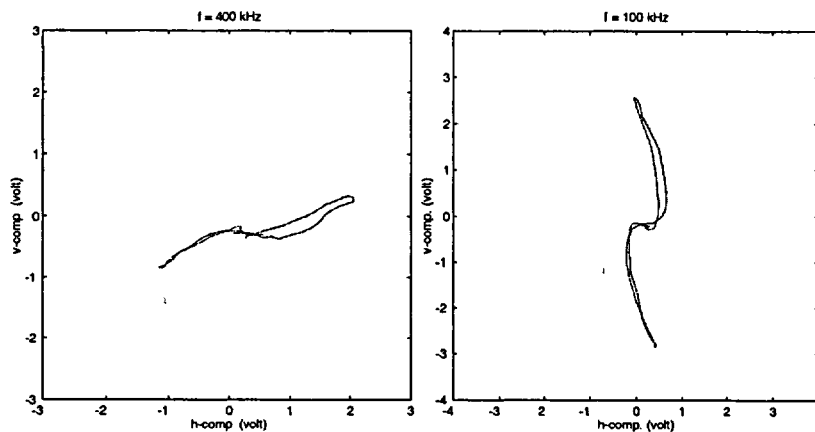
Fig. 3.17. *(a) Stripchart and (b) lissajous display of calibrated differential readings at 400 kHz (top) and 100 kHz (bottom) frequencies made with 18.3-mm (0.72-in.)-diameter magnetically biased bobbin probe on 22.2-mm (0.875-in.)-diameter Alloy 600 tube. Response from in-line ASME standard is shown on left; response of test specimen SGL-432 is on right. Calibrated signal amplitude and phase at 400 kHz were estimated to be 3.4 v and 160°, respectively, suggesting <20% OD degradation.*
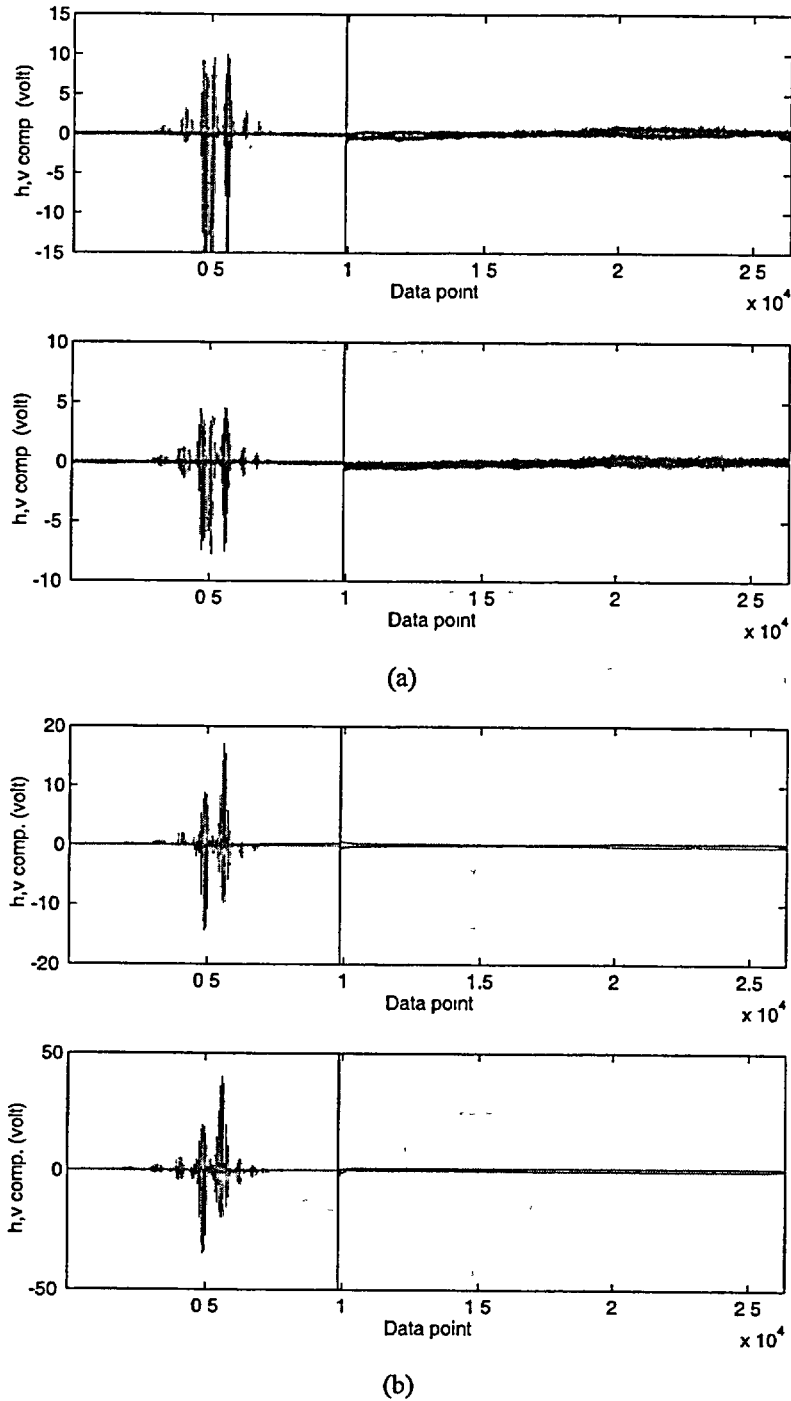
Fig. 3.18. Calibrated readings with (a) 2.92 mm (2.92-mm [0.115-in.]) pancake and (b) midrange +Point coils of three-coil rotating probe at 400 kHz (top) and 100 kHz (bottom) frequencies on 22.2-mm (0.875-in.)-diameter Alloy 600 tube. Response from 20-100% OD, 6.35-mm (0.25-in.)-long axial/circumferential EDM notches from in-line standard is shown on left; signal from test specimen SGL-432 is on right. No discernible indications are present in these traces, although a BC indication is present, as shown in Fig. 3.17.

33
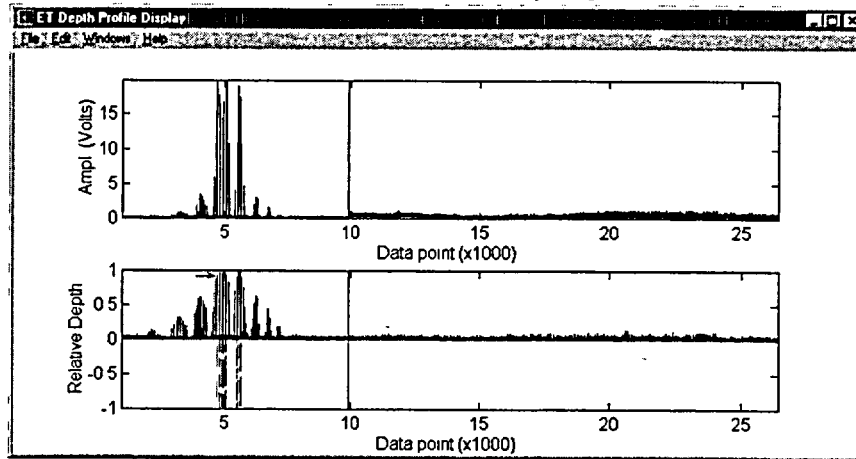
(a)
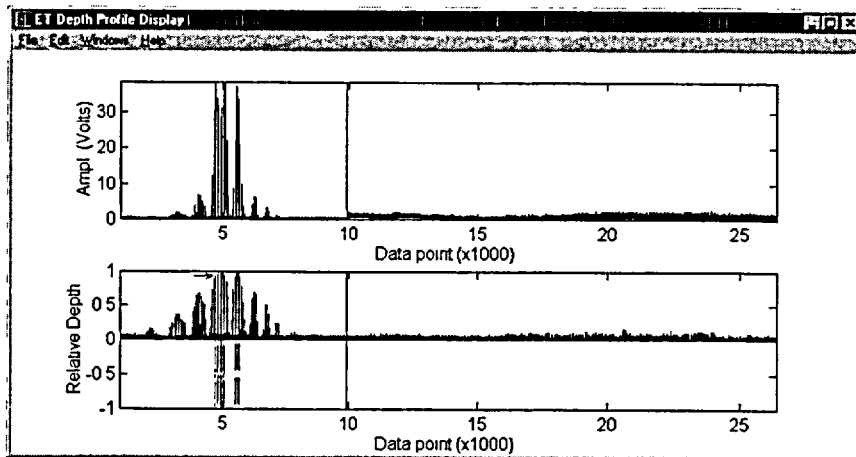
(b)

Fig. 3.19. *Outputs of multifrequency depth profile algorithm at (a) 400|300|200 kHz and (b) 300|200|100 kHz for specimen SGL-432. Selected data segments show calibrated amplitude in volts (top), and normalized multifrequency depth profile (bottom) for 20-100% OD, 6.35-mm (0.25-in.)-long axial/circumferential EDM notches from in-line standard followed by test specimen. Degradation extent around scan location 20 x 10³ suggests ≈20-40% OD flaw with maximum depth being slightly to right. Eddy current readings are from 2.92 mm (2.92-mm [0.115-in.]) pancake of three-coil rotating probe.*

Table 3.2. List of laser-cut samples and their nominal dimensions. Also listed are single-frequency NDE results from mag-biased bobbin and +Point probes, along with multiparameter depth estimates with 2.92-mm (0.115-in.) pancake probe.

Notch Geometry	Tube I.D.	Specimen Type	No. of Notches	Notch Length (mm)	Ligament Width (mm)	Notch Depth (% TW)			
						Nominal Value	Bobbin Coil	+Point	Multi-param.
Single (Type 1)	5528-1-1	1	1	6.35	N/A	80	58	75	75
	5528-1-2	1	1	6.35	N/A	80	51	68	74
	5528-1-3	1	1	8.89	N/A	80	56	75	76
	5528-1-4	1	1	8.89	N/A	80	58	75	73
	5528-2-1	1	1	12.7	N/A	80	44	67	69
	5528-2-2	1	1	12.7	N/A	80	27	56	61
Ligament (Type 2)	5516-4-3	2	2	12.7	0.25	80	35	53	72
	5516-4-2	2	2	12.7	0.13	80	50	62	70
Dotted Line (Type 3)	5528-3-1	3	6	12.7	0.13	80	53	69	70
	5528-3-2	3	6	12.7	0.25	80	45	74	73
	5528-3-3	3	6	12.7	0.25	40	42	66	61
Side Step (Type 4)	5528-3-4	4	6	12.7	0.13	80	61	75	76
	5469-2-1	4	6	12.7	0.25	80	45	71	74
	5469-2-2	4	6	12.7	0.25	40	43	56	60
2x3 Side (Type 5)	5469-2-3	5	6	12.7	0.25	80	52	77	79
	5469-2-4	5	6	12.7	0.50	80	45	64	78
6 Claw (Type 6)	5469-3-1	6	6	12.7	0.25	80	56	78	80
	5531-3-1	6	6	12.7	0.50	80	58	76	79
Parallel (Type 7)	5469-3-3	7	2	360°	0.13	80	44	95	75
	5469-3-4	7	2	360°	0.25	80	37	92	74
p-Side Step (Type 8)	5469-4-1	8	6	360°	0.25	80	39	88	70
	5469-4-2	8	6	360°	0.13	80	54	98	70
T (Type9)	5469-4-3	9	2	180° x 0.5	N/A	80	48	62	69
L (Type 10)	5469-4-4	10	2	180° x 0.5	N/A	80	53	68	72

samples from the available data set at a frequency of 400 kHz. Each image is composed of reconstructed data segments from an EDM notch standard, followed by the tube containing the laser-cut flaw. In all cases, the EC profile conforms to the actual flaw geometry. However, the lack of spatial resolution in most cases limits the ability of the image to provide the detail necessary to view small ligaments (nominal widths of $\approx$0.13-0.50 mm [0.005–0.02 in.]) between segmented flaws. The resolution of the EC probe that is dependent on the coil dimensions and frequency of operation dictates the coil's field of view. The image resolution is also limited by the sampling rate and probe travel speed, which is typically adjusted to provide a reasonable trade-off between resolution and data size.

Spatial resolution could be improved through signal enhancement and restoration schemes. Resolution enhancement techniques such as frequency and spatial domain deconvolution algorithms are currently being evaluated. A detailed description of the findings on the analysis of laser-cut specimens through utilization of multiparameter depth estimation and Fourier domain deconvolution will be provided in future reports. Comparative studies are being carried out to evaluate the accuracy of these techniques against conventional data analysis procedures. This collection of specimens that will be used for the pressure and leak-rate studies provide an ideal data set for assessing conventional EC NDE methods and will be used in our ongoing studies for implementation and verification of improved data analysis algorithms.

Conventional and Multiparameter Analysis of Laser-Cut Specimens

Preliminary analysis of EC inspection results on the laser-cut specimens was performed using inspection data from bobbin and RPC probes. All data were analyzed with the Eddynet98™ analysis software. Bobbin results were calibrated with reference to an in-line ASME machined hole standard in accordance with the conventional bobbin calibration of voltage amplitude and phase. The primary frequency was taken as f = 400 kHz, and the signal amplitude for all other channels was normalized in reference to the primary channel. The +Point™ results were calibrated in reference to an 18-notch EDM standard containing 6.35-mm (0.25-in.)-long axial/circumferential flaws of various OD/ID depths, taking f = 300 kHz as the primary channel. A single OD calibration curve for the bobbin and two separate (OD/ID axial and circumferential) +Point phase-angle calibration curves were used to estimate flaw depths.

Representative stripchart, lissajous, and isometric plots of inspection results with magnetically biased (mag-biased) bobbin and mid-range +Point probe for two laser-cut specimens are shown in Figs. 3.24 and 3.25. Although all flaws were detected by both types of probes, the sizing estimates for the two probe types vary significantly.

Subsequent multiparameter analysis on the laser-cut specimens used the data from 2.92 mm (0.115-in.) primary pancake coil of a three-coil rotating probe at 400, 300, and 200 kHz frequencies. Figures 3.26-3.31 display selected results of the analysis using the multiparameter approach. Each figure contains the voltage amplitude and relative depth of the selected sample.

Although all flaws were detected with all three techniques described in this section, the sizing estimates vary significantly between bobbin and RPC probes and, to a lesser extent,
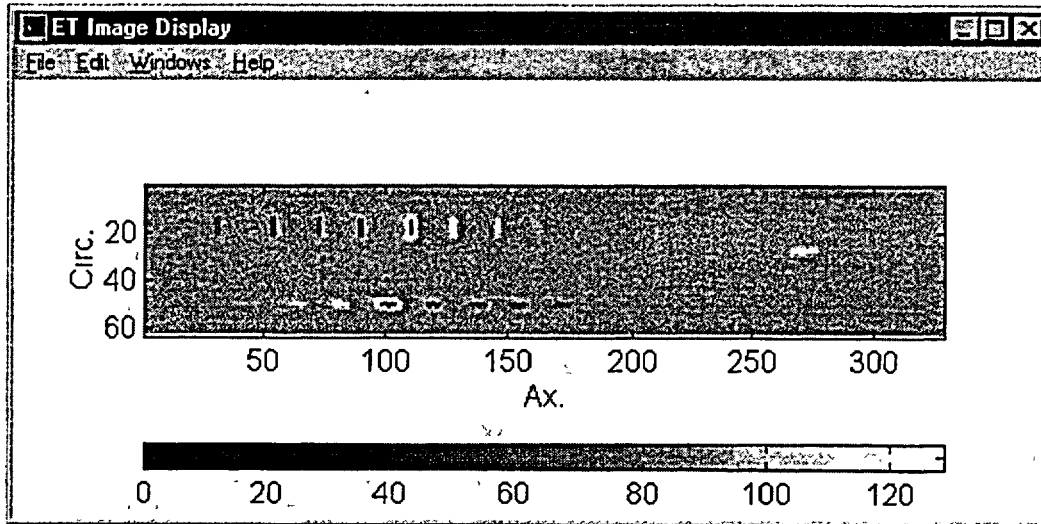
Fig. 3.20. *Image display of RPC inspection results at 400 kHz showing data segments from in-line standard followed by Type-1 laser-cut specimen. Response from in-line standard with 6.35-mm (0.25-in.)-long axial/circumferential EDM notches of various depths is at left; response from laser-cut specimen containing 6.35-mm (0.25-in.)-long 80% OD (nominal depth) axial notch is at right.*
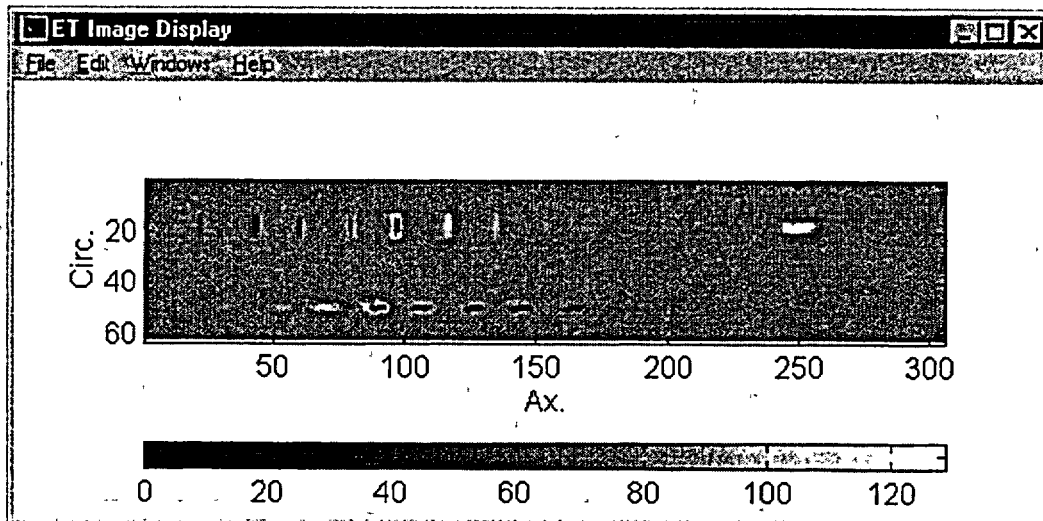
Fig. 3.21. *Image display of RPC inspection results at 400 kHz showing data segments from in-line standard followed by Type-5 laser-cut specimen. Response from in-line standard with 6.35-mm (0.25-in.)-long axial/circumferential EDM notches of various depths is at left; response from laser-cut specimen containing two sets of 12.7-mm (0.25-in.)-long, 80% OD TW circumferentially offset parallel flaws (three axial notches) with 0.51-mm (0.02-in)-wide ligaments is at right.*

37
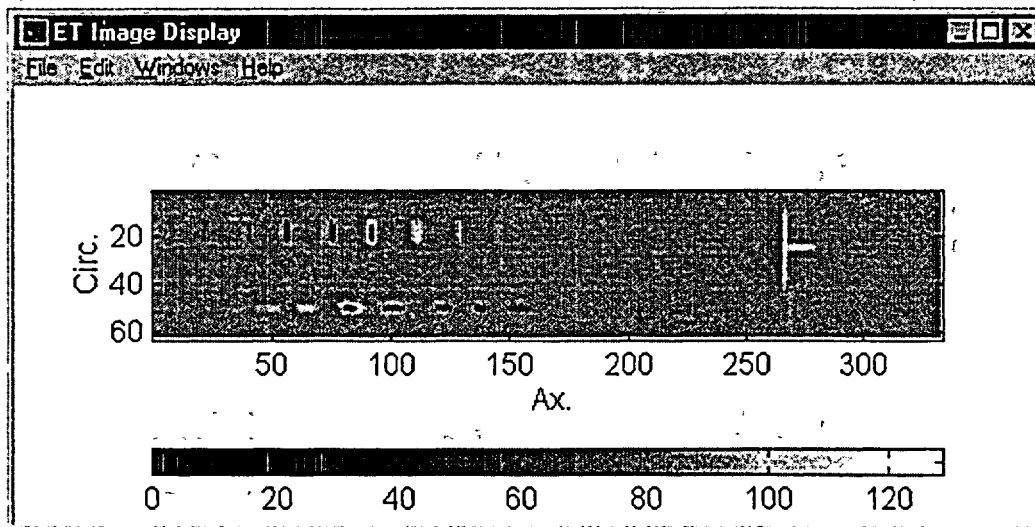
Fig. 3.22. *Image display of RPC inspection results at 400 kHz showing data segments from in-line standard followed by Type-9 laser-cut specimen. Response from in-line standard with 6.35-mm (0.25-in.)-long axial/circumferential EDM notches of various depths is at left; response from laser-cut specimen containing T-shaped flaw composed of 12.7-mm (0.5-in.)-long axial and 180° long circumferential notch of 80% OD (nominal depth) TW is at right.*
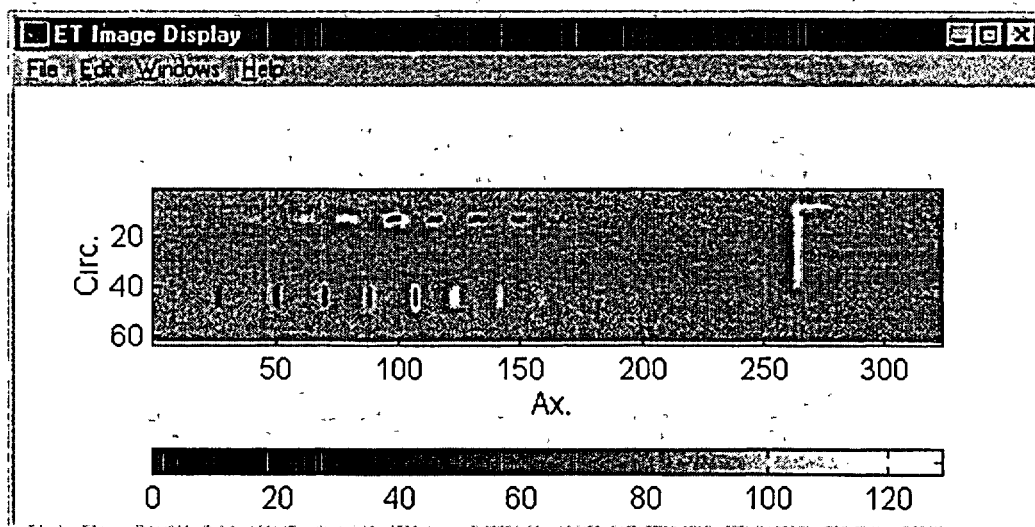
Fig. 3.23. *Image display of RPC inspection results at 400 kHz showing data segments from in-line standard followed by Type-10 laser-cut specimen. Response from in-line standard with 6.35-mm (0.25-in.)-long axial/circumferential EDM notches of various depths is at left; response from laser-cut specimen containing L-shaped flaw composed of a 12.7-mm (0.5-in.)-long axial and 180° long circumferential notch of 80% OD (nominal depth) TW is at right.*
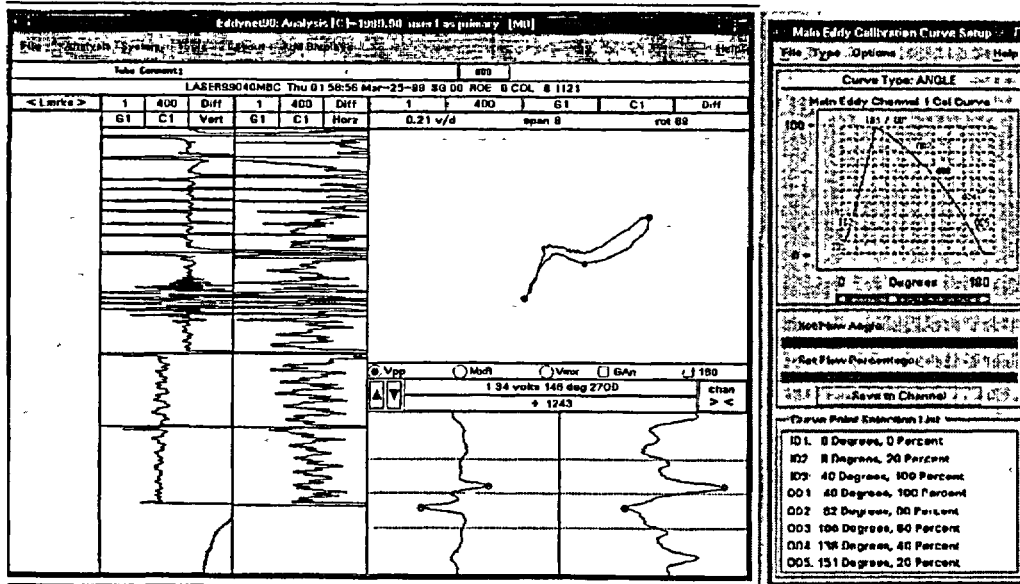
(a)
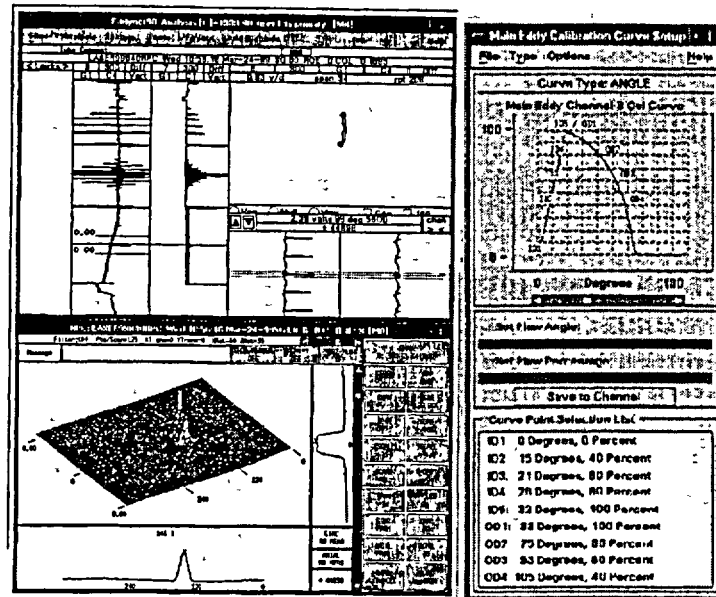
(b)

Fig. 3.24. Representative stripchart, lissajous, and isometric plots of inspection results with (a) mag-biased bobbin and (b) mid-range +Point probe for laser-cut type-1 specimen #5528-2-2 analyzed with Eddynet98 software. Also shown at right of each figure is phase-angle calibration curve used for estimating flaw depths. Bobbin results were calibrated in reference to an in-line ASME machined hole standard, taking $f = 400$ kHz as primary channel. +Point results were calibrated in reference to 18-notch EDM standard with 6.35-mm (0.25-in.)-long axial/circumferential flaws of various OD/ID depths, taking $f = 300$ kHz as primary channel.

39
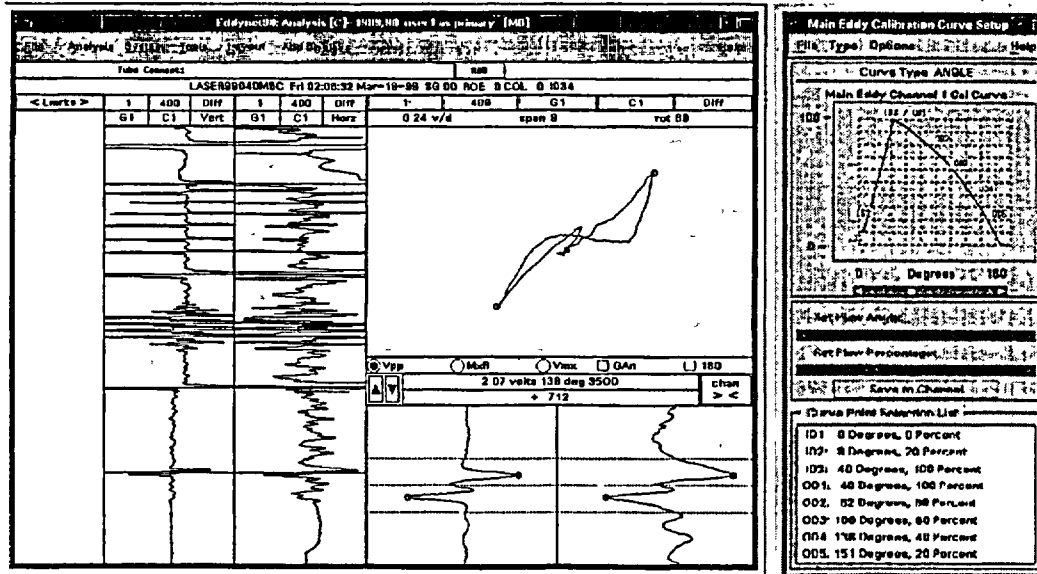
(a)
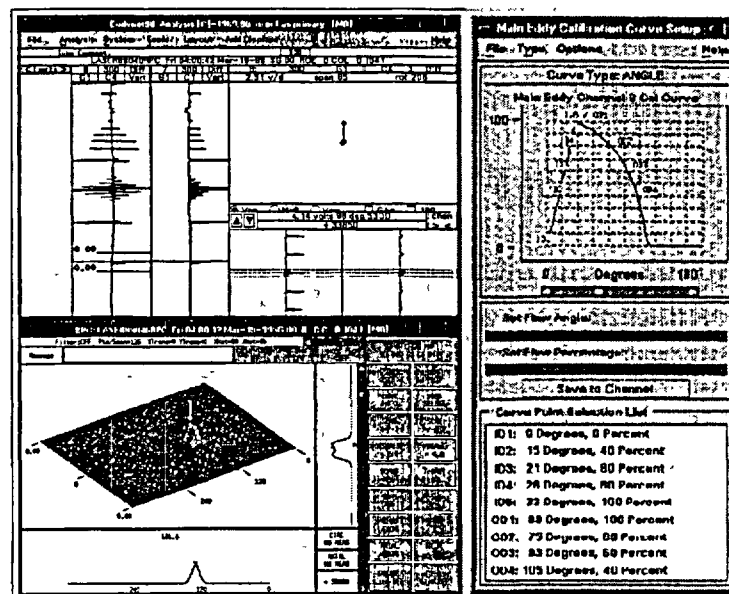
(b)

Fig. 3.25. *Representative stripchart, lissajous, and isometric plots of inspection results with (a) mag-biased bobbin and (b) mid-range +Point probe for laser-cut type-2 specimen #5516-4-3 analyzed with Eddynet98 software. Also shown at right of each figure is phase-angle calibration curve used for estimating flaw depths. Bobbin results were calibrated in reference to in-line ASME machined hole standard, taking f = 400 kHz as primary channel. +Point results were calibrated in reference to 18-notch EDM standard with 6.35-mm (0.25-in.)-long axial/circumferential flaws of various OD/ID depths, taking f = 300 kHz as primary channel.*
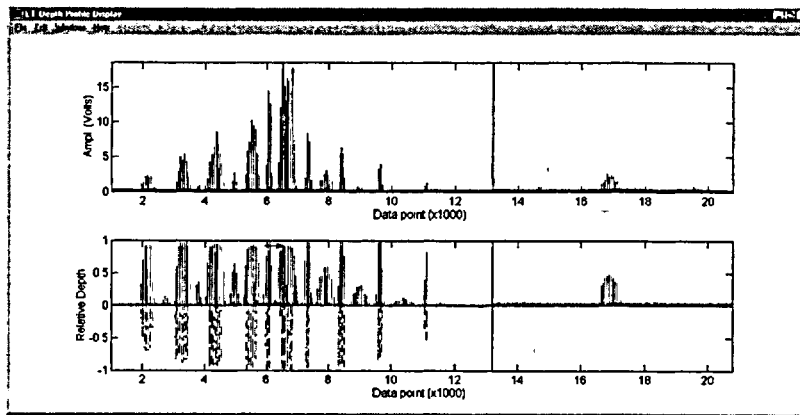
Fig. 3.26. *Representative display of multiparameter analysis results showing calibrated voltage amplitude profile (top) and estimated relative depth. Profiles are composed of 18-notch standard (left) with axial/circumferential OD/ID EDM flaws followed by Type-1 specimen #5528-1-1 (right).*
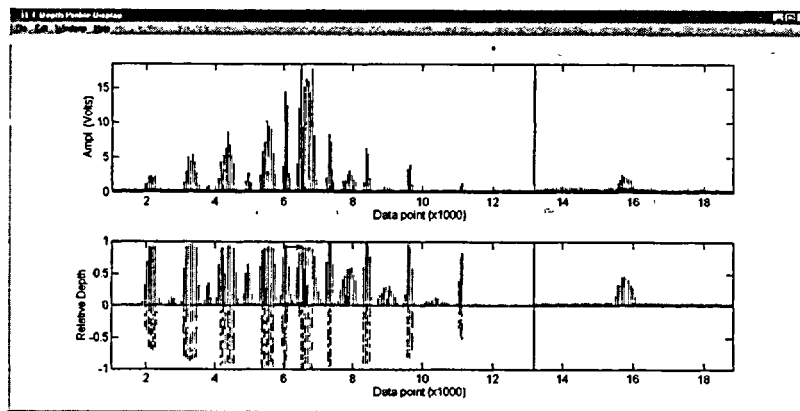
Fig. 3.27. *Representative display of multiparameter analysis results showing calibrated voltage amplitude profile (top) and estimated relative depth. Profiles are composed of 18-notch standard (left) with axial/circumferential OD/ID EDM flaws followed by Type-1 specimen #5528-1-2 (right).*

41
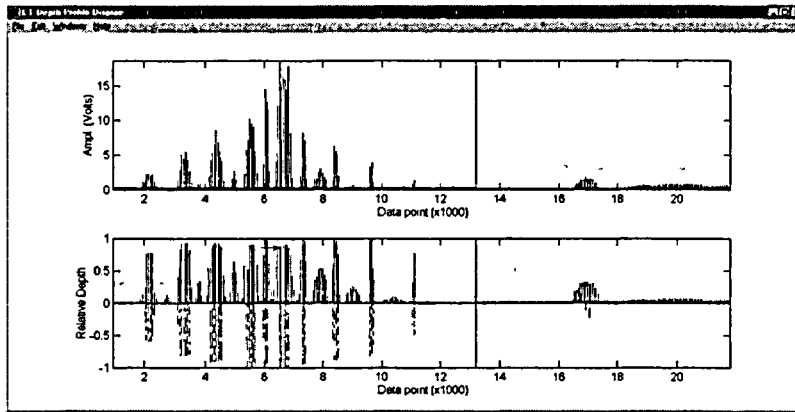
Fig. 3.28. *Representative display of multiparameter analysis results showing calibrated voltage amplitude profile (top) and estimated relative depth. Profiles are composed of 18-notch standard (left) with axial/circumferential OD/ID EDM flaws followed by Type-2 specimen #5516-4-3 (right).*
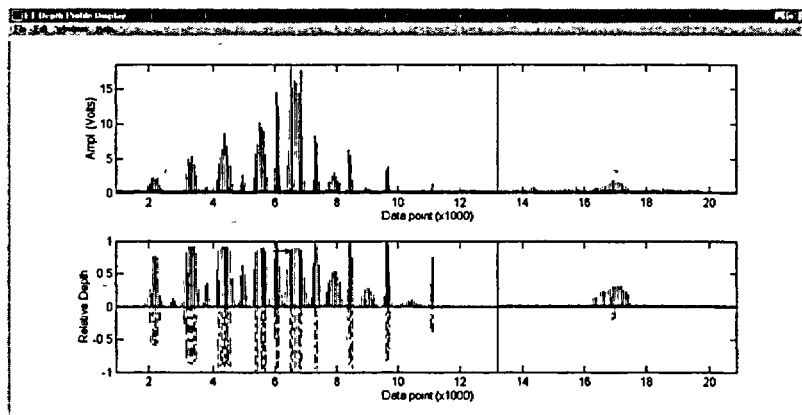
Fig. 3.29. *Representative display of multiparameter analysis results showing calibrated voltage amplitude profile (top) and estimated relative depth. Profiles are composed of 18-notch standard (left) with axial/circumferential OD/ID EDM flaws followed by Type-2 specimen #5516-4-2 (right).*
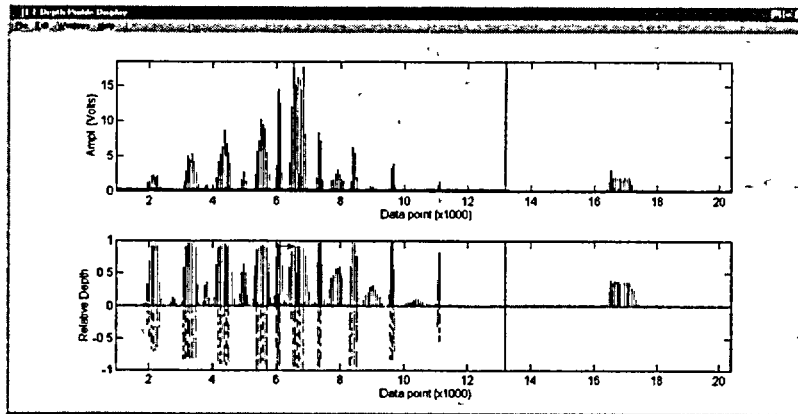
Fig. 3.30. Representative display of multiparameter analysis results showing calibrated voltage amplitude profile (top) and estimated relative depth. Profiles are composed of 18-notch standard (left) with axial/circumferential OD/ID EDM flaws followed by Type-9 specimen #5469-4-3 (right).
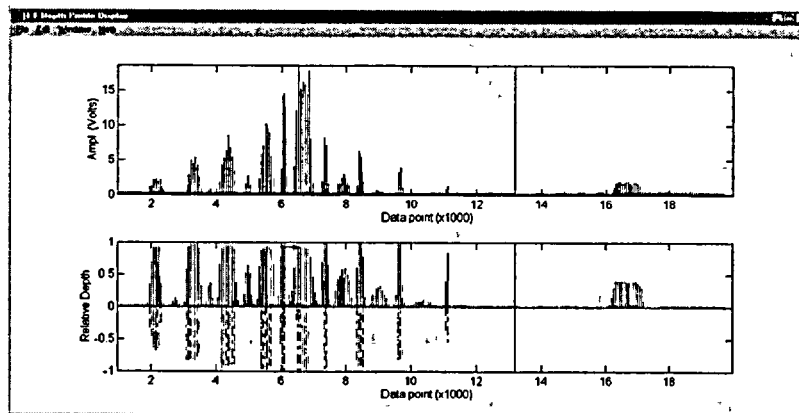
Fig. 3.31. Representative display of multiparameter analysis results showing calibrated voltage amplitude profile (top) and estimated relative depth. Profiles are composed of 18-notch standard (left) with axial/circumferential OD/ID EDM flaws followed by Type-10 specimen #5469-4-4 (right).

43

between the two RPC methods. The multiparameter sizing estimates, although closer to the single-frequency +Point estimates, show smaller overall scatter of the sizing results.

Preliminary metallographic studies show that the actual depths of the laser cut notches are significantly different than the nominal depths provided by the vendor. Quantitative comparison of the depths predicted by the various NDE methods with the actual depths cannot be made until metallographic results are available.

3.3 Improving Spatial Resolution of RPC data

Preliminary results of recent studies on signal processing methods pertaining to the multiparameter analysis of EC inspection data are presented next. In particular, the application of pseudoinverse filters to the restoration of RPC indications is described. The primary purpose of this ongoing investigation is to evaluate the effectiveness of real-time approximate deconvolution algorithms for improving spatial resolution and, in turn, sizing accuracy of rotating probes for crack-like indications. A collection of laser-cut notch specimens described in the previous section was utilized for the initial benchmark evaluation of the proposed signal processing scheme. As described earlier, manufactured defect geometries in these tubes range from single axial to multiple axial/circumferential ligamented notches. Nominal OD flaw depths for the majority of tubes were specified to be 80% TW, with two samples having 40% TW depth. EC readings on this collection of 22.2–mm (0.875-in.) Alloy 600 tubing was recently analyzed using conventional and alternative methods. Multiple-frequency NDE results on all the available specimens were collected with a standard bobbin and a 3-coil rotating probe.

So far, results of this investigation suggest that, in general, pseudoinverse filters, when applied discerningly, can help reduce EC signal background variations, improve spatial resolution, and, in turn, improve multiparameter sizing of crack-like indications. The proposed signal processing scheme will be further verified by including laboratory-produced samples from the ANL SG mock-up facility.

3.3.1 Application of Pseudo-Deconvolution to Eddy Current Signal Restoration

The application of approximate deconvolution/inverse-filtering schemes to real-time processing of multifrequency inspection results is currently being investigated. This study was prompted by the need for more accurate characterization of complex cracking morphologies in SG tubing. Deconvolution techniques are used in a wide range of signal processing applications, primarily to recover signals distorted by the sensing environment. In EC inspection applications, pseudoinverse filters could be effective for enhancement of spatial resolution that is degraded by the finite spread of the coil-induced fields. Better separation of flaw indications from extraneous signals could, in turn, improve the estimation of flaw depth determined from the phase-angle information of multifrequency data. Frequency-dependent signal restoration could also help reduce differences in probe response at different frequencies. This could be particularly beneficial for multifrequency mixing techniques in which the differences in the coil impulse response at the base and auxiliary frequencies could significantly contribute to the level of mix residuals.

The fundamental limitation of deconvolution in application to EC signal restoration could be attributed to the flow of current in a conducting medium that is governed by the diffusion phenomenon. This suggests that distortion is not simply a modulation of signal amplitude. Instead, the waveform could experience complete alteration of structure that is not linearly dependent on its original form. Another factor that could significantly influence the degree to which a signal can be recovered is the lack of separation between the spectral content of flaw indications and extraneous signals. Internal/external artifacts and design discontinuities (e.g., conducting and magnetic deposits, tube dimensional variations, external support structures, etc.) could produce signal trajectories with spectral components that are close to those from flaw indications. Furthermore, practical sampling rates that are typically used for acquisition of ISI data with rotating probes do not render continuous smooth signals that are essential for optimal restoration by inverse-filtering schemes. Finally, it is important to note that physically realizable optimal inverse filters are often unstable. For this reason, approximate deconvolution algorithms may provide the best alternative for real-time restoration of EC flaw signals for practical ISI applications.

3.3.2   2-D Discrete Model

Degradation of probe's spatial resolution in two dimensions (2-D) could, in general, be described by the following discrete convolution model:

$$g(x,y) = \sum_{m=0}^{M-1} \sum_{n=0}^{N-1} f(m,n)h(x-m, y-n) + \eta(x,y)$$

$$\equiv h(x,y) * f(x,y)$$

(3.1)

where f is the nondistorted signal (probe input), g is the measured signal (probe O/P), h is the probe impulse response, η is the additive noise, and $*$ denotes the convolution operation. With prior knowledge of the distortion model, the original signal may then be recovered through deconvolution, either directly by polynomial division in the spatial domain, or more efficiently by transformation into frequency domain. The inverse-filtering operation in the Fourier domain could be expressed as

$$\hat{f}(x,y) = \mathcal{F}^{-1} \left\{ \frac{G(u,v)}{H(u,v)} \right\},$$

(3.2)

where $\hat{f}$ is the new estimate of the original signal. The distorted frequency-domain signal $G(u,v)$ and Probe transfer function $H(u,v)$ are defined as

$$G(u,v) = \mathcal{F}\{g(x,y)\}$$

(3.3)

$$H(u,v) = \mathcal{F}\{h(x,y)\},$$

(3.4)

in which the transformed variables (u,v) are inversely proportional to the sample spacing in the original spatial domain. Equation 3.2 suggests that the level to which a signal can be restored is dependent on knowledge of the degradation function.

Representative amplitude response (1-D circumferential trace) of a rotating probe to a narrow axial flaw is shown in Fig. 3.32(a). The coil is a standard 2.92-mm (0.115-in.)-diameter pancake that was excited at a frequency of 300 kHz. The machined flaw is an axial notch of length 6.35 mm (0.25 in.) and depth of 100% TW. The trace in this figure was resampled at approximately twice the minimum prescribed ISI sampling rate of rotating probes. As an approximation to the coil response in Fig. 3.32(a), two different functions were considered in this study. Figure 3.32(b) displays Gaussian and Lorenzian functions of the form

$$\mathcal{G}(x) = Ae^{-\alpha(x-\beta)^2} \tag{3.5}$$

$$\mathcal{L}(x) = \frac{A}{1+\alpha(x-\beta)^2}, \tag{3.6}$$

in which β determines the peak position, and the parameter α is inversely proportional to the variance for the Gaussian function and to the width at half-height for the Lorenzian function. Values of the parameter β in Fig. 3.32(b) were selected such that the two functions have approximately the same widths at the half-height.

Although both Gaussian and Lorenzian functions could be considered as close approximations to the coil impulse response, the former can be adjusted to better match the measured response. This is expected, since the coil impedance is a complex exponential function (i.e., sinusoidal response). However, the Gaussian function, which often is the principal choice for simulating the coil impulse response, may not be the optimal choice for inverse-filtering applications. The sharp taper of this function could result in amplification of high-frequency signal components and false indications. The smoothly decreasing Lorenzian function, on the other hand, could resolve this problem associated with the use of Gaussian function as the impulse response of the coil.

Figure 3.33 displays a series of 2-D kernels that was constructed from 1-D Gaussian and Lorenzian functions of Fig. 3.32(b). The two types of kernels considered in this study consisted of (i) two superimposed orthogonal 1-D functions and (ii) "true" 2-D impulse response made by rotating a 1-D function about its vertical axis. Although both the Gaussian and Lorenzian functions have been implemented as part of a 2-D deconvolution algorithm, for all test cases considered so far the results have pointed to the consistency and improved stability of the Lorenzian over the Gaussian impulse response for restoration of RPC indications.

3.3.3 Test Case Results on RPC Signal Restoration

Preliminary evaluation of the 2-D deconvolution scheme that is integrated into a multiparameter data analysis algorithm was carried out using a subset of laser-cut notch specimens. A description of the sample/flaw geometries, along with the analysis of EC inspection results using bobbin and +Point™ probes, as well as multiparameter data analysis, was reported earlier. Inspection results that were acquired with a standard mid-range pancake coil were preprocessed by using both types of 2-D kernels described in the previous
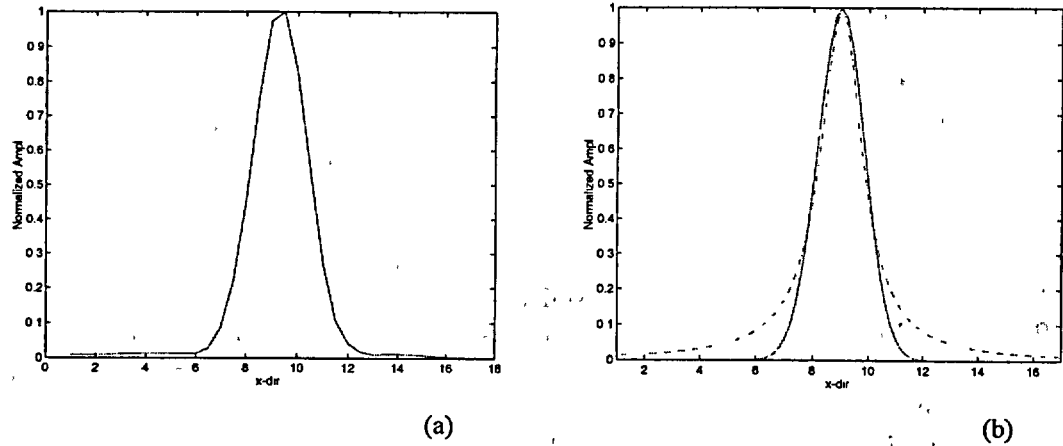
Fig. 3.32. (a) Typical amplitude response of RPC (2.92-mm [0.115-in.] pancake) to a 100% TW, 6.35-mm (0.25-in.)-long axial EDM notch at 300 kHz and (b) normalized Gaussian [solid line] and Lorenzian (dashed line) impulse responses having approximately the same parameters.
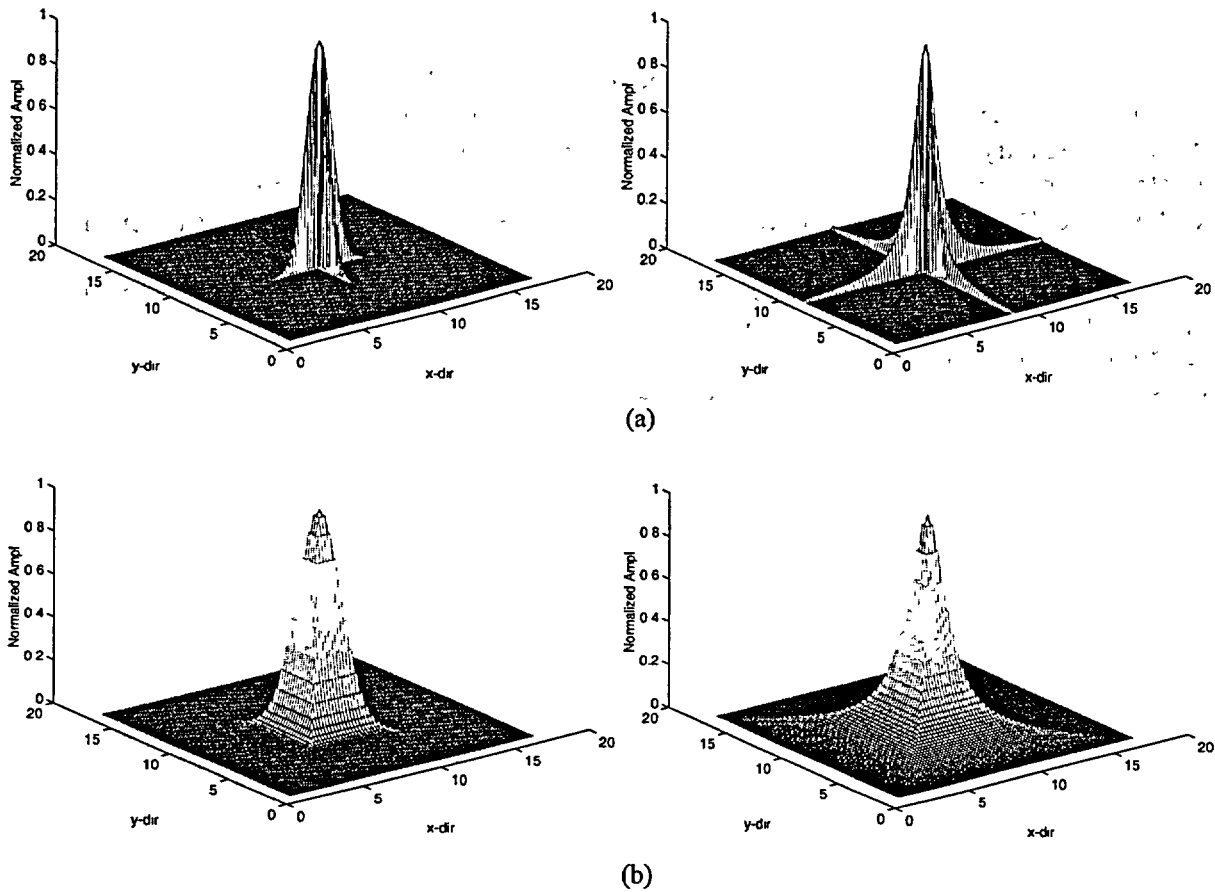
Fig. 3.33. Spatial domain 2-D kernels for Gaussian (left) and Lorenzian (right) impulse responses constructed by (a) two orthogonal 1-D functions and (b) rotation of 1-D function about vertical axis.

47

section. To display the outcome of the inverse-filtering scheme, intermediate results with a Lorenzian impulse response are presented at a single frequency. However, it should be noted that for multiparameter data analysis, the code automatically calculates the impulse response parameters for all the available excitation frequencies. A user-defined segment of the EC trace, typically from the available tube standard, is initially used to calculate these parameters.

Figure 3.34(a) shows a terrain plot of the original C-scan data from a Type-1 laser-cut specimen (#5528-1-1) containing a single axial notch of length 6.35 mm and nominal OD depth of 80%TW. Figures 3.34(b) and (c) display the restored signals subsequent to application of the 2-D kernels that were shown in Figs. 3.32(a) and (b), respectively. In both cases, the deconvolved signals display better spatial resolution and lower baseline variation. The improvement in spatial resolution could most clearly be observed from comparison of the original and restored response at opposite ends of the axial flaw in which the flaw ends in the deconvolved signal are better defined. This is also reflected in the lissajous trace displayed alongside the terrain plot. Similar improvement in spatial resolution is also expected in the circumferential direction. NDE maximum depth estimates for this sample were 58% by BC (phase-angle) and 75% by multiparameter analysis of RPC (2.92-mm [0.115-in.] pancake) data.

Figures 3.35-3.41 show the results of inverse filtering on a selected subset of laser-cut specimens with one or both types of 2-D lorenzian kernels. In all cases, the restored data show improved spatial resolution and reduction of the baseline noise level. It is important to note that the primary objective of the proposed deconvolution scheme as a preprocessing tool for multiparameter analysis of EC inspection results is to maximize the separation between crack-like indications and extraneous signals with minimum loss of information from the original data. For all test cases shown here, the results also indicate less ambiguity in the measurement of the phase-angle of restored indications in comparison to those from the original readings. Studies are currently underway to further evaluate the applicability of inverse filters as efficient signal processing schemes for the analysis of EC inspection results. Effectiveness of the algorithms will also be tested by including various lab-produced specimens from the SG mock-up.
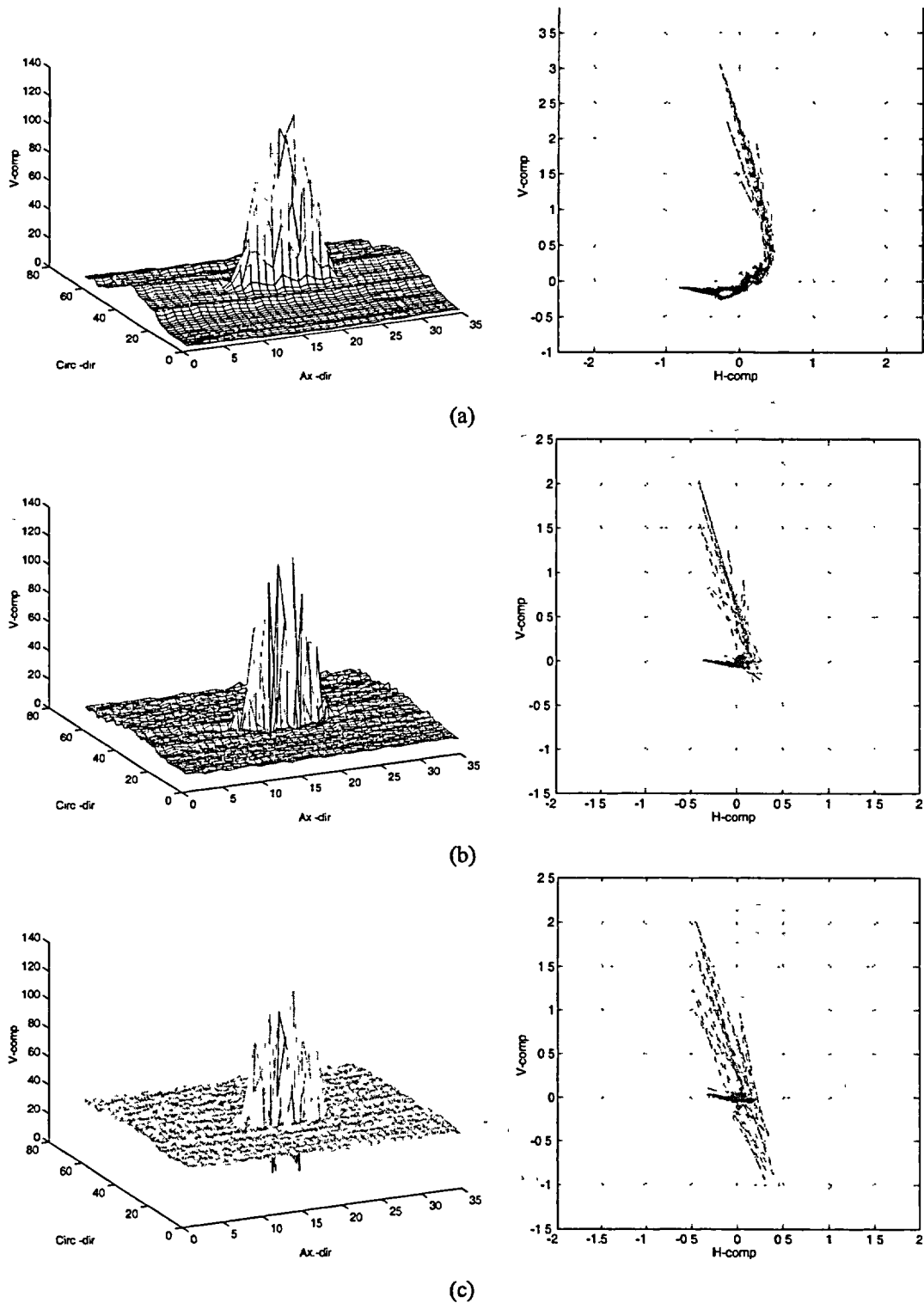
Fig. 3.34. (a) Original and (b)-(c) restored signals with 2-D Lorenzian kernels of Fig. 3.34 for Type-1 laser-cut specimen #5528-1-1 with nominal OD flaw depth of 80% TW. In both cases, the deconvolved signal displays higher spatial resolution and lower baseline variation. NDE maximum depth estimates were 58% by bobbin coil (phase-angle) and 75% by multiparameter analysis of RPC (2.92-mm [0.115-in.] pancake) data.

49
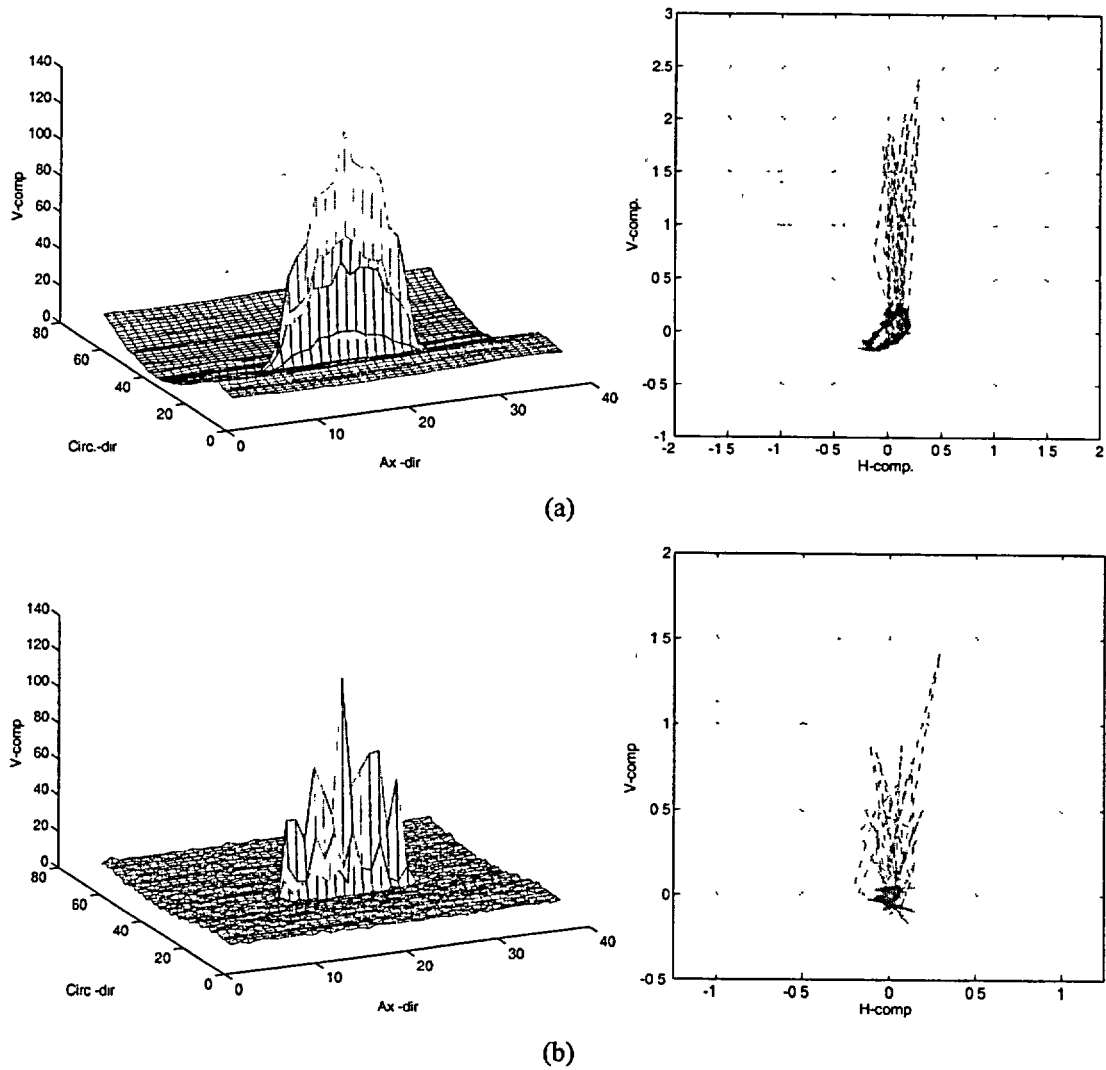
Fig. 3.35. (a) Original and (b) restored signal for Type-2 Laser-cut specimen #5516-4-3 with nominal OD flaw depth of 80% TW. NDE maximum depth estimates were 35% by bobbin coil (phase-angle) and 72% by multiparameter analysis of RPC (2.92-mm [0.115-in.] pancake) data.
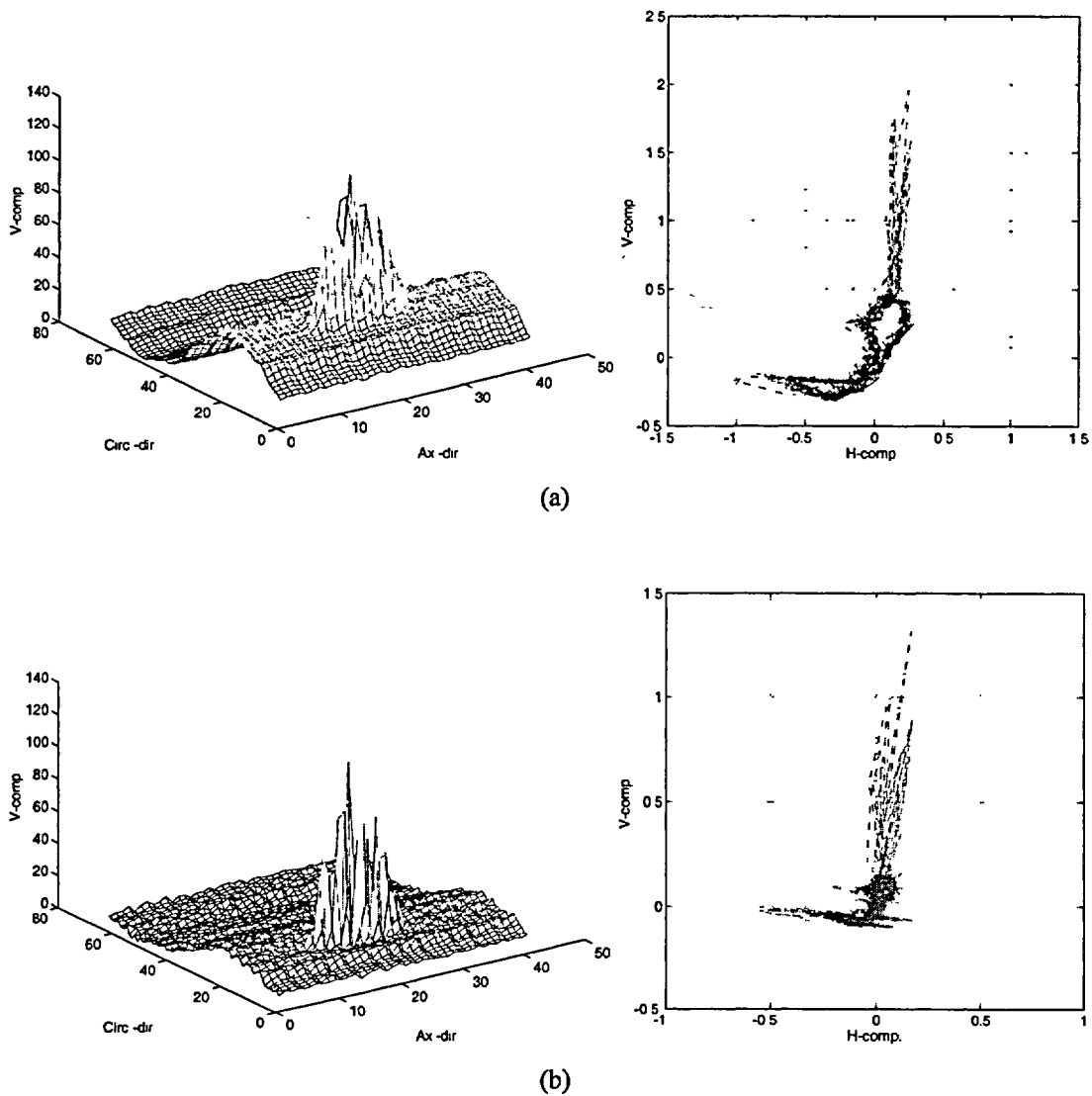
Fig. 3.36. *(a) Original and (b) restored signal for Type-3 Laser-cut specimen #5528-3-3 with nominal OD flaw depth of 40% TW. NDE maximum depth estimates were 42% by bobbin coil (phase-angle) and 61% by multiparameter analysis of RPC (2.92-mm [0.115-in.] pancake) data.*

51
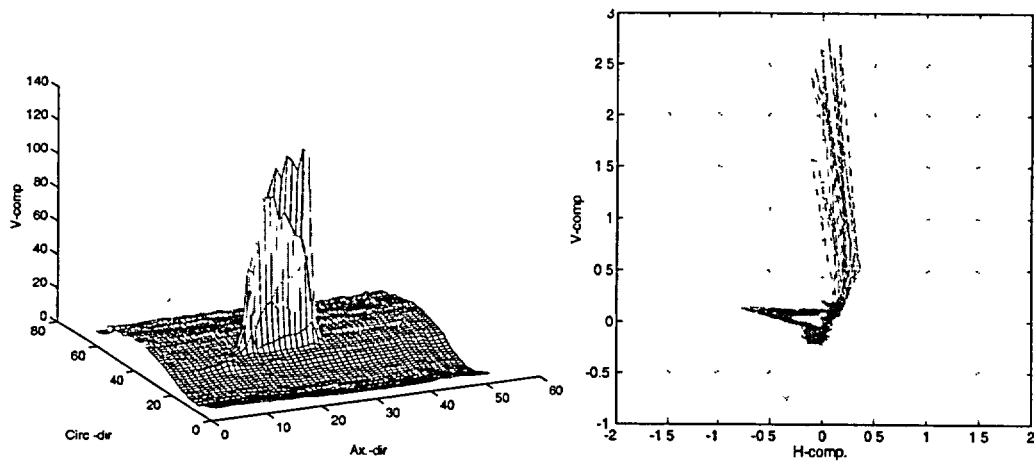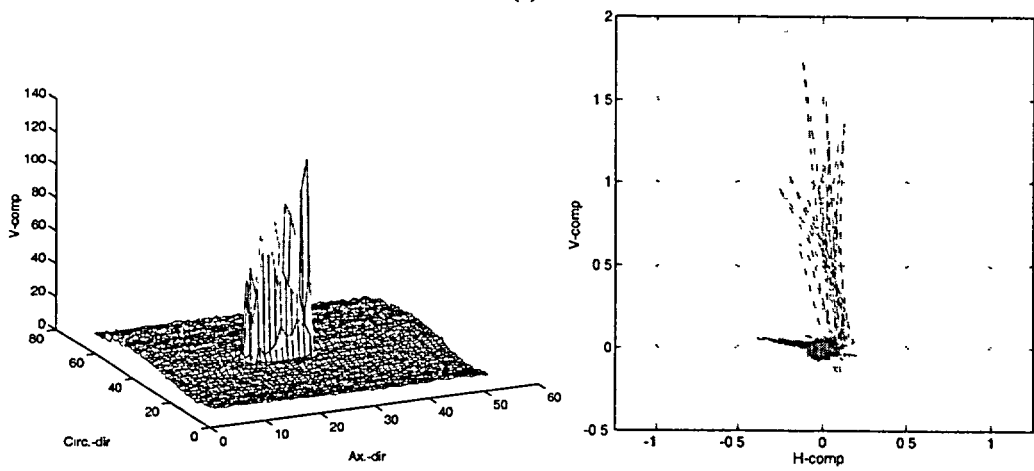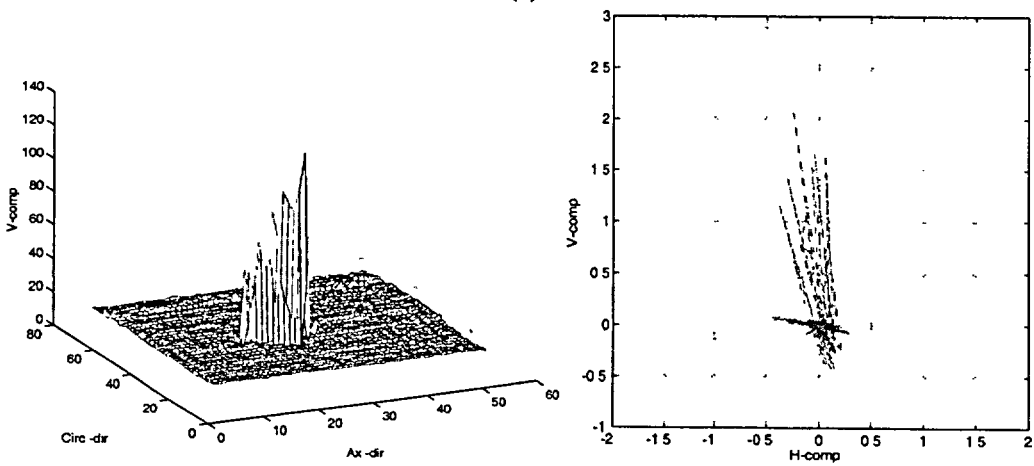
Fig. 3.37. (a) Original and (b)-(c) restored signals with 2-D Lorenzian kernels for Type-4 laser-cut specimen #5469-2-1 with nominal OD flaw depth of 80% TW. NDE maximum depth estimates were 45% by bobbin coil (phase-angle) and 74% by multiparameter analysis of RPC (2.92-mm [0.115-in.] pancake) data.
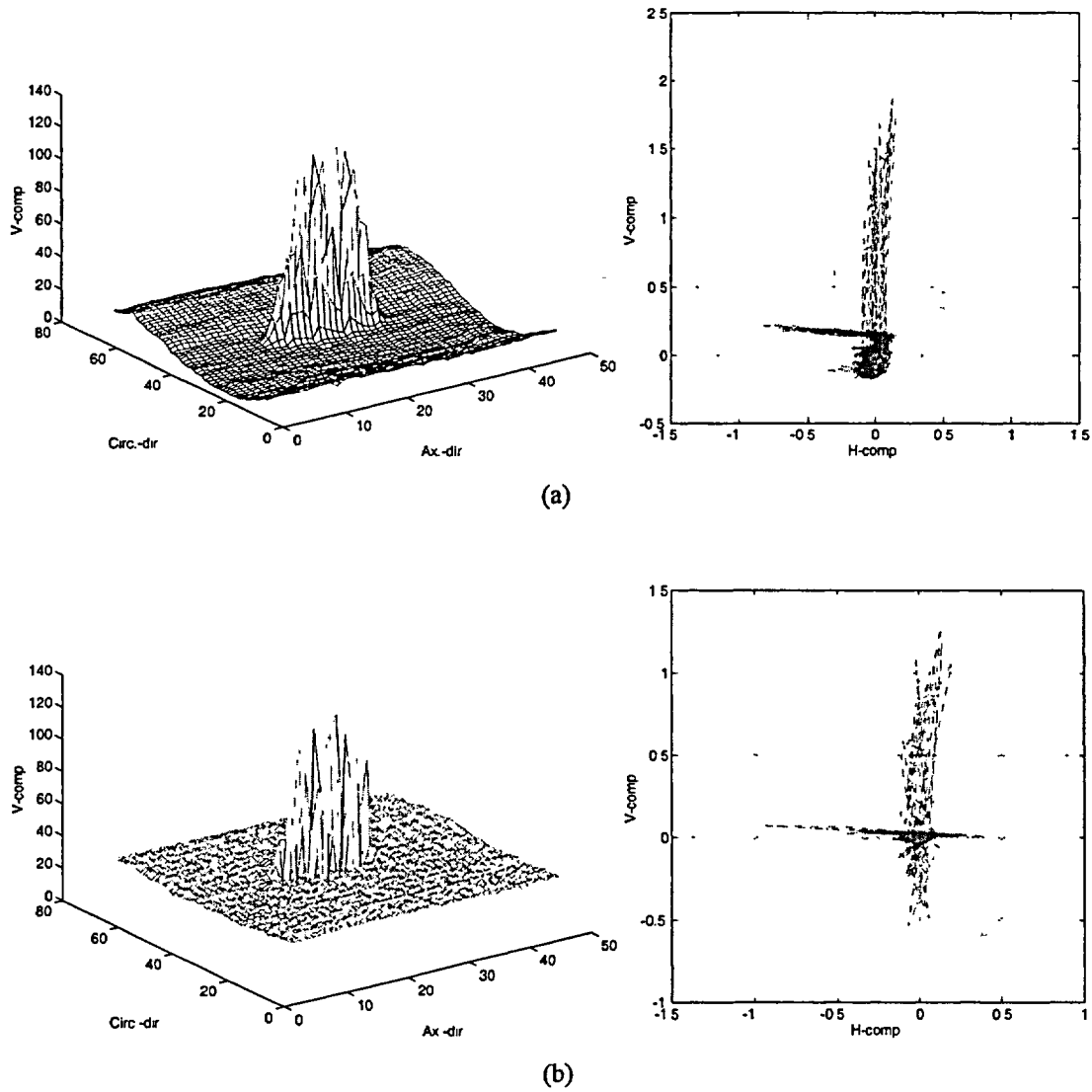
Fig. 3.38. *(a) Original and (b) restored signal for Type-4 Laser-cut specimen #5469-2-2 with nominal OD flaw depth of 40% TW. NDE maximum depth estimates were 43% by bobbin coil (phase-angle) and 60% by multiparameter analysis of RPC (2.92-mm [0.115-in.] pancake) data*
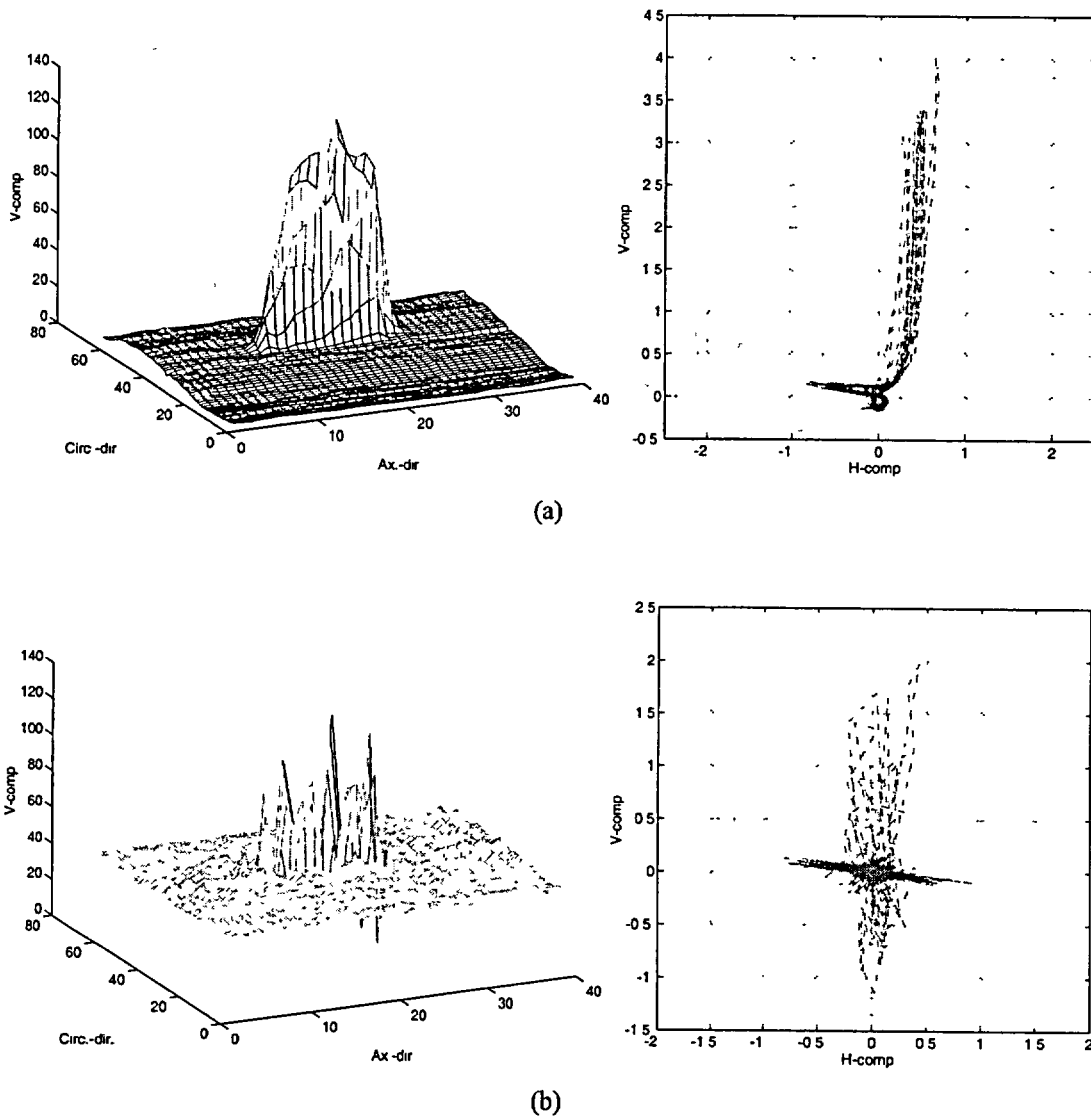
Fig. 3.39. *(a) Original and (b) restored signal for Type-5 Laser-cut specimen #5469-2-4 with nominal OD flaw depth of 80% TW. NDE maximum depth estimates were 64% by bobbin coil (phase-angle) and 78% by multiparameter analysis of RPC (2.92-mm [0.115-in.] pancake) data*
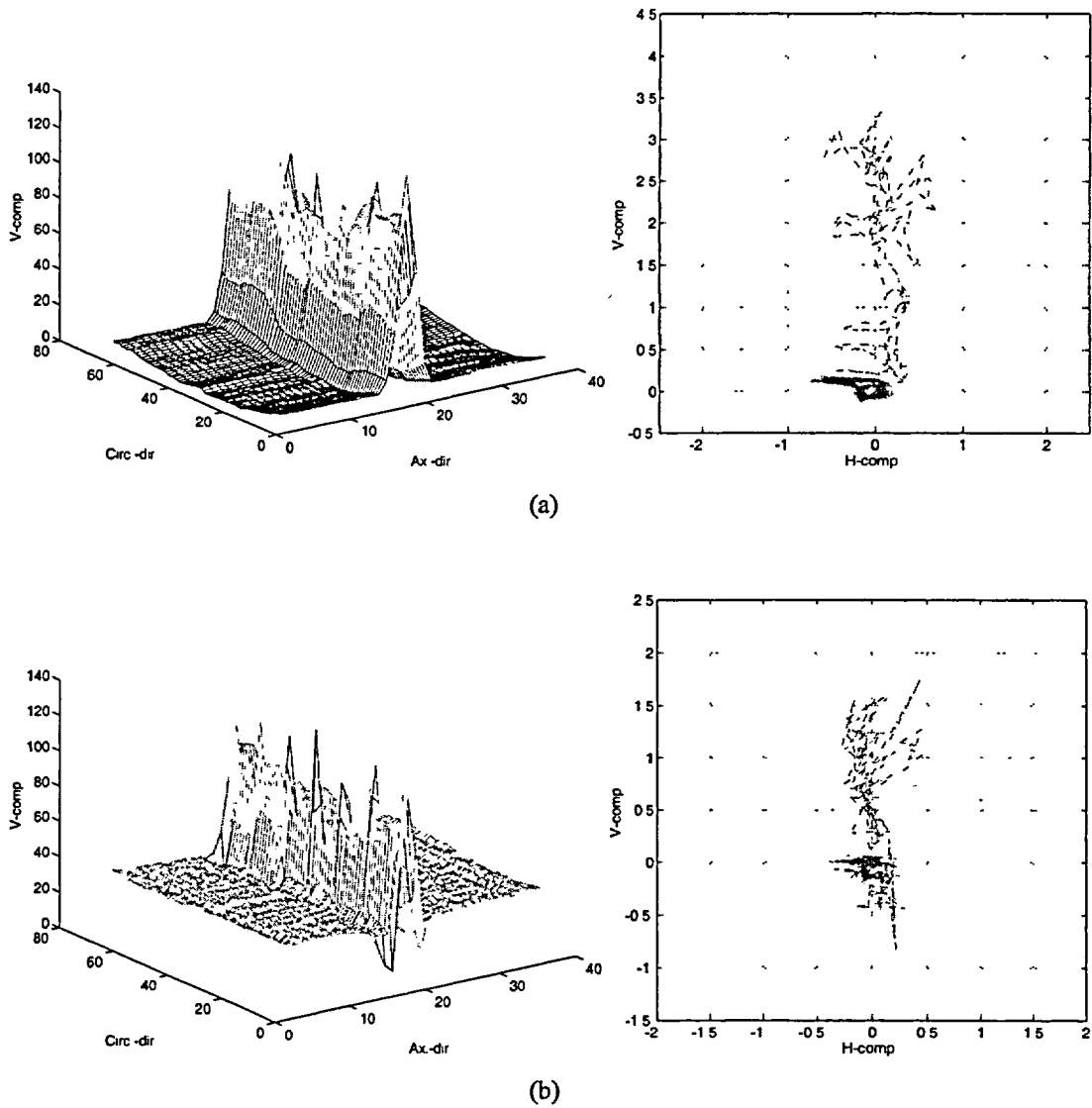
Fig. 3.40. *(a) Original and (b) restored signal for Type-8 Laser-cut specimen #5469-4-1 with nominal OD flaw depth of 40% TW. NDE maximum depth estimates were 39% by bobbin coil (phase-angle) and 70% by multiparameter analysis of RPC (2.92-mm [0.115-in.] pancake) data*
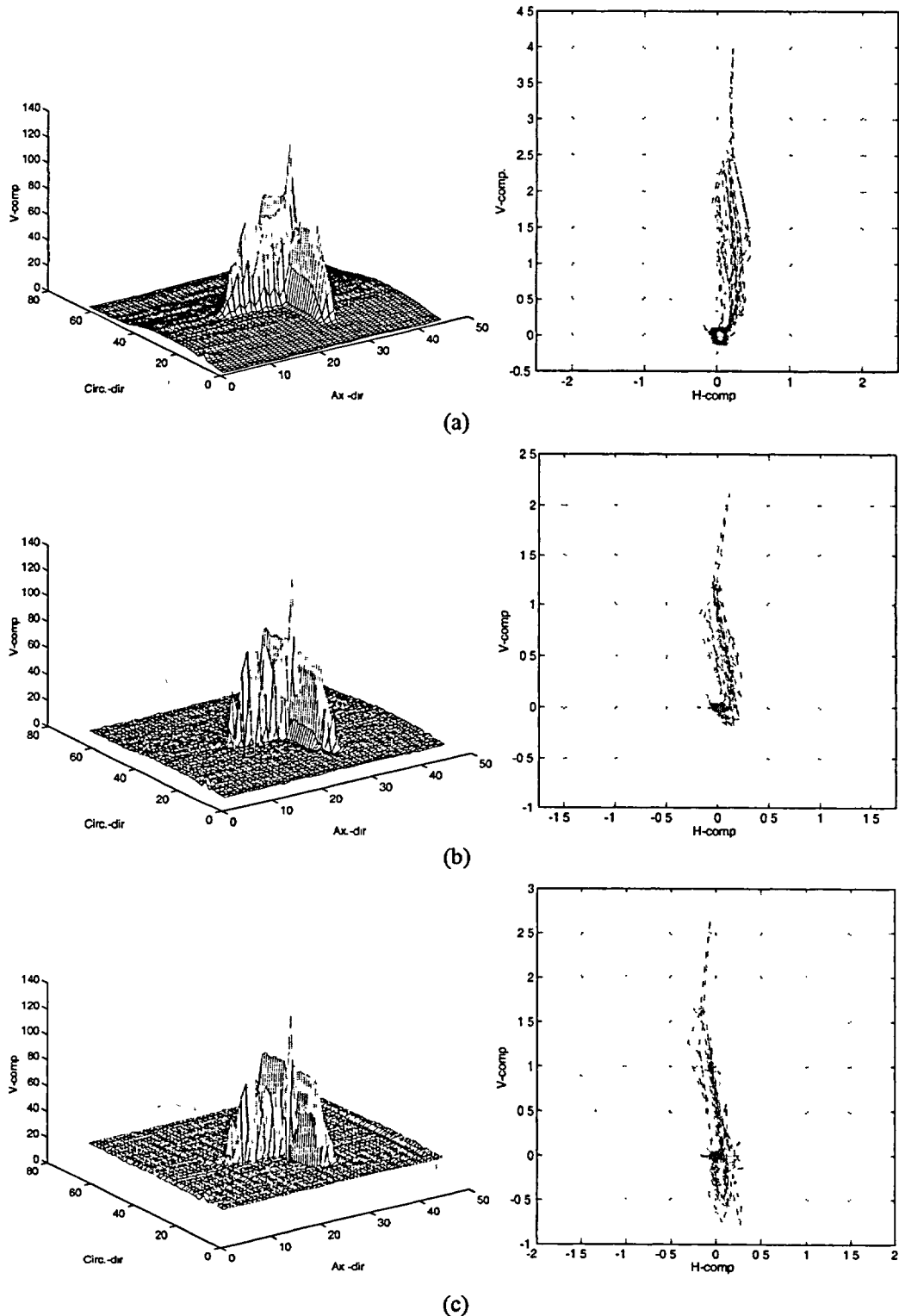
Fig. 3.41. (a) Original and (b)-(c) restored signals with 2-D Lorenzian kernels for Type-9 laser-cut specimen #5469-4-3 with nominal OD flaw depth of 80% TW. NDE maximum depth estimates were 48% by bobbin coil (phase-angle) and 69% by multiparameter analysis of RPC (2.92-mm [0.115-in.] pancake) data.

4 Research on Degradation Modes and Integrity (K. E. Kasza, S. Majumdar, J. Y. Park, W. J. Shack, and D. R. Diercks)

4.1 Production of Laboratory-Degraded Tubes

Because degraded tubing from operating or retired SGs is difficult and expensive to obtain and the availability of such tubing is limited, it is necessary to produce prototypical degradation in tubes as a part of this program. These tubes are to be used to evaluate NDE equipment and techniques in the SG mock-up and for pressure and leak-rate testing. Techniques for Alloy 600 tubes have been developed to produce SCC degradation of various sizes, depths, and orientations that are prototypical of field-degraded SG tubes.

4.1.1 Production of Cracked Tubes

The production of laboratory-degraded tube specimens continued throughout the reporting period. Alloy 600 tubes of 22.2-mm (7/8-in.) diameter (Heats NX8527 from Valinco and NX7968 from PNNL) were subjected to the cracking process. These tubes were cracked by exposing them to a 1 M aqueous solution of sodium tetrathionate ($Na_2O_6S_4 \cdot 2H_2O$) at room temperature and atmospheric pressure. Before exposure to the tetrathionate solution, the specimens were solution-heat-treated at 1100°C ($\approx$2012°F) for 10 min and aged at 600°C ($\approx$1112°F) for 48 h to produce a microstructure that is susceptible to cracking.[1] During this reporting period, approximately 250 of these tubes have been processed in the tetrathionate solution for axial or circumferential ODSCC and IDSCC at straight, roll-expanded, and dented tube sections. Some of the heat-treated tubes have been installed as uncracked blanks in the NDE SG tube mock-up (see Section 2.1).

Several techniques have been explored in an effort to produce segmented SCC, including surface defects, shot-peening, localized environmental exposure, low load, and applied electrochemical potential. A localized electrochemical potential technique with low applied load and area masking appears to be most effective to date.

Degraded tubes have nondestructively been examined by optical microscopy, dye-penetrant techniques, and EC NDE. The lengths and orientations of cracks in the tubes varied widely. Crack depths also ranged from 5 to 100% TW, as determined by EC NDE. Figures 4.1-4.24 show examples of optical microscopy, dye-penetrant examination, and EC NDE results for various SCCs in the tube specimens.

Figures 4.1 and 4.2 show the EC NDE measurements and the dye penetrant examination results for specimen SGL-413 with an axial ODSCC indication. The depth of the ODSCC is estimated to be $\approx$90% TW. Figure 4.3 is an optical photomicrograph of an axial ODSCC at the surface in Specimen SGL-288 at a magnification of 100x. Figure 4.4 shows the dye-penetrant examination of axial ODSCC cracks in Specimen SGL-288. Two axial cracks of lengths 6 and 3 mm (0.24 and 0.12 in.) are seen. Figure 4.5 shows EC NDE results for the two axial ODSCC cracks. The maximum depth of these cracks was estimated to be $\approx$40% TW. Figure 4.6 is the dye-penetrant examination of axial ODSCC in Specimen SGL-415, showing that the crack is
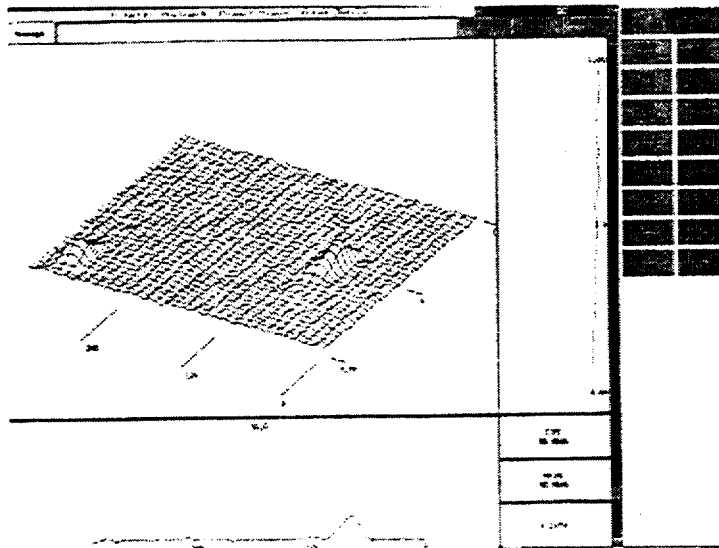
Fig. 4.1.   *Eddy current NDE test results for Alloy 600 Tube SGL-413 with a 90% TW axial ODSCC indication.*
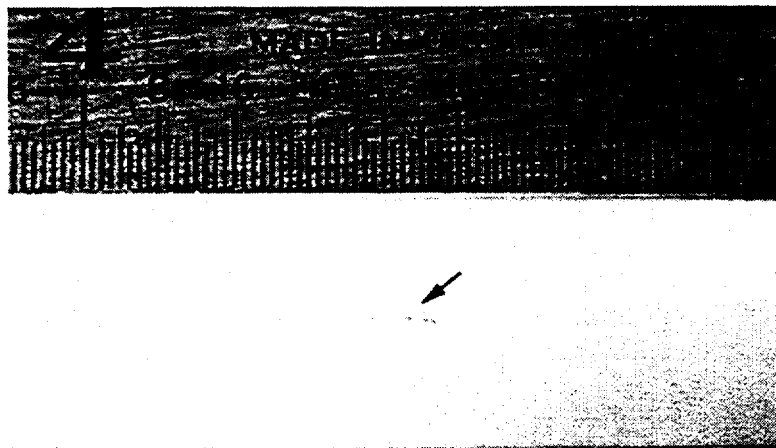
Fig. 4.2.   *Dye-penetrant results for Alloy 600 tube SGL-413 with a 5-mm- (0.20-in.)-long axial ODSCC indication.*

Fig. 4.3.   *Optical microscopy of axial ODSCC in Specimen SGL-288 at 100X.*
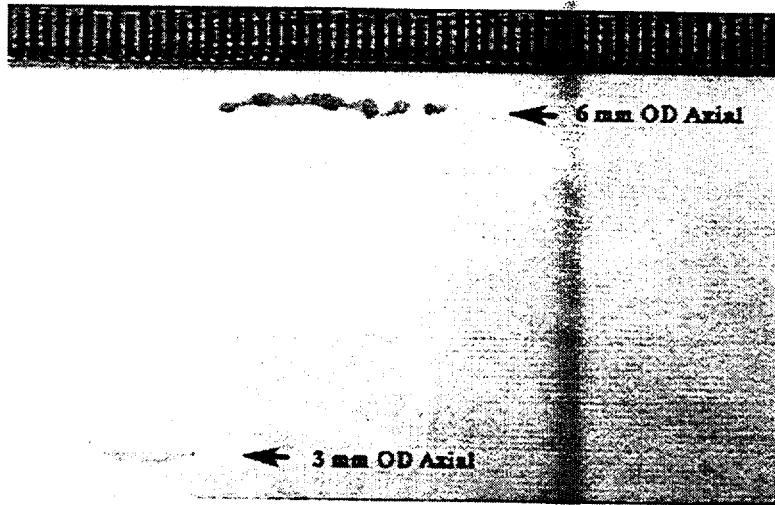
Fig. 4.4.   *Dye-penetrant examination of Specimen SGL-288 showing two axial cracks.*
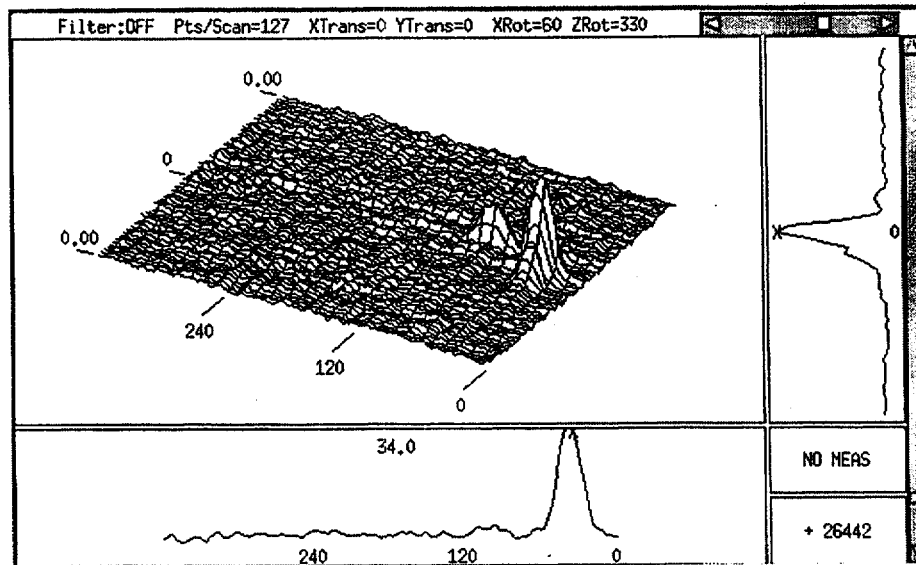
Fig. 4.5. *Eddy current NDE test results from Specimen SGL-288 showing an axial ODSCC indication.*

segmented. Figure 4.7 is the EC NDE result for specimen SGL-415. Two parallel 40% TW axial ODSCC indications are seen.

Figures 4.8 and 4.9 are dye-penetrant examination results and EC NDE results for a throughwall axial-circumferential ODSCC in Specimen SGL-418. Figure 4.10 shows dye-penetrant examination results for segmented axial ODSCC in Specimen SGL-495, and Figure 4.11 shows the EC NDE. Two axial SCCs (5 and 12 mm [0.20 and 0.47 in.] long) are separated by a 12-mm (0.47-in.)-long segment. Figure. 4-12 shows dye penetrant examination of the circumferential ODSCC in the roll-expanded region of specimen SGL-591. Figure 4.13 shows EC NDE results for specimen SGL-591. The depth of the ODSCC is estimated to be ≈80% TW. The ODSCC is segmented, and the overall length is about 5 mm (0.20 in.).

Figure 4.14 shows the dye-penetrant examination of the circumferential ODSCCs in the roll-expanded specimen SGL-571. The ODSCCs are segmented, and the overall length is ≈15 mm (0.59 in.). Figure 4.15 shows EC NDE results for specimen SGL-571. The depth of the ODSCC is estimated to be about 90% TW. Figure 4-16 shows dye-penetrant examination of the ODSCC in the roll-expanded region of specimen SGL-564. The ODSCC is mixed, with axial and circumferential components. The overall length is ≈16 and 6 mm (0.63 and 0.24 in.) for the axial and circumferential component. Figure 4-17 shows EC NDE results for specimen SGL-564 with an axial-circumferential ODSCC. The depth of the ODSCC is estimated to be ≈95% and 90% TW for the axial and circumferential components, respectively. Figure 4.18 shows NDE results for multiple ODSCC introduced into the roll-expanded SGL-366. Crack depth is estimated to be ≈45% TW.

A technique to introduce axial SCC in dented tubes was developed during the reporting period. Ten dented tubes from Heat NX8527 and five dented tubes from Heat NX7968 were
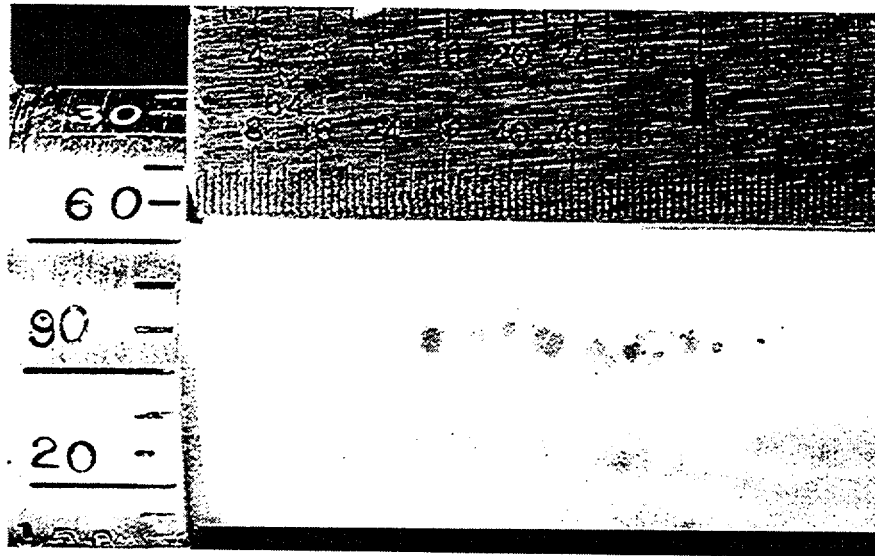
Fig. 4.6. Dye-penetrant examination of Tube SGL-415 showing segmented axial ODSCC.
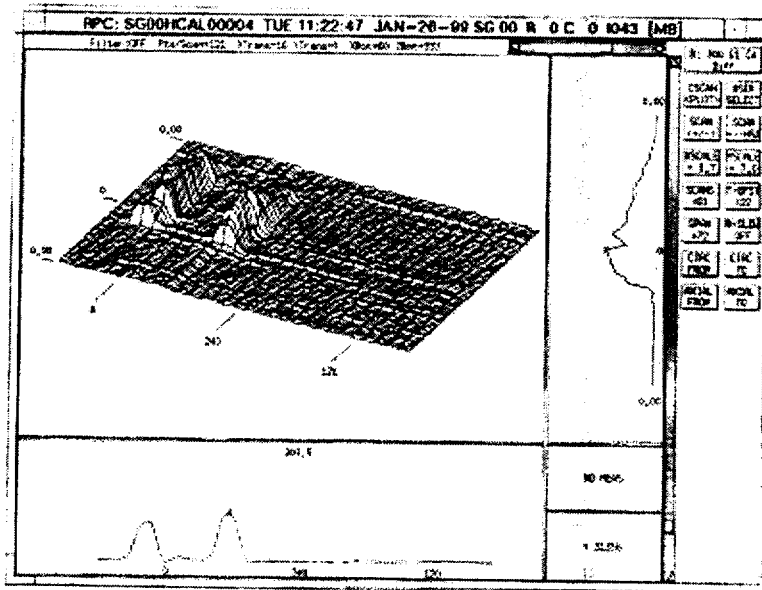
Fig. 4.7. Eddy current NDE test results for Tube SGL-415 showing two ≈40% TW axial ODSCC indications.

Fig. 4.8.   Dye penetrant examination of tube SGL-418 showing circumferential-axial
ODSCC.

Fig. 4.9.   Eddy current NDE test results for tube SGL-418 showing TW circumferential-axial
ODSCC indication.

62

Fig. 4.10. Dye-penetrant examination results for Alloy 600 tube SGL-495 showing segmented ODSCC indications.

Fig. 4.11. Eddy current NDE test results for Alloy 600 tube SGL-495 showing segmentation of axial ODSCC.

Fig. 4.12. *Dye-penetrant examination of roll-expanded Alloy 600 tube SGL-591 with 5–mm (0.20-in.)-long circumferential ODSCC indications.*
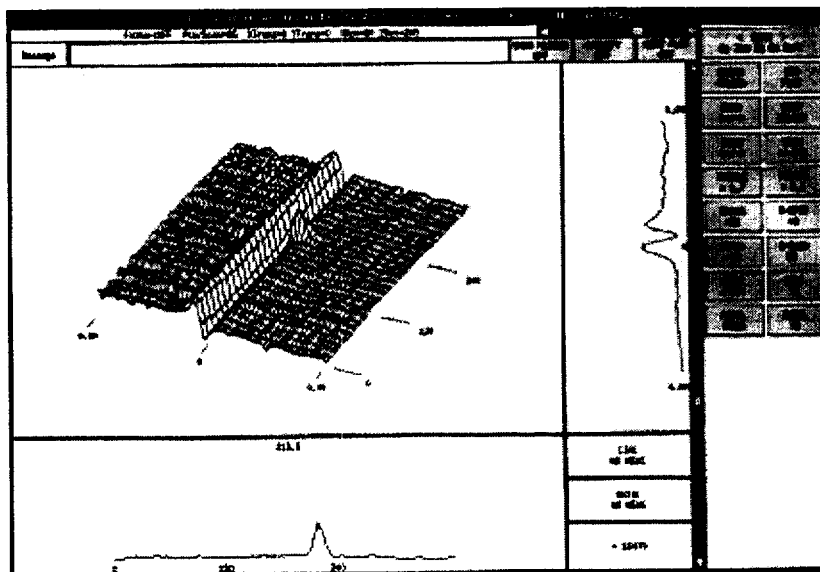
Fig. 4.13. *Eddy current NDE test results of roll-expanded Alloy 600 Tube SGL-591 with circumferential ODSCC indications of 80% TW depth.*
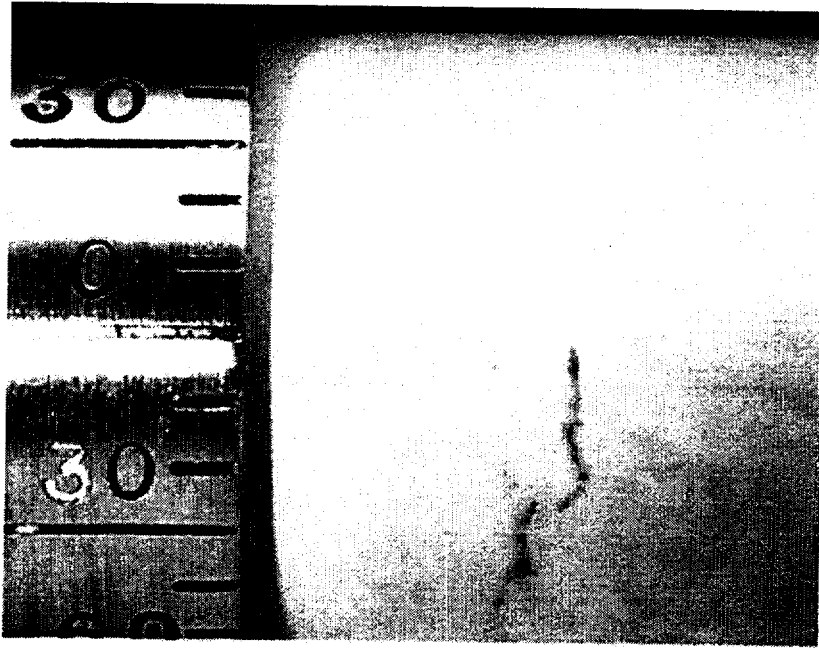
Fig. 4.14. *Dye penetrant examination of roll-expanded Alloy 600 tube SGL-571 with segmented circumferential ODSCC indications.*
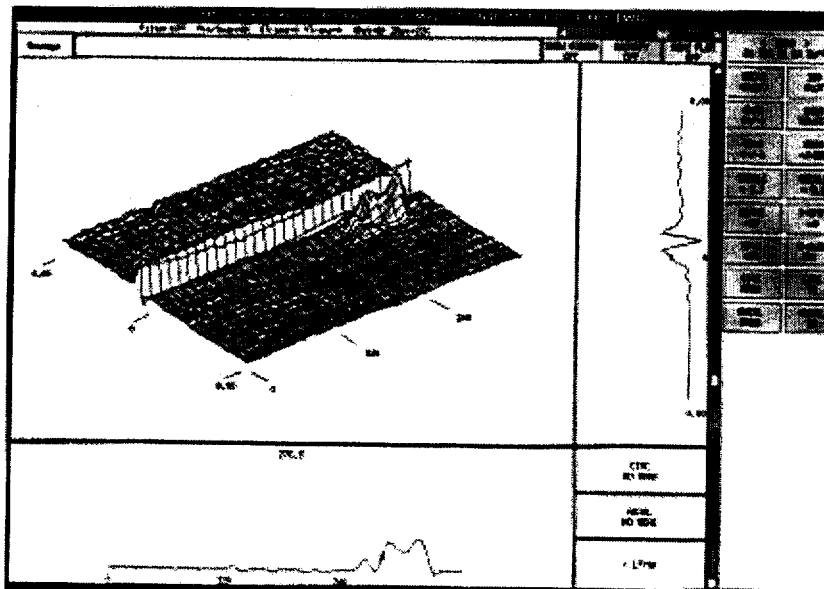
Fig. 4.15. *Eddy current NDE test results of roll-expanded Alloy 600 tube SGL-571 with circumferential ODSCC indications of 90% TW depth.*

65
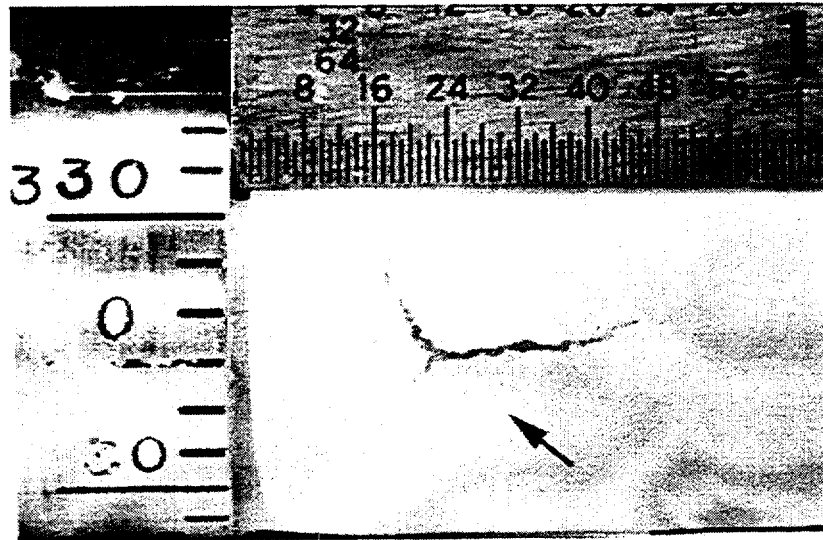
Fig. 4.16. Dye-penetrant examination of roll-expanded Alloy 600 tube SGL-564 with 16-mm (0.63-in.)-long axial and 6-mm (0.24-in)-long circumferential ODSCC indications.
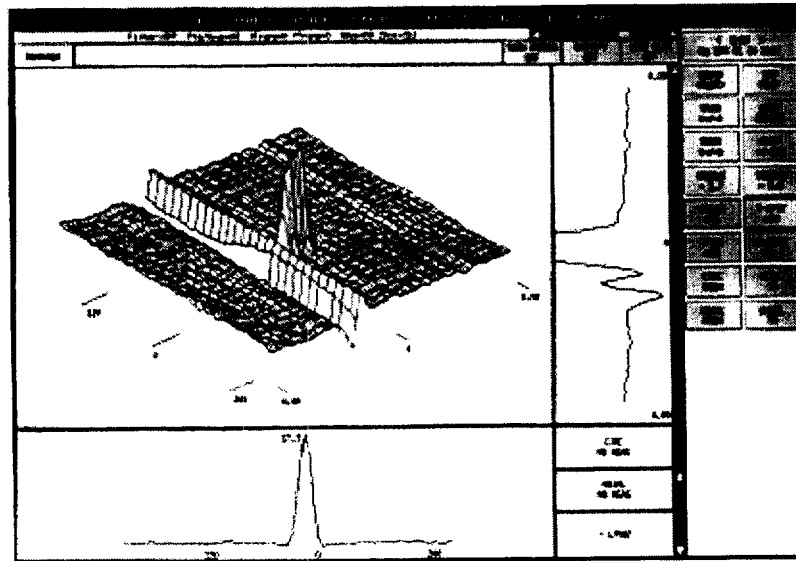
Fig. 4.17. Eddy current NDE test results of roll-expanded Alloy 600 tube SGL-564 with axial-circumferential ODSCC indications of 95 and 90% TW depth.
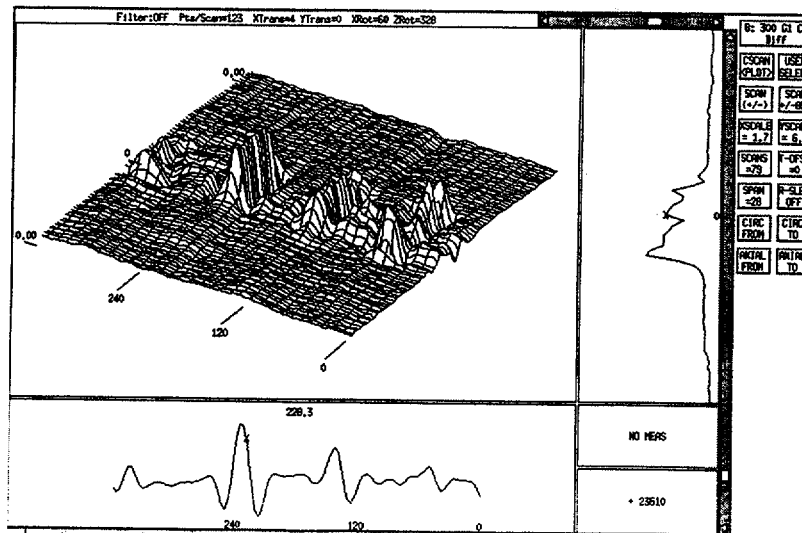
Fig. 4.18. *Eddy current NDE test results for Alloy 600 tube SGL-366 showing ODSCC indications in roll-expanded area.*

processed for axial SCC. Figure 4.19 is a photomacrograph of specimen SGL-397 showing a 12.7-mm (0.5-in.)-long mechanical dent introduced on the OD surface. Figures 4.20 and 4.21 are EC NDE results for the specimen SGL-397 before and after the introduction of axial IDSCC, respectively. The depth of the IDSCC is estimated to be ≈60% TW. Figure 4.22 shows dye penetrant examination results for dented specimen SGL-527, indicating segmented axial ODSCC. Figure 4.23 is a photomicrograph of the OD of the specimen SGL-527. Figure 4.24 is an example of a dye-penetrant examination of OD axial cracks in dented specimen SGL-447. Two parallel axial ODSCCs with lengths of 20 and 30 mm are seen.

The solution and sensitization heat treatments cause grain growth and a reduction in hardness and flow stress. Tensile tests were performed for eight tube specimens (SGMC001 through 008) at room temperature to measure the reduction of flow stress for Alloy 600 tubes (Heat NX8527). The results show that ultimate tensile and yield strengths of the as-received mill-annealed tubes are 696±14 MPa (101±2 ksi) and 317±14 MPa (46±2 ksi), while the corresponding values for the heat-treated tubes are 600±14 MPa (87±2 ksi) and 179±14 MPa (26±2 ksi), respectively. Thus, the flow stress of the material is reduced by ≈20% due to the heat treatments. A correction for this effect on mechanical properties will be required when these tubes are used for subsequent pressure and leak-rate testing. To minimize this effect on mechanical properties, different heat treating conditions are being investigated. In particular, specimens were heat treated at lower temperatures and tested for stress corrosion cracking. Twenty Alloy 600 tube specimens were solution-heat-treated at 990-1020°C (1814-1868°F) rather than 1100°C (2012°F) and are ready for SCC testing. Hardness measurements were performed for the Alloy 600 specimens from Heat No. NX8527 that were heat treated at different temperatures, and the results are summarized in Table 4.1. It appears that the hardness begins to drop substantially at solution-heat-treating temperatures of ≈990°C (1814°F) and greater.

Fig. 4.19.   Photomacrograph of specimen SGL-397 showing axial dent on OD surface.

Fig. 4.20.   Eddy current NDE test results from SGL-397 before degradation.
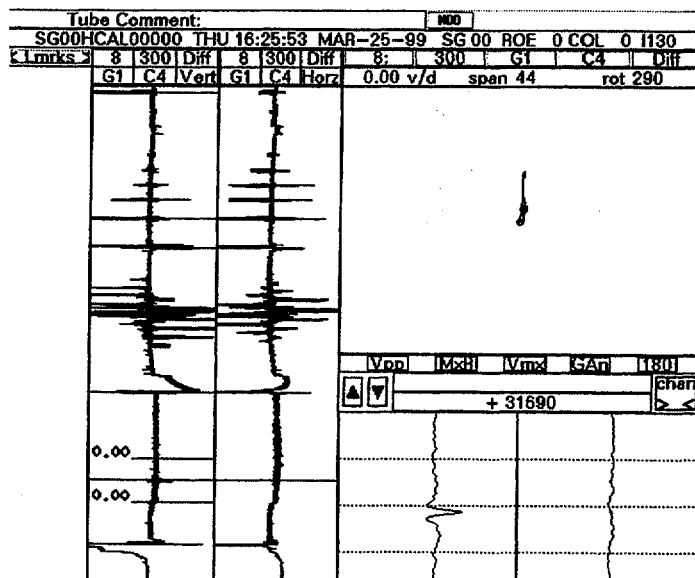
Fig. 4.21.   Eddy current NDE test results from specimen SGL-397 after degradation.

A new heat (Heat NX8620) of 22.2-mm (7/8-in.)-diameter Alloy 600 tubes was obtained for the program in addition to heats NX8527 and NX7968. This new heat was mill-annealed for 2 to 3 min at two different temperatures: 980°C (1796°F), Heat NX8520L, and 1060°C (1940°F), Heat NX8520H). The chemical composition of the new heat is presented in Table 4.2 along with that of heats NX8527 and NX7968. The hardnesses of this material as-mill-annealed and after sensitization were measured, and the results are summarized in Table 4.3. Further materials properties characterization will be conducted for this new heat.

To examine the influence of the oxide film on EC response, 10 cracked tubes were oxidized in high-temperature-water environments. Of these, five tubes (SGL-114, 159, 170, 182, and 187) were oxidized in deionized high-purity water with 8 ppm dissolved oxygen at 290°C (554°F) and 8.8 MPa (1280 psi) for 1680 h. Five additional tubes (SGL-127, 149, 169, 189, and 197) were oxidized in deionized high-purity water with 3 ppm dissolved oxygen at 290°C (554°F) for 120 h and then in a simulated primary water environment (1200 ppm B and 2 ppm Li) at 320°C (608°F) and 12.4 MPa (1800 psi) for 1400 h. Eddy current NDE was performed before and after the oxidation treatment. Results from the EC examinations of these specimens are described under Task 1 in Section 2.4 of this report. The BC voltages were found to increase significantly for the oxidized tubes, though the shape of the Lissajous figures remained unchanged. In contrast, the results for the +Point coil were inconclusive.

Three additional cracking facilities were constructed to increase the production rate of cracked tubes. Each facility will be able to handle four individual tube specimens to produce axial ODSCC. The existing cracking facilities were also refurbished to improve the stability of the applied loads. Efforts are continuing to produce additional degraded tubes with more complex geometries prototypical of field SCC, e.g., axial ODSCC with ligaments between small multiple cracks. Future efforts will focus on degrading tubes with denting or on producing cracking at the roll expansion.
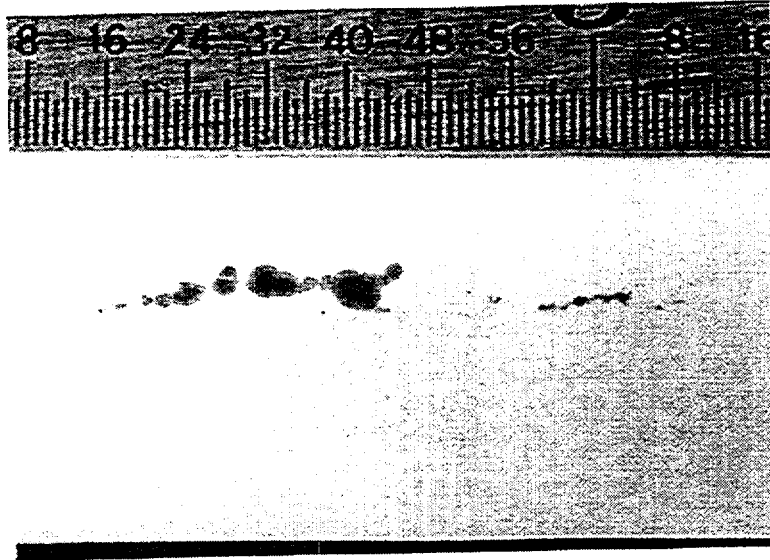
Fig. 4.22. Dye penetrant examination of dented Alloy 600 tube SGL-527 showing segmented axial ODSCC indication.
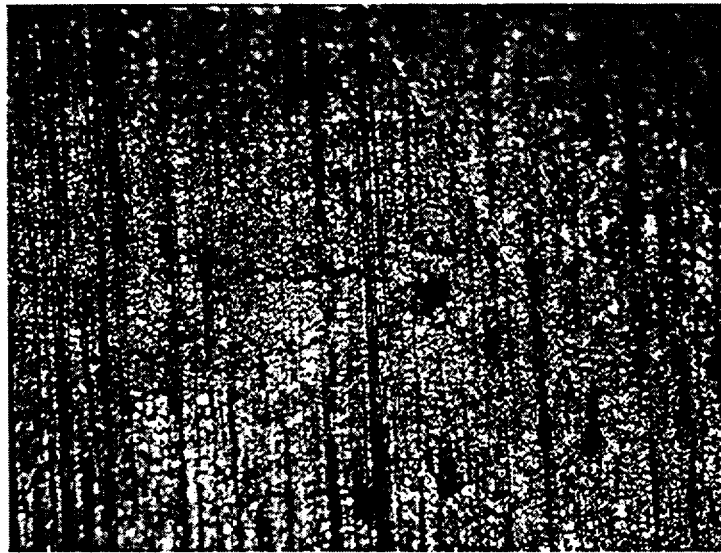
Fig. 4.23. Photomicrograph of dented Alloy 600 tube specimen SGL-527 showing an axial ODSCC (433X).

70
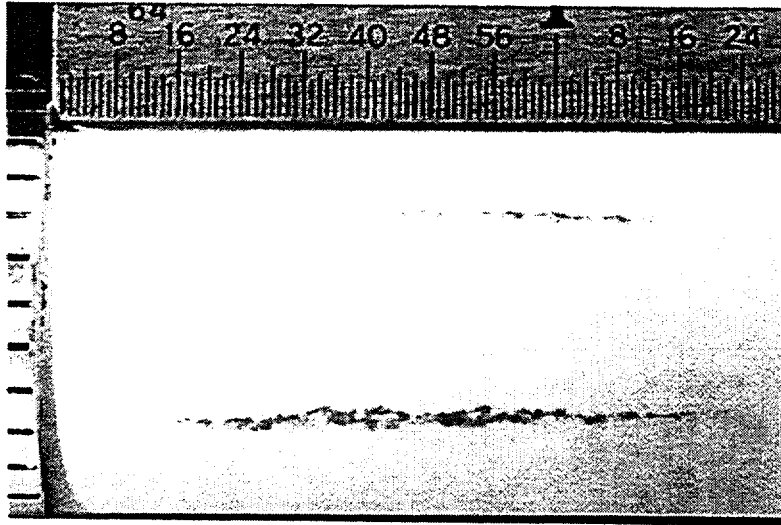
Fig. 4.24. Dye penetrant examination of dented Alloy 600 tube SGL-447 showing two parallel axial ODSCC indications.

Table 4.1. Hardness vs. heat treatment (Alloy 600, Heat NX8527)

Specimen ID	Heat Treatment	Vickers Hardness
5455-4	As Received	181
5457-3	As Received	176
SGL-684	960°C 20 min, 600°C 48 hr	165
SGL-694	970°C 20 min, 600°C 48 hr	169
SGL-673	980°C 20 min, 600°C 48 hr	173
SGL-710	990°C 20 min, 600°C 48 hr	161
SGL-703	1000°C 20 min, 600°C 48 hr	153
SGL-130	1100°C 10 min, 600°C 48 hr	136

Table 4.2. Chemical compositions of three heats of Alloy 600 (wt.%)

Element	Heat NX8520	Heat NX8527	Heat NX7968
Carbon	0.022	0.025	0.040
Manganese	0.19	0.21	0.24
Iron	8.03	8.49	8.38
Sulfur	<0.001	<0.001	0.001
Silicon	0.21	0.13	0.14
Copper	0.02	<0.01	0.18
Nickel	75.63	75.20	75.44
Chromium	15.40	15.35	15.58
Aluminum	0.21	0.23	a
Titanium	0.26	0.36	a
Cobalt	0.02	0.02	a
Phosphorus	0.004	0.005	a
Boron	0.004	0.001	a
Nitrogen	<0.01	<0.01	a

aNot reported.

Table 4.3. Hardness vs. heat treatment for heats NX8527 and NX8520

Heat No.	Heat Treatment	Vickers Hardness
NX8527	Mill annealed (940°C 3 min)	179
NX8527	Mill annealed + 1100°C 10 min. and 600°C 48 h	148
NX8520 L	Mill annealed (980°C 3 min)	162
NX8520 H	Mill annealed (1060°C 2 min)	146

4.2 Testing in the Pressure and Leak-Rate Test Facility

Testing continued in the high-temperature Pressure and Leak-Rate Test Facility through the first three months of the present reporting period, after which effort was diverted to the production of cracked tubes for the Steam Generator Tube Mockup (see Section 2.1) and the assembly of the High-Pressure Test Facility (see Section 4.3). The tests conducted in the Pressure and Leak-Rate Test Facility during this three-month period are described here.

These additional tests (beyond those described in the previous annual report[2]) were conducted on 22.2-mm (7/8-in.)-diameter Alloy 600 (Valinco heat NX8524) tubes containing axial OD electrodischarge machined (EDM) notches of various lengths and depths. Tests were also conducted on tubes containing multiple interacting flaws. The flawed tubes were all 0.56 m (22 in.) long, with the flaw centered at 0.15 m (6 in.) from the end of the tube that was fitted with a welded plug. The unplugged end of the tube is held in place in the test module vessel by a Swagelock fitting mounted on a blind flange with a hole that allows the flow from the blowdown vessel to enter the flawed tube. Tests have also been conducted on a specimen containing an axial ODSCC crack produced by Westinghouse with doped steam for comparison with ANL-produced SCC flaws. All SCC flaws were analyzed structurally, and the results are described in Section 4.5.3 and Ref. 3. These tests of SCC flaws were directed at addressing questions concerning flaw leak stability under constant temperature and pressure associated with normal operating and MSLB conditions. Tests were conducted at both room temperature and 282°C (549°F) to assess flaw behavior dependence on temperature.

4.2.1 Characterization of the Flaws

All flaws tested in the Pressure and Leak-Rate Test Facility are characterized before and after testing. In general, the EDM flaws tested are relatively easy to characterize with respect to flaw dimensions, but characterization of the SCC flaws is much more difficult. Because of the need to evaluate leak-rate and flaw-opening-pressure prediction capabilities and improve the models if necessary, accurate information on flaw pre- and posttest dimensions and leak area is essential. Procedures have been developed and implemented to obtain these data by using the following flaw characterization steps:

1. Eddy current NDE is used to obtain crack depth profiles and voltage information.

2. Ligament failure and burst pressures are estimated by analyses using the crack depth profiles determined by NDE.

3. Flaw regions are characterized by dye-penetrant techniques and digital photography.

4. Tubes are bubble-tested with low-pressure air (276 kPa, or 40 psi) in a water bath to identify regions of throughwall penetration.

5. Posttest destructive examination of specimens with part-throughwall flaws is carried out to help validate the estimated of depth obtained by NDE and to better understand the process of failure, i. e. how crack segments grew and linked to produce the failure.

For SCC flaws (as opposed to EDM notches), the use of dye-penetrant inspection and digital photography is an essential part of pre- and posttest flaw characterization to relate flaw characteristics to leak behavior. These procedures, along with image processing techniques involving NIH Image software, are used to obtain flaw information such as crack area, total linear length, location, and number of branch points. Computerized digital image analysis of flaw images yields a more systematic and less subjective characterization of flaw features than does use of an optical microscope or measuring manually from photographs.

Throughwall portions of the crack are identified by a low–pressure leak test. With the dye-penetrant still in the crack, the capped tube is mounted in a low-pressure (276 kPa, or 40 psi) pressurization apparatus and submerged in a water bath. The flaw region is observed with a low-magnification optical microscope underwater for gas bubbles indicating leaks.

4.2.2 Testing of Specimens with EDM Axial Notches

Tests on axial notches of length 25.4 and 9.0 mm (1.0 and 0.35 in.) at room and elevated temperature were performed. Testing of multiple axial flaws also began during this reporting period.

Single Axial Notches

Results from a test on a TW EDM 25-mm (1-in.)-long axial notch of initial width 0.19 mm (0.0075-in.) [tube T14EATWX1] at room temperature are presented. The pressurization of the tube was done in two stages. In the first stage, the internal pressure was increased in four steps (0.69, 6.9, 10.3, and 13.8 MPa [100, 1000, 1500, and 2000 psi]), at which point the test was stopped and the tube removed to measure flow area prior to higher-pressure testing in which unstable tearing was anticipated. This permitted a check on our ability to predict the flaw opening and the flow rate at this intermediate stage of pressurization. The flaw at this stage of the test is shown in Fig. 4.25. Based on a two-dimensional projection, the flaw opening area is 52 mm^2 (0.081 in.^{2}),. The measured flaw length was 24.9 mm (0.98 in.), and the maximum flaw width was 2.8 mm (0.11 in.). Based on the measured opening area, a pressure differential of 13.8 MPa (2000 psi), an orifice coefficient of 0.6, and the fluid density at 75°F, the orifice flow through the flaw would be 312 L/min (82.5 gpm). This is in good agreement with the experimentally observed flow rate of 302 L/min (79.8 gpm).

In the second stage of the test, the tube (T14EATWX1) was reinstalled in the facility and pressurized to higher levels. The test was restarted by quickly raising the pressure to 13.8 MPa (2000 psi) and holding for a short time to reestablish a flow rate of 302 L/min (79.8 gpm), in agreement with that observed when the test was interrupted. The pressure was then raised in a series of 0.69 MPa (100 psi) increments. The leak rate increased significantly with each increment of pressure. At ≈15.9 MPa (2300 psi), the flow rate increased abruptly and the pressure dropped momentarily before stabilizing at 12.8 MPa (1859 psi), at which point a flow rate of 1,098 L/min (290.0 gpm) was observed. Figure 4.26 shows the posttest flaw opening area; the unstable tearing that occurred at 15.9 MPa (2300 psi) is seen at each end of the notch. Figure 4.27 is a side view of the flaw bulge. The projected flow area is 170 mm^2 (0.264 in.^{2}), the projected length 21.8 mm (0.86-in.), and the maximum flaw width 11.7 mm (0.46 in.).

74
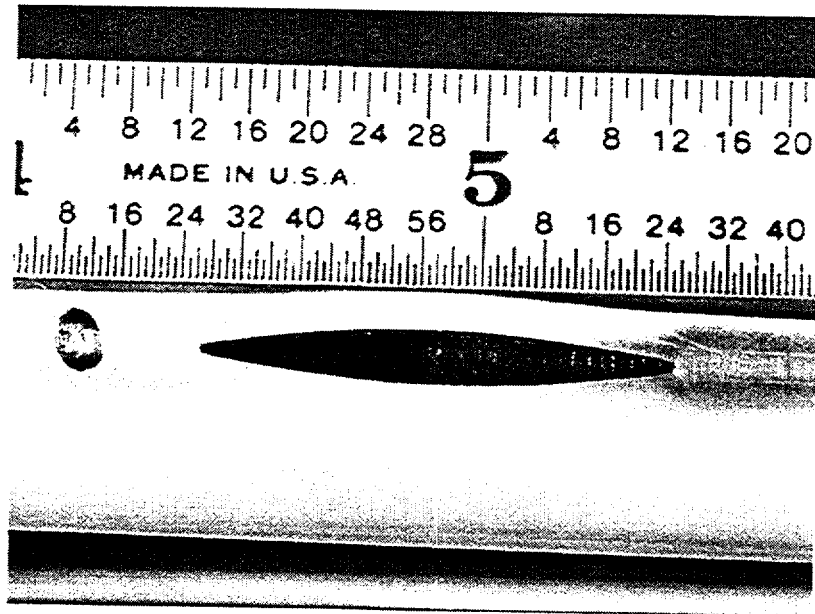
Fig. 4.25. Opening of 25.4-mm (1-in.)-long axial 100% TW EDM notch (tube T14EATWX1) after test was interrupted at 13.8 MPa (2000 psi) to measure flaw area.
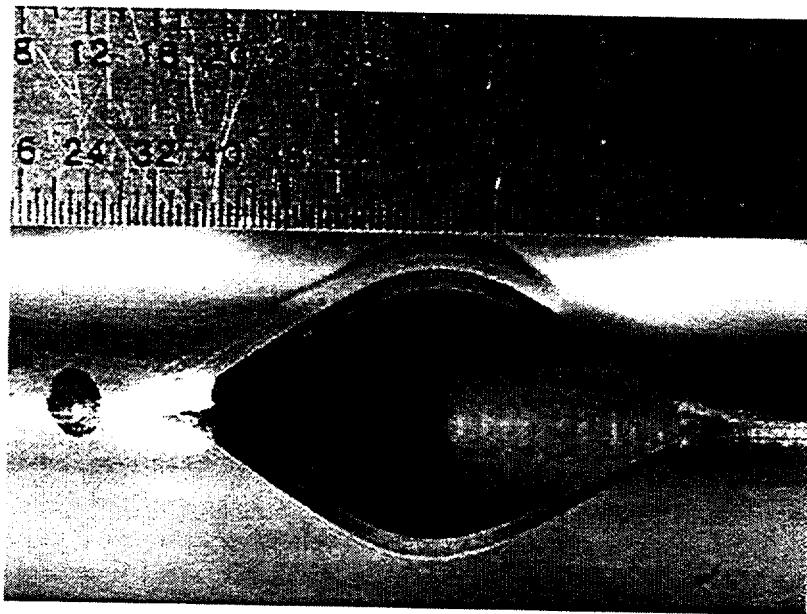
Fig. 4.26. Opening of 25.4-mm (1-in.)-long axial 100% TW EDM notch in tube shown in Fig. 4.25 (tube T14EATWX1) after continuing test to 15.9 MPa (2300 psi).
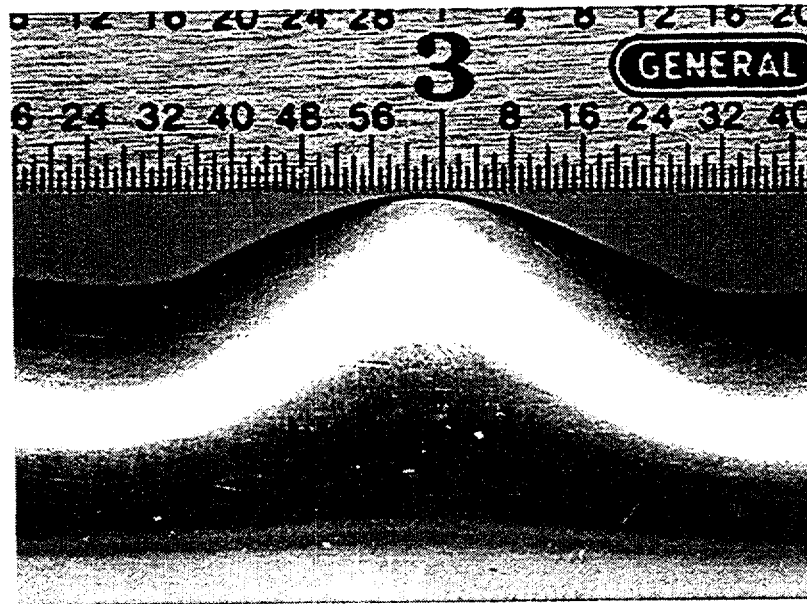
Fig. 4.27. *Side view of tube specimen shown in Fig. 4.26, showing three-dimensional bulging at failure site.*

Based on the measured opening area, the pressure differential of 12.8 MPa (1859 psi), an orifice coefficient of 0.6, and the fluid density at 75°F, the orifice flow rate is 984 L/min (260 gpm), which is 114 L/min (30 gpm) lower than that observed. This underprediction (in contrast to the accurate prediction for the first stage of the test) is probably the result of the large amount of bulging associated with the flaw (Fig. 4.27).

A simple geometric correction factor was obtained by comparing the curved arc length of the flaw, 24.3 mm (0.958 in.) with the projected length, 21.8 mm (0.86 in.). The ratio is 1.114. Applying this correction factor to the flaw opening area gives an orifice flow rate of 1,096 L/min (289.5 gpm), in good agreement with experiment.

A pressurization test was also performed on tube T13EA90X.35, which has a partial TW axial ODSCC EDM flaw of length 8.9 mm (0.35 in.), width of 0.19 mm (0.0075-in.), and a uniform 90% throughwall depth. This flaw length is shorter than any previously tested. The tube was first tested at room temperature, with the pressure increasing in 0.69 MPa (100 psi) increments up to 19.3 MPa (2800 psi). No flaw opening or tube leakage occurred, and the test was terminated at this pressure when the pressure relief valve began to leak. Upon removal and inspection, the tube showed virtually no crack widening or bulging of the tube wall. The tube was reinstalled and tested at 282°C (540°F) at increasing pressure up to 19.3 MPa (2800 psi). Again the tube did not leak, and post-test inspection revealed no change in the flaw width or tube bulging. The observed >19.3 MPa (2800 psi) ligament failure pressure exceeds the prediction of both the ANL and Battelle models. The ANL model predicts a failure pressure of 18.6 MPa (2700 psi) at room temperature and 16.9 MPa (2450 psi) at 282°C (540°F), and the Battelle model predictions are 12.4 and 11.0 MPa (1800 and 1600 psi), respectively. Failure pressures observed in previous tests on tubes with notches of 12.7 mm (0.5 in.) or longer were very close to the predicted values.

76

Tests were also performed on two identical tubes each with two aligned axial EDM TW notches separated by a short axial ligament. The notches were each 6.35 mm (0.25 in.) long and 0.19 mm (0.0075 in.) wide and were separated by a 0.25-mm (0.01-in.)-long full-wall-thickness ligament.

The first of these two tubes (T24EATWX.5 LIG) was tested at room temperature at pressures up to 17.2 MPa (2500 psi). Figure 4.28 is a posttest photograph of the flaw; little structural distortion is evident, and the flaw exhibited only a 50-75 μm (0.002-0.003 in.) increase in width at the end next to the ligament. Calculations indicated that the ligament would tear at a pressure considerably lower than 13.8 MPa (2000 psi). However, posttest inspection after pressurization to 17.2 MPa (2500 psi) with no failure revealed no tearing of the ligament, although stretch marks were evident on the ligament outer surface. The observed leak rate through the flaw during the test was essentially identical to that calculated for the two individual notches. At pressures of 14.5 and 17.7 MPa (2100 and 2500 psi), the flaw flow rate was 14.8 and 18.5 L/min (3.9 and 4.9 gpm), respectively. However, as described earlier, single axial notches shorter than $\approx$12.7 mm (0.5 in.) appear to exhibit higher strengths (i.e., higher opening pressures and smaller flow areas) than predicted by the models that have been found to accurately predict the behavior of longer axial notches.

The second tube (T25EATWX.5 LIG) was tested at 282°C (540°F). Ligament tearing occurred at 15.5 MPa (2250 psi). The tearing coincided with an abrupt increase in flow rate as the two notches merged. The resulting leak rate corresponded to that expected for the resulting 12.7-mm (0.5-in.) notch. The posttest appearance of tube T25EATWX.5 LIG after testing at pressures up to 17.9 MPa (2600 psi) is shown in Fig. 4.29. Ligament tearing and appreciable flaw widening are apparent.

At 14.5 MPa (2100 psi) (ligament intact) and 17.2 MPa (2500 psi) (ligament torn), the flow rates for tube T25EATWX.5 LIG were 17.0 and 32.2 L/min (4.5 and 8.5 gpm), respectively. At the maximum test pressure of 17.9 MPa (2600 psi), the flow rate was 35.6 L/min (9.4 gpm). This tube had a higher flow rate at all pressures, even before ligament tearing, than did tube T24EATWX.5 LIG at room temperature as would be expected because of the somewhat reduced flow stress at the higher temperature. After tearing, the notch behaved like a longer, and hence weaker, flaw.

4.2.3   Testing of Specimens with Laboratory-Produced SCC Flaws

Results from tests on four Alloy 600 tubes with laboratory-produced axial ODSCC of nominal length 12.7 mm (0.5 in.) were presented in the previous report.[2] The tubes were cracked in an aqueous sodium tetrathionate solution after a sensitization heat treatment. A 22.2-mm (7/8-in.)-diameter Alloy 600 tube (T505CATW2-10) with an axial ODSCC flaw produced by Westinghouse with doped steam was tested during the present reporting period (Test W 2-10). ANL tubes 177 and 195 were tested at room temperature, and ANL tubes 104 and 219 were tested at 282°C (540°F). The Westinghouse tube W 2-10 was tested at both temperatures.
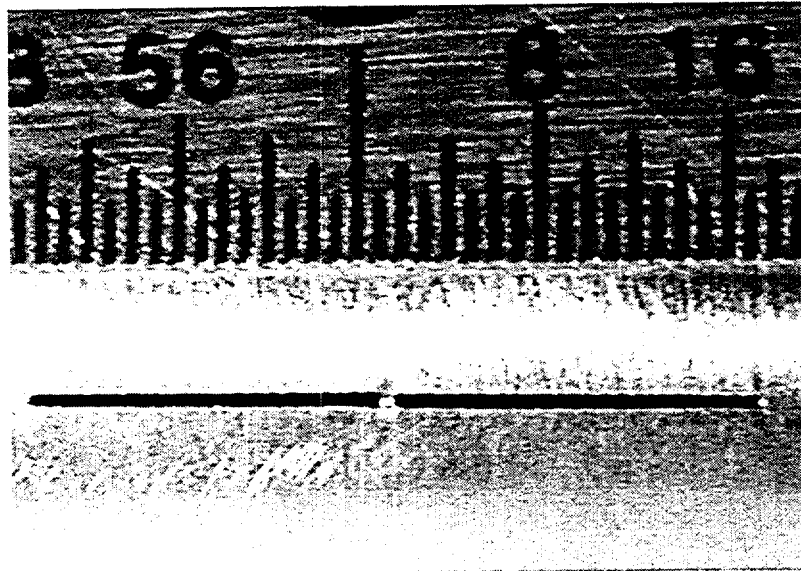
Fig. 4.28.   Posttest photograph of tube T24EATWX.5 LIG tested at room temperature at up to 17.2 MPa (2500 psi), showing little flaw distortion and intact ligament.
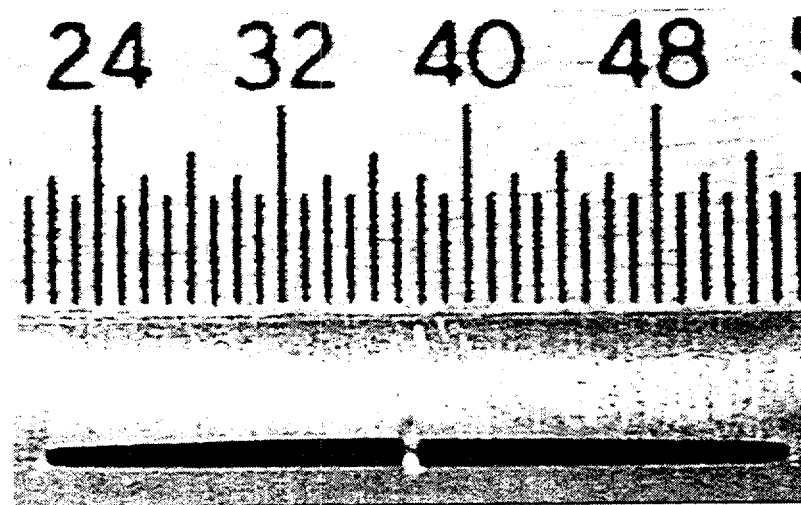
Fig. 4.29.   Posttest photograph of tube T25EATWX.5 LIG tested at 282°C (540°F) at up to 17.9 MPa (2600 psi), showing appreciable flaw notch widening and torn ligament.

The four ANL-produced tubes were selected as having the same nominal axial ODSCC crack length of 12.7 mm (0.5 in.), as determined by dye-penetrant examination, as well as other similarities. The Westinghouse tube had an axial ODSCC flaw of similar length. Figure 4.30 shows the pretest image of the flaw in the Westinghouse tube accentuated by dye-penetrant. The flaw is axial and has an overall length of 12.4 mm (0.49 in.). Bubble-testing at 276 kPa (40 psi) revealed that the flaw had two locations of throughwall penetration, coinciding with the two largest dye stains in Fig. 4.30. Each penetration exhibited very small

Fig. 4.30. Pretest dye-penetrant digital image of Westinghouse ODSCC cracked tube produced using doped steam (Test T505CATW2-10).

intermittent bubble generation. The largest dye stain on the right exhibited a larger bubble size and higher generation frequency than that on the left.

For comparison with the Westinghouse test, the following observations summarize the results from the tests of the four ANL-produced SCC tubes (Tests SGL-177, SGL-195, SGL-104, and SGL-219):

1. All SCC flaws were very tight and had regions of throughwall penetration, as determined by bubble testing. However, none of the four flaws exhibited detectable water leakage at pressures below 8.3 MPa (1200 psi), nor was leakage detected during a 2-h (or greater) hold time at this pressure. Detectable leakage did not occur until much higher pressures were attained.

2. Posttest inspection showed that three flaws opened significantly in width along their entire length, even into the extremities of the Y branches on each end of the main flaw. The exception was Test SGL-177, for which the nominal EC voltage of 4 V was considerably lower than the values of 6-10 V observed for the other three tubes. Additionally, the latter three tubes had several obvious posttest secondary cracks emanating from the main crack, even though these cracks were barely perceptible in pretest characterizations. Furthermore, the region around the flaws was raised noticeably upward, or puckered. However, Test SGL-177 exhibited very little puckering. Tests previously conducted on 12.7-mm (0.5-in.)-long axial EDM notches over the same pressure range produced significantly less puckering.

3. Specimens in three of the four tests (SGL-195, SGL-177, and SGL-219) exhibited crack tearing under constant temperature and pressure conditions, which caused the leak rate to increase under constant pressure.

4. Specimen flaws in three of the four tests (SGL-195, SGL-104, and SGL-219) suddenly opened to their full extent at pressures less than that associated with MSLB, yielding flow rates of 23 to 38+ L/min (6 to 10+ gpm). These three tubes had the highest EC voltages (6-10 V). This behavior suggests that once a small ligament tears, there is a strong tendency for other ligaments to tear in a domino fashion (sometimes after a delay under constant pressure) until the crack is completely open over its full extent. Test SGL-177, which had the lowest voltage (4 V), had a leak rate of only 1.7 L/min (0.44 gpm) and did not exhibit this behavior.

The detailed structural analysis predictions and a proposed flaw behavior model for these flaws and the Westinghouse flaw (T505CATW2-10) is presented in Section 4.5.3.

Eddy current examinations suggest that all four ANL-produced SCC flaws had variable crack depths along their lengths (see Section 4.5), with maximum depths of 75 to 95%. The Westinghouse tube exhibited a similar crack depth profile. The throughwall regions identified by bubble testing in both the Westinghouse and the four ANL flaws were not seen by EC techniques because of their tightness and very small axial extents. The EC BC voltage for the Westinghouse tube was 4.5 V, very close to the 4.0 V exhibited by the ANL tube in Test SGL-177. The other three ANL tubes had higher EC voltages in the range of 6-10 V. The crack depth profile for the Westinghouse tube was used not only to qualitatively prescreen the flaw for similarity with the ANL flaws but also in calculations to estimate the initial flaw-opening pressure. Analysis indicates that the Westinghouse tube was most similar to the ANL tube in Test SGL-177, although somewhat stronger. Hence, the Westinghouse tube was expected to exhibit leak behavior similar to that of the ANL tube. Because of the similarity to the ANL tube, which was tested at room temperature, the initial testing phase for the Westinghouse tube was also conducted at room temperature, with follow-on testing at 282°C (540°F).

In the room-temperature test of the Westinghouse tube, the pressure was increased from 0 in 1.4-2.1 MPa (200-300 psi) increments, with hold times of 15-30 min at each level until 8.3 MPa (1200 psi) was reached. The pressure was held at this level for 2 h. Like the four ANL specimens, the Westinghouse tube exhibited no observable leakage during this portion of the test, even though all of these tubes were shown to have localized throughwall penetration during bubble testing at very low pressure. Following the 2-h hold at 8.3 MPa (1200 psi), the pressure was increased in a series of steps to 17.2 MPa (2500 psi) over 45 min. Again, no leak was observed. After a subsequent hold time of 3.25 h at this pressure, a leak rate of ≈0.04 L/min (0.01 gpm) was detected. The 17.2 MPa (2500 psi) pressure was held overnight, and the tube continued to leak, with the leak rate increasing to ≈0.068 L/min (0.018 gpm) by the following morning. The pressure on the Westinghouse tube was then raised to 18.6 MPa (2700 psi) and held at this level for 5.5 h, at which time a leak rate of 0.12 L/min (0.032 gpm) was measured. The room-temperature phase of the test was terminated at this point. Thus, the Westinghouse tube, like SGL-177, developed a leak under constant pressure and exhibited an increasing, although somewhat lower, leak rate over an extended hold period.

The blowdown tank was refilled with water, and the tube was then tested at 282°C (540°F) and 18.6 MPa (2700 psi) to determine the leak rate at this temperature and to see if the crack would open further. The flow rate was observed to increase from ≈0.30 L/min (0.08 gpm) to 0.72 L/min (0.19 gpm) during a 2-h hold at this pressure. The test was then terminated and the tube was removed. A posttest photograph of the flaw is shown in

Section 4.5.3 (Fig. 4.85). The flaw has opened slightly over its entire axial extent (see pretest photograph of Fig. 4.30). Like Test SGL-177, no flaw-zone puckering was evident.

The above behavior suggests that ligament failure in an SCC flaw may occur progressively, sometimes with delays under constant loading conditions. In flawed specimens in which the width of the remaining ligament is highly variable, initial leakage occurred abruptly at pressures significantly lower than those predicted by the equivalent rectangular crack approach (See Section 4.5.3). The experimental evidence of time-dependent increase of leak rate possibly due to progressive ligament rupture at 282°C (540°F), as well as at room temperature, highlights the fact that no criterion for predicting time-dependent ligament rupture is currently available. More laboratory-cracked tubes with SCC flaws and, eventually, service-degraded tubes with SCC flaws, will be tested to develop a better understanding of tube flaw behavior.

4.3 High-Pressure Test Facility

Design and construction of a new room-temperature tube testing facility with a maximum operating pressure of 51.7 MPa (7,500 psi) and a maximum flow rate of 48.4 L/min (12.8 gpm) has been completed and has successfully undergone shakedown and performance quantification testing. This facility is being readied for the testing of tubes with SCC flaws produced at ANL and of tubes with more complex tight segmented laser-cut notches.

The room-temperature High-Pressure Test Facility permits pressure testing of tubes that cannot be failed in the high-temperature Pressure and Leak-Rate Test Facility, which has a 20.7 MPa (3000 psi) pressure limit. Most high-pressure tube test facilities have very low flow capabilities so that almost all very deep or throughwall flaws must be tested using a bladder and frequently a backup foil to prevent leakage through the flaw resulting in system depressurization. Very short pressurization times of ≈2-3 s are used to minimize the tendency for bladder extrusion and leakage through the flaw. The Argonne facility, because of its 48.4 L/min (12.8 gpm) flow capability at 51.7 MPa (7500 psi), allows tubes with small TW flaws to be tested without the use of a bladder. When bladders and foils are required, the small leaks that can occur during tube pressurization may not result in an aborted test.

This facility can also be used for very-long-duration crack stability tests and for long-duration crack jet impingement erosion tests on adjacent tubes, since water can be continuously supplied from an outside source during a test. The apparatus is also capable of measuring very low flow rates (considerably less than the 0.04 L/min [0.01 gpm] lower limit for the Pressure and Leak-Rate Test Facility) through the use of flaw leak collection and timed measurement of water mass. Additionally, the optical access to the crack location permits real-time ultra-high-speed video recording (2000-12,000 frames per second) of crack and jet dynamic behavior during testing.

4.3.1 Facility Description

Figure 4.31 is a schematic diagram of the High-Pressure Test Facility, and Fig. 4.32 is a photograph of the overall facility. The facility is pressurized by a constant-rpm single-acting triplex constant-displacement pump driven by a 60-hp electric motor (see Figure 4.33) that

81
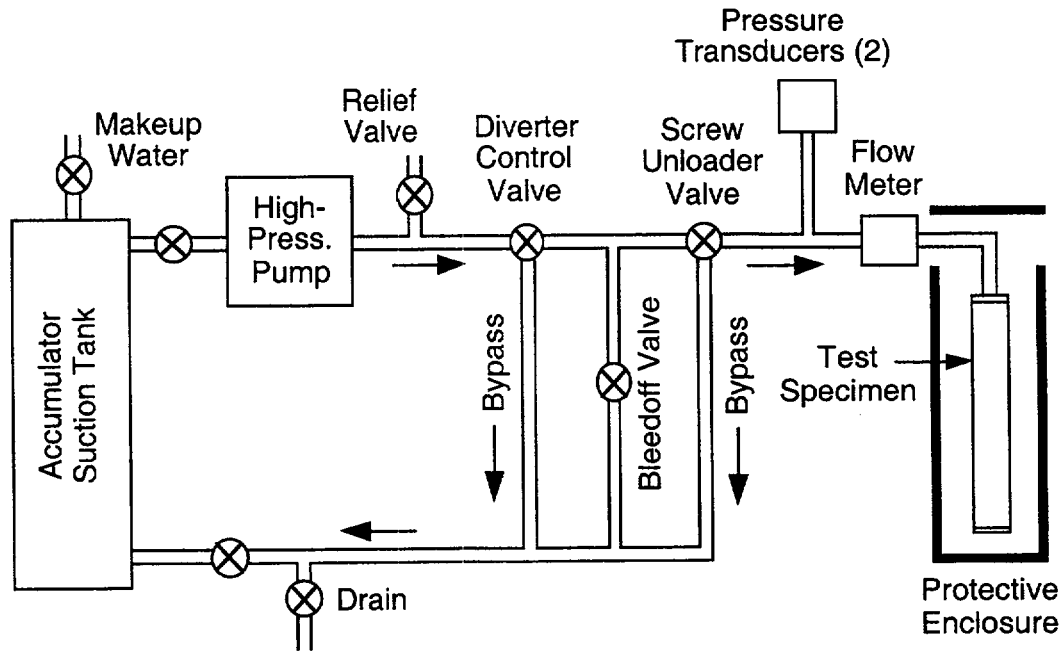
Fig. 4.31. Schematic diagram of High-Pressure Test Facility pressurizer and associated components.
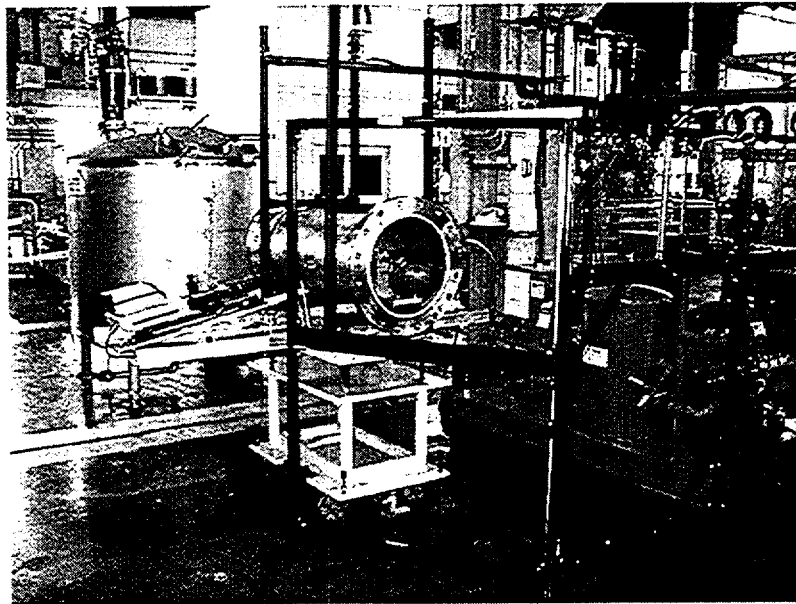
Fig. 4.32. Overall view of major components of High-Pressure Test Facility: water pump pressurizer, test module, tube support, video system, and 3000-L (800-gal) tank for conducting tests on field-pulled tubes. Also shown is Lexan™ personnel-protection barrier.
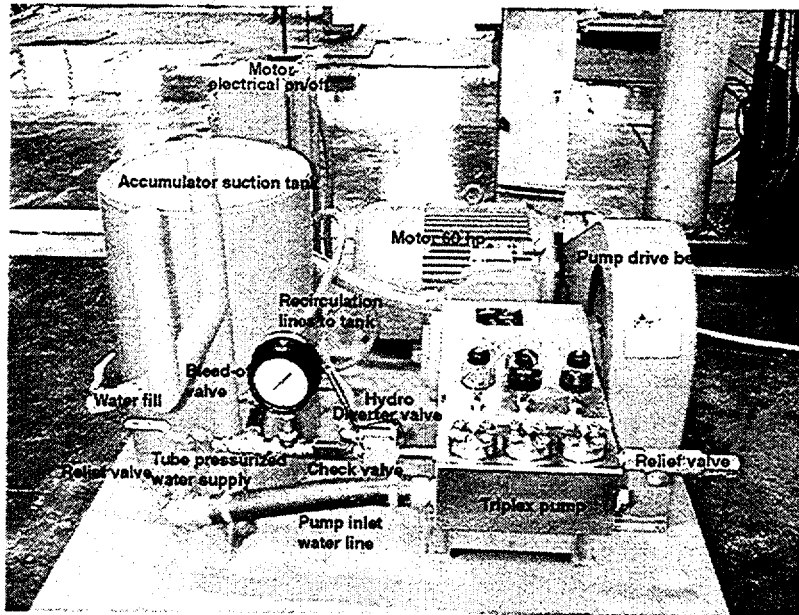
Fig. 4.33. Water pump pressurizer

provides a constant 48.4 L/min (12.8 gpm) flow of water at up to 51.7 MPa (7500 psi). The pump-generated pressure pulsations were found to be small, <0.34 MPa (<50 psi). The pump has two overpressurization protection safety relief valves, one located on the pump and the other on the 139-L (40-gal) water accumulator suction tank. The lever-operated hydro-diverter control valve furnished with the pressurizer was modified to work in series with a screw unloader valve, that allows more positive, finer remote control of tube pressurization. The pressurizer water pump system was also modified to operate with a continuous supply of water from the building water system by installing a pressure regulating valve on the water line supplying the pump accumulator suction tank. The facility operation is no longer limited by the 40 gal reservoir supplied with the pump, and thus extended-duration leak tests can now be conducted. Pump-generated water heating can be avoided by bleeding water to the drain during long-duration tests and adding cold makeup water.

The test module protective enclosure shown in Fig. 4.34 consists of an 0.46-m (18–in.)-diameter, 1.02-m (40-in.)-long stainless steel pipe. A transparent Lexan™ plate at each end of the test module confines the water jets and spray produced by a leaking tube. The ultra-high-speed video camera and light source for illuminating the test tube are also shown in Fig. 4.34.

The tube support system, shown in Fig. 4.35, consists of two collars that fit around the tube and can be located anywhere along its length. It can provide either single or two-point lateral support. The ability to vary tube lateral support conditions is important in testing tubes with circumferential flaws, where flaw behavior is sensitive to tube constraint. The two-point support also prevents axially flawed tubes from undergoing significant bending from jet thrust upon failure.

The basic operation of the facility can be described with reference to Figs. 4.31-4.35 according to the following steps:

83
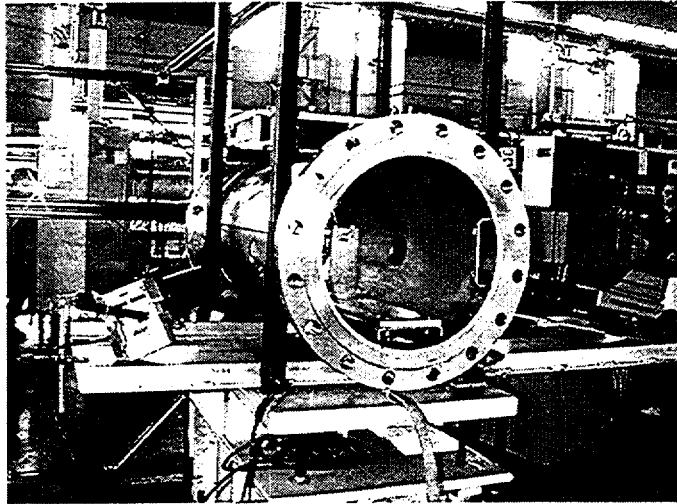
Fig. 4.34. *Test module and high-speed video camera and high-intensity light source mounted on test module support table.*
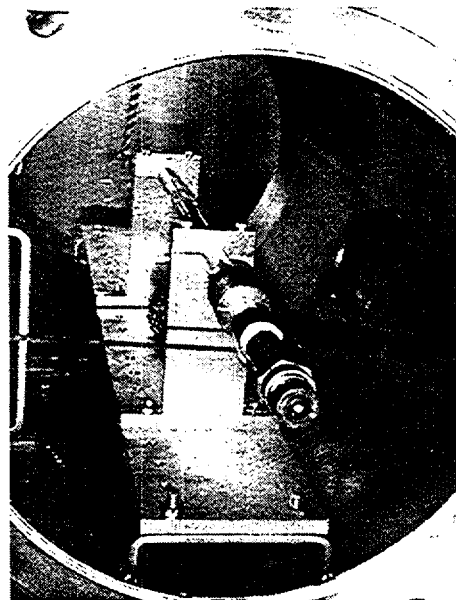
Fig. 4.35. *Tube support system.*

1. The tube to be tested is mounted in the test module and fastened to the supply hose that feeds water from the high-pressure pump. All air is bled from the supply line and test specimen through a high-pressure valve fastened to the downstream end of the tube. This valve is then closed during the test.

2. The accumulator suction tank is filled with water. If the test is expected to produce some leakage before failure or to be of extended duration, the water supply line to the accumulator tank can be opened to provide a continuous water supply for long-duration testing. Both tap water and deionized water are available.

3. The high-pressure bleedoff valve and the diverter control valve are both set fully open and the pump is then turned on, causing flow recirculation through the bypass lines to the accumulator suction tank. The tube specimen will be pressurized at <275 kPa (<40 psi) at this point. For long-duration tests, water temperature rise caused by pump heating is minimized by dumping water to the building drain and adding cool makeup water to the accumulator tank.

4. The high-pressure bleedoff valve is then fully closed, and the diverter control valve is slowly closed to direct the flow to the test specimen, causing its internal pressure to rise. The diverter control valve allows the pressure to be established at any value in the range from 0 to 51.7 MPa (0 to 7500 psi). Downstream and in series with the diverter valve is a spring-loaded screw unloader valve, which furnishes a more precise linear control of pressure than can be obtained using the diverter control valve. When this valve is used, the diverter control valve is set to the fully closed position, allowing flow and pressure to be controlled by the screw unloader valve, which also has a bypass line.

5. When the desired maximum test pressure has been reached or the tube has failed, the test is terminated by opening the diverter control valve, turning the pump off, and opening the high-pressure bleedoff valve.

Tube pressure is read on an analog pressure gauge and is also measured and recorded by two redundant pressure transducers. A sustained flow of up to 48.4 L/min (12.8 gpm) can be maintained through a leaking specimen at any pressure up to 51.7 MPa (7500 psi), depending on flaw geometry and flow resistance. The flow is measured by both timed direct collection and weighing of water from the test module and by a flowmeter immediately upstream of the tube. All data are recorded redundantly on both a multi-channel strip chart recorder and a dedicated computer digital data acquisition system that uses LabView software.

The tube pressurization rate can be varied from quasi-steady-state (<0.7 MPa/s or <100 psi/s) to 7-21 MPa/s (1000-3000 psi/s), which encompasses the EPRI guideline range for burst testing, to 70 MPa/s (10,000 psi/s). Pressurization over the full range of the system, 0-52 MPa (0-7500 psi), is possible at all of these pressurization rates. The screw unloader valve provides very precise and reproducible linear pressure control at all pressurization rates. The potential also exists for programmed control of pressurization for more complex pressure transient histories.

4.3.2 Results from High-Pressure Test Facility

Facility checkout, the establishment of test protocols and initial flaw testing were conducted through a series of tests on 22.2-mm (7/8-in.)-diameter Alloy 600 SG tubes with small circular orifice holes and EDM axial notches. The circular orifice hole flaws allowed facility checkout with continuous flow, and the part-throughwall flaws permitted operation with no flow until ligament tearing or tube burst occurred during pressurization. These tests are described below.

Circular-Hole Tests

A 0.80-mm (1/32-in.)-diameter sharp-edge circular-orifice-flawed test tube was held in the test module by the two-point constraint lateral support. Two test runs were made with the tube, the first with pressure plateaus up to 51.7 MPa (7500 psi) and the second with plateaus to 34.5 MPa (5000 psi). For both runs, six to eight pressure plateaus were held for nominally 5 min each, with total test time of ≤35 min. For each pressure plateau, the flaw flow rate and pressure were measured. The pressurizer control operated very smoothly over the full range, and the pressure pulsations generated by the triplex pump were <0.34 MPa (<50 psi). The turbine flowmeter readings were checked against the timed collection of water from the flaw, and the two results were in agreement. The system installed for controlled dump of water from the pressurizer water accumulator tank was successful in preventing excessive pump heating of the water during these 35-min tests.

The tube was examined visually after each test, and interesting structural changes were observed. It should be noted that this same flaw geometry had been used in previous shakedown tests of the Pressure and Leak-Rate Test Facility, and no tube changes were noted during several short-duration tests. Posttest examination of the aluminum plate holding the test specimen mounting brackets, which is parallel to the tube and upon which the orifice jet impacts from an ≈125-mm (≈5-in.) standoff distance, revealed two large jet-impact erosion craters, one for each test. The craters were nominally 1.6-3.2 mm (1/16-1/8 in.) deep and ≈3.2-6.3 mm (1/8-1/4-in.) wide. The crater for the highest pressure test was the largest. The tube wall had also undergone some plastic distortion at the location of the two support brackets. Additionally, some erosion in the Alloy 600 tube orifice hole was detected after the first test, and the second test of this same tube yielded a higher flow rate than predicted by the circular-orifice flow model, even at the initial low pressures. This suggests that the hole geometry/area was increased by jet erosion during the first test.

EDM Axial Notch Tests

Prior to testing the SCC flaws, tubes with OD axial EDM TW and part-TW notches predicted to be unstable at <51.7 MPa (7500 psi) are being tested. These tests were used to develop and validate techniques for testing with and without bladders and various bladder/shim combinations. These tests also can be used to assess the influence of bladders and pressurization rate on ligament tearing and unstable flaw failure pressures. A total of 42 flawed specimens of several different designs have been fabricated, with some flaw geometries in triplicate for the assessment of test reproducibility and other test parameter effects on the data. These notches are all 0.19 mm (0.0075 in.) wide and of four axial lengths, namely 6.35,

12.7, 19.1, and 25.4 mm (0.25, 0.5, 0.75, and 1.0 in.). Flaws depths are 60, 80, 90, and 100% TW.

The flaw geometries ensure that the tests will encompass a range of failure behaviors. For example, the 12.7-mm (0.5-in.)-long 60% TW flaw is expected to exhibit unstable tearing, or bursting, at a pressure of 38.6 MPa (5,600 psi) simultaneous with ligament failure. This is in contrast to an 80% TW flaw of this length, which will first undergo ligament tearing at 25.5 MPa (3700 psi) and subsequent unstable bursting at 30.3 MPa (4,400 psi). For this flaw geometry, when ligament failure occurs, the flow rate will be well above the maximum 48.4 L/min (12.8 gpm) system capability, and pressurization to a higher level is not possible. Hence, this flaw would require a bladder to achieve the flaw burst pressure. In contrast, the 60% TW flaw of the same length can be burst without a bladder; this flaw geometry can then also be tested with a bladder to allow assessment of the influence of bladders on burst data. These flaw geometries are also being tested at different pressurization rates.

Three identical 80% TW 19.1-mm (0.75-in.)-long axial notches (OM107, OM122, and OM109) were tested in three different pressurization scenarios. A slow quasi-steady-state pressurization rate resulted in ligament tearing at 21.4 MPa (3100 psi), pressurization at 13.8 MPa/s (2000 psi/s) produced ligament tear at 24.2 MPa (3510 psi), and pressurization at 48.3 MPa/s (7000 psi/s) produced ligament tear at 26.4 MPa (3830 psi). The predicted ligament tearing pressure for this flaw geometry is 20.7 MPa (3000 psi), which is in good agreement with the quasi-steady pressurization rate test OM107.

Figures 4.36-4.38 show the posttest flaw openings. All three flaws exhibited ligament failure but no discernible unstable tearing at the notch ends. In addition to the increase in ligament failure pressure with pressurization rate, there is a slight increase in maximum notch opening width with increasing pressurization rate.

The behavior of the 12.7-mm (0.5-in)-long 80% TW flaw (OM120) under a quasi-steady-state pressurization rate without a bladder was similar to that of the 19.1-mm (0.75-in)-long 80% TW flaw tested under similar conditions. A posttest photograph of the flaw OM120 is shown in Fig. 4.39. It experienced ligament tearing at a pressure of 26.9 MPa (3900 psi), which is in reasonable agreement with the predicted value of 25.5 MPa (3700 psi). No discernible unstable tearing occurred at the notch ends. Testing of this flaw at faster rates of pressurization is underway to see if the ligament tear pressure will exhibit a dependence on pressurization rate, as did the 19.1-mm (0.75-in.)-long flaws.

The 80% TW flaws of 12.7 and 19.1-mm (0.5- and 0.75-in.) length have also been tested with bladders to see if unstable tearing would occur. The tests were performed with a 2.4-mm (3/32-in.)-thick wall hard Tygon bladder and no backup metal foil. Figures 4.40 and 4.41 show photographs of how a bladder with an OD slightly smaller than the tube ID is sealed in the tube with a bored tapered Teflon plug to prevent water penetration between the bladder and the tube ID. For an initially TW flaw, such leakage would result in possible premature flaw leakage and possibly prevent further pressurization if the leakage is excessive.

Figures 4.42 and 4.43 are posttest photographs of flaw opening for the bladder testing of the 80% TW flaws of 12.7 mm (0.5 in.) (OM121) and 19.1 mm (0.75-in.) (OM123) lengths,
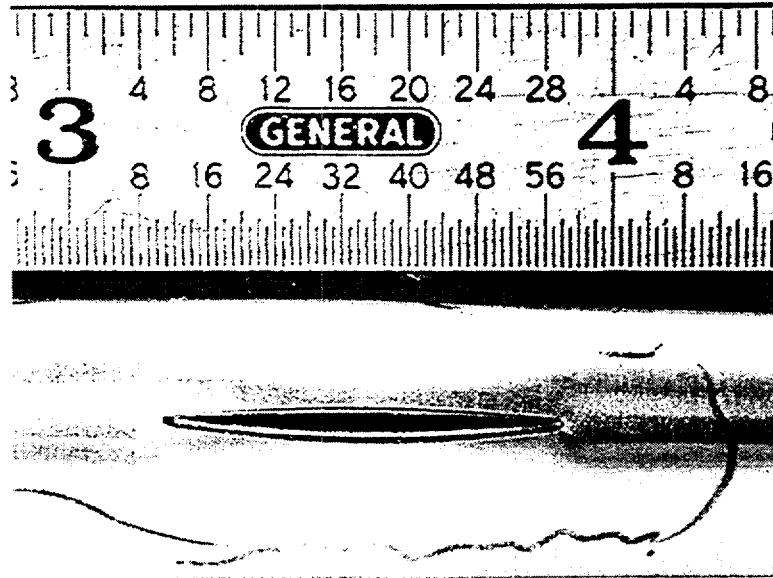
Fig. 4.36. *Posttest appearance of specimen OM107 (19.1-mm [0.75-in.]-long 80% TW axial EDM notch), tested without bladder at a quasi-steady-state pressurization rate. Ligament tearing occurred at 21.4 MPa (3100 psi).*
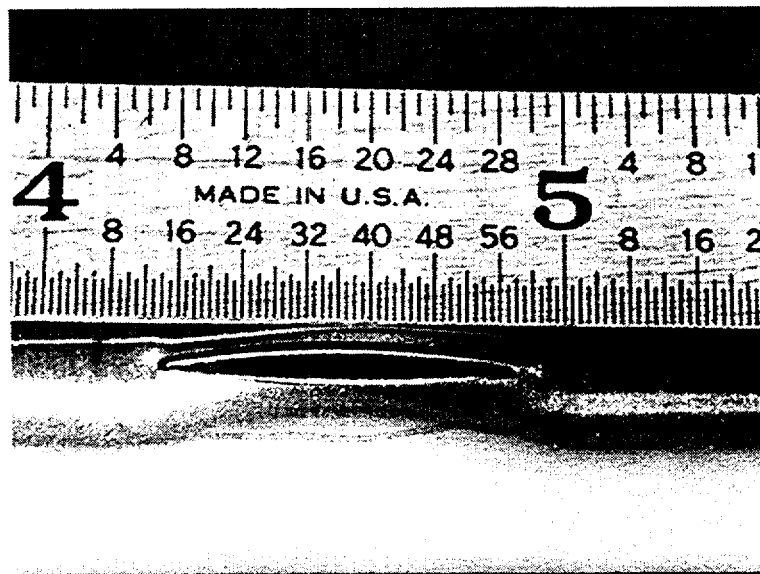
Fig. 4.37. *Posttest appearance of specimen OM122 (19.1-mm [0.75-in.]-long 80% TW axial EDM notch), tested without bladder at a pressurization rate of 13.8 MPa/s (2000 psi/s). Ligament tearing occurred at 24.2 Mpa (3510 psi).*
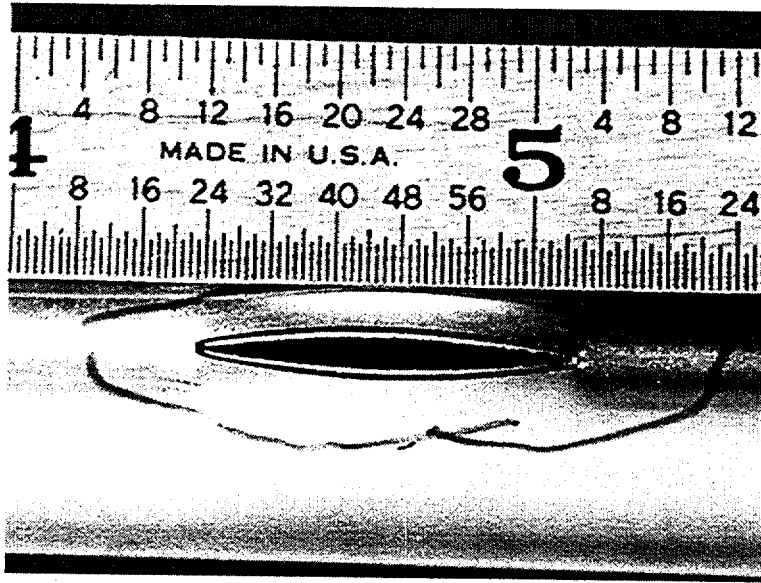
Fig. 4.38. *Posttest appearance of specimen OM109 (19.1-mm [0.75-in.]-long 80% TW axial EDM notch), tested without bladder at a pressurization rate of 48.3 MPa/s (7000 psi/s). Ligament tearing occurred at 26.4 MPa (3830 psi).*
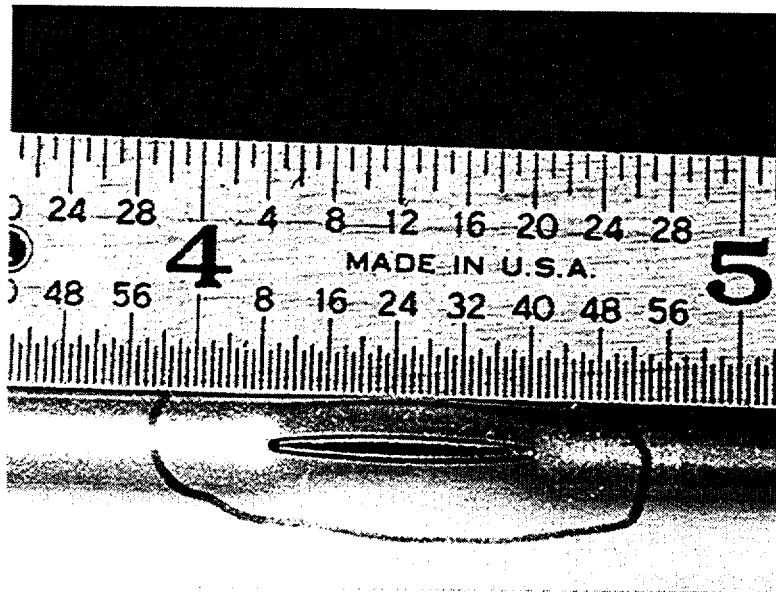
Fig. 4.39. *Posttest appearance of specimen OM120 (12.7-mm [0.5-in.]-long 80% TW axial EDM notch), tested without bladder at a quasi-steady-state pressurization. Ligament tearing occurred at 26.9 MPa (3900 psi), as compared to the predicted failure pressure of 25.5 MPa (3700 psi).*

89
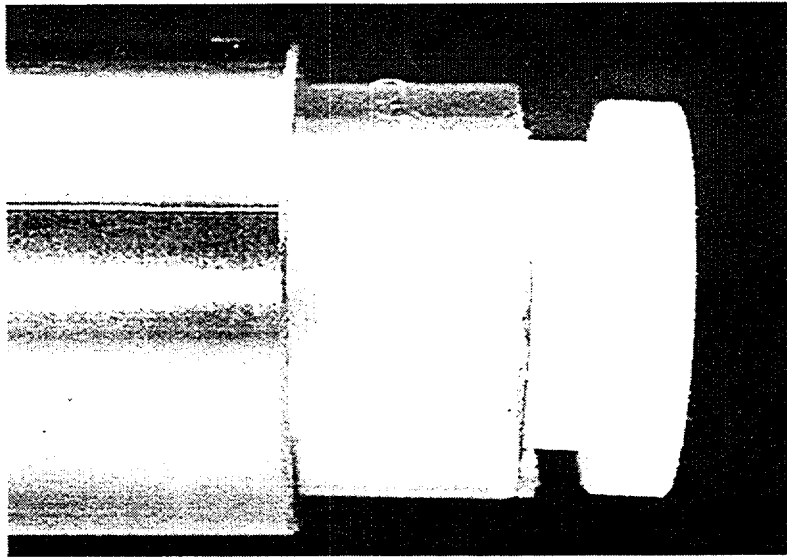
Fig. 4.40.   Side view of tube with bladder and bored plug seal being installed.
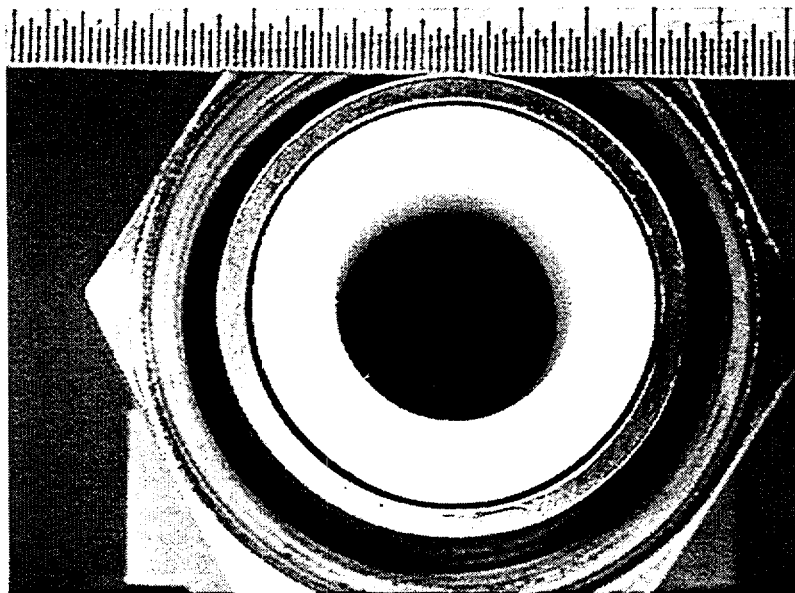
Fig. 4.41.   End view of tube with bladder and plug installed.

90
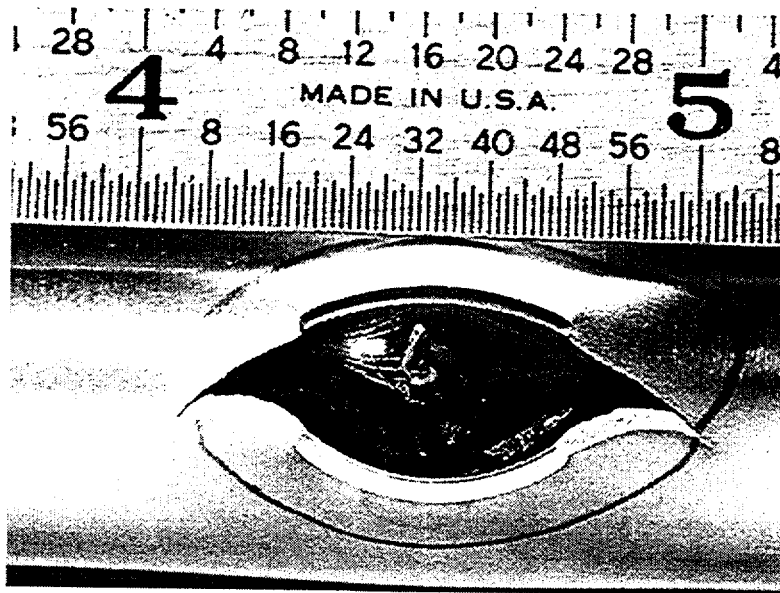
Fig. 4.42. *Posttest appearance of specimen OM121 (12.7-mm [0.5-in.]-long 80% TW axial EDM notch), tested with bladder at a pressurization rate of 13.8 MPa/s (2000 psi/s). Flaw burst occurred at 29.0 MPa (4200 ps)i, as compared to the predicted failure pressure of 30.3 MPa (4400 psi).*
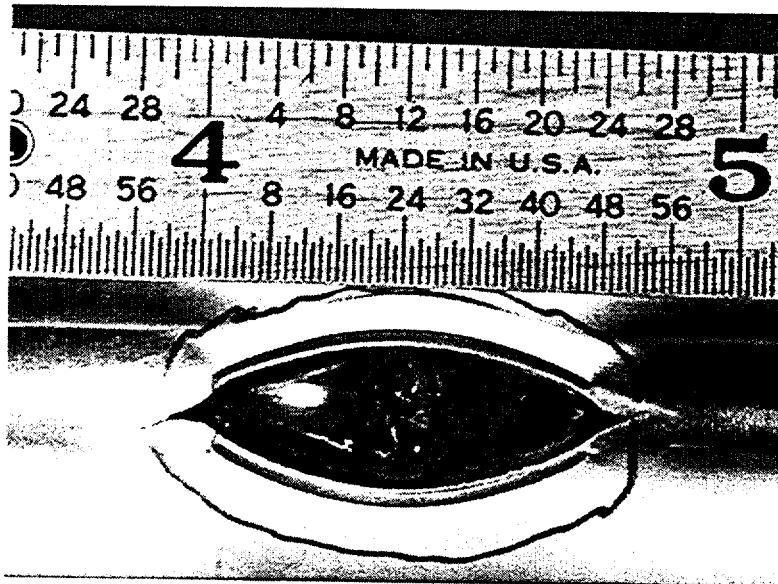
Fig. 4.43. *Posttest appearance of specimen OM123 (19.1-mm [0.75-in.]-long 80% TW axial EDM notch), tested with bladder at a pressurization rate of 13.8 MPa/s (2000 psi/s). Flaw burst occurred at 21.9 MPa (3180 psi), as compared to the predicted failure pressure of 22.8 MPa (3300 psi).*

respectively. These tests were conducted at a nominal pressurization rate of 13.8 MPa/s (2000 psi/s). Clearly, both flaws experienced significant unstable bursting, with a large amount of tearing at both ends of each original notch. As noted above (Figs. 4.37 and 4.39), these flaws experienced ligament tearing but could not be burst without a bladder. The experimental/predicted unstable burst pressures for the 12.7 and 19.1-mm (0.5 and 0.75-in.)-long 80% TW flaws were 29.0/30.3 MPa (4200/4400 psi) and 21.9/22.8 MPa (3180/3300 psi), respectively. These flaws will also be tested with bladders at different pressurization rates.

A 12.7-mm (0.5-in.)-long 60% TW flaw, unlike an 80% TW flaw of the same length, is predicted to exhibit unstable tearing or bursting simultaneous with ligament tearing at a pressure of 38.6 MPa (5,600 psi). Hence, this flaw can be tested with and without a bladder to assess the influence of bladders on burst data. Figure 4.44 shows a post-test photograph of tube OM113 with such a flaw that was tested without a bladder at a pressurization rate of 13.8 MPa/s (2000 psi/s). The flaw burst unstably without a bladder at 40.7 MPa (5900 psi), as compared to the predicted burst pressure of 38.6 MPa (5600 psi).

Figure 4.45 is a posttest photograph of Tube OM112 with the same flow geometry tested with a 2.4-mm (3/32-in.)-thick hard bladder at a pressurization rate of 13.8 MPa/s (2000 psi/s). The flaw burst at 41.4 MPa (6000 psi), versus the predicted value of 38.6 MPa (5600 psi). Use of the bladder caused significantly more unstable tearing of the notch ends than in Tube OM113. However, most important, the burst pressure was almost the same as for Tube OM113, which failed at 40.7 MPa (5900 psi).

Presented next are results from tests on tubes with a 12.7-mm (0.5-in.)-long 100% TW EDM axial OD notch. This flaw cannot be unstably burst in the High-Pressure Test Facility without the use of a bladder because the flow rate at the burst pressure exceeds the 48.4 L/min (12.8 gpm) limit of the facility. This flaw geometry was tested with two different bladder types using the same pressurization rate of 13.8 MPa/s (2000 psi/s). Tube OM102 was tested with a hard Tygon™ bladder having a 2.4-mm (3/32-in.)-thick wall, and Tube OM101 was tested with a 3.2-mm (1/8-in.)-thick hard bladder. The post-test results for the thinner bladder test (OM102) are shown in Fig. 4.46. As shown in the side view, the bladder has extruded through the flaw opening created by ligament tearing, and, as seen in the top view, the flaw has undergone a very slight amount of unstable tearing at both ends. The flaw unstably burst at 29.6 MPa (4300 psi), which is close to the predicted value of 30.3 MPa (4400 psi).

Figure 4.47 shows the posttest appearance of tube OM101, which was tested with the thicker bladder. The thicker bladder did not extrude through the flaw, in contrast to tube OM102, and significantly more flaw bulging and unstable tearing took place at the notch ends. Tube OM101 burst at 29.6 MPa (4296 psi), which is good agreement with the predicted value of 30.3 MPa (4400 psi), despite the more extensive tearing with the thicker bladder. Thus, the proper use of bladders produces a unique value for the unstable burst pressure for a given flaw geometry, irrespective of the extent of tearing. However, it is readily apparent that the resulting leak areas can be drastically different. The question therefore arises concerning the correct area to be used at unstable burst for the purposes of predicting the leak flow rate. It is believed that this can only be determined through a detailed simulation of flaw structure and fluid dynamic interactions during burst.
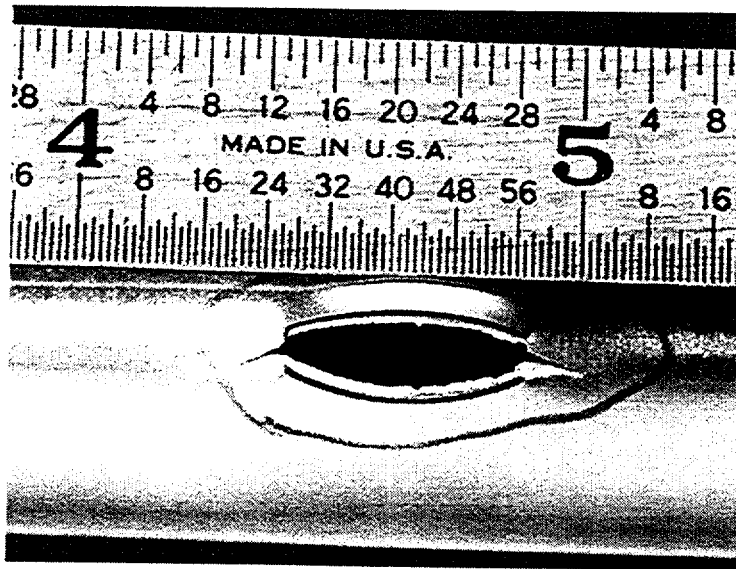
Fig. 4.44. Tube OM113 with a 12.7-mm (0.5-in.)-long 60% TW EDM axial OD notch, tested without a bladder.
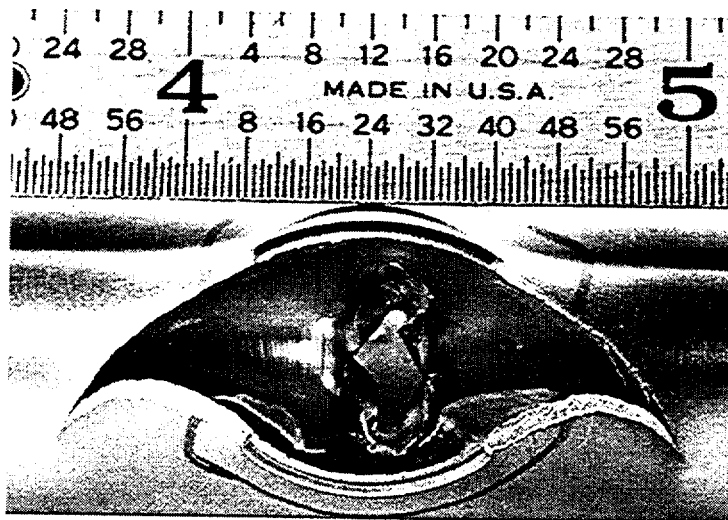
Fig. 4.45. Tube OM112 with a 12.7-mm (0.5-in.)-long 60% TW EDM axial OD notch, tested with a bladder.
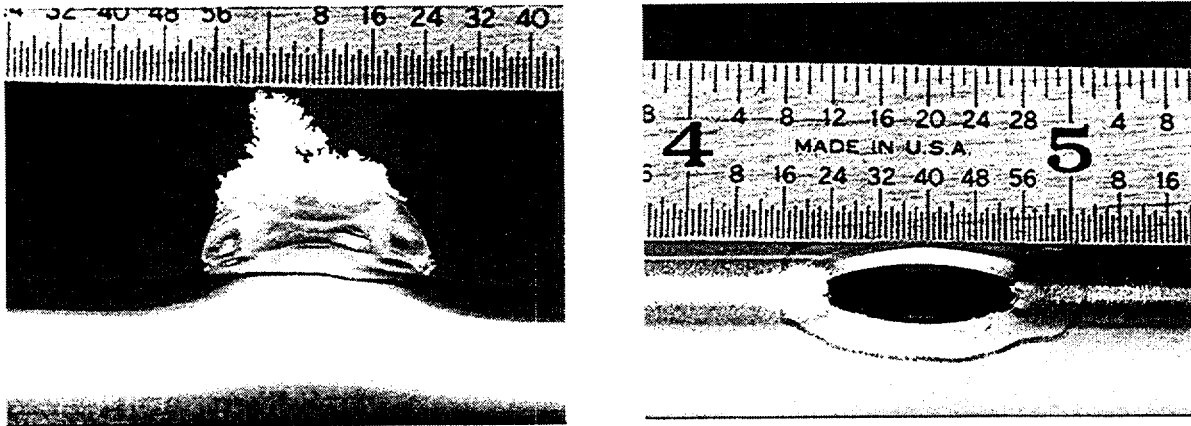
Fig. 4.46.   Side (left) and top (right) views of Tube OM102 with a 12.7-mm (0.5-in.)-long 100% TW EDM axial notch, tested with a 2.4-mm (3/32-in.)-thick hard bladder at a pressurization rate of 13.8 MPa/s (2000 psi/s).
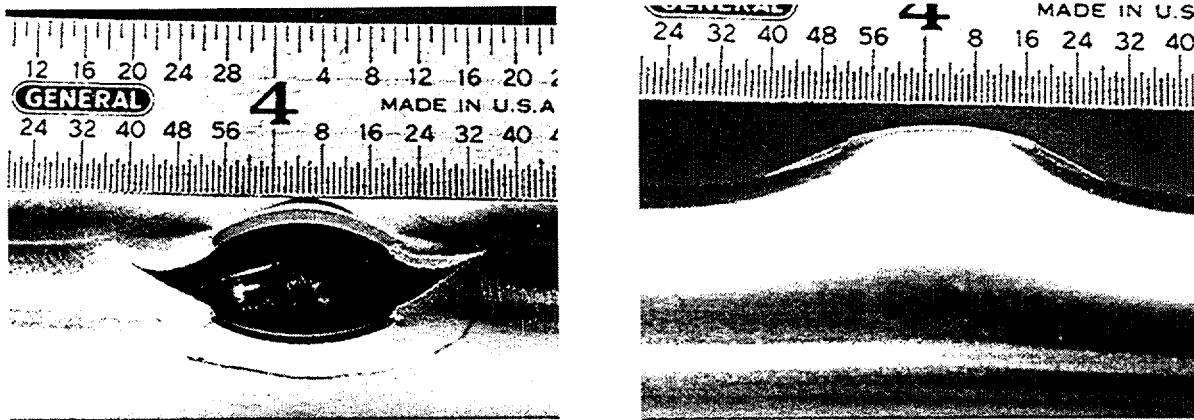
Fig. 4.47.   Top (left) and side (right) views of tube OM101 with a 12.7-mm (0.5-in.)-long 100% TW EDM axial OD notch, tested with a 2-4-mm (18-in.)-thick bladder at a pressurization rate of 13.8 MPa/s (2000 psi/s).

4.4 Pre–Test Analysis of Crack Behavior

4.4.1 Model for Predicting Failure of Partially Supported Tube with a Circumferential Crack

Circumferential cracks in SG tubes are often detected at the top of the tube sheet in PWR nuclear generating plants. Analytical models[4] for the failure of tubes with circumferential cracks predict that the pressure required to cause onset of crack extension may fall within the design-basis accident condition (17 MPa, or 2500 psi) if the tube section that contains the crack is free to bend and the crack is sufficiently long (>180°). It is also known that if the crack section is fully constrained against rotation, the failure pressures are significantly increased and cracks must be much longer (>300°) to be of concern. In an actual SG, the tubes are neither free to bend nor fully constrained. The degree of constraint on a circumferential crack at the top of the tube sheet depends on the span between the top of the tube sheet and the first TSP or baffle plate (15-125 cm or 6-50 in.). Recent tests on SG tubes have shown that tubes that are laterally supported fail at significantly higher pressures than tubes that are free to bend.[5]

An extensive series of tests on failure and leak rates in circumferentially flawed reactor coolant piping subjected to externally applied forces and moments has been conducted at Battelle under the USNRC-sponsored Degraded-Piping[6] and Short Cracks in Piping and Piping Welds Programs.[7]

A simplified stability analysis of circumferentially cracked reactor piping was presented by Tada et al.,[8] who analyzed the pipe as a beam whose cracked section was subjected to plastic limit moment. A similar approach was followed by Smith to analyze failure[9] and leakage[10] of a TW circumferential crack in piping. Smith[11] also emphasized the importance of the crack-system compliance on the onset and stability of crack extension and leakage through a crack. In all of these analyses, plasticity was confined to the crack section, while the rest of the pipe responded elastically. In this report, we use the similar approaches to analyze the problem of failure of SG tubes with circumferential cracks under internal pressure loading in the absence of externally applied forces and moments, and we consider the case where plastic deformation may spread to sections other than that of the crack.

Description of Model

Consider a tube of mean radius R, wall thickness h, and length L, containing a TW circumferential flaw of angular length 2θ at any axial location. The tube can be subjected to various edge conditions. For example, the tube may be clamped at one end (simulating the tubesheet) and simply supported at the other end (simulating the first TSP). Figure 4.48 shows such a tube with the crack at the top of the tube sheet. Under internal pressure loading, FEA shows that a tube in the configuration of Fig. 4.48 deforms as shown in Fig. 4.49 with a definite crack flank rotation and crack tip opening displacement. In the present report, limit load analysis will be used to estimate failure pressure of tubes made of ductile materials such as Alloy 600.

We assume that the tube is thin and is under internal pressure loading only (no constraint on axial deformation of the tube), and that the onset of crack extension occurs after the
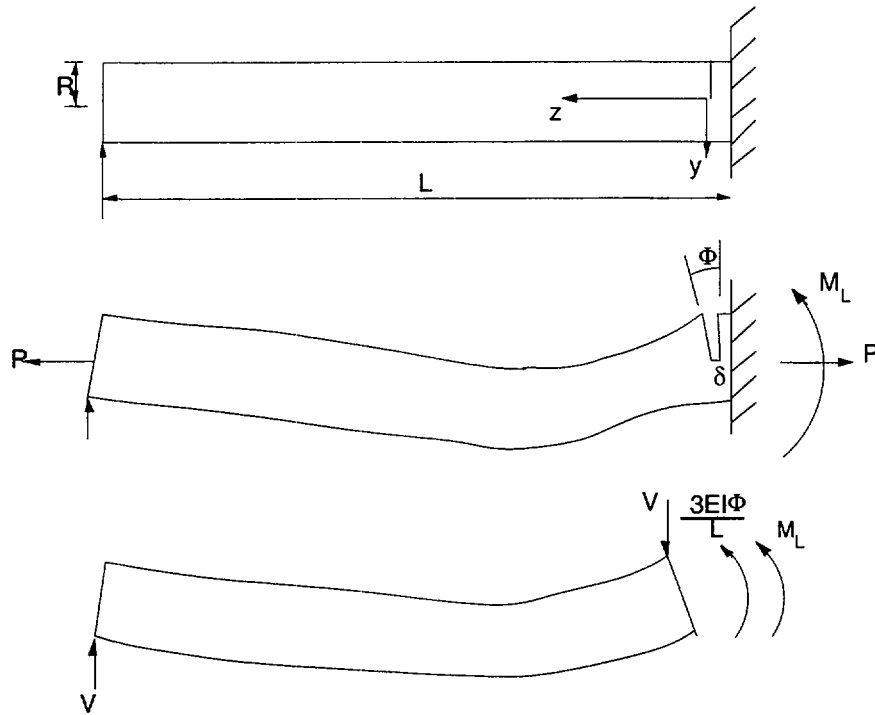
Fig. 4.48. Geometry, loading, and idealized deformation of tube with single TW circumferential crack.
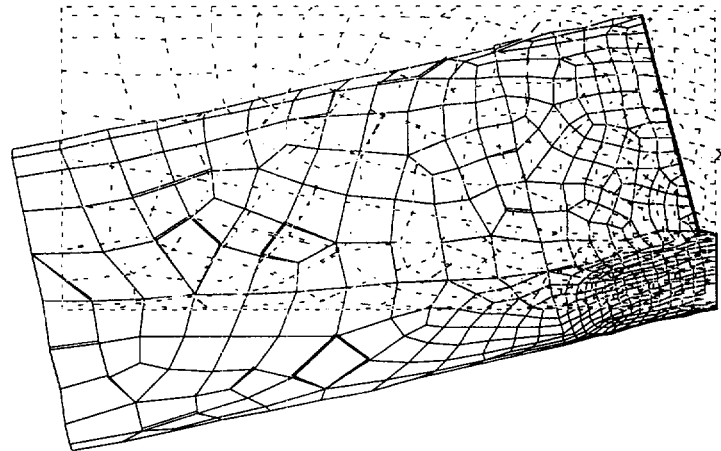
Fig. 4.49. Calculated (by FEA) displaced (solid line) and original (dashed line) shape of laterally supported tube (L/R = 26) with single 240° TW circumferential crack at clamped edge.

attainment of the limit state. The last assumption is valid if the Battelle Screening Criterion[12] is satisfied, i.e.,

$$\frac{E\delta_c}{R\bar{\sigma}}\left(1 - \frac{\theta}{\pi}\right) \geq 1, \tag{4.1}$$

where E is the Young's modulus, δ_c is the critical crack tip opening displacement, and $\bar{\sigma}$ is the flow stress. Thus, for Alloy 600 SG tubing with E = 207,000 MPa (30,000 ksi), $\bar{\sigma}$ = 483 MPa (70 ksi), R = 10 mm (0.4 in.), and 2θ = 270°, we find that $\delta_c \geq 0.1$ mm (0.004 in.), which is generally satisfied by all ductile alloys.

The stress distribution through the section containing the crack at the limit-state is shown in Fig. 4.50. We further assume that plastic deformation is limited to only the section containing the crack, while the rest of the tube responds elastically.

The bending moment (about the tube centerline) and axial force equilibria of the stress distribution of the limit-state (Fig. 4.50) give the following:

$$M_L = 4\bar{\sigma}R^2h\left(\frac{1}{2}\sin\theta - \sin\beta\right) \tag{4.2}$$

and

$$\beta = \frac{\pi - \theta}{2} - \frac{P}{4\bar{\sigma}Rh} = \frac{\pi - \theta}{2} - \frac{\pi pR}{4\bar{\sigma}h}, \tag{4.3a}$$

or

$$\frac{p}{p_b} = \frac{pR}{\bar{\sigma}h} = 2\left(1 - \frac{\theta}{\pi}\right) - \frac{4\beta}{\pi}, \tag{4.3b}$$

where β defines the location of the plastic neutral axis, p is the internal pressure, and p_b is the burst pressure of an unflawed tube.

Plasticity Confined to Crack Section

Denoting the calculated bending moment (positive counterclockwise in Fig. 4.50) in an undefected tube at the crack location (z = 0) by M (for internal pressure loading, M = 0) and by considering the equilibrium of the bending moment in the elastic part of the tube just to the left of the crack section with the plastic limit moment M_L acting just to the right of it (see Fig. 4.48).

$$M = -M_L + \frac{3EI\phi}{L} = 0, \tag{4.4}$$

where I is the bending moment of inertia (πR^3h), and Φ is the rotation at the cracked section due to crack opening (Fig. 4.48). Equation 4.4 is applicable for the configuration shown in

97
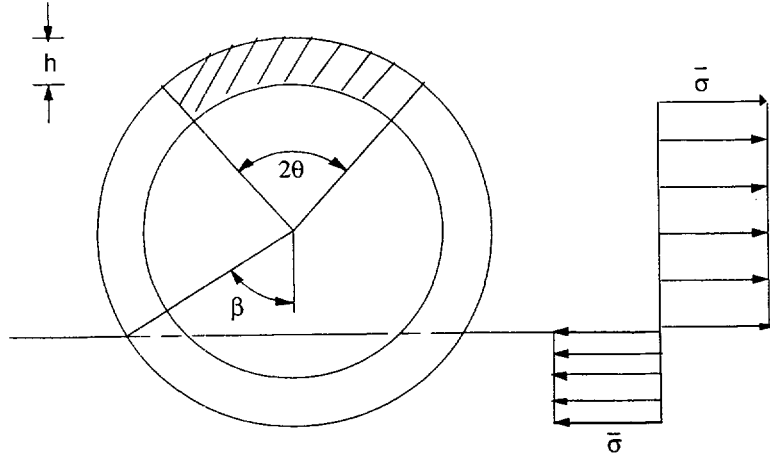
Fig. 4.50. Stress distribution through section at collapse of a tube with single TW circumferential crack

Fig. 4.48. It can be generalized for any set of edge conditions and crack locations by using an effective length L_e. The generalized version of Eq. 4.4 is as follows:

$$M = -M_L + \frac{EI\phi}{L_e} = 0.$$

(4.4a)

The relationships between L and L_e for several crack locations and edge conditions are given in Table 4.4. The plastic rotation Φ_c about the neutral axis at the onset of crack extension is related to the critical crack tip opening displacement δ_c by

$$\phi_c = \frac{\delta_c}{R(\cos\beta + \cos\theta)}.$$

(4.5)

Combining Eqs. 4.2, 4.4a, and 4.5 at the point of crack initiation,

$$\left(\tfrac{1}{2}\sin\theta - \sin\beta\right)(\cos\beta + \cos\theta) - c = 0,$$

(4.6a)

where

$$c = \frac{\pi E \delta_c}{4 L_e \bar{\sigma}}.$$

(4.6b)

Equation 4.6a can be solved for the critical value $\beta = \beta_c$, which when substituted in Eq. 4.3b, gives the crack initiation pressure p_c. Note that the equation for the free-bending case can be obtained by setting $L_e = \infty$, i.e., c = 0 in Eq. 4.6a.

The onset of crack extension can also be expressed in terms of the critical value of the plastic component of the deformation J integral J_P, which, for the bending case, is defined in terms of the plastic rotation ϕ as follows:

Table 4.4. *Effective lengths of tubes for several circumferential crack locations and edge conditions.*

Edge conditions and crack location	Effective length
Clamped — Clamped (crack at center)	$L_e = L/4$
Clamped — Clamped (crack offset)	$L_e = L$
S.S. — Clamped	$L_e = L/3$
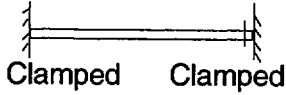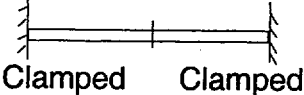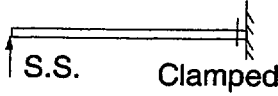
$$J_P = -\int_0^\phi \left(\frac{\partial M}{\partial A}\right)_\phi d\phi,$$
(4.7)

where $A = 2Rh\theta$. In the context of limit analysis $J = J_P$ and $M = M_L$, as given in Eq. 4.2. Differentiating Eq. 4.2 with respect to θ and noting from Eq. 4.2 that at constant rotation, i.e., at constant pressure,

$$\frac{\partial \beta}{\partial \theta} = -\frac{1}{2},$$

$$J = R\bar{\sigma}\int_0^\phi (\cos\beta + \cos\theta)d\phi = R\bar{\sigma}\phi(\cos\beta + \cos\theta).$$
(4.8)

Thus, the critical plastic rotation is given in terms of the critical J integral J_c as follows:

$$\phi_c = \frac{J_c}{R\bar{\sigma}(\cos\beta + \cos\theta)}.$$
(4.9a)

Comparing Eq. 4.5 and 4.9, we recover the familiar equation

$$J_c = \bar{\sigma}\delta_c.$$
(4.9b)

A plot of the fracture toughness $K_{JC} = \sqrt{EJ_C}$ versus the critical crack tip opening displacement is shown in Fig. 4.51. For ductile alloys, the critical crack tip displacement is somewhere in the range of 0.76-2.54 mm (0.03-0.1 in.).

Crack Opening Area (COA). If the critical crack opening displacement is not exceeded and there is no crack extension, the crack opening area can be expressed in terms of the rotation Φ and crack size by
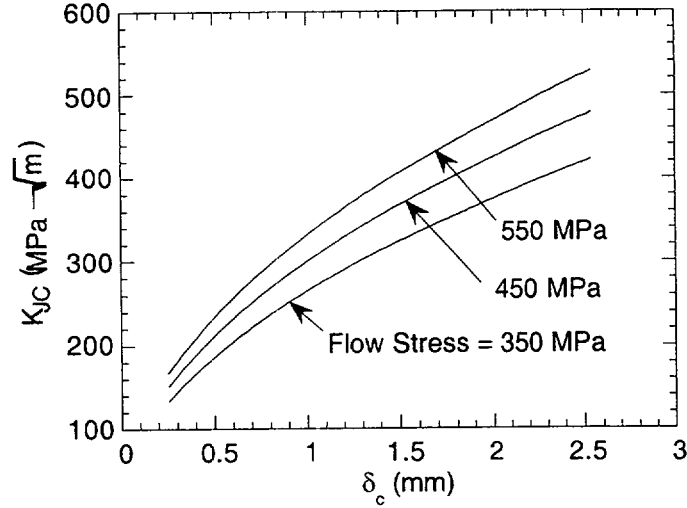
Fig. 4.51. Variation of fracture toughness with critical crack tip opening displacement.

$$A = 2R^2\phi \int_0^\theta (\cos\beta + \cos\alpha)d\alpha = 2R^2\phi(\theta\cos\beta + \sin\theta). \tag{4.10a}$$

Using Eqs. 4.4a and 4.2, Eq. 10a reduces to (for $\phi \le \phi_c$)

$$A = \frac{8L_e R\bar{\sigma}}{\pi E}(\theta\cos\beta + \sin\theta)\left(\frac{1}{2}\sin\theta - \sin\beta\right). \tag{4.10b}$$

At the point of crack initiation, $\phi = \phi_c$ and $\beta = \beta_c$, which when substituted in Eq. 4.10b, gives (using Eq. 4.5)

$$A = A_c = 2R\delta_c \frac{(\theta\cos\beta_c + \sin\theta)}{(\cos\beta_c + \cos\theta)}. \tag{4.10c}$$

Instability.

Unstable failure need not necessarily be associated with onset of crack extension. If the crack is to be unstable at onset of crack extension under constant loading, the following condition must be satisfied (using Eq. 4.4a) for

$$\frac{dM}{d\phi} = \frac{dM_L}{d\phi}\bigg|_I + \frac{EI}{L_e} < 0, \tag{4.11}$$

with $\dfrac{dM_L}{d\phi}$ measured at the onset of crack extension. Equation 4.11 can be expressed in terms of the familiar tearing modulus by first differentiating Eq. 4.8 with respect to θ,

$$\frac{dJ}{d\theta} = \frac{\partial J}{\partial\theta} + \frac{\partial J}{\partial\phi}\frac{d\phi}{d\theta} = R\bar{\sigma}\left[-\phi\left(\sin\theta - \frac{1}{2}\sin\beta\right) + \frac{d\phi}{d\theta}(\cos\beta + \cos\theta)\right] \tag{4.12a}$$

100

and then solving

$$\frac{d\phi}{d\theta} = \frac{\dfrac{dJ}{d\theta} + J\dfrac{\sin\theta - \dfrac{1}{2}\sin\beta}{\cos\beta + \cos\theta}}{R\bar{\sigma}(\cos\beta + \cos\theta)}.$$

(4.12b)

Differentiating Eq. 4.2 with respect to ϕ, using Eq. 4.12b, and rearranging, we obtain the condition of instability as

$$\frac{2L_e}{\pi R}(\cos\beta + \cos\theta)^2 - \frac{EJ}{R\bar{\sigma}^2}\frac{\sin\theta - \dfrac{1}{2}\sin\beta}{\cos\beta + \cos\theta} > \frac{E}{\bar{\sigma}^2}\frac{dJ}{da},$$

(4.13a)

where a is the crack length ($Rd\theta = da$). We can identify the left-hand-side of Eq. 4.13a as the applied tearing modulus, T_{APP}, and the condition of instability can be written as

$$T_{APP} = \frac{2L_e}{\pi R}(\cos\beta + \cos\theta)^2 - \frac{EJ}{R\bar{\sigma}^2}\frac{\sin\theta - \dfrac{1}{2}\sin\beta}{\cos\beta + \cos\theta} > T_{MAT}.$$

(4.13b)

Note that Eq. 4.13b is the same as that given by Smith.[10] For ductile materials with high crack growth resistance, the J-term is usually negligible. In such cases, we can simplify Eq. 4.13b as

$$T_{APP} \approx \frac{2L_e}{\pi R}(\cos\beta + \cos\theta)^2 > T_{MAT}.$$

(4.13c)

For many ductile alloys, $T_{MAT} \approx 200$.

Results. A plot of the failure (onset of crack extension) pressure versus crack angle is shown in Fig. 4.52 for various values of the elastic stiffness parameter c. Note that even for a low value of c (i.e., large L_e), tubes with long cracks behave as if they were fully constrained. For $c \geq 0.5$, tubes with any crack behave as if they were fully constrained. Figure 4.52 also shows the maximum angular lengths of TW circumferential cracks corresponding to typical pressures during normal operation and design basis accident conditions. If we use the nominal values E = 207,000 MPa (30,000 ksi) and $\bar{\sigma}$ = 483 MPa (70 ksi) for the mechanical properties in Eq. 4.6b, we then calculate

$$c = 300\frac{\delta_c}{L_e}.$$

(4.6b)

The value of the critical crack tip opening displacement δ_c must be obtained from failure tests on tubes with circumferential cracks. Plots of the calculated normalized failure (onset of crack extension) pressure as a function of the span are shown in

Figs. 4.53a-b for a 180° crack at several locations, edge conditions, and for critical crack tip opening displacements of 0.25 and 0.75 mm (0.01 and 0.03 in.), respectively. Similar plots for a 240° crack and a 270° crack are shown in Figs. 4.54a-b and 4.55a-b, respectively. Depending on the span, the model predicts that the failure pressure is increased significantly

101
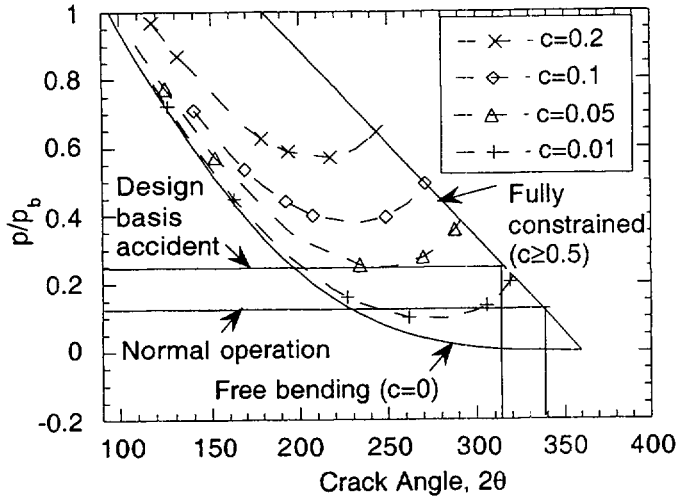
Fig. 4.52.
Variation of failure pressure, normalized by unflawed burst pressure, of tube with crack angle of single TW circumferential crack.

(a)

(b)
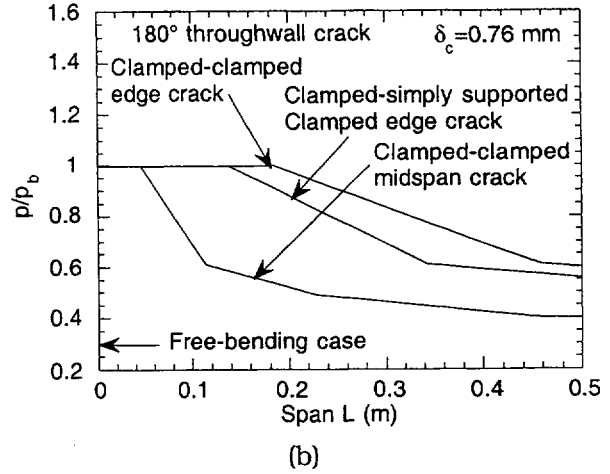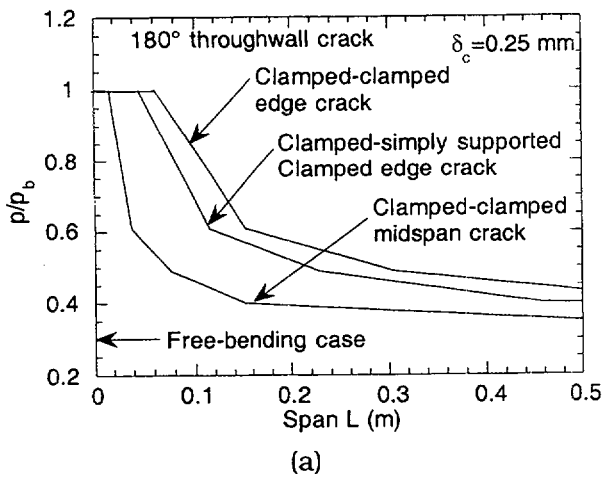
Fig. 4.53. Variation of failure pressure, normalized by unflawed burst pressure, of tube with 180° TW crack with span for several edge conditions, crack locations and δ_c values of (a) 0.25 mm (0.01 in.) and (b) 0.76 mm (0.03 in.).

compared to that under a free-bending condition. As expected, a midspan crack is far more damaging than an edge crack. For a 180° TW crack in a clamped, simply supported tube, the failure pressure is undiminished from the burst pressure of an unflawed tube if the span is less than 0.5 and 1.4 m (20 and 55 in.) for critical crack opening displacements of 0.25 and 0.75 mm (0.01 and 0.03 in.), respectively. A similar tube with a 240° crack will behave as a fully constrained tube, i.e., will experience a 33% reduction in failure pressure from the burst pressure of an unflawed tube if the span is less than 1.3 and 3.6 m (50 and 140 in.) for critical crack opening displacements of 0.25 and 0.75 mm (0.01 and 0.03 in.), respectively. A tube with a 270° crack will behave as a fully constrained tube, i.e., will experience a 50% reduction in failure pressure from the burst pressure of an unflawed tube if the span is less than 2.3 and 7.0 m (90 in and 275 in.) for critical crack opening displacements of 0.25 and 0.75 mm (0.01 and 0.03 in.), respectively.

The variation of the applied tearing modulus (using Eq. 4.13b) with pressure is shown in Figs. 4.56a-b for a 1.2-m (48-in.)-long tube with a 120° and 240° TW crack, respectively. Also,

102
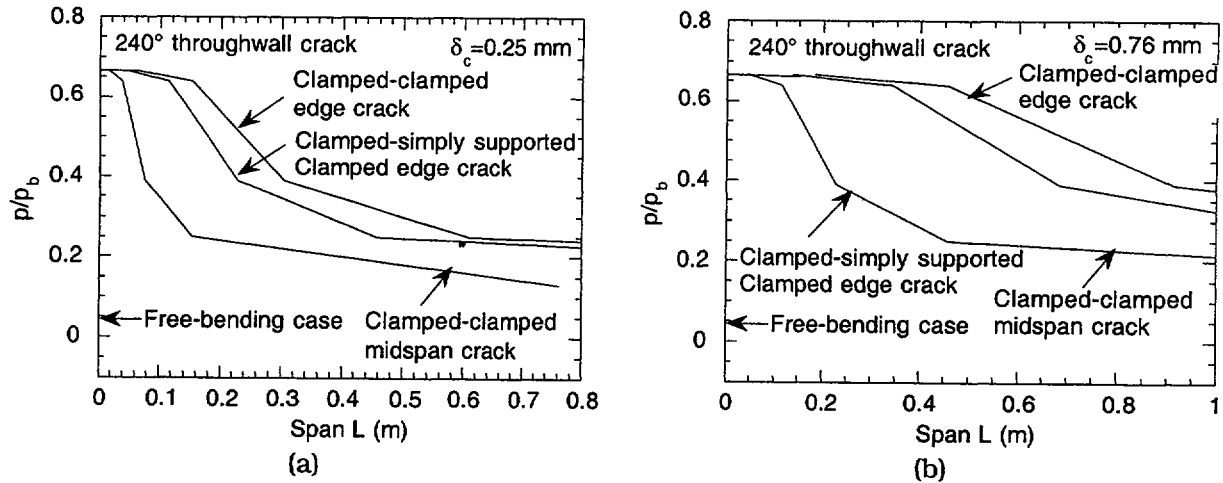
Fig. 4.54. *Variation of failure pressure, normalized by unflawed burst pressure, of tube with 240° TW crack with span for several edge conditions, crack locations, and δ_c values of (a) 0.25 mm (0.01 in.) and (b) 0.76 mm (0.03 in.).*
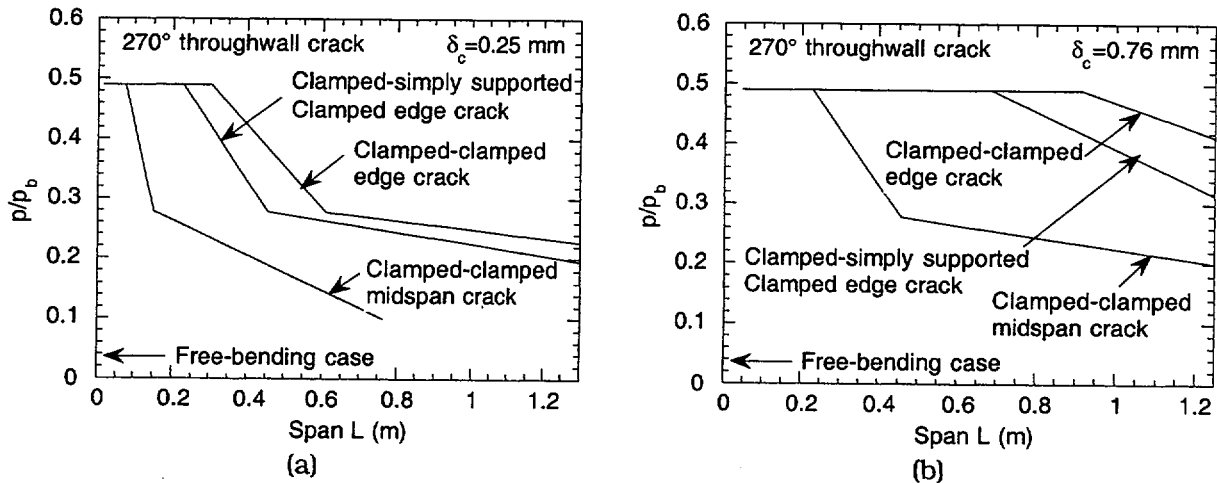
Fig. 4.55. *Variation of failure pressure, normalized by unflawed burst pressure, of tube with 270° TW crack with span for several edge conditions, crack locations and δ_c values of (a) 0.25 mm (0.01 in.) and (b) 0.76 mm (0.03 in.).*

shown in the figures are the pressures at which a crack tip opening displacement of 1.3 mm (0.05 in.) is reached as indicative of the pressures for the onset of crack extension. In the case of the 120° crack, the J-term of Eq. 4.13a is small compared to the applied tearing modulus. Because the applied tearing modulus is less than $T_{MAT} = 200$, the crack should propagate stably after the onset of crack extension. For the 240° crack, the J-term is not negligible unless the pressure at the onset of crack extension is small (p/p_b <<0.3). However, since the J-term (positive) in Eq. 4.13a has a stabilizing influence, the initial crack growth will be stable in both cases.

Limitations of the model. The onset of yielding away from the crack plane can be calculated by using the current model and assuming a loading path consisting of first applying the

103
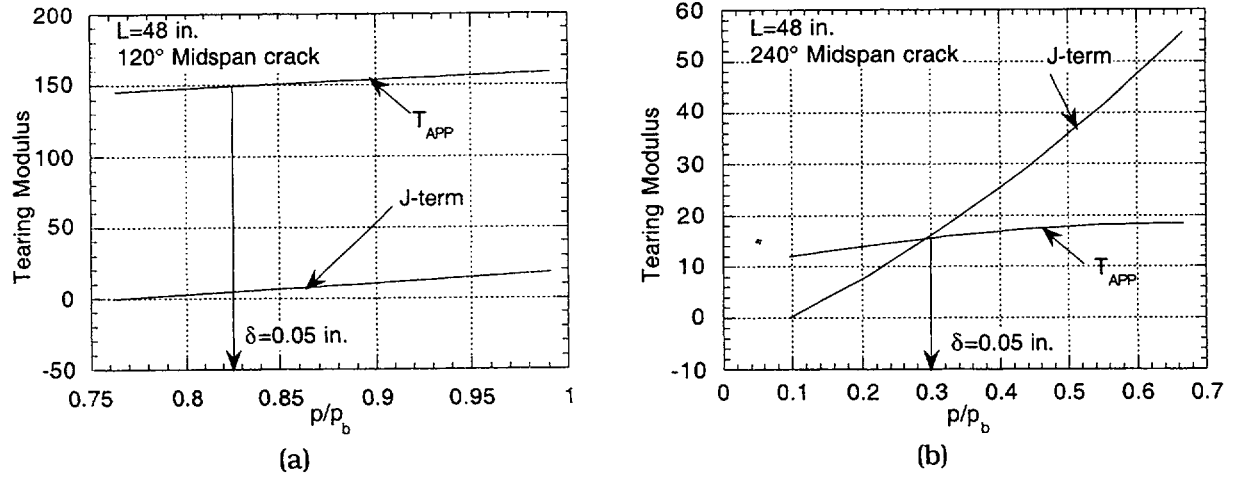
Fig. 4.56. Variation of applied tearing modulus and J-term in Eq. 4.13 with pressure (normalized by the unflawed burst pressure) of clamped edge tube with midspan cracks of angular length (a) 120° and (b) 240°.

membrane stresses due to pressure, keeping the bending stresses at zero, and then applying the bending stresses holding the membrane stresses constant. Although the axial bending analysis in the current model is uniaxial, the axial yield stress S_y is adjusted to account for the biaxial stress effect by assuming it to vary with the hoop stress σ_h as follows (Fig. 4.57a):

$$S_y = \begin{cases} \sigma_y - \dfrac{\sigma_h}{2} & \text{for } \sigma_h \le \sigma_y \\ \dfrac{\sigma_y}{2} & \text{for } \sigma_h > \sigma_y \end{cases}, \tag{4.14}$$

where σ_y is the virgin uniaxial yield stress. If we denote the bending moment to cause first yielding in an uncracked section just adjacent to the cracked section by M_y,

$$M_y = \frac{S_y I}{R}, \tag{4.15a}$$

and Eq. 4.2 can be written in a nondimensional form as follows:

$$\frac{M_L}{M_y} = \frac{4}{\pi} \frac{\bar{\sigma}}{S_y} \left(\frac{1}{2} \sin \theta - \sin \beta \right). \tag{4.15b}$$

Thus, the condition for first yielding in an undefected section just adjacent to the cracked section by bending is

$$\frac{M_L}{M_y} = \frac{4}{\pi} \frac{\bar{\sigma}}{S_y} \left(\frac{1}{2} \sin \theta - \sin \beta \right) = 1. \tag{4.16a}$$

Noting that yielding of the undefected tube section can occur either by axial bending or by yielding in the hoop direction by membrane hoop stress, we find that the pressure to cause first yielding (denoted by p_y) is the lesser of the following two values:

104
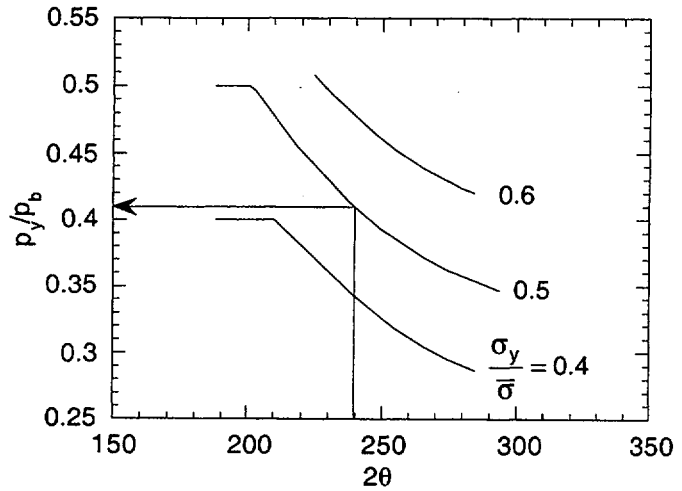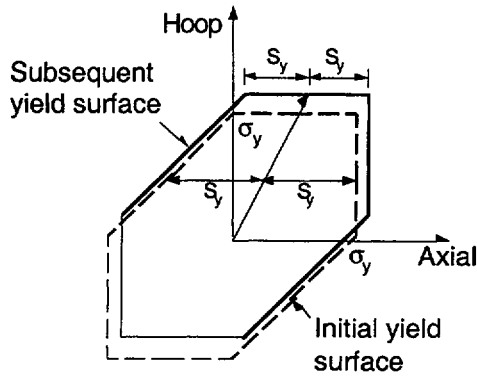
Fig. 4.57. *(a) Determination of axial yield strength Sy for bending analysis using Tresca criterion and (b) predicted variation of pressure to first yield the tube away from crack plane with crack angle as a function of ratio between yield and flow stress.*

$$\frac{p_y}{p_b} = \left\{ \frac{\frac{2\sigma_y}{\bar{\sigma}} - \frac{8}{\pi}\left(\frac{1}{2}\sin\theta - \sin\beta\right)}{\frac{\sigma_y}{\bar{\sigma}}} \right. \tag{4.16b}$$

Since β is a function of pressure (Eq. 4.3a), Eq. 4.16b must be solved numerically. A plot of the pressure to first yield versus crack length is shown in Fig. 4.57b for various values of yield to flow stress ratios.

4.4.2   Finite-Element Analysis

To provide a basis for comparison with the analytical models, an incremental elastic-plastic FEA that uses a multilinear kinematic hardening rule was conducted for a tube (L/R = 60, simply supported at one end and clamped at the other) with a 240° TW circumferential crack at the clamped end under internal pressure loading. The assumed stress-strain curve is shown in Fig. 4.58. The difference between kinematic and isotropic hardening rules should be small for the nearly radial loading path used for the problem at hand. Comparisons of the variation of the crack section rotation and support reaction with pressure are shown in Figs. 4.59a-b, respectively. The slight discrepancies between the FEA results and the model predictions at low pressures are due to neglecting the elastic deformation in the model. However, the FEA results diverge from the model calculations significantly as the pressure exceeds ≈50% of the unflawed tube burst pressure. This is because at these higher pressures, tube sections away from the crack plane experience significant plastic deformation (Fig. 4.60), which is assumed to be negligible in the model. Note that with $\sigma_y/\bar{\sigma}$ = 0.5, the analytical model predicts (Fig. 4.61 b) onset of yielding in a tube containing a 240° crack at p/p_b = 0.43, which agrees very well with the FEA result. Thus, the limit of applicability of the current model depends on the crack angle as well as the strain hardening behavior ($\sigma_y/\bar{\sigma}$) of the material (Fig. 4.57b).

105
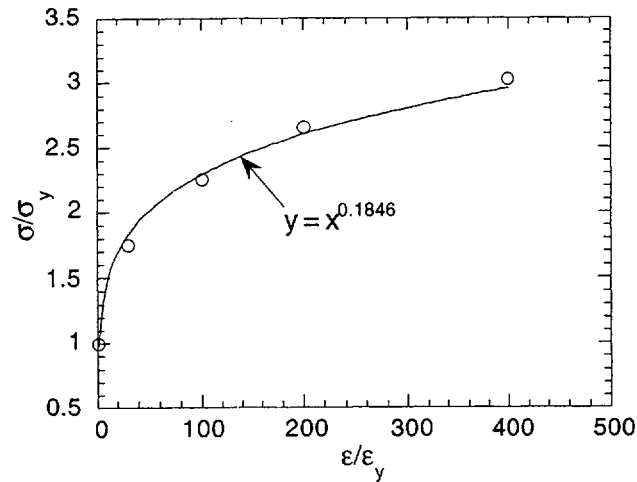
Fig. 4.58.   *Normalized uniaxial stress-strain curve (symbols used in FEA) and power-law fit.*
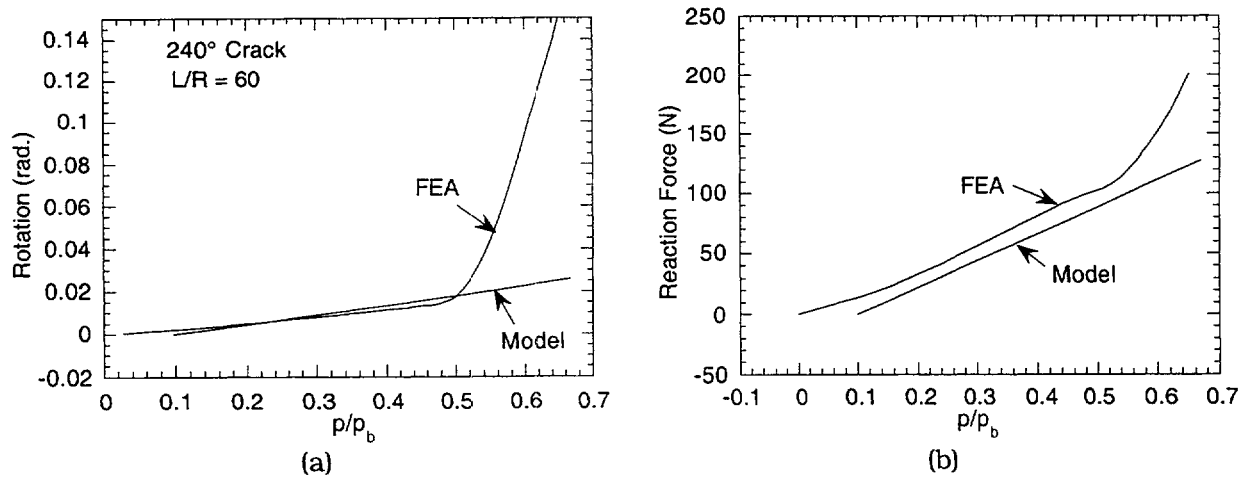
Fig. 4.59.   *Comparison of model prediction and elastic-plastic FEA results ($\sigma_y / \bar{\sigma} = 0.5$) for (a) crack section rotation and (b) support reaction force of tube simply supported at one end and clamped at the other (as in Fig. 4.53) at various normalized pressures.*

Plasticity allowed to occur away from crack section.

When plasticity spreads to sections other than that containing the crack, Eq. 4.4 is no longer applicable, and a new nonlinear relationship between bending moment and rotation must be derived. We consider two types of plastic deformation laws for this analysis. First, we consider a material with a bilinear stress-strain curve (with tangent modulus E_T),

$$\frac{\varepsilon}{\varepsilon_y} = \begin{cases} \dfrac{\sigma}{\sigma_y} & \text{for } \sigma \le \sigma_y \\[2mm] 1 + \left(\dfrac{\sigma}{\sigma_y} - 1\right)\dfrac{E}{E_T} & \text{for } \sigma > \sigma_y \end{cases} \qquad (4.17a)$$

106
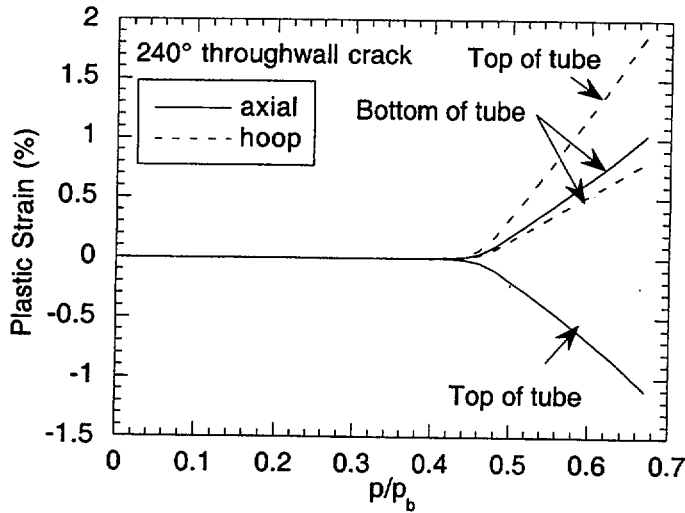
Fig. 4.60. *Calculated (by FEA with yield stress/flow stress = 0.5) variation of plastic strains, with normalized pressure, at top and bottom of section located at axial distance 4R from crack in laterally supported tube (L/R = 60) with single 240° TW circumferential crack at clamped edge.*
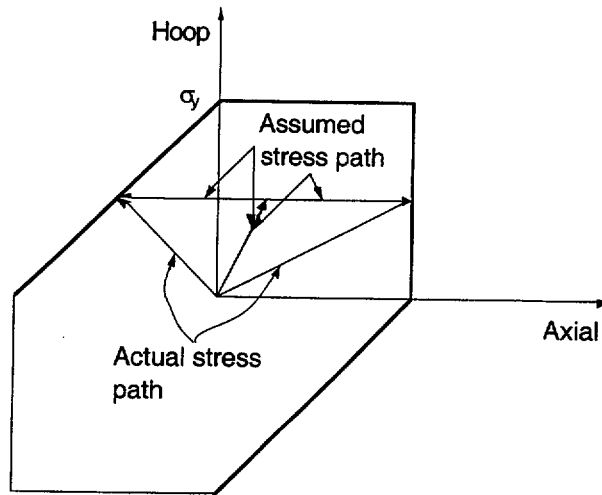
Fig. 4.61. *Radial loading path used in FEA is replaced in model by nonradial path consisting of loading to final pressure (at 2 to 1 stress ratio), followed by applying axial bending stress at constant hoop.*

and second, a material with a power-law hardening stress-strain curve is considered,

$$\frac{\varepsilon}{\varepsilon_y} = \begin{cases} \dfrac{\sigma}{\sigma_y} & \text{for } \sigma \le \sigma_y \\[2ex] \left(\dfrac{\sigma}{\sigma_y}\right)^{\frac{1}{m}} & \text{for } \sigma > \sigma_y \end{cases}$$

(4.17b)

In both cases, we continue to assume that the section containing the crack is at the plastic limit state with flow stress $\bar{\sigma}$, the assumption being that the crack section experiences extensive plastic deformation long before any plastic yielding occurs away from the crack section.

To keep the analysis tractable for the current analytical model, we make a simplifying assumption that the stresses and total deformation at any pressure can be obtained by considering a nonradial loading path, consisting of first loading radially to the final pressure (hoop to axial membrane stress ratio of 2:1) at zero axial bending stress and then applying the axial bending stresses, holding the pressure-induced membrane stresses constant (Fig. 4.61). This assumption allows us to use the same yield surface (Eq. 4.14 and Fig. 4.57a) for all axial locations and makes it possible to obtain an analytical solution for the bending problem. The relatively good agreement between the model prediction and the FEA results, to be discussed later, shows that this assumption is probably reasonable as long as no unloading or reversed yielding occurs.

With the above assumptions, we determine a relationship between the bending moment and rotation in the elastic-plastic regime by a detailed analysis of axial bending of the tube subjected to an end moment M_0 at a constant internal pressure p. For $p > p_y$, a length of the tube extending from $z = 0$ to $z = z_y$ will deform plastically, while the rest of the beam $L > z > z_y$ will remain elastic. The stress distributions in a plastically deforming section are shown in Figs. 4.62a and 4.62b for the bilinear and power law hardening stress-strain curve, respectively. At every section, there will be an elastic core extending from $\theta = -\beta_y$ to $\theta = \beta_y$, with β_y varying from $\beta_y = \beta_0$ at $z = 0$ to $\beta_y = \pi/2$ at $z = z_y$.

By stress integration and using the definition of z_y, the bending moment at any section is given by

$$\frac{M}{M_y} = \frac{2}{\pi \sin \beta_y} \left[\left(1 - \frac{E_T}{E} \right) \left(\beta_y + \frac{1}{2} \sin 2\beta_y \right) + \frac{\pi E_T}{2E} \right] = \frac{L - z}{L - z_y} \tag{4.18a}$$

for the bilinear stress-strain curve and

$$\frac{M}{M_y} = \frac{2}{\pi \sin \beta_y} \left(\beta_y - \frac{1}{2} \sin 2\beta_y \right) + \frac{4}{\pi} \left(\frac{1}{\sin \beta_y} \right)^m \int_{\beta_y}^{\frac{\pi}{2}} \sin^{m+1} \theta d\theta = \frac{L - z}{L - z_y} \tag{4.18b}$$

for the power-law hardening curve, where M_y corresponds to the bending moment at first yield away from the crack section.

Differentiating Eqs. 4.18a-b and solving,

$$\frac{d\beta_y}{dz} = \frac{1}{(L - z_y)} \frac{1}{f(\beta_y)}, \tag{4.19}$$

where
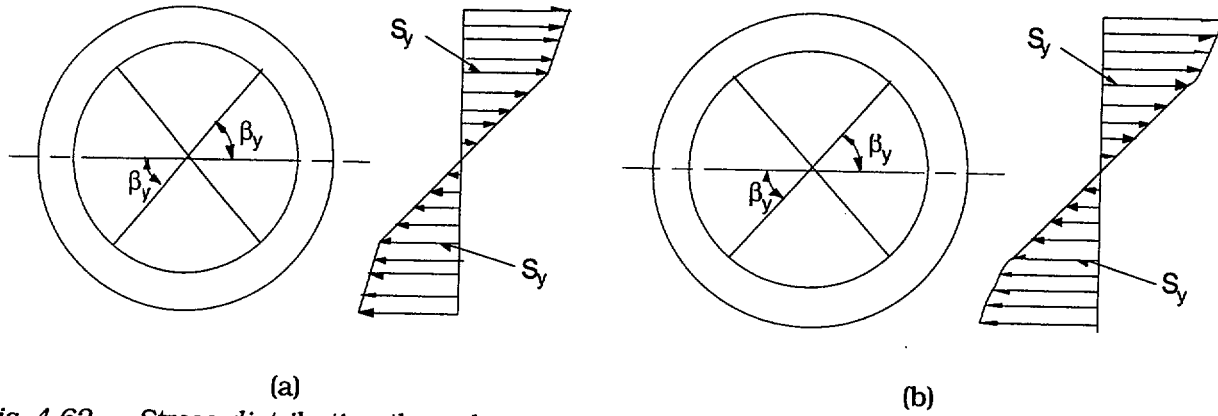
Fig. 4.62. *Stress distribution through section away from crack section after yield: (a) bilinear for bilinear stress-strain curve and (b) nonlinear for power-law hardening curve.*

$$f(\beta_y) = \frac{2}{\pi} \frac{\left(1 - \frac{E_T}{E}\right)\left(\beta_y - \frac{1}{2}\sin 2\beta_y\right) + \frac{\pi E_T}{2E}}{\sin\beta_y \tan\beta_y} \qquad (4.20a)$$

for the bilinear stress-strain curve and

$$f(\beta_y) = \frac{2}{\pi}\left[\frac{\beta_y - \frac{1}{2}\sin 2\beta_y}{\sin\beta_y \tan\beta_y} + \frac{2mI_m}{\sin^m\beta_y \tan\beta_y}\right] \qquad (4.20b)$$

for the power-law hardening stress-strain curve with

$$I_m = \int_{\beta_y}^{\frac{\pi}{2}} \sin^{m+1}\theta d\theta. \qquad (4.20c)$$

The equation for bending is given by

$$\frac{d^2 w}{dz^2} = -\frac{\kappa_y}{\sin\beta_y}, \qquad (4.21a)$$

where w is the transverse deflection and

$$\kappa_y = \frac{M_y}{EI} = \frac{S_y}{ER}. \qquad (4.21b)$$

Making a transformation of independent coordinate from z to β_y with the help of Eq. 4.19,

$$\frac{dw}{dz} = \frac{1}{(L - z_y)}\frac{1}{f(\beta_y)}\frac{dw}{d\beta_y} \qquad (4.22a)$$

and

109

$$\frac{d^2w}{dz^2} = \left[\frac{1}{(L-z_y)}\right]^2 \frac{1}{f(\beta_y)} \frac{d}{d\beta_y}\left[\frac{1}{f(\beta_y)}\frac{dw}{d\beta_y}\right]$$

$$= -\frac{\kappa_y}{\sin\beta_y}. \tag{4.22b}$$

Integrating Eq. 4.22b from $\beta = \beta_o$ (i.e., $z = 0$) to $\beta = \pi/2$ (i.e., $z = z_y$), and denoting the slope at $z = 0$ by ϕ_o,

$$\left.\frac{dw}{dz}\right|_{z=z_y} = \phi_o - \kappa_y(L-z_y)\int_{\beta_o}^{\frac{\pi}{2}} \frac{f(\beta_y)}{\sin\beta_y}d\beta_y. \tag{4.23a}$$

In a similar fashion,

$$w|_{z=z_y} = \phi_o\big((L-z_y)\big)\int_{\beta_o}^{\frac{\pi}{2}} \frac{f(\beta_y)}{\sin\beta_y}d\beta_y - \kappa_y(L-z_y)^2 \int_{\beta_o}^{\frac{\pi}{2}} f(\beta_y)\int_{\beta_o}^{\beta_y}\frac{f(\beta_y)}{\sin\beta_y}d\beta_y d\beta_y. \tag{4.23b}$$

The slope and displacement at $z = z_y$ from the elastic part of the beam are

$$\left.\frac{dw}{dz}\right|_{z=z_y} = \frac{M_y(L-z_y)}{2EI} + C_1 \tag{4.24a}$$

and

$$w|_{z=z_y} = -\frac{M_y}{6EI}(L-z_y)^2 - C_1(L-z_y), \tag{4.24b}$$

where C_1 is an arbitrary constant. Combining Eqs. 4.24a and 4.24b,

$$(L-z_y)\left.\frac{dw}{dz}\right|_{z_y} + w|_{z_y} = \frac{\kappa_y}{3}(L-z_y)^2. \tag{4.24c}$$

Satisfying continuity of slope and displacement at $z = z_y$, using Eq. 4.24c, and solving gives

$$\frac{\phi_o M_o}{\phi_y M_y} = \frac{3I_1 + 3I_2 + 1}{1 + I_3}, \tag{4.25}$$

where

$$\frac{M_o}{M_y} = \frac{2}{\pi\sin\beta_o}\left[\left(1 - \frac{E_T}{E}\right)\left(\beta_o + \frac{1}{2}\sin 2\beta_o\right) + \frac{\pi E_T}{2E}\right] \tag{4.26a}$$

for the bilinear stress-strain curve and

110

$$\frac{M_o}{M_y} = \frac{2}{\pi \sin \beta_o}\left(\beta_o - \frac{1}{2}\sin 2\beta_o\right) + \frac{4}{\pi}\left(\frac{1}{\sin \beta_o}\right)^m \int_{\beta_o}^{\frac{\pi}{2}} \sin^{m+1}\theta\, d\theta \qquad (4.26b)$$

for the power-law hardening stress-strain curve,

$$\phi_y = \frac{1}{3}L\kappa_y = \frac{M_y L}{3EI}, \qquad (4.26c)$$

$$I_1 = \int_{\beta_o}^{\frac{\pi}{2}} \frac{f(\beta_y)}{\sin \beta_y}d\beta_y, \qquad (4.27a)$$

$$I_2 = \int_{\beta_o}^{\frac{\pi}{2}} f(\beta_y)\int_{\beta_o}^{\beta_y} \frac{f(\beta_y)}{\sin \beta_y}d\beta_y d\beta_y, \qquad (4.27b)$$

and

$$I_3 = \int_{\beta_o}^{\frac{\pi}{2}} f(\beta_y)d\beta_y. \qquad (4.27c)$$

We can represent the rotation in terms of a function G of the bending moment as follows, with the tangent modulus E_T as a parameter for the bilinear stress-strain curve:

$$\phi = \phi_y G\left(\frac{M}{M_y}; \frac{E_T}{E}\right). \qquad (4.28a)$$

In a similar fashion, for the power-law hardening case, we can represent the rotation in terms of a different function G of the bending moment with the exponent m as a parameter,

$$\phi = \phi_y G\left(\frac{M}{M_y}; m\right). \qquad (4.28b)$$

A plot of the end rotation versus the applied moment for various values of tangent modulus is shown in Figs. 4.63a-b for the case of bilinear stress-strain curve. For perfect plasticity ($E_T = 0$), the limit moment is reached in ≈ 1.7 times the rotation for initial yield. The bending moment capability of the section increases with increasing value of tangent modulus. However, the plastic rotation is considerably greater than the elastic rotation even for a tangent modulus of $E_T/E = 1/50$. In a similar fashion, a plot of the calculated end rotation versus the applied moment for the power-law hardening case is shown in Fig. 4.64. In both cases, the function G can be represented by a cubic polynomial of the bending moment (see Figs. 4.63b and 4.64):

$$G(x) = \begin{cases} x & \text{for } x \leq 1 \\ A + Bx + Cx^2 + Dx^3 & \text{for } x > 1. \end{cases} \qquad (4.28c)$$

Equation 4.4 can be generalized for the elastic-plastic case as follows:

111
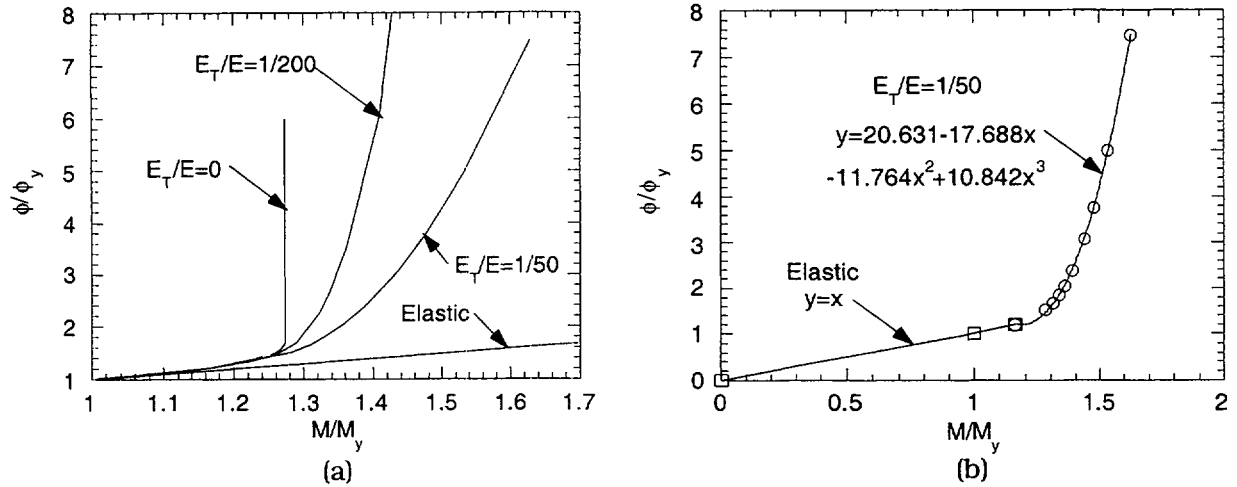
Fig. 4.63.   Rotation vs. applied bending moment for configuration of Fig. 4.48 (a) for various values of E_T and (b) polynomial fit to curve for $E_T/E = 1/50$.
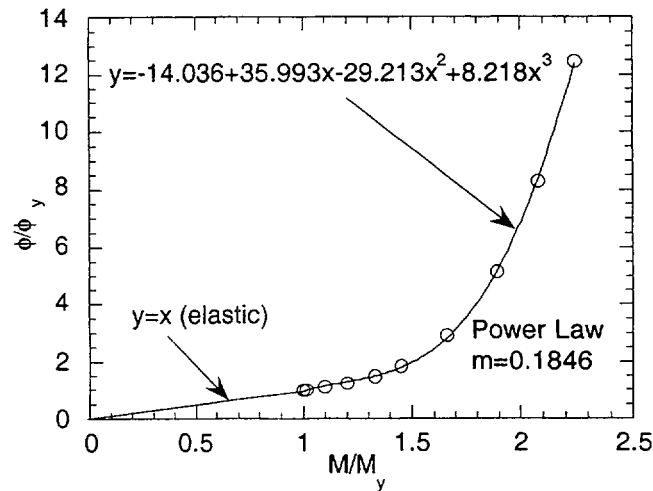
Fig. 4.64.   Model-calculated normalized rotation versus applied bending moment for configuration of Fig. 4.48 and polynomial fit to results for power-law hardening stress-strain curve with exponent $m = 0.1846$ (Fig. 4.58).

$$-\frac{M_L}{M_y} + G^{-1}\left(\frac{\phi}{\phi_y}\right) = 0,$$ (4.29a)

or, alternatively

$$\phi = \phi_y G\left(\frac{M_L}{M_y}\right).$$ (4.29b)

Onset of Crack Initiation

Combining Eqs. 4.29b and 4.5, at the point of crack initiation,

$$\left(\cos\beta_c + \cos\theta\right)G\left(\frac{M_L}{M_y}\right) = \frac{3E\delta_c}{LS_y} = \frac{3\pi E\delta_c}{4L\bar{\sigma}}\frac{4}{\pi}\frac{\bar{\sigma}}{S_y}$$

$$= \frac{4c}{\pi}\frac{\bar{\sigma}}{S_y}, \tag{4.30a}$$

where M_L/M_y is given by Eq. 4.15b, c is defined in Eq. 4.6b, and Eq. 4.14 can be rewritten as follows:

$$\frac{S_y}{\bar{\sigma}} = \begin{cases} \dfrac{\sigma_y}{\bar{\sigma}} - \dfrac{p}{2p_b} & \text{for } \dfrac{p}{p_b} \le \dfrac{\sigma_y}{\bar{\sigma}} \\[2ex] \dfrac{p}{2p_b} & \text{for } \dfrac{p}{p_b} > \dfrac{\sigma_y}{\bar{\sigma}}. \end{cases} \tag{4.30b}$$

Equation 4.30a can be solved for the critical value $\beta = \beta_c$ which, when substituted in Eq. 4.3b, gives the crack initiation pressure p_c.

The onset of crack extension can also be expressed in terms of the critical value J_c of the plastic component of the deformation J integral J_p, and Eqs. 4.7, 4.8, and 4.9a-b still hold.

Instability

Proceeding as before, if the crack is to be unstable at onset of crack extension under constant loading, the following condition must be satisfied (using Eq. 4.29a):

$$\frac{dM}{d\phi} = -\frac{dM_L}{d\phi}\bigg|_I + \frac{3EI}{L}\frac{dG^{-1}\left(\dfrac{\phi}{\phi_y}\right)}{d\left(\dfrac{\phi}{\phi_y}\right)} = -\frac{dM_L}{d\phi}\bigg|_I + \frac{3EI}{L}\frac{1}{\dfrac{dG\left(\dfrac{M}{M_y}\right)}{d\left(\dfrac{M}{M_y}\right)_{M-M_L}}} < 0, \tag{4.31}$$

where $dM_L/d\phi$ is measured at the onset of crack extension. Using Eqs 4.12a and 4.12b and following the procedure that was used to derive Eq. 4.13b, we find the condition for unstable failure to be

$$T_{APP} = \frac{2L}{3\pi R}\left(\cos\beta + \cos\theta\right)^2 \frac{dG\left(\dfrac{M}{M_y}\right)}{d\left(\dfrac{M}{M_y}\right)}\bigg|_{M=M_L} - \frac{EJ}{R\bar{\sigma}^2}\frac{\sin\theta - \dfrac{1}{2}\sin\beta}{\cos\beta + \cos\theta} > \frac{E}{\bar{\sigma}^2}\frac{dJ}{da} = T_{MAT} \tag{4.32}$$

Results

Figure 4.65a shows a comparison of the variation of crack section rotation with pressure as predicted by the model using a bilinear stress-strain curve with that calculated by FEA. A

reasonable correlation between the clamped-edge rotation by FEA and the model prediction can be obtained by assuming $E_T/E = 1/100$ and $\sigma_y/\bar{\sigma} = 0.5$. Figure 4.65b shows a similar comparison for the model using a power-law hardening stress-strain curve (Fig. 4.58). As expected, the model using power-law hardening stress-strain curve fits the FEA data better than that using the bilinear stress-strain curve. The stresses calculated by FEA are in good agreement with the elastic-plastic model (Fig. 4.66a-b) using either stress-strain curve.

Figures 4.67a-b show the calculated pressures for crack initiation versus crack angle plots for various values of the toughness parameter c, calculated using the elastic-plastic model with a bilinear stress-strain curve and a power-law hardening curve, respectively. Note that for high values of c, crack initiation pressures (Figs. 4.67a-b) predicted by the models that allow for plastic deformation away from the crack section can be significantly lower than those (Fig. 4.52) predicted by the model in which plastic deformation is confined to the crack section. In particular, the minimums in the curves predicted by the latter model (Fig. 4.52) disappear in the former models (Figs. 4.67a-b). The plasticity effects are, of course, absent at lower values of c corresponding to lower crack initiation pressures.

Because the value of c for PWRs is expected to be in the range of 0.5-1, the occurrence of plasticity away from the crack plane is not a concern in PWRs. However, laboratory leak-rate and failure tests on circumferentially cracked tubes, such as those reported by the Belgians[2] generally involve significant plastic deformation away from the crack plane. Failure curves that are based on tests that were performed on circumferentially cracked SG tubes by the Belgians are similar to those in Fig. 4.67b.

Crack opening areas for a 240° crack, calculated by the current model (Eq. 4.10c, with β_c calculated from Eq. 4.30a) and by the small-scale yielding Paris/Tada model,[13] are shown in Fig. 4.68. It is assumed that onset of crack extension does not occur before maximum pressure is reached. In Fig. 4.68, the curve labeled $L = \infty$ corresponds to the free-bending case, whereas the curve labeled $L = 0$ corresponds to the fully constrained case. Results from the Paris/Tada model, which is restricted to small-scale yielding in the crack plane and is independent of the span L, are plotted up to pressure levels significantly above the range of applicability. It is evident that lateral restraint to bending significantly reduces the COA when compared with the tube cross-sectional area, even under a design-basis accident condition ($p/p_b \approx 0.25$).

The calculated tearing-modulus-vs.-pressure plots (Figs. 4.69a-b) show a marked increase in tearing modulus with plastic yielding using either stress-strain curve. The bilinear stress-strain curve (Fig. 4.69a) results in higher values of T_{APP} for the 240° crack than those (Fig. 4.69b) calculated with power-law hardening, because the stress increases linearly with pressure in the bilinear case, whereas it remains relatively bounded in the power-law hardening case (Fig. 4.58). Figure 4.69b shows that T_{APP} increases to high values for the power-law hardening case in a tube with shorter cracks ($\leq 180°$), indicating that the driving force for crack instability, which is negligible as long as plasticity is confined to the crack plane, increases rapidly with plastic yielding away from the crack plane. This is to be expected because the loss of bending stiffness of the tube with plastic yielding produces a higher elastic follow-up, which causes the tube to behave like one with a much longer effective span. However, even with the enhanced values of T_{APP}, tubes with longer cracks ($\geq 240°$) may not fail
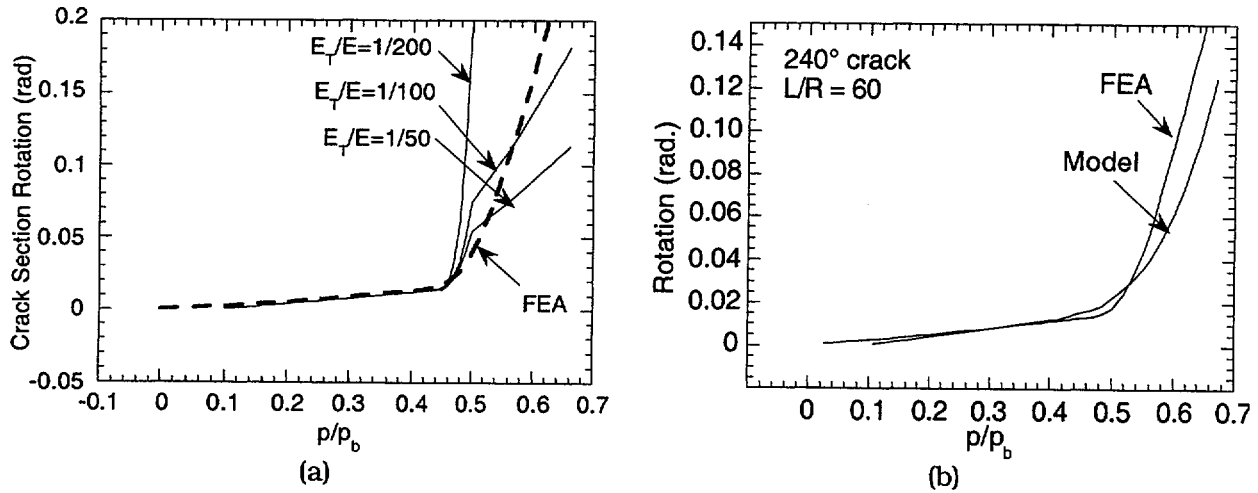
Fig. 4.65. *Variation of crack section rotation with normalized pressure as calculated by FEA ($\sigma_y / \bar{\sigma} = 0.5$) and those calculated by a model that allows for plastic yielding away from crack plane using (a) bilinear stress-strain curve and (b) power-law hardening stress-strain curve.*
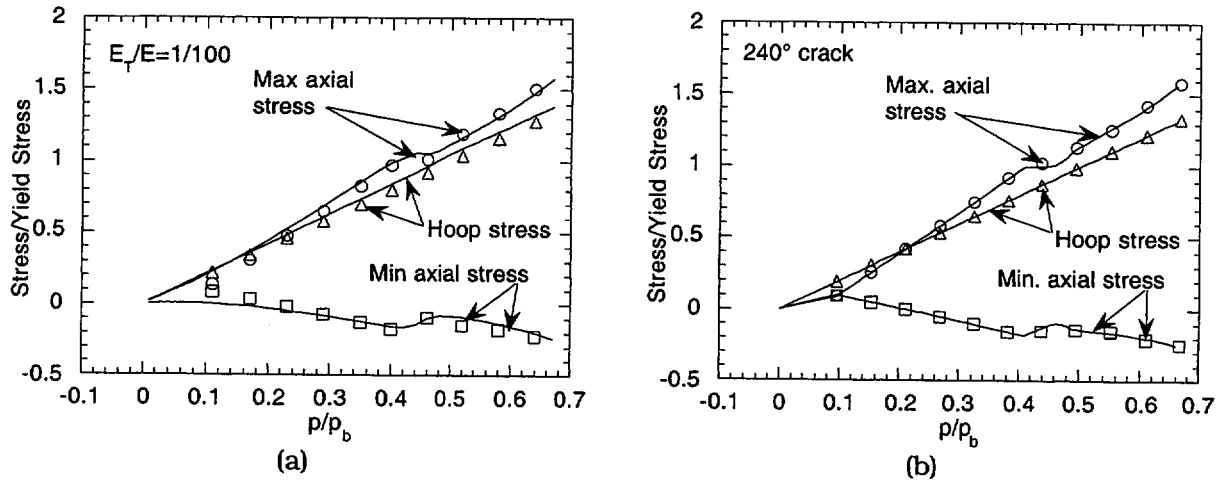
Fig. 4.66. *Model predictions for stresses, allowing for plastic deformation ($\sigma_y / \bar{\sigma} = 0.5$) away from crack plane, using (a) bilinear stress-strain curve and (b) power-law hardening stress-strain curve and elastic-plastic FEA results for stresses at section located at distance 4R from crack plane in tube (L/R = 60) simply supported at one end and clamped at the other (as in Fig. 4.49) at various pressures. Symbols, and lines without symbols, represent model calculations and FEA results, respectively.*

by unstable tearing at the onset of crack extension (T_{MAT} for ductile alloys like Alloy 600 is typically ≈200) and will very likely fail by plastic collapse after some stable crack growth. Because, for values of c that are typical for SG tubes (0.5–1), the pressure for onset of crack extension (Fig. 4.67a-b) is already close to the pressure that corresponds to the fully constrained case, the extent of stable crack growth should be small.

115
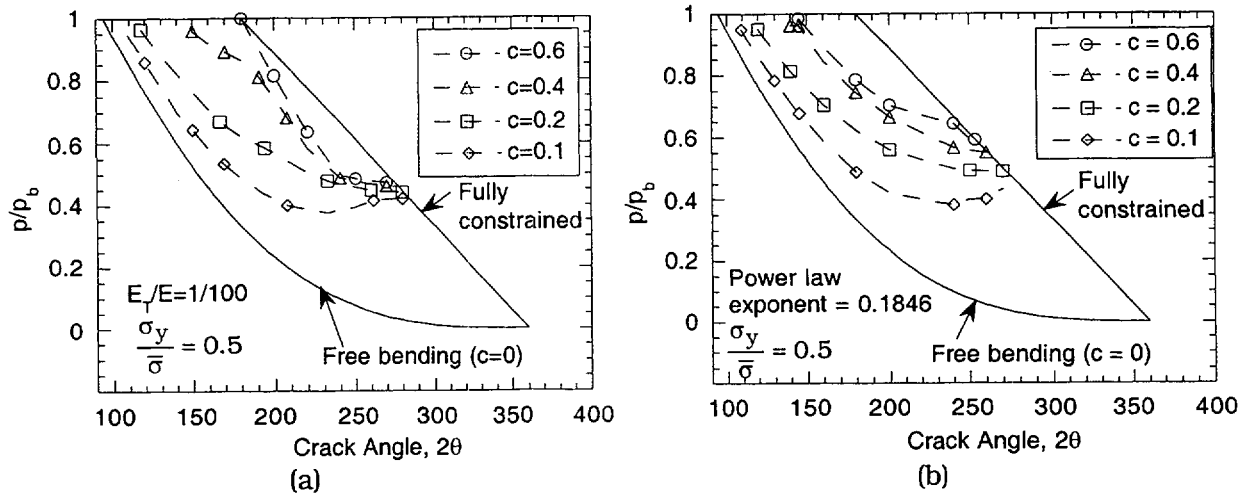
Fig. 4.67. *Calculated variation of pressure, normalized by unflawed burst pressure, with crack angle for onset of crack growth in tube with single TW circumferential crack, using elastic-plastic model with (a) bilinear stress-strain curve and (b) power-law hardening stress-strain curve.*
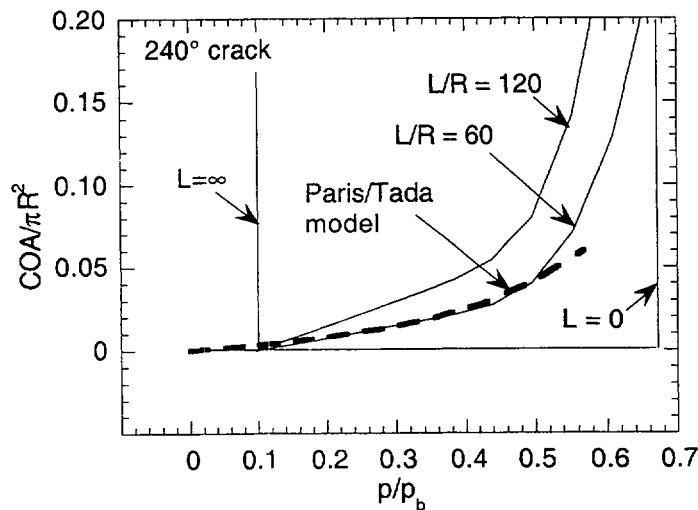
Fig. 4.68. *Normalized crack opening area vs. pressure plots calculated by Paris/Tada model (dashed line) and by current model (solid lines) for $L/R = 0$ (fully constrained), 60, 120, and infinitely (free-bending) long simply supported clamped tube with 240° crack at clamped edge.*

Conclusions

An approximate model is presented for calculating crack opening area and failure pressure of laterally supported SG tubes with a TW circumferential crack at a clamped edge. The results show that the critical crack tip opening displacement, as well as the span and the boundary conditions, are important determining factors for the pressure at onset of crack extension. For typical mechanical properties and spans that are expected in PWR SGs, tubes with TW cracks behave as if fully constrained against rotation, and plastic deformation is confined to the section containing the crack. Crack opening areas during normal operation and design-basis

116
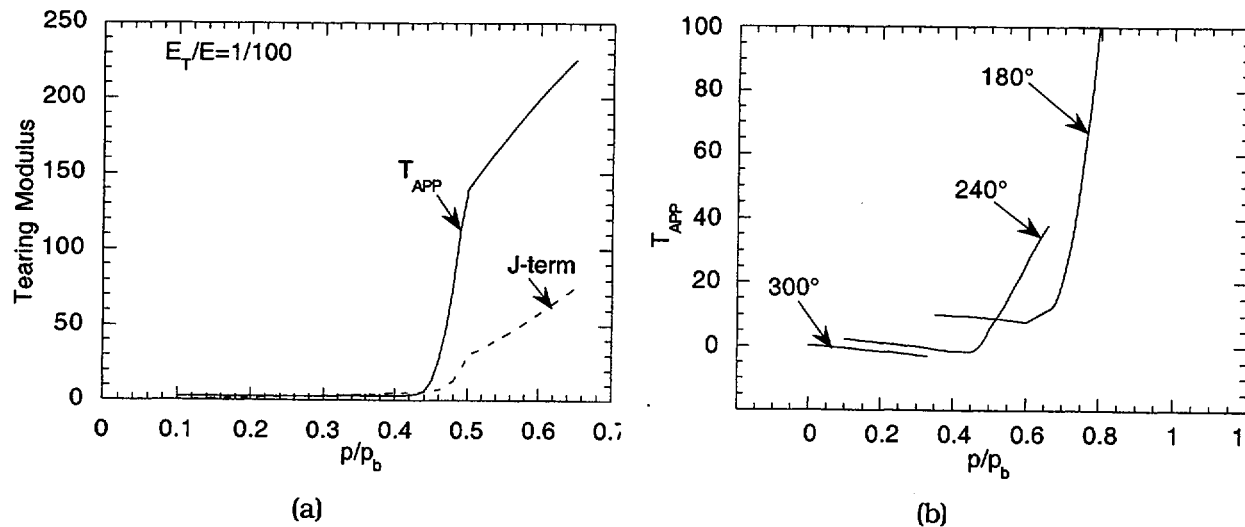
Fig. 4.69. Calculated variation of applied tearing modulus with pressure, normalized by unflawed burst pressure, for single TW circumferential crack in a tube, using elastic-plastic model with (a) bilinear stress-strain curve for 240° crack and (b) power-law hardening stress-strain curve for 180°, 240°, and 300° cracks.

accidents are small when compared with the tube cross-sectional area for a SG tube with ≤240° TW crack at the top of the tube sheet.

A model that allows for plastic deformation away from the crack plane is also proposed. The plasticity constitutive law is assumed to be either a bilinear stress-strain curve or a power-law hardening stress-strain curve. Comparison with finite element analysis shows that the FEA results are closer to those predicted by the power-law hardening model than those by the bilinear model, as would be expected. The predicted shapes of the crack initiation pressure versus crack angle plots by the power-law hardening model are smoother than those predicted by the bilinear model. The minima in the curves predicted by the earlier model, which assumes that plasticity is confined to the crack section, disappear in both elastic-plastic models that allow for plasticity away from the crack section, and the curves are similar to the experimental curves obtained by the Belgians.

Although plasticity is confined to the crack section for normal operating and design-basis accident conditions of PWRs, significant plastic deformation usually occurs away from the crack section in leak-rate and failure tests of SG tubes in the laboratory. The simplified model, which can account for plastic deformation away from the crack plane, predicts failure pressure curves that are similar to curves derived from test data. The model also predicts a significant increase in the applied tearing modulus with the onset of plastic deformation away from the crack plane; however, failure by unstable tearing is more likely with short cracks (<180°) than with long cracks.

For typical SG tubes (span ≈ 0.6-1.2 m [24-48 in.]) with δ_c >0.76 mm (0.03 in.) (K_{JC} >220 MPa·m$^{1/2}$ [200 ksi·in.$^{1/2}$]) and containing a circumferential TW crack at the top of tube sheet, any crack of ≤180° does not reduce the failure pressure from the burst pressure of an unflawed tube. Also, tubes with TW cracks of ≥240° will behave as if they were fully constrained against bending and will have significantly greater failure pressures than the same

117

tubes under free bending condition. Thus, for typical mechanical properties of SG tubes, the longest TW circumferential cracks at the top of tube sheet that are predicted to experience onset of crack initiation during normal operation and design basis accident conditions are 310° and 340°, respectively. A further conservative factor in the current model is the assumption that the tubes are free to expand or contract in the axial direction at the tube support plates. If, as experience with real SGs suggests, the tubes are locked in at the tube support plates and require several thousands of pounds of axial loads to pull them free during removal from service, the axial tensile force due to internal pressure must first overcome this lock-in force before the circumferential cracks see any driving force for crack initiation and growth.

4.5 Posttest Analysis of Tests

All pressure and leak-rate tests conducted to date on specimens with laboratory-grown SCC cracks have been analyzed with available models for ligament rupture and leak rate. Failure pressures, leak rates, etc., depend on the mechanical properties (primarily flow stress) of the tubing. The minimum ASME code requirements for yield and ultimate tensile strengths of Alloy 600 SG tube are 240 and 550 MPa (35 and 80 ksi), respectively, which corresponds to a minimum flow stress of 400 MPa (58 ksi). Some older SGs may have tubes with properties close to the code minimum. The actual flow stress of SG tubes in most current plants can vary widely depending on the age and heat of material used. Yield strength can range from 280 to 410 MPa (40 ksi to 60 ksi), while the ultimate tensile strength can range from 620 to 760 MPa (90 to 110 ksi), which potentially cover a range of flow stress of 450 to 590 MPa (65 to 85 ksi). The yield and ultimate tensile strengths of our as-received tubing are 296 and 676 MPa (43 and 98 ksi), respectively, right in the middle of the ranges reported above. However, because of the annealing and sensitizing heat treatments given to our tubes with laboratory-grown SCC cracks, their yield and ultimate tensile strengths are estimated to be reduced to 179 and 607 MPa (26 and 88 ksi), respectively. Thus, although the yield strength of our heat-treated tubing falls below the code minimum, the ultimate tensile strength is sufficiently above the code minimum to give a flow stress that is close to the code minimum. In order to compare results from one material with results from a different material, the effect of variations in the mechanical properties must be accounted for, i.e., the results must be normalized in terms of the flow stress. Analyses of the pressure and leak-rate tests have been used to develop procedures for accounting for flow stress effects. In addition, these analyses shed some light on the mechanisms of failure during the pressure tests.

In the case of the heat-treated tubing used in our tests, the heat treatment reduces the room-temperature flow stress of the as-received tubing by ≈20%. Using the procedures that have been developed, data generated on annealed and sensitized material can be interpreted in terms of the behavior of the as-received material. The same procedures would be used to convert the present data to predict the behavior of tubing with a different yield strength.

4.5.1 Leak-Rate Tests on Notched Specimens

Leak-rate tests on 22.2-mm (7/8-in.)-diameter Alloy 600 tubes containing 12.7- and 25.4-mm (0.5- and 1.0-in.)-long TW axial EDM notches have been conducted on both as-received and heat-treated materials. The heat treatment, which is used to accelerate production of stress corrosion cracks in the laboratory, involves a solution treatment at 1100°C followed by a sensitizing treatment at 700°C, which reduces the yield strength of the tube from

296 to 179 MPa (43 to 26 ksi). Such a reduction in yield strength will have a significant influence on the crack opening area and, hence, on the leak rate. Therefore, we first investigate the predictive capability of the standard leak-rate equation for the leak-rate tests conducted on as-received and heat-treated specimens with EDM notches.

The formula used to calculate the volumetric leak-rate Q is as follows:

$$Q = 0.6A\sqrt{\frac{2\Delta p}{\rho}}, \tag{4.33a}$$

or, using English units,

$$Q = 180.2A\sqrt{\frac{\Delta p}{\rho}}, \tag{4.33b}$$

where A is the flaw opening area in in.^{2}, Δp is the pressure differential across the tube wall in psi, and ρ is the density (62.27 lb/ft^3 at RT and 45.9 lb/ft^3 at 288°C). In contrast to that of a circular hole, whose area remains relatively constant under increasing pressure, the area of a crack or notch increases with pressure and must be taken into account for calculating the leak rate. Crack opening areas were calculated by the Zahoor model,[14] which is described below.

Zahoor Model for Crack Opening Area

The crack opening area by the Zahoor model[14] for an axial TW crack in a thin-walled tube is given by

$$A = 2\pi c_e^2 V_o \sigma / E, \tag{4.34}$$

where

σ = hoop stress = pR/h,

p is the differential pressure across the tube wall,

E is the Young's modulus, R and h are the mean radius and thickness of tube,

$V_o = 1 + 0.64935\lambda_e^2 - 8.9683 \times 10^{-3}\lambda_e^4 + 1.33873 \times 10^{-4}\lambda_e^6$,

$\lambda_e^2 = c_e^2 / Rh$,

$c_e = c\left[1 + \frac{F}{2}\left(\frac{\sigma}{S_y}\right)^2\right]$,

$F = 1 + 1.2987\lambda^2 - 2.6905 \times 10^{-2}\lambda^4 + 5.3549 \times 10^{-4}\lambda^6$,

$\lambda^2 = c^2 / Rh$, and

S_y is the yield strength and c is the crack half-length.

The flaw opening area for an EDM notch was obtained by adding the initial flaw area (equal to flaw length multiplied by flaw width) to the crack opening area given by Eq. 4.34. Crack opening areas calculated by Eq. 4.34 were found to agree well with FEA results (Fig. 4.70).

Calculated and observed leak rates at room temperature for a 12.7-mm (0.5-in.)-long EDM notch in as-received and heat-treated tubes are shown in Fig. 4.71a. Note that the curves for as-received and heat-treated tubes diverge as the pressure is increased beyond 6.9 MPa (1000 psi). At 17.2 MPa (2500 psi), the leak rate in a heat-treated material is greater by a factor of 3 than that in the as-received tube. The predicted leak rates are reasonably close to the observed leak rates for both tubes.

A similar plot for an as-received tube with a 25.4-mm (1-in.)-long EDM notch is shown in Fig. 4.71b. This test specimen was depressurized after a pressure of 13.8 MPa (2000 psi) was attained. Subsequently, it was repressurized and tested to failure. The measured crack opening areas were used to calculate the leak rates, which agree remarkably well with the observed leak rates (Fig. 4.71b). A similar plot for a 0.25 in. flaw in an as received tube is shown in Fig. 4.72a. The predicted leak rates are reasonably close to the observed leak rates for all tubes. Thus, Eq. 4.33b appears to predict the leak rates through EDM notches at room temperature very well.

A leak-rate test at 288°C on an as-received tube with a 12.7-mm (0.5-in.)-long EDM notch has also been conducted. Because high-temperature tensile data are not available for the 22.2–mm (7/8-in.)-diameter tubing, the yield strength at 288°C needed for calculations was obtained from tensile data on 12.7-mm (0.5-in.)-diameter bar stock as reported by INEEL.[15] The calculated leak rate is reasonably close to the measured value, as shown in Fig. 4.72b.

Thus, the standard smooth-edge-orifice leak rate equation (Eqs. 4.33a-b) appears to predict the leak rates through EDM notches at room temperature and 282°C very well. The difference in leak rate between room temperature and 282°C can be accounted for by the difference in the density of water. Also, reasonable correlation between the Zahoor model predictions and the measured leak rates indicate that the crack opening areas are reasonably estimated by Eq. 4.34. Whether the same set of equations can predict leak rates through tight and nonplanar stress corrosion cracks remains to be seen.

4.5.2 Calibration Curves to Correct for Flow Stress

All pressure and leak-rate tests on laboratory-grown stress corrosion cracks at ANL have been and will continue to be conducted on Alloy 600 tubes subjected to prior annealing and sensitizing heat treatments. The yield and flow stresses of these heat-treated tubes are considerably lower than those of the as-received tubes. To convert the failure pressure and leak-rate data from the heat-treated tubes to the as-received tubes, we must multiply the measured failure pressure and divide the leak-rate data on heat-treated tubes by appropriate correction factors (>1).
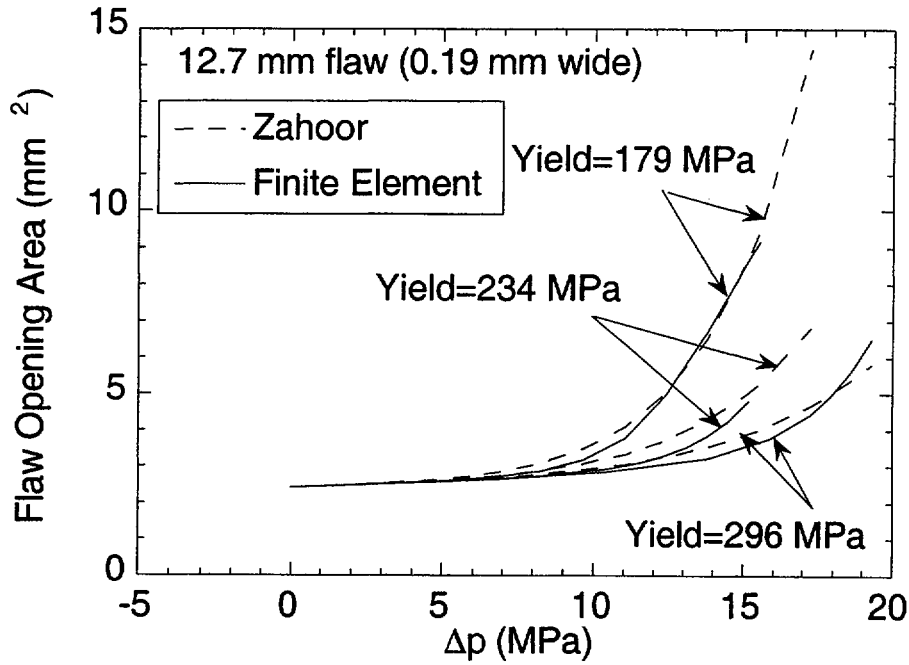
Fig. 4.70. Predicted crack opening area (by FEA and Zahoor model) of 12.7-mm (0.5-in.)-long TW crack (laboratory-grown) in heat-treated tube as functions of pressure.

(a)

(b)
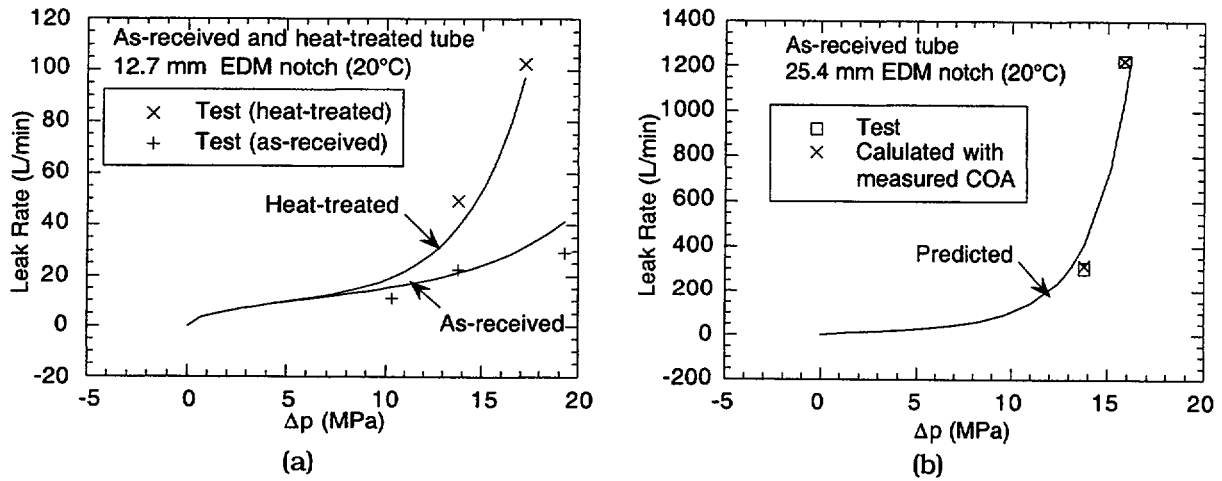
Fig. 4.71. Calculated (solid line) vs. experimentally measured (symbols) leak rates at 20°C for as-received and heat-treated 22.2-mm (7/8-in.)-diameter tubes with (a) 12.7–mm (0.5-in.) and (b) 25.4-mm (1-in.)-long TW axial EDM notches. Cross symbols in Fig. 4.71b denote calculated leak rates using posttest measured crack opening areas.

121
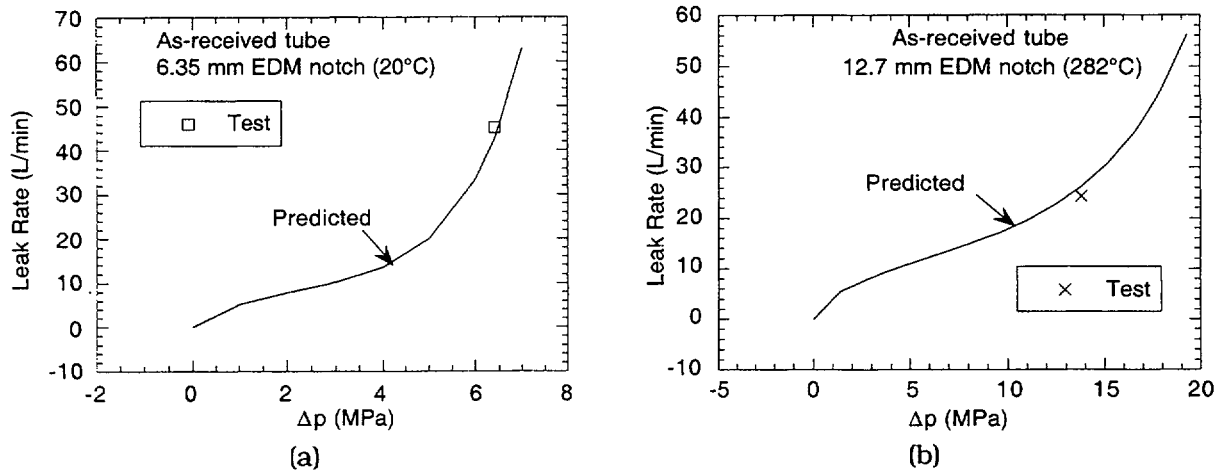
Fig. 4.72. *Comparison of calculated (solid line) versus experimentally measured (symbol) leak rates in as-received 22-mm (7/8-in.)-diameter tubes with (a) 6.35-mm (0.25–in.)-long flaw at 20°C and (b)12.7-mm (0.5-in.)-long flaw at 282°C.*

Correction factor for ligament rupture and tube burst pressures

The room-temperature flow stress of our as-received Alloy 600 tube is estimated to be about 20% greater than that of the sensitized tube. Thus, a correction factor of 1.2 should be applied to either the ligament failure pressure or unstable burst pressure of the heat-treated tube to obtain that of the as-received 22.2-mm (7/8-in.)-diameter tube. Until flow stress data at high temperature are available, the same correction factor should also be applied at 282°C.

Correction factor for leak rate

The correction factor for accounting for the effect of changes in mechanical properties on leak rate is more complex, because it depends on pressure, temperature, and crack area or length. It also depends on whether the flaw is initially a tight SCC crack or a 0.19-mm (0.0075-in.)-wide EDM notch.

To derive the leak-rate correction factors, we used the Zahoor model (Eq. 4.34) to calculate the flaw opening area and Eq. 4.33b to calculate the volumetric leak rate through EDM flaws. The effect of the material flow properties on leak rate enters through their effect on the flaw opening area A.

Variations of the leak-rate correction factor with pressure, flaw length, and temperature are given in Fig. 4.73a for tight SCC cracks and in Fig. 4.73b for 0.19-mm (0.0075-in.)-wide EDM notches. These curves are based on room-temperature yield strengths of 296 and 179 MPa (43 and 26 ksi) for the as-received and heat-treated tubes, respectively. The yield strengths are assumed to be reduced by 10% at 282°C. Note that the leak-rate correction factors for notches are generally lower than those for cracks. Also, the longer the crack (or notch), the higher the correction factor.

122

4.5.3 Leak-Rate Tests on Specimens with Laboratory-Grown SCC Cracks

The leak-rate tests on laboratory-grown SCC cracks were described in the 1998 Annual Report.[15] In this annual report, we present analyses conducted for these tests.

Estimation of TW crack length from leak-rate data

To apply the leak-rate correction factors (Fig. 4.73a) to a laboratory grown SCC crack, we must first establish an effective length for the TW segment of the crack after ligament rupture and verify that ligaments separating the axial segments are ruptured so that in effect we have a single TW crack. This creates an uncertainty for an initially part-TW laboratory grown SCC crack, because the geometry of the crack, such as the lengths of the TW segments of the crack after ligament rupture and whether the ligaments between the axial segments survive the test, cannot be reliably estimated from the pre-test EC +Point data.

There are several ways to obtain the effective TW crack length. Together with visual observation of the crack morphology at the OD surface, these lengths should be compared with each other to check for consistency.

1. The most rigorous but laborious and time-consuming way to obtain the length of the TW segment of the crack is by posttest sectioning of the specimen.

2. A far less laborious but nonetheless useful approach is to pressurize the ruptured tube with gas while the tube is submerged in water and estimate the crack length from the length of the emerging bubble zone.

3. We can calculate analytically an effective TW crack length from the measured leak rate by using Eq. 4.33b and the Zahoor model for calculating the crack opening area (Eq. 4.34), assuming that even if the crack was initially segmented axially, all the ligaments between the segments are ruptured before the leak-rate data are taken.

4. Finally, we can use the pretest crack morphology as measured by EC +Point method, together with the ANL correlation for ligament rupture pressure, to calculate the crack length, assuming that even if the crack was axially segmented initially, all ligaments between the segments are ruptured before rupture of the through-thickness crack tip ligament.

Estimation of TW crack length by ligament rupture model

Ideally, we can use the ANL correlation for ligament rupture pressure of part-TW rectangular cracks to estimate the length of the TW segments of the cracks after crack-tip ligament rupture. However, laboratory-grown SCC cracks are irregular in shape and have variable depth along their length. Instead of being a single planar crack, they are composed of a family of crack segments in different planes. Local variations in crack depth and geometry are smoothed out in the EC measurements because the EC signals are necessarily averaged over a finite volume, and hence the EC data tend to show a relatively smooth variation of crack depth along the crack length. This is evidenced by the fact that although all the SCC

123
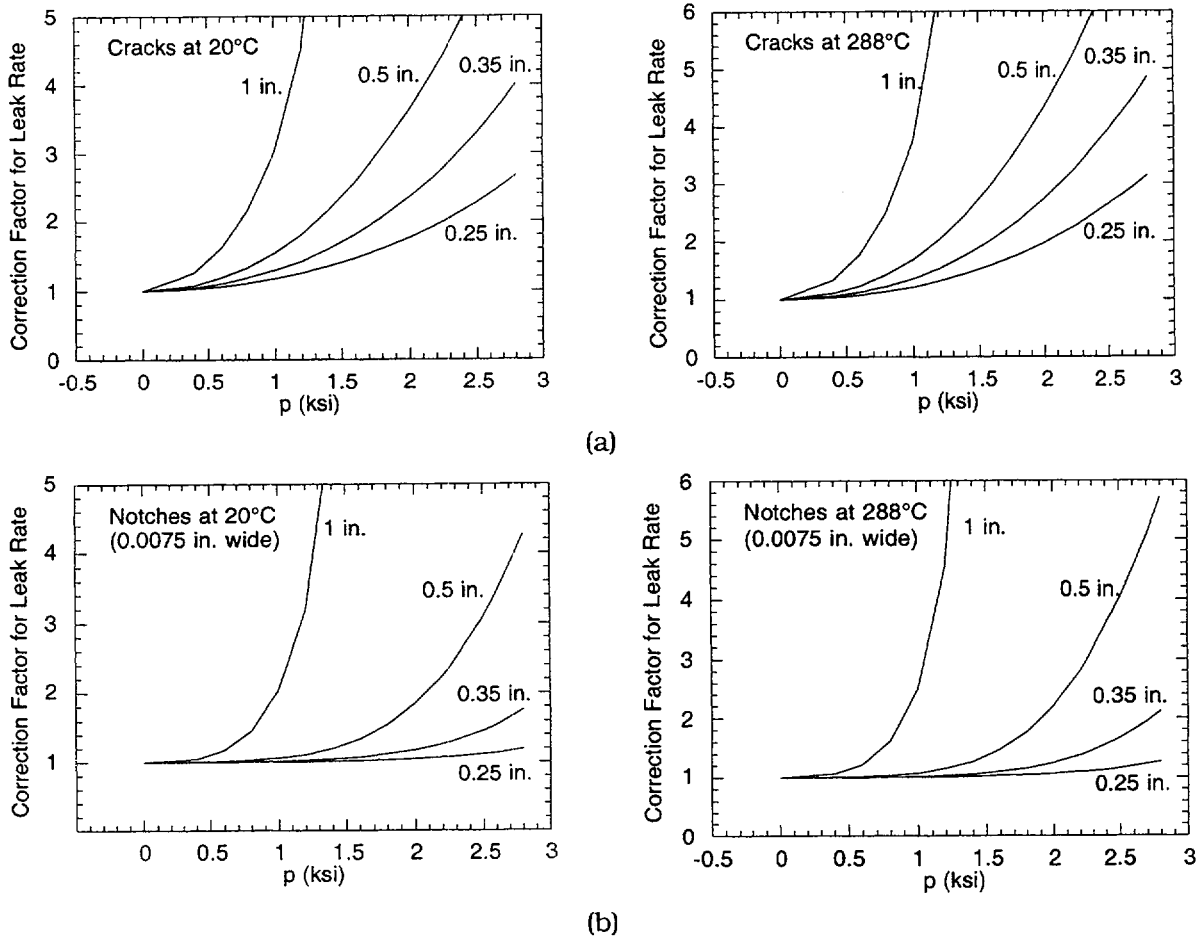
Fig. 4.73. *Correction factors for obtaining leak rates in as-received Alloy 600 tubes from sensitized tube data at 20°C and 288°C for tubes containing (a) single TW axial cracks without axial segments and (b) initially 0.19-mm (0.0075-in.)-wide rectangular TW axial notches.*

specimens tested to date (including a "doped-steam" cracked specimen supplied by Westinghouse) have shown leakage under low gas pressure before test, the EC +Point method has failed to detect or identify the locations of these TW segments. However, no leakage of water was detected through these cracks until much higher pressures were applied.

Currently, no widely accepted models are available for predicting the ligament failure pressure of cracks with such complex geometries. From a limit analysis viewpoint, it can be argued that the collapse behavior of a crack tip ligament with an irregular point-by-point variation of crack depth should be similar to that of a crack with a smoothed-out "average" crack depth profile. For the present, we assume that the average profile measured by the EC +Point method is the one that is relevant for limit analysis. With this assumption, although the real crack may have short TW segments at a number of locations, from the viewpoint of plastic collapse of the ligament, the tube behaves as if it has a smoothly varying average ligament thickness (or crack depth) profile.

Because the measured crack depth profile by EC +Point is generally not rectangular (e.g., see Fig. 4.74a), the following procedure was used to establish the length and depth of an equivalent rectangular crack:[*]

1. Choose a crack depth d_0 and assume that any crack segment with depth $d < d_0$ does not adversely affect the crack tip ligament rupture pressure of the tube. In other words, replace the original crack depth profile with a new crack depth profile in which any crack segment with depth $d < d_0$ is replaced by $d = 0$. The choice of d_0 determines the length of an equivalent rectangular crack.

2. The depth of the equivalent rectangular crack is determined by equating its area to the area under the newly defined crack depth profile in step 1. For example, in Fig. 4.74a, the choice of $d_0 = 70\%$ fixes the length and depth of the equivalent rectangular crack at 10 mm (0.4 in.) and 85%, respectively.

3. Generate a series of candidate equivalent rectangular cracks by parametrically varying d_0, use the ANL correlation for calculating the ligament rupture pressures for all the candidates, and select the one that gives the lowest ligament rupture pressure as the applicable equivalent rectangular crack. Generally, a couple of trials for d_0 were sufficient for cracks with relatively uniform ligament thickness as in specimen SGL-104 (Fig. 4.74a). The length of the equivalent crack was used as an estimate for the length of the TW segment of the crack after ligament rupture. Determination of the equivalent crack size can be automated by a computer code.

Estimation of TW crack lengths for laboratory-grown SCC cracks

The procedure for estimating TW crack length is illustrated here by using the tests conducted at ANL to date. A summary of all TW crack lengths estimated by the different methods is included in Table 4.5. Figures 4.74a-c show the crack depth profile (by EC +Point) for specimen SGL-104, the calculated ligament rupture pressures corresponding to three equivalent rectangular cracks, and calculated leak rates for various crack lengths at pressures for which experimental leak rates (at 282°C) were measured, respectively. The ligament rupture model (Fig. 4.74b) predicts a failure pressure of 18.0 MPa (2610 psi), compared with experimentally measured 16.2 MPa (2350 psi), for an equivalent crack length of 10 mm (0.40 in.). The leak-rate model (Fig. 4.74c) predicts the effective TW crack length to be between 0.38 in. (9.6 mm) and 0.39 in. (9.9 mm) from the measured leak rates of 6.2 and 5.6 gpm at 2500 (17.2 MPa) and 2350 psi (16.2 MPa), respectively. The leak rate in this test did not increase during a 15 min constant-pressure hold at 17.2 MPa (2500 psi). It should be noted that a >24-h hold at constant pressure and room temperature did not increase the leak rate through a rectangular EDM slot. A posttest view of the crack at the OD surface is shown in Fig. 4.75, which also includes a marker identifying the estimated TW crack length. A comparison with Fig. 4.74a indicates that the estimated crack length corresponds to the crack length over which the depth equals or exceeds about 70% of the wall thickness. Note that the estimated TW crack length is significantly shorter than the OD surface crack length of 16 mm (0.63 in.).

---

[*]Similar equivalent rectangular crack approaches have been used by others, e.g., see Report by Aptech Engineering Services, Inc. in Docket No. 50-361, Steam Generator Run Time Analysis for Cycle 9, San Onofre Nuclear Generating Station, Unit 2, September 25, 1997.
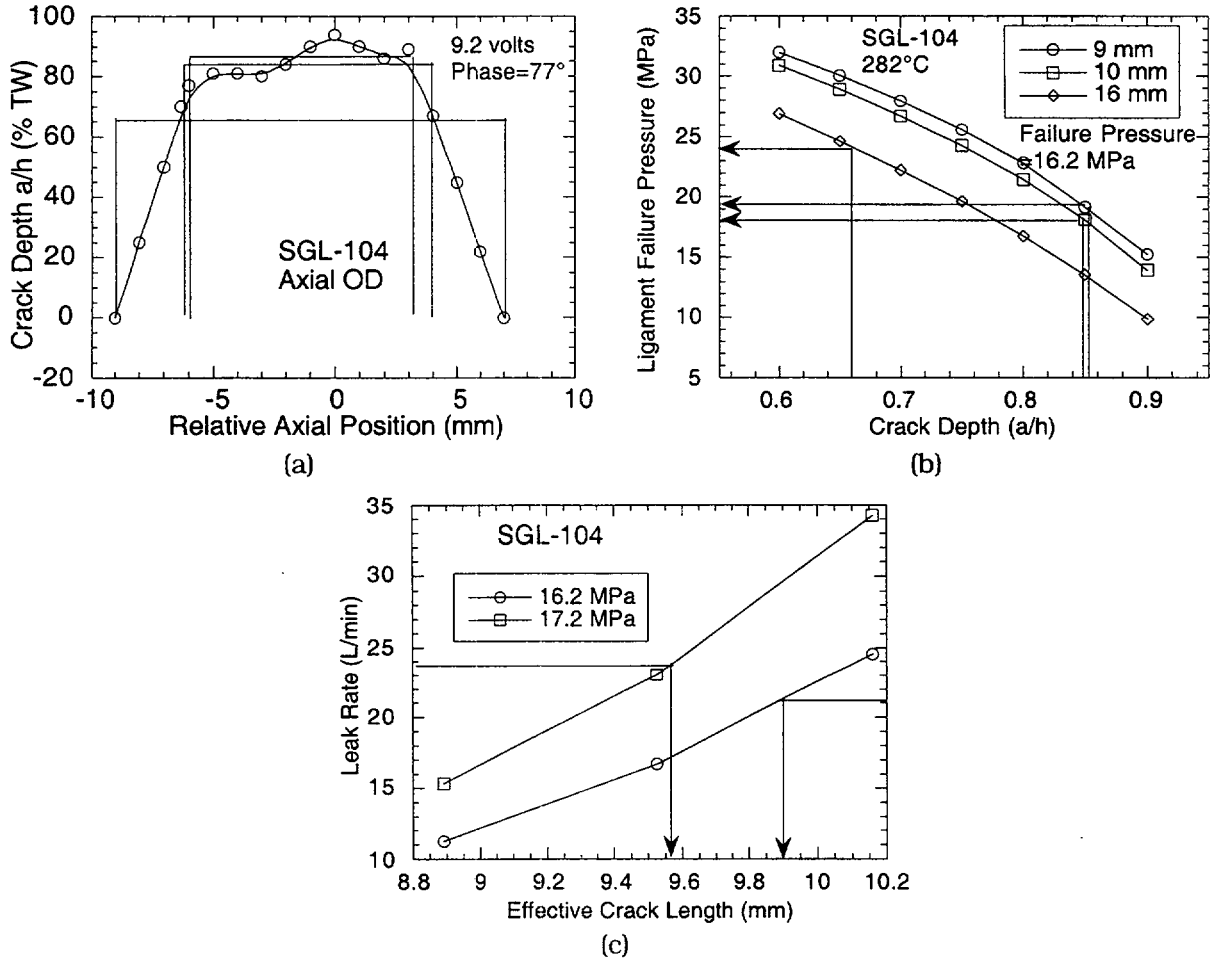
Fig. 4.74. (a) Estimated crack depth profile from EC +Point data, (b) calculated ligament failure pressures for two equivalent rectangular crack sizes, and (c) effective TW crack length estimated from leak-rate data for test SGL-104 conducted at 288°C.

Figures 4.76a-c show similar plots for test SGL-195, which was conducted at room temperature. The ligament rupture model predicts a failure pressure of 16.5 MPa (2390 psi) for an equivalent crack length of 12.3 mm (0.48 in.). In this test, the leak rate was <0.04 L/min (<0.01 gpm) at 14.7 MPa (2129 psi), suggesting a TW crack length of <2 mm (<0.08 in.). The leak rate abruptly increased to 29.9 L/min (7.9 gpm) at 15.1 MPa (2188 psi) and then to 32.6 L/min (8.6 gpm) at 15.5 MPa (2250 psi). Estimated TW crack length corresponding to the largest leak rate is 12 mm (0.47 in.). The leak rate did not increase during a 15-min hold at 15.5 MPa (2250 psi). A posttest view of the crack at the OD surface is shown in Fig. 4.77, which also includes a marker identifying the estimated TW crack length. A comparison with Fig. 4.76a shows that the estimated crack length corresponds to the crack length over which the depth equals or exceeds about 70% of the wall thickness.

Figures 4.78a-c show similar plots for test SGL-177, which was also conducted at room temperature. Note that in contrast to the previous cases, the ligament thickness in this specimen was highly nonuniform (Fig. 4.78a). The ligament rupture model (Fig. 4.78b) predicts

Test No.	Pressure (MPa) Ligament rupture	Max. Test	Max. Leak Rate (L/min)	Estimated Final Throughwall Crack Length (mm) by Sectioning	Submerged Bubble	Leak Rate model	Lig. Rupture Model	Calc. Lig. Rupture Pressure (MPa)
SGL-104[a]	16.2	17.2	23.6	-	-	9.9	9.9	18.0
SGL-195[b]	15	15.5	32.7	-	-	11.9	12.2	16.5
SGL-177[b,c]	16.9	19.3	1.7	-	4.8	5.3	8.9	30.0
SGL-219[a,c]	13.3	16.2	39.0	-	-	10.9	10.4	20.0
W 2-10[c,d]	16.9	18.6	0.7	-	-	4.8	10.9	20.0

[a] Conducted at 282°C (540°F).

[b] Conducted at 20°C (68°F).

[c] Test showed evidence of time-dependent ligament rupture

[d] Test was initially conducted at 20°C (68°F) and later repressurized at 282°C (540°F).
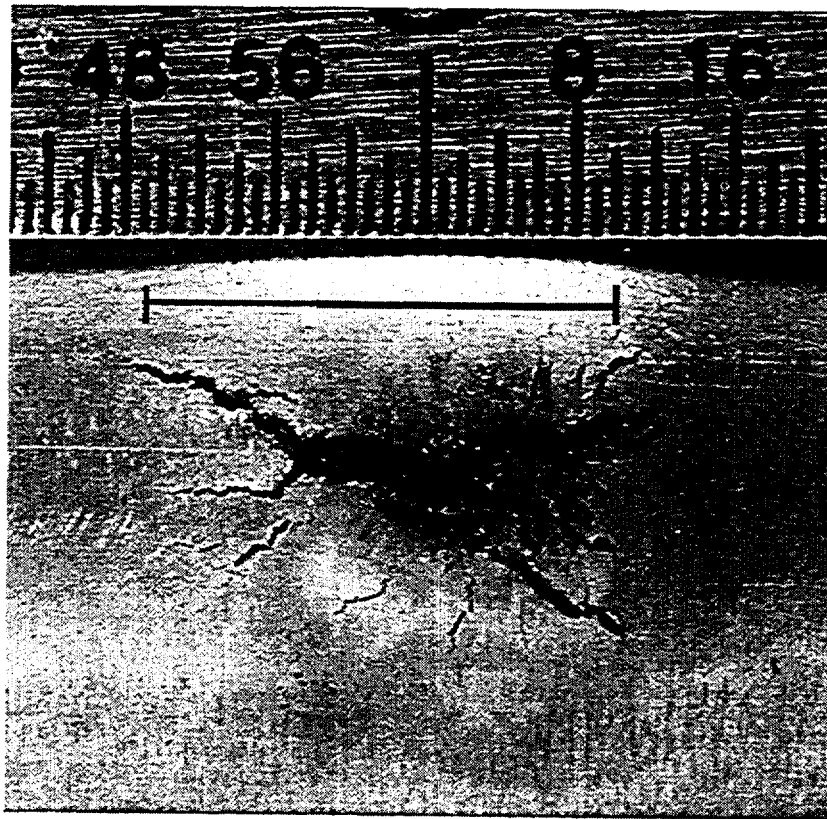
Fig. 4.75. Posttest view of OD crack of specimen SGL-104. Marker indicates effective TW crack length (10 mm or 0.39 in.) calculated from measured leak rate.

(a)

8.4 V

Crack Depth a/h (%TW)

Relative Axial Position (mm)

(b)

Failure Pressure=15.1 MPa
Crack Length=12.3 mm

Ligament Failure Pressure (MPa)

SGL-195

a/h

(c)

SGL-195

Leak Rate (gpm)

2129 psi
2250 psi

Effective Crack Length (mm)
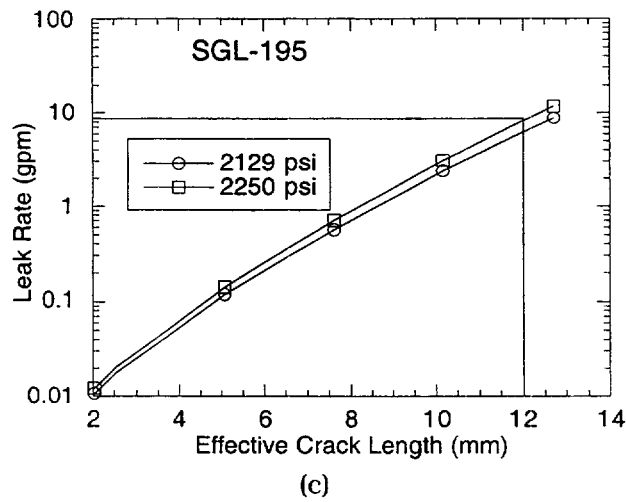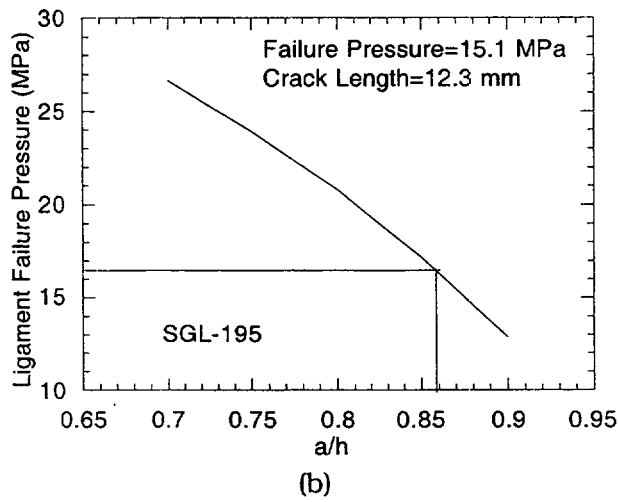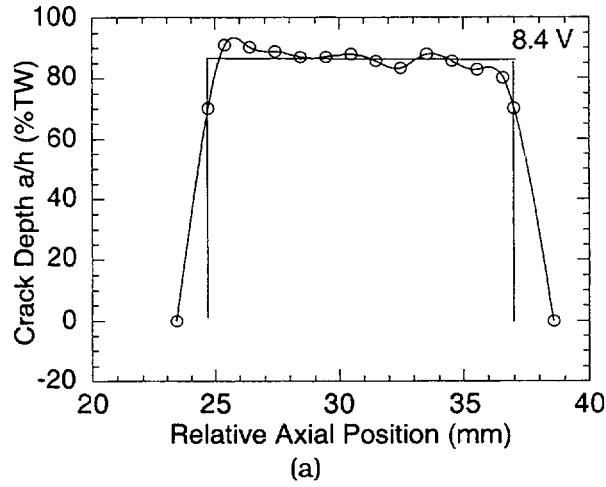
Fig. 4.76.
(a) Estimated crack depth profile from EC +Point data, (b) calculated ligament failure pressure for equivalent rectangular crack, and (c) effective TW crack length estimated from leak-rate data for test SGL-195 conducted at 20°C.

Fig. 4.77. Post-test view of OD crack of specimen SGL-195. Marker indicates effective TW crack length (12 mm or 0.47 in.) calculated from measured leak rate.

a failure pressure of 30 MPa (4350 psi) for an equivalent crack length of 9 mm (0.35 in.). The predicted failure pressure is significantly greater than the experimentally observed 16.9 MPa (2450 psi).

However, the leak rate in this test was essentially zero for the first 100-min hold at 16.9 MPa (2450 psi), after which a leak rate of 0.04 L/min (0.01 gpm) was detected. The leak rate abruptly increased from 0.04 to 0.26 L/min (0.01 to 0.07 gpm) after a further 60-min hold at the same pressure. The leak-rate model (Fig. 4.78c) implies that the TW crack length increased abruptly from 1.5 mm (0.06 in.) to 3.7 mm (0.15 in.). The leak rate increased to 1.7 L/min (0.44 gpm) when the pressure was increased to 19.3 MPa (2800 psi), suggesting that the TW crack length increased to 5.5 mm (0.22 in.), which again corresponds (Fig. 4.78a) approximately to the length over which the crack depth exceeds 70% wall thickness. A posttest picture of the crack (Fig. 4.79a) that also includes a marker of length 5.5 mm (0.22 in.). A comparison of the posttest crack (Fig. 4.79a) with its pretest dye-penetrant-enhanced view (Fig. 4.79b) shows that although some secondary cracks opened up, the surface length of the main crack did not increase during the test. This specimen was internally pressurized under water with 280 kPa (40 psi) air after the test. From the emerging air bubble, it was estimated
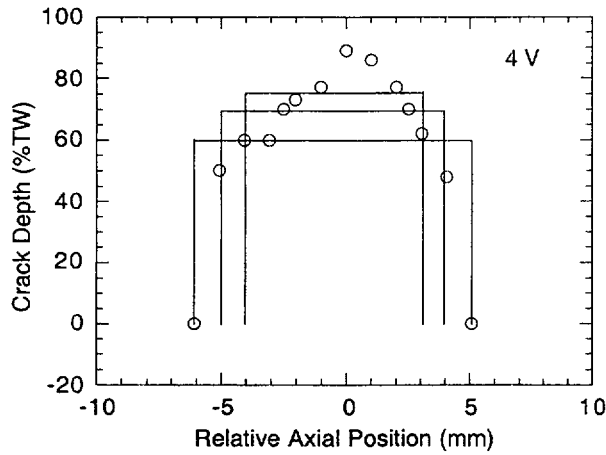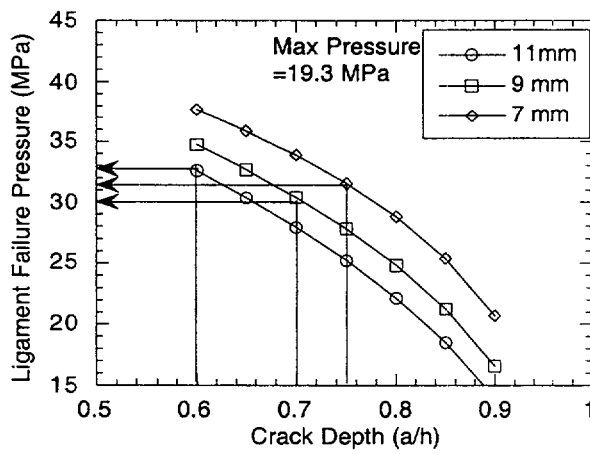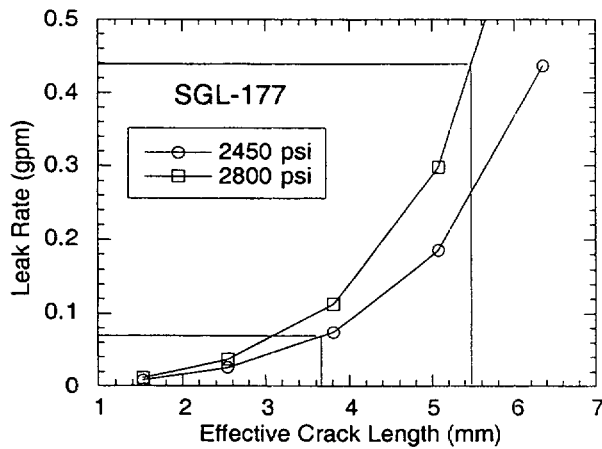
Fig. 4.78.
(a) Estimated crack depth profile from EC +Point data, (b) calculated ligament failure pressure for two equivalent rectangular cracks and (c) effective TW crack length estimated from leak-rate data for test SGL-177 conducted at 20°C.
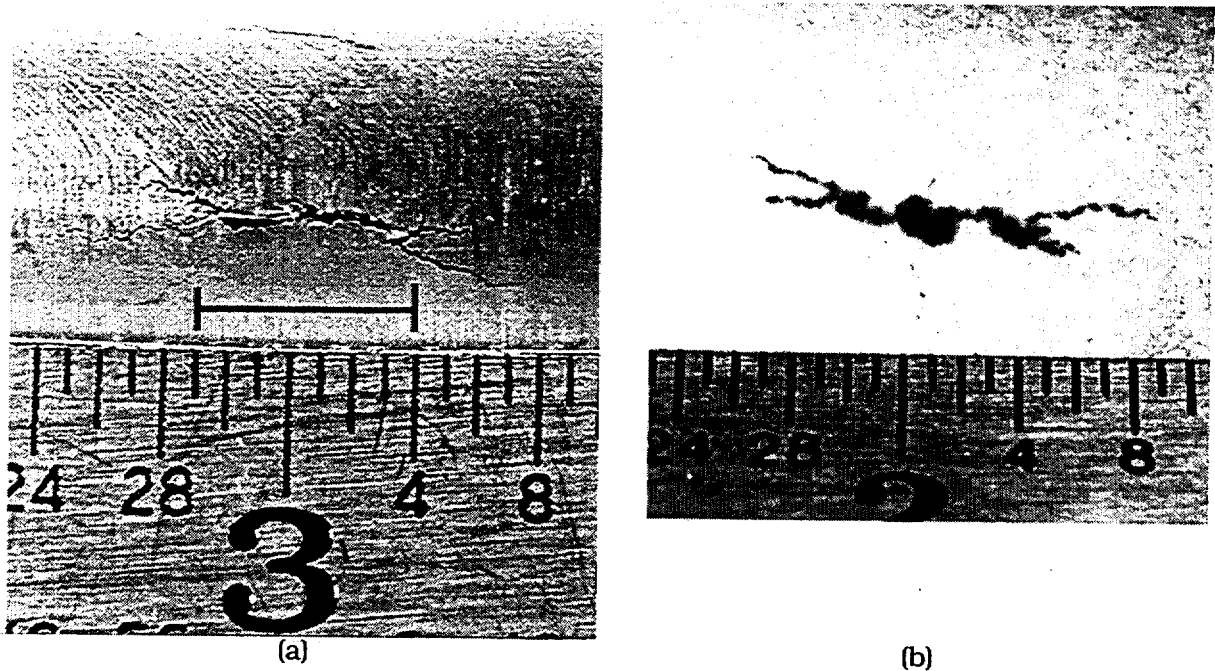
Fig. 4.79. (a) Post- and (b) pretest dye-penetrant-enhanced views of crack in test specimen SGL-177. Marker in (a) indicates effective TW crack length (5.5 mm or 0.22 in.) calculated from measured leak rate.

that the length of the TW segment of the crack was ≈4 to 4.8 mm (0.16 to 0.19 in.). In view of the additional crack opening due to pressurization, the measured length of the TW segment of the crack is reasonably close to that calculated from the measured leak rate. Two questions that remain unresolved from this test are (a) how long the leak rate would have continued to increase in a time-dependent fashion if the pressure were held constant at 19.3 MPa (2800 psi) indefinitely, and (b) whether the full ligament would have ruptured if the pressure, instead of being held constant, were rapidly increased to the calculated ligament rupture pressure.

Figures 4.80a-c show similar plots for test SGL-219, which was conducted at 282°C. Like test SGL-177, this specimen also had a highly nonuniform ligament thickness and may even have been segmented (Fig. 4.80a). The ligament rupture model (Fig. 4.80b) predicts a failure pressure of 20 MPa (2900 psi) for an equivalent crack length of 10.5 mm (0.41 in.). Predicted failure pressure is significantly greater than the experimentally measured 13.3 MPa (1925 psi). The leak rate for this specimen increased from 3.7 L/min (0.97 gpm) (but did not increase during a 90-min hold) at 13.3 MPa (1925 psi) to 14.0 L/min (3.7 gpm) at 16.2 MPa (2346 psi). Figure 4.80c suggests that the effective crack length is between 8.4 and 9.3 mm (0.33 and 0.37 in.). During an 11-min constant-pressure hold at 16.2 MPa (2346 psi), the leak rate increased steadily from 14.0 to 39.0 L/min (3.7 to 10.3 gpm,) which would suggest that the effective TW crack length increased to 11 mm (0.43 in.) during the hold period. The flow remained constant at 39.0 L/min (10.3 gpm) for the next 9 min at the same pressure. Note that although the final estimated TW crack length is reasonably close to that predicted by the ligament rupture model, the predicted rupture pressure is significantly greater than the experimental maximum pressure. A posttest view of the crack at the OD surface is shown in Fig. 4.81, which also includes a marker identifying the estimated TW crack length.
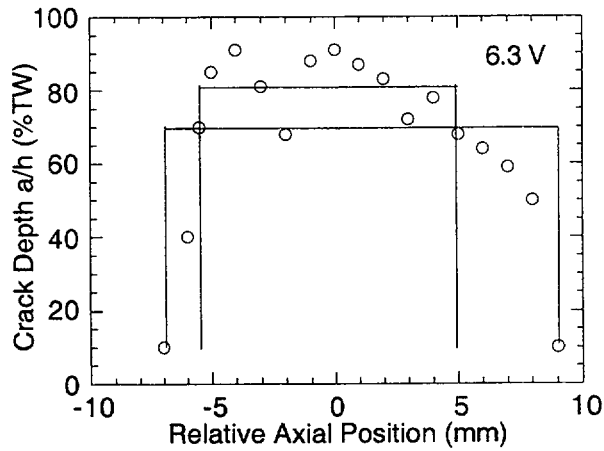
(a)
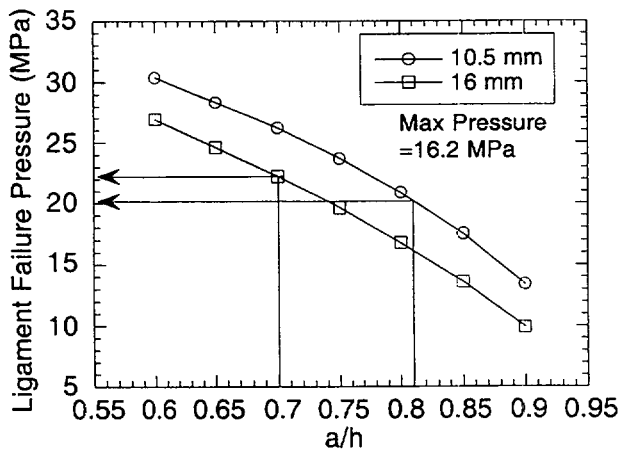
(b)
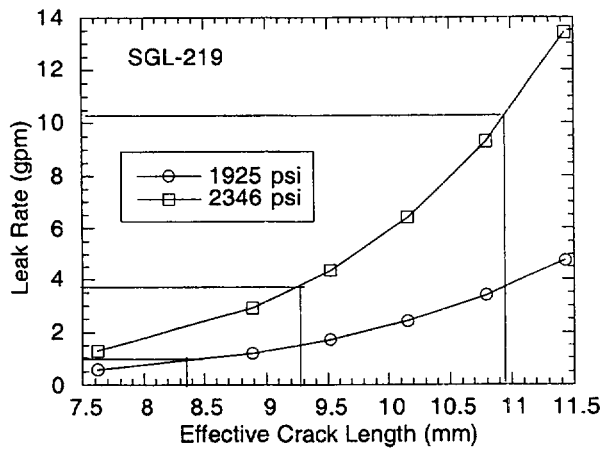
(c)

Fig. 4.80.
(a) Estimated crack depth profile from EC +Point data, (b) calculated ligament rupture pressure for two equivalent rectangular cracks, and (c) effective TW crack length estimated from leak-rate data for test SGL-219 conducted at 288°C.
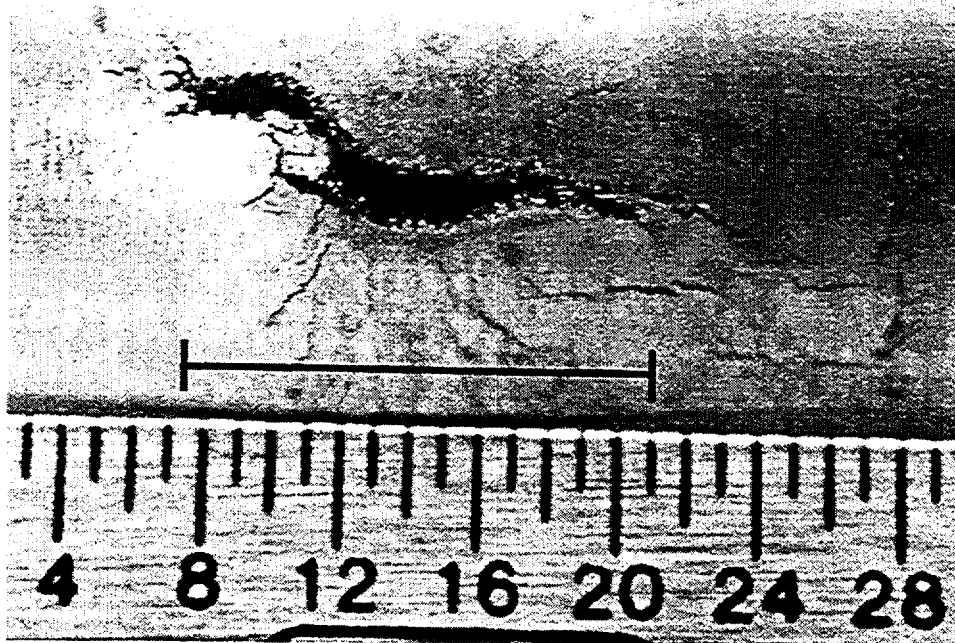
Fig. 4.81. *Posttest view of OD crack of specimen SGL-219. Marker indicates effective TW crack length (11 mm or 0.43 in.) calculated from measured leak rate.*

A comparison with Fig. 4.80a suggests that the estimated final crack length corresponds to the length over which the crack depth exceeds 70% of the wall thickness. None of the ANL specimens showed the presence of OD axial segments separated by ligaments at the end of the tests, implying that all such ligaments most likely ruptured during the tests.

An additional pressure and leak-rate test was conducted on a Westinghouse-supplied tube with a SCC crack generated in doped steam. Figure 4.82 shows the pretest crack depth profile by EC +Point. Ligament thickness for this specimen was highly nonuniform, as in test specimen SGL-177. Two equivalent rectangular crack profiles (Figs 4.83a-b) were used for calculating the ligament rupture pressure. The yield strength and flow stress of the Westinghouse tube were estimated from a few hardness tests at room temperature to be 240 and 485 MPa (35 and 70 ksi), respectively. The ligament rupture pressure was calculated to be 22.0 and 20.0 MPa (3190 and 2900 psi) at room temperature (Fig. 4.83a) and 282°C (Fig. 4.83b), respectively, for an equivalent crack length of 11 mm (0.43 in.). However, as in test SGL-177, this specimen developed a leak rate of 0.04 L/min (0.01 gpm) after a >3-h hold at 17.2 MPa (2500 psi) at room temperature, and the leak rate increased to 0.068 L/min (0.018 gpm) after an overnight hold at the same pressure. Figure 4.84 implies that the effective TW crack length increased from 1.8 to 2.3 mm (0.07 to 0.09 in.) during this hold period. The leak rate then increased to 0.12 L/min (0.032 gpm) after a >5-h hold at 18.6 MPa (2700 psi), which would imply a final effective TW crack length of 2.8 mm (0.11 in.). The same specimen was later pressurized to 18.6 MPa (2700 psi) at 282°C and held at constant pressure. The leak rate was observed to increase from 0.30 to 0.72 L/min (0.08 to 0.19 gpm) during a 2-h hold. Figure 4.84 implies that the effective TW crack length increased from 3.6 to 4.8 mm (0.14 to
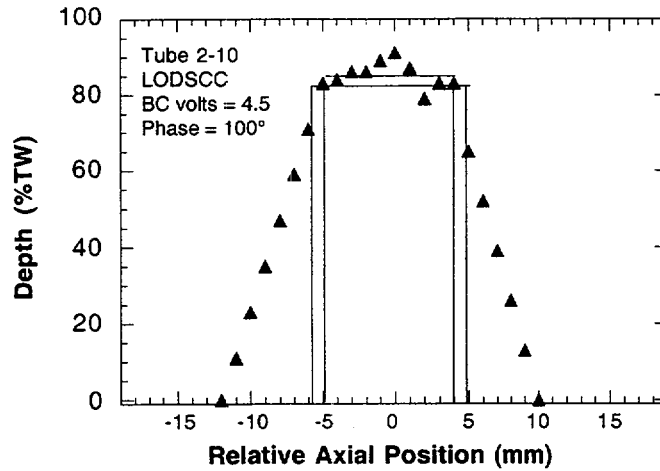
Fig. 4.82. Estimated crack depth profile from EC +Point data for Westinghouse tube 2-10.
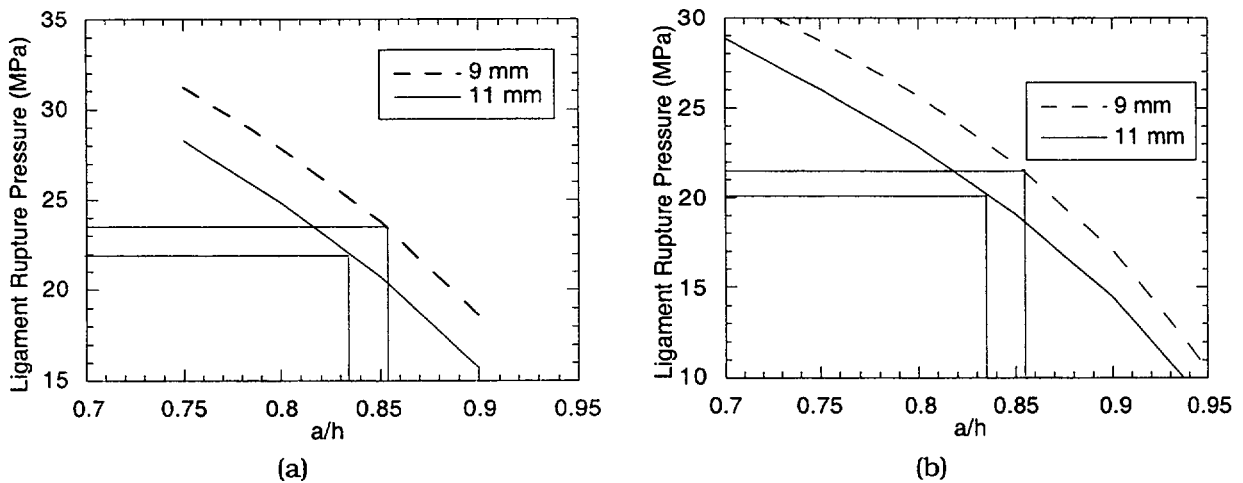
Fig. 4.83. Calculated ligament rupture pressure for two equivalent rectangular cracks in Westinghouse tube 2-10 at (a) room temperature and (b) 288°C.

0.19 in. during the hold period. The ligament rupture model overestimates the TW crack length, even though the final test pressure is close to the predicted ligament rupture pressure (cf. SGL-219). A posttest view of the crack at the OD surface is shown in Fig. 4.85, which also includes a marker identifying the estimated TW crack length at 4.8 mm (0.19 in.).

In contrast to the ANL specimens, the estimated posttest TW crack length for the Westinghouse specimen is significantly shorter than that observed visually. A closer examination of Fig. 4.85 shows that in contrast to the ANL specimens in which none of the ligaments between axial segments survived the test, the crack in the Westinghouse specimen had at least three axial segments (undetected by the EC +Point method) separated by 0.4-mm (0.015-in.)-thick surface ligaments that survived the pressure loading. It is not clear whether
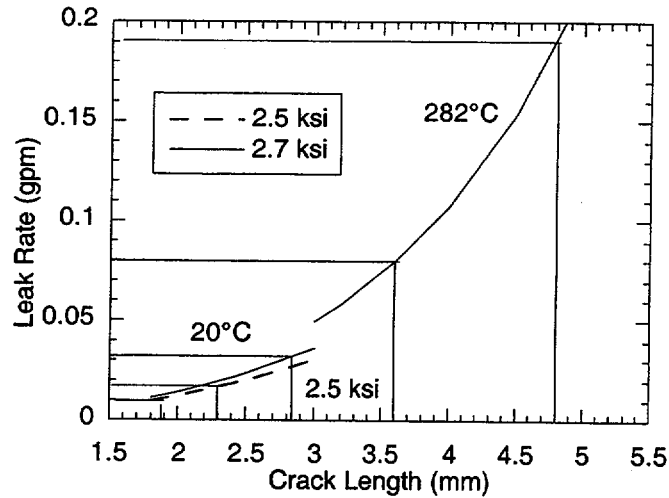
Fig. 4.84. *Calculated leak rate in Westinghouse tube 2-10 vs. crack length for two pressures at room temperature and for 2.7 ksi at 282°C.*
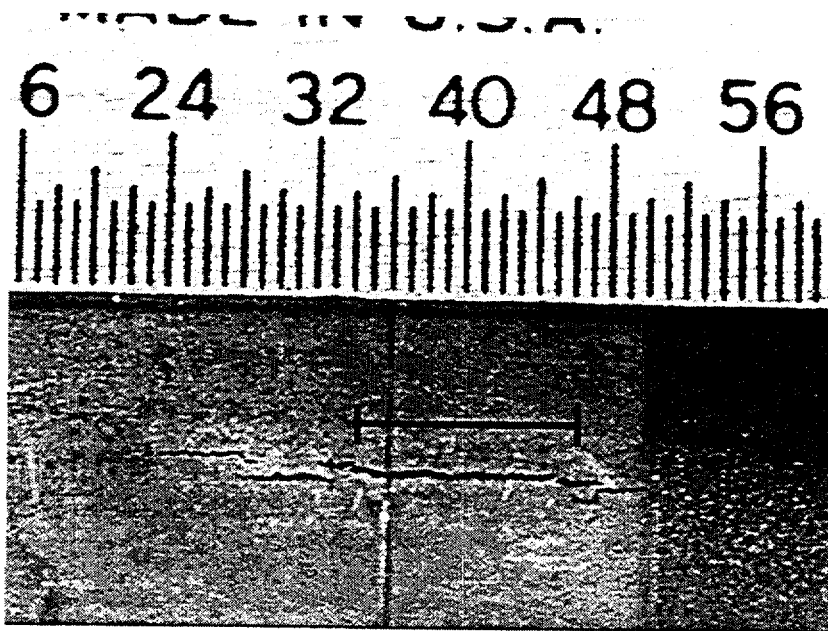
Fig. 4.85. *Posttest view of OD crack of Westinghouse specimen 2-10. Marker indicates effective TW crack length (4.8 mm or 0.19 in.) calculated from measured leak rate.*

the ligaments between the segments persist through the full thickness of the tube wall. It is likely that the effective crack length calculated from the leak rate would be much closer to that observed visually if the stiffening effects of the ligaments on the crack opening area were taken into account. Also, the ligament rupture model using the equivalent rectangular crack approximation most likely underestimates the pressure to rupture the through-thickness crack tip ligament significantly (and overestimates the TW crack length) in this case for the same reason.

135

Discussions of results

If the pretest crack depth profile is reasonably uniform and deep (80-90%) as measured by EC +Point, a significant portion of the through-thickness crack tip ligament can rupture abruptly at a pressure that can be calculated by the ANL correlation. Posttest pictures of the OD surface did not reveal the presence of surface ligaments in these specimens. Effective TW crack lengths estimated by the ligament rupture model using the EC +Point data are reasonably close to those estimated from the leak-rate data and correspond closely to a segment of the crack that is >70% TW thickness. In these specimens, the leak rate generally increased abruptly from 0 or ≤0.04 L/min (≤0.01 gpm) to >19 L/min (>5 gpm) under increasing pressure loading, indicating sudden rupture of the ligament, but did not increase under a constant-pressure hold subsequent to ligament rupture. It is not clear (although it appears likely) that leakage would have initiated eventually in similar specimens in a time-dependent fashion had they been subjected to a constant-pressure hold at a lower pressure before full ligament rupture.

For specimens with highly nonuniform crack tip ligament thickness (as measured by EC +Point) with predicted ligament failure pressures that are greater than our system capability (i.e., 19.3 MPa [2800 psi]), the ligaments can fail locally during a constant-pressure hold at a lower pressure than the predicted failure pressure. The effective TW crack lengths for these specimens can subsequently increase due to time-dependent ligament rupture at both room temperature and 282°C. In some cases, leakage began only after many minutes of constant-pressure hold, following which the leak rate often increased gradually or intermittently during constant-pressure holds (minutes), indicating that the ligament was undergoing time-dependent rupture. It is not clear how long the time-dependent ligament rupture process would have continued had the constant pressure been applied indefinitely. Based on very scant data, it appears that the time-dependent ligament rupture process occurs at a much slower rate (hours rather than minutes) in the higher-strength Westinghouse tube than in the lower-strength heat-treated ANL tubes. Also, the time-dependent rupture process occurs more rapidly at 282°C than at room temperature. A procedure for converting the constant-pressure-hold data on time-dependent leak rate from heat-treated tube to as-received tube must be developed in the future.

In all ANL specimens tested to date, the lengths of the TW segments of the cracks calculated from leak-rate data are close to the lengths of the most open part of the cracks, as evident visually from posttest pictures of the specimens. None of these pictures showed the presence of axial segments separated by ligaments. For test SGL-177, the posttest measured length of the TW segment of the crack (by the bubble technique) is reasonably close to that calculated from the measured leak rate. Also, the effective TW crack lengths calculated from the leak-rate data correspond to a length of the crack that is >70% TW thickness (as measured by EC +Point method). In contrast to the ANL specimens, the calculated TW crack length for the Westinghouse specimen is much shorter than that observed visually. However, a posttest picture of the OD surface of this specimen revealed at least three axial segments separated by ligaments, showing that the effective TW crack length can be seriously underestimated from the measured leak rate if the effects of the ligaments on the crack opening area are not taken into account.

136

Based on the above discussion, we tentatively propose the following procedure for calculating the leak-rate correction factors for tests conducted between 10.3 and 19.3 MPa (1500 and 2800 psi) on laboratory-grown deep and approximately planar SCC cracks 9-16 mm (0.35-0.63 in.) long (with possibly a few initial nonleaking TW segments):

From the measured leak rate at a given temperature and pressure, estimate the effective TW crack length by using Eq. 4.33a, the Zahoor model for flaw opening area (Eq. 4.34) and the flow properties of the annealed and sensitized material, assuming that even if the crack was initially segmented axially, all the ligaments between the segments are ruptured before the leak-rate data are taken. If the crack remains segmented at the time the leak rate is measured, a different set of correction factors must be developed to take into account the geometry of the remaining ligaments.

It is recommended that the calculated effective TW crack length should be confirmed by posttest immersion bubble test. If possible, TW crack lengths in a few of the SCC specimens should also be measured by posttest sectioning. In particular, it should be established whether any of the ligaments separating the axial segments survived the test.

The leak-rate correction factor can be obtained from Fig. 4.73 a for a given temperature, pressure, and effective TW crack length. These curves are inapplicable if the crack remains axially segmented at the time the leak rate is measured. The correction factor gives the leak rate in the as-received tube having the same effective TW crack length as in the heat-treated tube subjected to the same temperature and pressure. This does not imply that the as-received tube with the same pretest crack morphology as the heat-treated tube would experience the calculated leak rate if subjected to the same pressure history as the heat-treated tube. .

Currently, we do not have a method for converting the time-dependent leak-rate data for the heat-treated tube to those for the as-received tube.

4.5.4   Conclusions on Failure Mechanisms

The conclusions here are drawn from limited number of tests on approximately planar (macroscopically) SCC cracks, 9-16 mm (0.35-0.63 in.) long, as measured by pretest EC +Point, during pressure and leak-rate tests at 10.3-19.3 MPa (1500 to 2800 psi). They require verification by further testing on specimens with different crack sizes and morphology, including posttest sectioning of some of the specimens.

In all specimens tested to date, including that supplied by Westinghouse, very short TW segments already existed before testing, as evidenced by leakage of gas at 275 kPa (40 psi). However, the same specimens did not show measurable water leakage even up to 10.3 MPa (1500 psi), implying that these TW segments were so short and tortuous that they did not open significantly under pressure to allow leakage of water. The time-dependent history and magnitude of leakage from a laboratory-grown SCC crack during pressure testing depends critically on the sequence of rupture events of the ligaments between axial segments and the through-thickness crack tip ligaments (some of which are initially breached). Two extreme scenarios are helpful in discussing these effects during pressurization of the tube, although in

reality there will be a mixture. At one extreme (Scenario 1), if all or even a significant fraction of the ligaments between the axial segments rupture before through-thickness rupture of a significant fraction of crack tip ligaments (including those already breached before the test), we would expect to see an abrupt initiation of large leakage when the crack tip ligaments finally fail by plastic collapse. It would be expected that in these cases, the ligament rupture model based on a long equivalent rectangular part-through crack would predict the rupture pressure reasonably well. ANL specimens SGL-104 and SGL-195 tended to follow this pattern.

At the other extreme (Scenario 2), if the through-thickness crack tip ligament of one or more axial segments rupture before any of the ligaments separating the axial segments, the total leakage remains low because the crack-opening areas of the individual TW segments are small. In these cases, the initial pressure to cause measurable leakage can be much lower than the ligament rupture pressure calculated for a full rectangular part-through crack because the leakage will be due to gradual opening of short TW segments (including the preexisting TW segments), as well as successive rupture of ligaments at the through-thickness tips of shallower segments with increasing pressure. The continuous or intermittent time-dependent increase of the leak rate during a constant-pressure hold may be due to anelastic effects and/or sequential rupture of the through-thickness ligaments of the crack segments. Although more data are needed to confirm this, the time-dependent rupture process appears to be faster at higher temperatures and lower flow stresses. Occasional failure of ligaments between axial segments can also contribute towards the intermittent increases of leak rate. However, as long as some of the ligaments separating the axial segments survive, the total leak rate under Scenario 2 will be much lower than that under Scenario 1. The Westinghouse specimen appeared to follow this pattern. Ultimately, with increasing pressure, all the ligaments separating the axial segments will eventually rupture even under Scenario 2, and the leak rates under both scenarios would converge. The actual failure path followed by any particular specimen is controlled by the relative thicknesses and widths of the various crack-tip ligaments and the ligaments between the various axial segments. Therefore, it is recommended that a series of specimens with multiple laser-cut notches (to keep the notch width small compared to ligament widths) with several ligament widths be tested to establish failure criteria for the various ligaments.

A shortcoming of the EC +Point method as it is practiced today is that although it can detect narrow through-thickness crack tip ligaments quite accurately, it fails to detect narrow ligaments between axial crack segments. Thus, if the +Point data are used ignoring the presence of axial segments, the leak rate may be significantly overestimated. Conversely, the crack length can be seriously underestimated from the measured leak rate if the segmented nature of the axial crack is not taken into account. Although the ligaments between axial segments were ruptured in most of the ANL specimens, at least three survived in the Westinghouse specimen up to 18.6 MPa (2700 psi) at 282°C. It would be extremely useful for future development of leak-rate and failure models for SG tubes if a procedure can be developed to estimate the number, size, and shape of the ligaments between axial crack segments from the EC +Point data.

4.6   Behavior of Electrosleeved Tubes at High Temperatures

The behavior of Electrosleeved* tubes during a severe accident is of interest, because Electrosleeves have potential use for the repair of steam generator tubes. Although the nanocrystalline Electrosleeve material has better mechanical properties than those of Alloy 600 at reactor operating temperatures, it loses strength at high temperatures because of grain growth, which raises concern regarding its integrity during severe accidents. No relevant data were initially available, and so the high-temperature behavior of Electrosleeved tubes with notches was investigated analytically.

Prediction of failure of a complex composite material like the Electrosleeved steam generator tubing under severe accident transients is a difficult problem. The Electrosleeve material is almost pure Ni and derives its strength and other useful properties from its nanocrystalline grain structure, which is stable at reactor operating temperatures. However, as mentioned above, it undergoes rapid grain growth at the high temperatures expected during severe accidents, resulting in a loss of strength and a corresponding decrease in the flow stress. The magnitude of this decrease depends on the time-temperature history during the accident. Low-temperature tensile data on Electrosleeve material (without the tube) are available, but available tensile data at high temperatures in either the aged or unaged condition are very limited. Initially, the assumption was made that there were no experimental failure data available on Electrosleeved tubes with cracks. Therefore, analytical models were exclusively relied upon to predict failure of the composite structure with flaws, using the available tensile data to determine the parameters of the models.

Following initial modeling and analysis, Framatome Technologies, Inc. (FTI) provided failure data from six tests on unsleeved and Electrosleeved tubes with and without notches under simulated severe accident loading. In contrast to the prediction by the model that the damaging effect of notch length should level off with increasing notch length, the FTI test data indicated that the failure temperature of the Electrosleeved tube decreased almost linearly with notch length. On the other hand, the failure temperatures of the unsleeved and degraded tubes were predicted quite accurately by the flow stress model for Alloy 600 presented in Ref. 17. One of the tests was on an undegraded Alloy 600 tube and involved a long hold time at constant temperature, which the flow stress model cannot handle. However, the creep rupture model for Alloy 600 tubing presented in Ref. 17 predicts the failure time of this specimen within a factor of 2.

Subsequent to its initial tests, FTI supplied twelve Electrosleeved tube specimens, three of which have 51-mm (2-in.)-long TW notches for testing at ANL. Eight other specimens were notched by EDM at ANL with notch lengths of 13, 25 and 76 mm (0.5, 1, and 3 in.), all nominally 100% TW of the parent tube. All specimens were tested to failure using a temperature and pressure history that closely simulated those for a station blackout (SBO) with a depressurized secondary side (Case 6). This report describes the basis for the analytical models and shows how they were revised on the basis of the test results. Although the initial model overestimated the failure temperatures of the FTI tests, the failure temperatures were predicted accurately by the revised model. Finally, the models are used to predict failure of Electrosleeved steam generator tubing during postulated severe accidents.

---

* Electrosleeve is a trademark of Ontario Power Generation, Inc.

Two approaches were developed for predicting failure of the Electrosleeved tube, both based on the flow stress failure model, as discussed in Ref. 17. The first is an approximate analytical procedure based on a linear damage rule hypothesis. The second is a more mechanistically based approach that accounts for the loss of flow stress due to grain growth. The predicted failure temperatures by both approaches led to comparable results. Although the work in Ref. 17 showed that a creep model gave a more accurate prediction of failure at high temperatures than a flow stress model, insufficient data are available to conduct a creep analysis of the Electrosleeved tube at present. However, based on comparison with limited experimental failure data, it is believed that in the absence of hold times at constant temperature, flow stress models give reasonable estimates of failure temperatures for Electrosleeved tubes with notches. Predictions of the relative strength of tubes with and without repairs are probably more accurate than predictions of failure temperatures. The reference geometry of Electrosleeved tubes considered in this report is a 22-mm (7/8-in.)-diameter, 1.27-mm (0.050-in.)-wall-thickness Alloy 600 tubing, with a nominal 0.97-mm (0.038-in.)-thick Electrosleeve at the ID surface.

4.6.1 Problem Description and Assumptions

The Electrosleeved tube is a composite with a fine-grained Ni layer bonded to the ID surface of the 7/8-in.-diameter, 0.050-in.-wall-thickness Alloy 600 tube (Fig. 4.86). An axial crack of various lengths is assumed to exist through the full thickness of the tube wall.

The Electrosleeve material is stronger than the tube material at normal reactor operating temperature. However, at high temperatures, it begins to lose its strength because of grain growth. The thermal aging effect is a complicated phenomenon consisting of at least two steps. In the first step, the grain boundary phosphide precipitates, which prevent grain growth from occurring, are dissolved. In the second step, grain growth occurs predominantly by grain boundary diffusion at lower temperatures when the grain size is small and gradually switches to lattice diffusion with increasing temperature and grain size. Both steps involve thermally activated processes. A model was developed for predicting grain growth under variable temperature condition.

A schematic diagram of an Electrosleeved tube is shown in Fig. 4.86. For evaluating the structural integrity of the tube, either an axial crack of various lengths or a 360° circumferential crack is assumed to exist through the full thickness of the parent tube wall. During a severe accident, the tube is subjected to a time-varying temperature and pressure (Δp) history. To predict failure of the crack tip ligament, a flow stress model was used. The flow stress failure criteria for both the axial and circumferential cracks can be stated as follows:

$$\sigma_{lig} = H(T, t),$$
(4.35a)

where H is the hardness or flow stress (dependent on the temperature history) of the Electrosleeve and σ_{lig} is the ligament stress, which for the two types of crack is given by

$$\sigma_{lig} = \begin{cases} m_p \sigma_h & \text{for axial cracks} \\ \sigma_A & \text{for circumferential cracks} \end{cases}.$$
(4.35b)
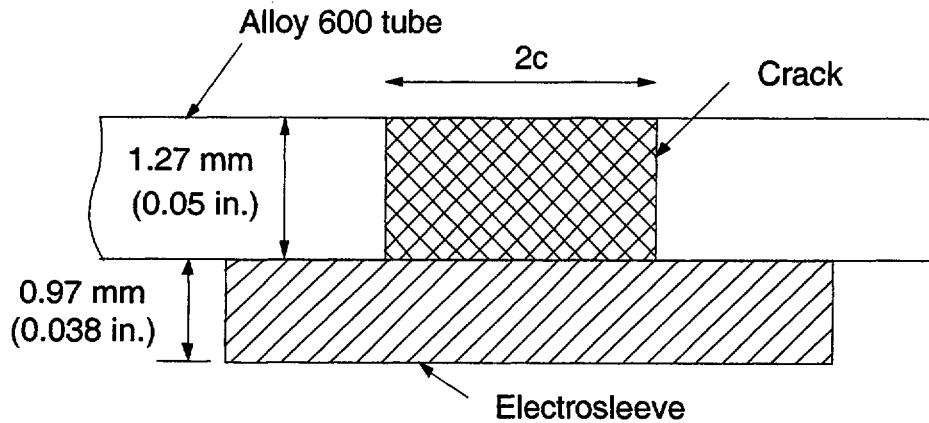
Fig. 4.86. Reference geometry for Electrosleeved steam generator tube with axial crack.

where m_p, which depends on the axial crack length and depth, is the ligament stress magnification factor, σ_h is the hoop stress (calculated using the mean radius and total thickness of the tube and the sleeve), and σ_A is the axial stress based on net section of the tube and the sleeve. During severe accidents, the Δp across the tube wall and the tube wall temperature are ramped up at various rates. In the flow stress model, failure is predicted to occur when the magnified stress in the crack tip ligament equals or exceeds the flow stress. Initially, we assumed that the stress magnification factor mp for the crack tip ligament in the Electrosleeve is given by the same equation as used for a single-layer shell in Ref. 17. However, finite element analyses showed that the effective value of m_p is reduced when the flow stress of the Electrosleeve is significantly lower than that of the parent tube.

The model for predicting grain growth of the electrosleeve material was combined with a flow stress model (where the flow stress is determined from grain size via the Hall-Petch relationship) for predicting failure under temperature histories that are expected to occur during severe accidents.

4.6.2 Determination of m_p for Axial Cracks

Initially, the hoop stress magnification factor m_p for the crack tip ligament in the Electrosleeve was estimated from the equation for a single-layer shell used in Ref. 17. However, the m_p factor could be reduced if the flow stress of the Electrosleeve ligament is significantly lower than that of the parent tube. In fact, detailed analyses of available tensile data of the Electrosleeve (to be discussed later) showed that at the temperatures of interest, the flow stress ratio between the parent tube and the Electrosleeve ranges from 2 to 3. To determine the effect of the flow stresses of the Electrosleeve and Alloy 600 on m_p, a series of finite element analyses (FEA) was conducted for a bilayer tube with a 100% TW crack in the outer layer (simulating Alloy 600) under a constant temperature and increasing pressure loading. The ratio between the flow stress of the outer layer and the inner layer (simulating the Electrosleeve) was varied from 1 to 3. The results, plotted in Figs. 4.87a-b, confirm that the values of m_p are indeed reduced significantly when the flow stress ratio is increased. The m_p factor as computed from FEA results generally varies with pressure. However, the behavior for long cracks is different from that for short cracks, as shown in Figs. 4.87a-b. For long cracks, m_p increases with

141
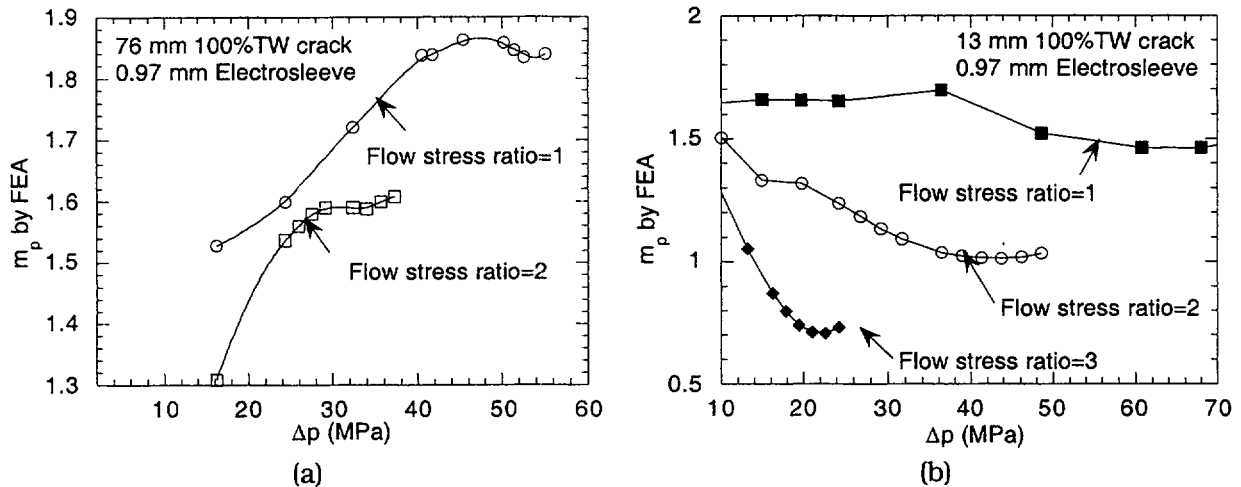
Fig. 4.87. Variation of m_p factor with pressure for (a) 76-mm (3-in.)-long and (b) 13-mm (0.5-in.)-long cracks for various values of flow stress ratios between tube and Electrosleeve.

pressure and tends to level off at higher pressure. Behavior for the shorter 12.7 mm (0.5 in.) crack is just the opposite; it decreases with pressure and tends to level off at higher pressure. However, in both cases, the m_p factor increases rapidly (suggesting onset of failure) with further increase in pressure in a regime where the Electrosleeve experiences significant plastic yielding away from the crack tip ligament. The values of m_p at the point where it levels off (i.e., just prior to failure) were used in the failure models. As shown in Fig. 4.88, the m_p obtained from FEA (for flow stress ratio = 1) agrees well with that calculated with the ANL correlation for cracks ≤ 25 mm (1 in.), but levels off with increasing crack length beyond 51 mm (2 in.). On the other hand, the m_p calculated by the ANL correlation continues to increase with increasing crack length, although the actual increases are small beyond a crack length of 51 mm (2 in.).

Note that the m_p factor for the 12.7 mm (0.5 in.) crack can drop below 1 for an Electrosleeve if the decrease in flow stress is large. Although m_p is decreasing with increasing pressure for short crack, the average ligament stress (or plastic strain) is still increasing with increasing pressure because m_p is obtained by dividing the average ligament stress by the nominal hoop stress in the uncracked section. Nor does a value of $m_p < 1$ imply that the Electrosleeve/Alloy 600 composite tube wall away from the crack will fail before the crack tip ligament. The average stress in the Electrosleeve ligament relative to its flow stress always remains higher than the average stress in the Electrosleeve/Alloy 600 composite tube wall (away from the crack section) relative to its thickness-weighted flow stress.

Because the FEA grid may not have been sufficiently fine to obtain highly accurate solutions, the FEA results were used to calculate the ratio between the m_p for the Electrosleeved tube and that for the homogeneous tube as a function of the ratio between the flow stress of the parent tube and the Electrosleeve, as shown in Fig. 4.89. This m_p ratio was then used to scale the m_p calculated by the ANL correlation[17] for a homogeneous tube to obtain the effective m_p of the Electrosleeved tubes with notches, as indicated in Eq. 4.36 (FSR denotes flow stress ratio):

$$m_p(\text{eff.}) = \frac{m_p(\text{FEA})}{m_p(\text{FEA}, \text{FSR} = 1)} \times m_p(\text{ANL}). \tag{4.36}$$

142
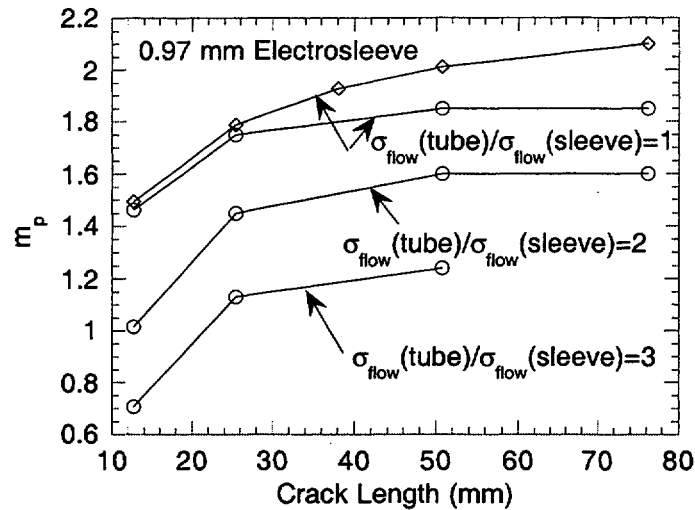
Fig. 4.88. Comparison of m_p values calculated by ANL correlation with those by FEA for ratios of flow stress of Alloy 600 to Electrosleeve material of 1, 2, and 3. Tube wall and Electrosleeve thicknesses were assumed equal to 1.27 mm (0.050 in.) and 0.97 mm (0.038 in.), respectively.
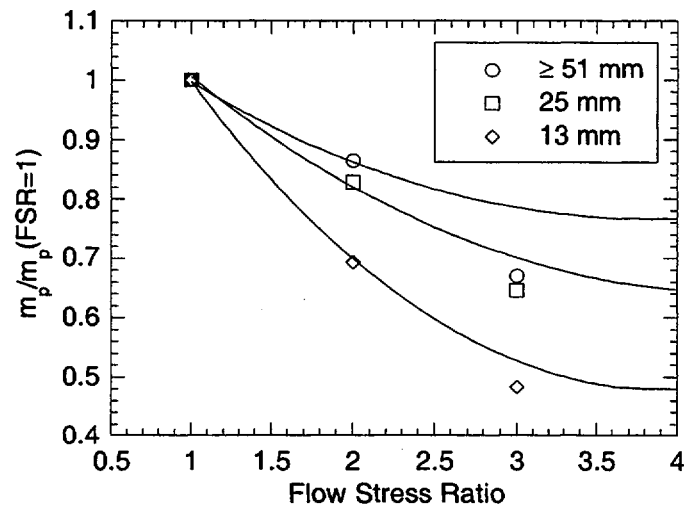
Fig. 4.89. Variation of m_p reduction factor with flow stress ratio (FSR) as calculated from FEA results for various crack lengths.

4.6.3   Material properties data for Electrosleeve

The initial development of the model was based on three sets of material properties data contained in a report by FTI titled "Electrosleeving Qualification for PWR Recirculating Steam Generator Tube Repair," Report No. BAW-10219P, Rev. 03, October 1998. Subsequently, FTI provided two additional sets of data, one describing the time-dependent decrease in flow stress of the Electrosleeve material upon isothermal aging and the other dscribing failure tests on Electrosleeved tubes with notches under simulated severe accident transients.

143

As stated previously, The FTI data show that the Electrosleeve material is stronger than the tube material at normal reactor operating temperature, but it begins to lose its hardness because of grain growth at temperatures $\geq 400°C$ (Fig. 4,90). The thermal aging effect is a complicated phenomenon consisting of at least two steps. In the first step, the phosphide precipitates in the grain boundary, which prevent grain growth, are dissolved, and in the second step grain growth occurs. The starting or initial hardness of the FTI isothermal aging specimens show a very large specimen-to-specimen scatter. Therefore, the loss of hardness data for each specimen was normalized with respect to its initial hardness, as shown in Fig. 4.90. The data in Fig. 4.90 suggest that the hardness of the material begins to decrease, albeit at a relatively slow rate, starting very early. The nucleation times for this process for specimens aged at >425°C are relatively short and are ignored in the nucleation model to be discussed later. The data in Fig. 4.90 also suggest the existence of a second process with longer nucleation times that involves very rapid decrease in hardness with time and is very likely linked to the process of rapid grain growth. The reciprocal of the incubation time for the onset of rapid loss of hardness (rapid grain growth) has a temperature-dependent activation energy as shown in Fig. 4.91. For analyses of loss of hardness, the continuously varying activation energy curve Q was replaced by the step function indicated in Fig. 4.91. Sensitivity studies, which are presented later in the report, showed that the results are not sensitive to the form chosen for Q.

Data for the yield and ultimate tensile strengths of the Electrosleeve material are given in the FTI report from room temperature to 343°C (650°F). The flow stress, which is the average of the yield and ultimate tensile strengths, as a function of temperature is shown in Fig. 4.92. The single high-temperature flow stress data of the Electrosleeve in Fig. 4.92 was estimated from a tensile test conducted on aged material and will be discussed later. Initially, in the absence of any other flow stress data at high temperature, the solid line in Fig. 4.92 was used as an estimate for the unaged flow stress curve of the Electrosleeve. It should be remembered that during a severe accident, the actual flow stress of the Electrosleeve is reduced from the unaged curve (H) shown in Fig. 4.92 because of grain growth. The high-temperature tests conducted by ANL (to be discussed later) and FTI suggested that the unaged flow stress of the Electrosleeve material is lower than that shown in Fig. 4.92.

FTI also submitted to the NRC data from a series of tensile tests at 343°C on specimens exposed to isothermal preaging treatment at high temperatures for various times (Fig. 4.93). The data at 760°C are for a tensile test conducted at 760°C. This particular specimen was heated at a slow linear ramp of $\approx 5.8°C/min$ from 327°C. The effective aging time at 760°C was estimated from an activation energy of 35 kcal/mole to be 39 min.

FTI also provided failure data from six tests on internally pressurized tubes that were subjected to a variety of temperature ramps simulating those expected during SBO accidents. The initial temperature ramp rate up to $\approx 500°C$ varied between 3-5°C/min, which was generally followed by a ramp rate of 7-9°C/min until failure. However, in some cases the ramp rate was gradually decreased to 1.2°C/min above 705°C. Three tests were conducted on unsleeved Alloy 600 tubes with and without any degradation and three on Electrosleeved tubes (22.2-mm [7/8-in.]-diameter) with 12.7, 25.4, and 50.8-mm (0.5-,1-, and 2-in.)-long TW axial notches in the parent tube.
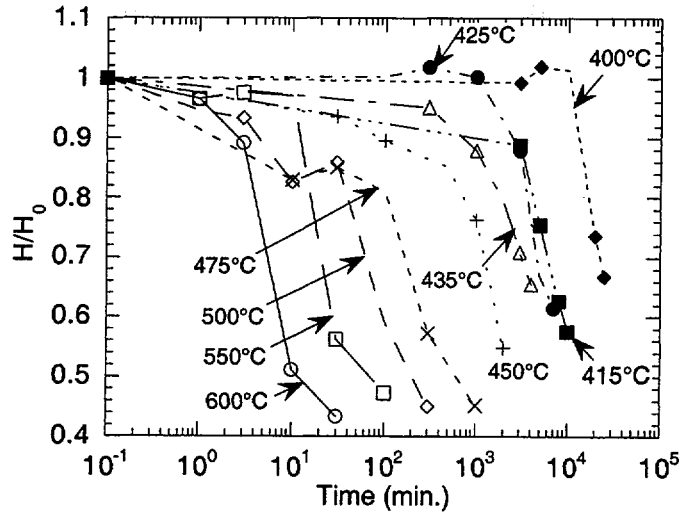
Fig. 4.90. *Variations of normalized Vickers Hardness Number (VHN) of Electrosleeve material with time under isothermal aging at various temperatures.*
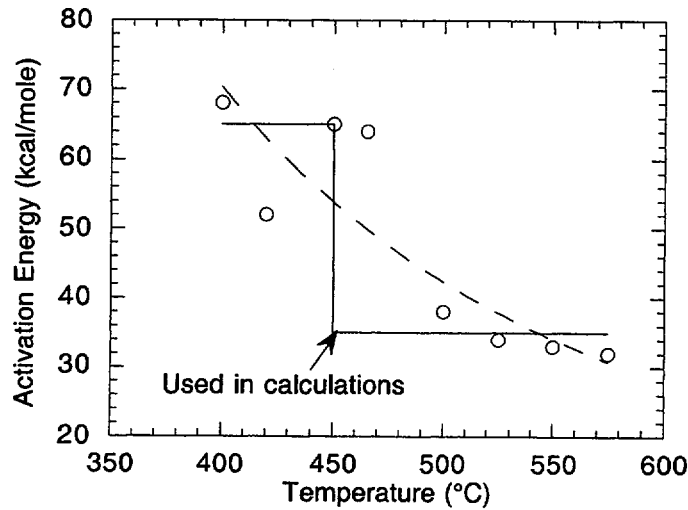
Fig. 4.91. *Variation of activation energy for reciprocal of time to onset of rapid reduction of flow stress (or grain growth) with temperature.*

4.6.4. Analytical Models

Two analytical models were originally developed for estimating the failure temperature under severe accident transients—a model based on linear damage rule and a model based on the Hall-Petch relationship. In both models, a basic assumption is the existence of a temperature-dependent unaged (i.e., without grain growth) flow stress curve of the Electrosleeve. This unaged flow stress curve is largely a theoretical construct of the models because to establish it directly from tensile tests at high temperatures would be difficult due to the grain growth that would occur in the specimens unless the specimens could be heated,

145
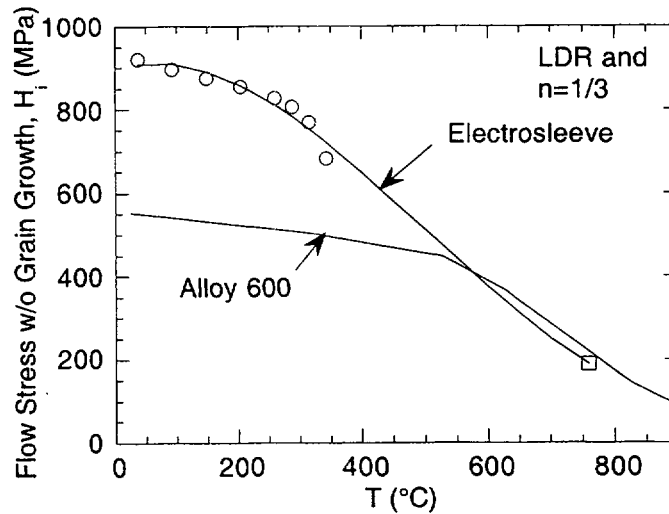
Fig. 4.92. *Flow stress (without aging) vs. temperature plot for Electrosleeve material and Alloy 600. Electrosleeve data (square symbol) at 760°C were estimated from tensile data on a single specimen preaged and tested at 760°C, using n = 0.33. The Electrosleeve flow stress curve of was subsequently modified on the basis of ANL tests.*
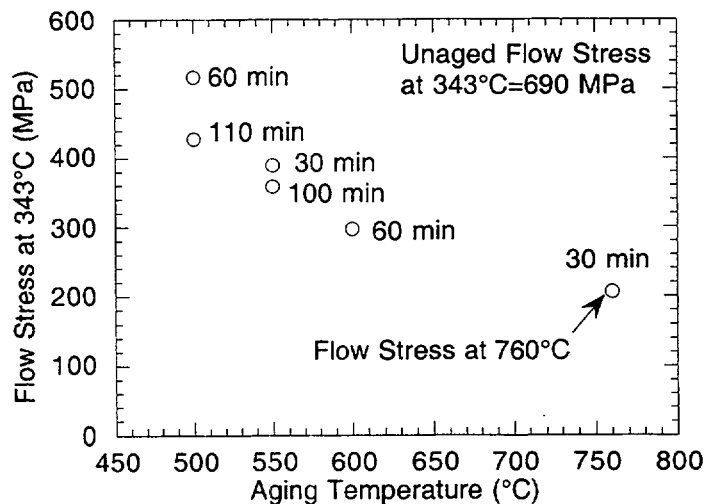
Fig. 4.93. *Flow stress data on Electrosleeve material preaged for various times at high temperatures. All tensile tests were conducted at 343°C, except for that on specimen preaged at 760°C, which was conducted at 760°C.*

stabilized, and tested very rapidly. Therefore, it was calculated from high-temperature failure data by using the models. Ideally, high-temperature failure tests on specimens subjected to severe accident temperature and pressure ramps should be used to derive the flow stress curve of the Electrosleeve. Because such test data were not available when the models were first developed, the unaged flow stress curve of the Electrosleeve was derived initially from analyses of the FTI tensile test data on specimens preaged at 760°C. Subsequently, the flow stress curve of the Electrosleeve was recalculated on the basis of high-temperature failure tests conducted at ANL.

Both models gave comparable results for failure temperatures. Because the Hall-Petch model was more mechanistically based, it was selected for use in failure prediction.

Model based on Hall-Petch equation

In this model, the "nucleation" phase is explicitly separated from the "growth" phase of the grain-growth phenomenon. As mentioned earlier, it was assumed that the Electrosleeve has an initial "unaged" flow stress curve $H_i(T)$, e.g., Fig. 4.92. The hardness or flow stress (at a sufficiently high strain rate) of the Electrosleeve material was assumed to depend on the grain size by the Hall-Petch relationship, i.e.,

$$H(T) = Ad^{-n}f(T), \tag{4.37}$$

where $H(T)$ is the flow stress at any temperature T, d is the grain diameter, n is the Hall-Petch exponent, and $f(T)$ is a correction factor for temperature. During high-temperature exposure, the growth rate of grain diameter was assumed as

$$\dot{d} = \begin{cases} 0 \text{ for } t < t_n \\ \dfrac{B}{d}\exp\left(\dfrac{-Q_g}{RT}\right) \text{ for } t \geq t_n, \end{cases} \tag{4.38}$$

where t_n is the nucleation time to loss of flow stress (i.e., onset of grain growth), B is a constant, Q_g is the activation energy for grain growth, $R = 1.987$ cal/mole/°C. Recrystallization due to plastic straining was ignored. The form of the grain growth rate equation was chosen such that under isothermal aging, the grain growth follows a parabolic law. Under isothermal aging, the reciprocal of the nucleation time $(1/t_n)$, which has an activation energy Q_n, is given by

$$\frac{1}{t_n} = C\exp\left(\frac{-Q_n}{RT}\right) \tag{4.39}$$

where C is a constant. The variation of Q_n with T is given in Fig. 4.91.

The tensile data reported by FTI on preaged specimens of Electrosleeve material were used to calculate the values of various parameters in Eqs 4.37-4.39. Integrating Eq. 4.38, using Eq. 4.39, and assuming $Q_n = Q_g = Q$,

$$d(t) = \left[d_i^2 - \frac{2B}{C} + 2Bt\exp\left(\frac{-Q}{RT}\right) \right]^{1/2}, \tag{4.40}$$

where d_i is the grain diameter of the as-received material and T is the aging temperature. Substituting Eq. 4.40 into Eq. 4.37, denoting the tensile testing temperature as T_o, the initial "unaged" flow stress at T_o as H_o, and solving,

$$t\exp\left(\frac{-Q}{RT}\right) = \frac{d_i^2}{2B}\left[\left(\frac{H_o}{H}\right)^{2/n} - 1\right] + \frac{1}{C}, \tag{4.41a}$$

147

where

$$H_o = A d_i^{-n} f(T_o). \quad (4.41b)$$

Results from the FTI tensile data (T_O = 343°C) on preaged specimens are plotted in Figs 4.94a-b for assumed values of n = 0.33 and n = 0.4, respectively. Both fits are quite good and reasonably close to the conventional value of 0.5. Values of $d_i 2/2B$ and $1/C$ were obtained from the slope and intercept of the linear fits. As mentioned earlier, the specimen that was aged for 30 min at 760°C was also tensile-tested at 760°C. Because this specimen was ramped from 327°C to 760°C at the slow rate of 5.8°C/min before constant-temperature aging, an analysis that used an activation energy of 35 kcal/mole gave an effective aging time at 760°C of 39 min. A reduction factor for the flow stress at 760°C compared to that at 343°C was obtained by fitting the data, excluding the 760°C data, and extrapolating the best-fit line to the value of the time-temperature parameter of the test, as shown by dotted lines in Figs 4.94a-b. The two flow stress curves, shown in Figs. 4.94 and 4.95, correspond to the two estimated values of flow stresses at 760°C by the two fits. The difference between the two flow stress curves is negligible.

Nucleation times to onset of loss of flow stress (i.e., grain growth) under isothermal aging were calculated with Eq. 4.39 and the step-wise varying approximation to the activation energy data shown in Fig. 4.92. The results, plotted in Fig. 4.96 for two Hall-Petch exponents, show that the two exponents give widely varying estimates for nucleation times. Nucleation times for the rapid loss of hardness as derived from the FTI data (Fig. 4.90), also plotted in Fig. 4.96, show that n = 0.33 fits the data better. The calculated curves of loss of hardness (for n = 0.33 and 0.4) with time under various isothermal aging are compared with the FTI data in Fig. 4.97. Although the model does not simulate the initial low rate of loss of hardness, it does represent the subsequent rapid loss of hardness reasonably well for both values of n.

Under a variable temperature history, Eq. 4.39 can be generalized to give the time to nucleation as follows:

$$C \int_0^{t_n} \exp\left(\frac{-Q}{RT(t)}\right) dt = 1. \tag{4.42}$$

Similarly, Eq. 4.38 can be integrated to give the grain diameter at any time t

$$d(t) = \begin{cases} d_i & \text{for } t < t_n \\ \left[d_i^2 + 2B \int_{t_n}^t \exp\left(\frac{-Q}{RT(t)}\right) dt \right]^{1/2} & \text{for } t \geq t_n \end{cases} \tag{4.43}$$

Substituting Eqs 4.42-4.43 into Eq. 4.37 and solving for the flow stress H at any time,

$$H(t) = \begin{cases} H_i(t) & \text{for } t < t_n \\ \left[1 + \frac{2B}{d_i^2} \int_{t_n}^t \exp\left(\frac{-Q}{RT(t)}\right) dt \right]^{-n/2} H_i(t) & \text{for } t \geq t_n \end{cases} \tag{4.44}$$

148
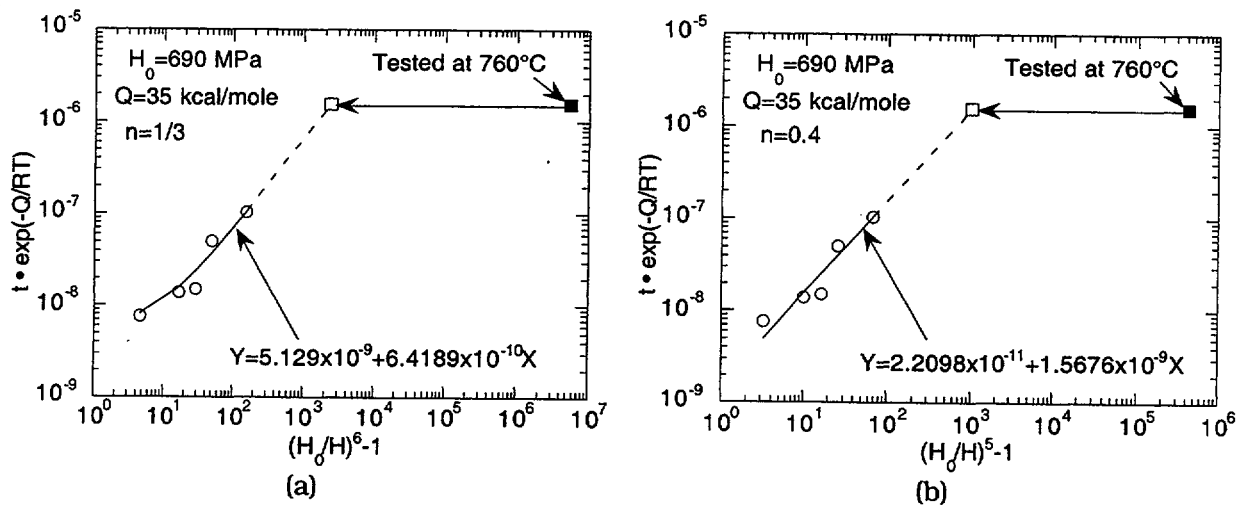
Fig. 4.94. Flow stress (unaged) parameter vs. temperature plot for Electrosleeve material. Data (open square symbol) at 760°C were estimated from tensile data (filled square symbol) on specimen aged and tested at 760°C, using a Hall-Petch exponent (a) n = 0.33 and (b) n = 0.40.
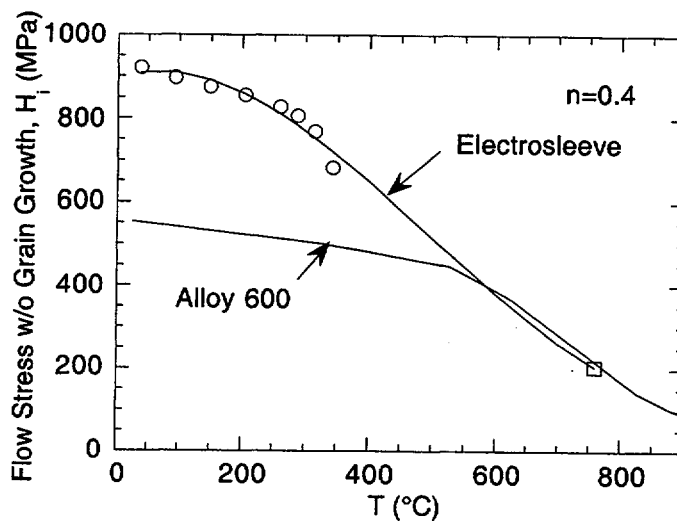
Fig. 4.95. Flow stress (unaged) vs. temperature plot for Electrosleeve material and Alloy 600. Electrosleeve data (square symbol) at 760°C were estimated from tensile data on single specimen preaged and tested at 760°C, using n = 0.4.

where $H_i(t)$ is the initial "unaged" flow stress at $T(t)$. Ligament failure is predicted to occur when Eq. 4.35a is satisfied.

4.6.5 Initial Analytical Results

The model using the Hall-Petch equations to represent the changes in the flow stress was used to calculate failure temperatures. The studies in Ref. 18 showed that the most severe challenge to the integrity of SG tube arises from station blackout (SBO) sequences in which the secondary system dries out and the primary system fails to depressurize (a "high–dry"
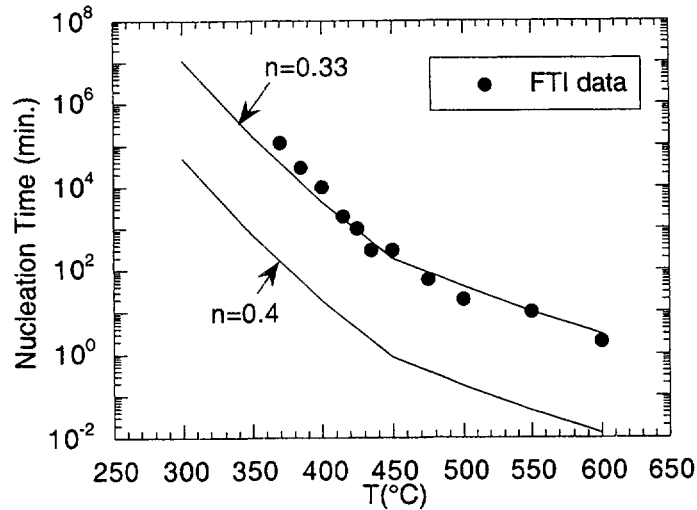
Fig. 4.96. Variation of calculated "nucleation" times to onset of rapid loss of flow stress (or grain growth) under isothermal aging with aging temperature for Hall-Petch exponents of n = 0.33 and n = 0.40, using a temperature-dependent activation energy given by step function in Fig. 4.81. Also shown are nucleation times for rapid loss of flow stress derived from FTI data shown in Fig. 4.92.
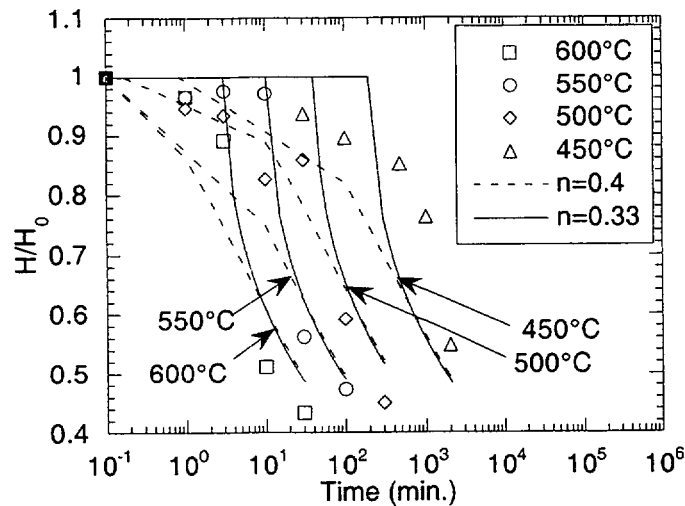
Fig. 4.97. Calculated variations of normalized Vickers hardness number (VHN) of Electrosleeve, using Hall-Petch model with n = 0.33 and n = 0.4, with the experimentally measured variations under isothermal aging at various temperatures.

sequence). In this case, the Δp across the tube wall is a constant 16.2 MPa (2.35 ksi). The time–temperature history was taken as bilinear with an initial 5°C/min segment to 670°C (1238°F), followed by 2°C/min segment until failure (Fig. 4.98). This temperature ramp is a simplified version of those used in Ref. 18 for the severe accident tests on flawed tubes without repairs. It is even more conservative than the Ref. 18 versions because the slower segment starts at a lower temperature. If another primary system component fails before the SG tube

150
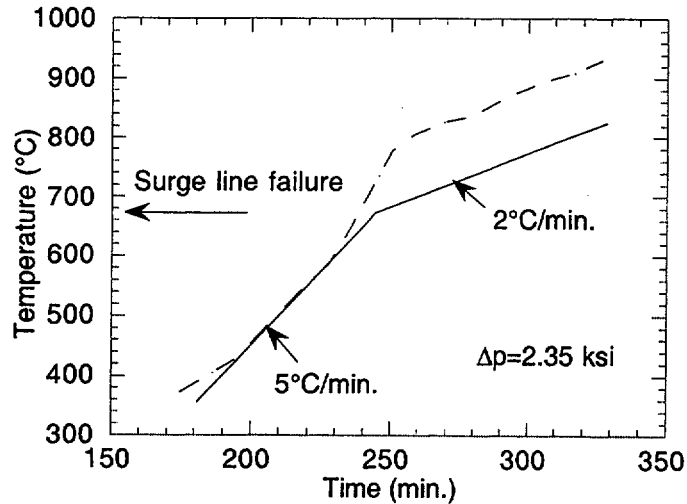
Fig. 4.98. Actual variation in time–temperature history for tests reported in NUREG–1570 (Ref. 18) (dashed line) and simplified scoping ramp ANL simulation (solid line) of temperature during an SBO (old case 6) severe accident transient. Internal pressure = 16.2 MPa (2.35 ksi).

fails, the system depressurizes and subsequent failure of the tubes is unlikely. The surge line is probably the limiting primary system component. Based on earlier calculations, it was assumed that the surge line would fail when the tube temperature is 674°C (1245°F) for this bilinear ramp. Subsequent discussions with NRC staff and additional thermohydraulic calculations led to the conclusion that this particular bilinear ramp, which will be referred to in the remainder of the report as the "scoping ramp." is an overly conservative representation of the "high–dry" SBO sequence, and thus a more realistic time–temperature history was used for most of the calculations. However, because calculations with the different histories are useful for understanding the sensitivity of the failure temperature to ramp rate, the results are still useful. Additional sensitivity studies were done with simple 1°C/min and 5°C/min ramps. Results are reported for both Electrosleeved and unsleeved tubes so that the relative strengths can be compared.

Results for Unsleeved Tubes

The data and the flow stress model presented in Ref. 17 showed that the failure temperature of an unflawed Alloy 600 tube is 840°C (1544°F), which is greater than the temperature corresponding to surge line failure. Thus, an unflawed tube is predicted to survive the scoping ramp.

An unsleeved Alloy 600 tube with the deepest cracks that can survive a Δp equal to three times the Δp during normal operation ($3\Delta p_{NO}$) was also considered; for these calculations $3\Delta p_{NO}$ was taken as 26.5 MPa (3.84 ksi). The maximum depths of 6.4, 12.7 and 25 mm (0.5, 1, and 2 in.) long cracks that satisfy this criterion are 76.6%, 67.1%, and 62%, respectively. The corresponding maximum depth for a 360° circumferential crack is 80%. Note that m_p = 2.32 for all these cracks, which will be collectively referred to as the $3\Delta p_{NO}$ crack. For this value of m_p the ligament stress σ_{lig} = 310 MPa (45 ksi). The corresponding failure temperature for both

151

the axial and circumferential cracks by the flow stress criterion is 681°C (see, e.g., Fig. 4.92), which is greater than the assumed surge line failure temperature (674°C). The creep rupture model, which is more accurate than the flow stress model, predicts a failure temperature of 728°C (1342°F). Thus the Alloy 600 tube with a $3\Delta p_{NO}$ crack is predicted to survive the scoping ramp.

Predicted Results for Electrosleeved Tubes

Figures 4.99a-b show the calculated reduction of flow stress of the Electrosleeve during the scoping ramp, as well as at 1°C/min for Hall-Petch exponents n = 0.33 and 0.4, respectively. Note that, for each transient, the variations of flow stress with temperature are almost identical for the two exponents. Further, for each exponent, there is a difference in the flow stress curves initially for the two transients. Although the two curves ultimately converge, the convergence occurs at a much higher temperature than all the predicted failure temperatures.

Figures 4.100a-b show the variation of the predicted failure temperatures (for n = 0.33 and 0.4) with axial crack length for an Electrosleeved tube with a TW crack in the parent tube subjected to the scoping ramp and to two other constant-temperature ramp rates. Note that the predicted failure temperatures corresponding to n = 0.33 and n = 0.4 differ by ≈5°. The predicted failure temperatures under the scoping ramp for all the cracks considered are above 681°C, which is the failure temperature of unsleeved tubes with a $3\Delta p_{NO}$ crack. The same is also true for the slower constant temperature ramp rate of 1°C/min for cracks ≤ 12.7 mm (0.5 in.).

The variation of failure temperature with the constant temperature ramp rate is shown in Fig. 4.101 for an Electrosleeved tube with a TW 360° circumferential crack in the parent tube. It is evident that the failure temperatures for such a tube under ramp rates >1°C/min (which includes the scoping ramp) exceed 681°C (1258°F), which is the failure temperature of unsleeved tubes with a $3\Delta p_{NO}$ crack. As before, the differences in the predicted failure temperatures using n = 0.33 and n = 0.4 are small.

Predicted vs. Observed Failure Temperatures for FTI Tests

As mentioned earlier, FTI performed tests on 22-mm (7/8-in.)-diameter unsleeved tubes, both degraded and undegraded, and Electrosleeved tubes with 100% deep axial notches in the parent tube. All the tests were conducted under a constant internal pressure = 16.2 MPa (2.35 ksi) and a variety of temperature ramps with the initial rate (at <500°C) ranging from 3 to 5°C/min. Above a temperature of 500°C (932°F), the notched Electrosleeved specimens were ramped at 7-9°C/min to failure, except for the test with a 12.7 mm (0.5 in.) notch. For this test, the ramp rate was gradually reduced to 1.2°C/min above 705°C (1301°F). Failure temperatures were calculated using the temperature ramps for each specimen supplied by FTI (Figs. 4.102a-c). The predicted failure temperatures for the notched unsleeved Alloy 600 tubes were independent of the temperature history. The comparison between the predicted and observed failure temperatures is shown in Table 4.6. The details of the notch and tube geometry of the specimens are included in Table 4.7. The predictions in Table 4.7 were made wityh a high–temperature flow stress curve for the Electrosleeve material that was based on
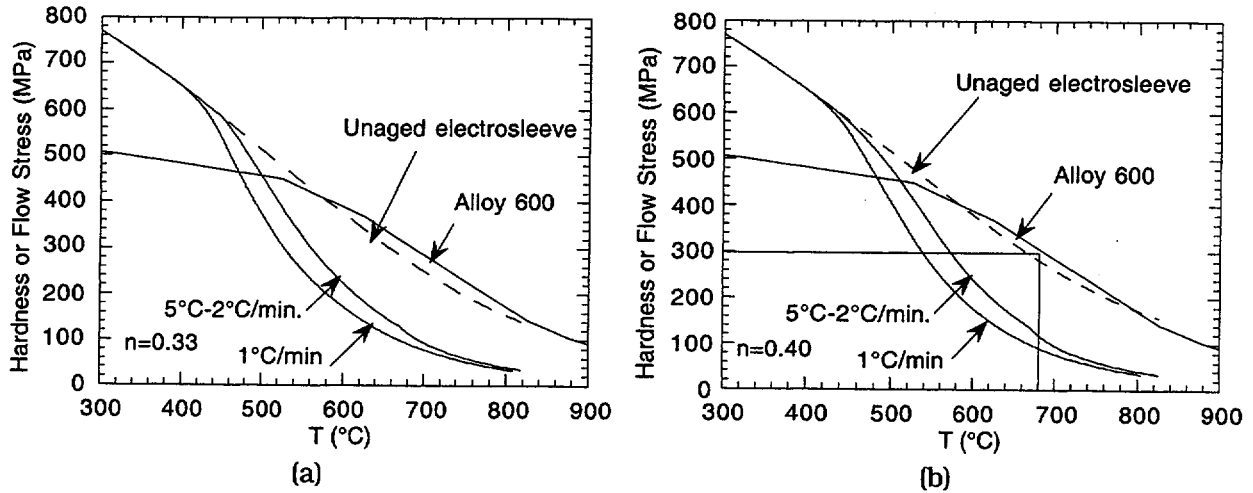
Fig. 4.99.   Calculated reductions of flow stress of Electrosleeve material with temperature, using Hall-Petch exponent (a) n = 0.33 and (b) n = 0.40, for scoping ramp (Fig. 4.98) and constant ramp rate of 1°C/min.
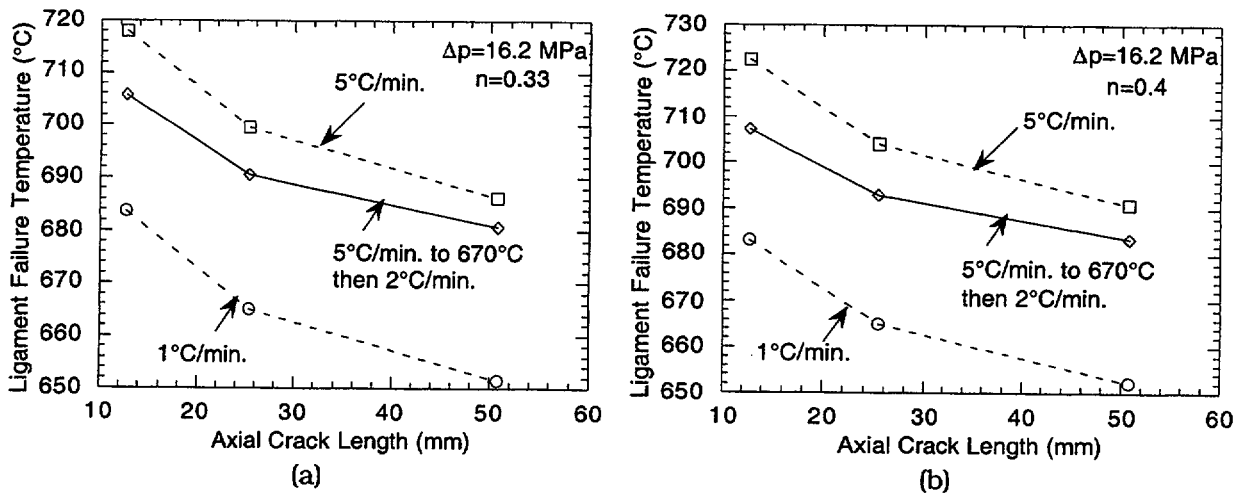
Fig. 4.100.   Predicted ligament failure temperatures by Hall-Petch model for Electrosleeved tubes with throughwall axial cracks under scoping ramp (Fig. 4.98) and constant temperature ramp rates of 1 and 5°C/min and constant internal pressure of 16.2 MPa (2.35 ksi), using (a) n = 0.33 and (b) n = 0.4.

limited high–temperature tensile test data provided by FTI. The predictions are in much better agreement with the observed values, if a modified flow stress curve that includes the results of additional ANL tests is used, as will be discussed later.

In all cases, the predicted failure temperatures overestimate the experimentally observed failure temperatures of the Electrosleeved tubes. The failure temperatures of the two degraded Alloy 600 tubes were predicted quite well by the flow stress model of Ref. 17. Note that these two tests are consistent with each other because the m_p value for a 50% deep 51 mm (2 in.) notch is ≈2, which is also the hoop stress magnification factor for a 50% uniformly thinned tube. The test on undegraded Alloy 600 involved a hold at constant temperature, which the

153
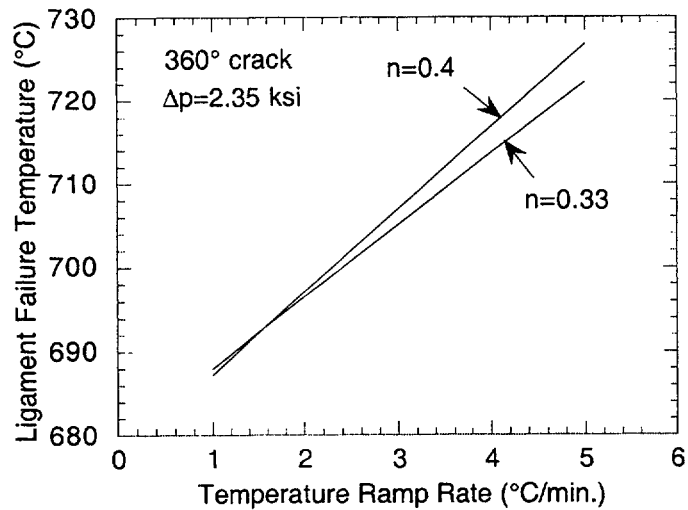
Fig. 4.101. Predicted ligament failure temperatures by Hall-Petch model for Electrosleeved tubes with a TW 360° circumferential crack under various temperature ramps with constant internal pressure of 16.2 MPa (2.35 ksi).

flow stress model cannot handle. However, the creep rupture model presented in Ref. 17 can predict the failure time within a factor of 2.

4.6.6 ANL Test Results

As mentioned earlier, FTI provided twelve Electrosleeved specimens, three of which were notched. Eight additional specimens were notched [≈0.2 mm (0.0075 in.) wide] at ANL by electrodischarge machining. Eleven tests were conducted at ANL. The time temperature history for these tests consisted of holding the pressure constant at 16.2 MPa (2.35 ksi) while ramping the temperature from 300°C to 545°C (572 to 1013°F) at 4.2°C/min, followed by 12.5°C/min ramp until failure (Figs. 4.103a-b). This closely simulates the SBO sequence identified as Case 6RU in Ref. 18 and is felt to be a more realistic representation of the sequences of interest than the scoping sequence used for the initial analytical studies. For this case, the tube temperature is 684°C when the surge line failure occurs. A summary of all the tests conducted by ANL and FTI is given in Table 4.8. Note that the FTI tests were conducted with different temperature ramps, as discussed in Section 4.6.3.

In all of the ANL specimens with 51- and 76-mm (2- and 3-in.)-long flaws the unsleeved tubes with and without Electrosleeves failed with large flaw openings (fish-mouth). Although the specimens without repairs also failed with large flaw openings, the Electrosleeve tubes with 13 and 25 mm (0.5 and 1 in.) flaws failed with no visible openings. Similar failure modes were also observed by FTI.

Revised Unaged Flow Stress Curve of the Electrosleeve

The failure temperatures for the ANL tests were used to recalculate the unaged flow stress curve of the Electrosleeve material using the Hall-Petch model (with n = 0.33) and the effective m_p factors from Fig. 4.89 and Eq. 4.36. The revised flow stress curve is compared with the

154

(a)

(b)
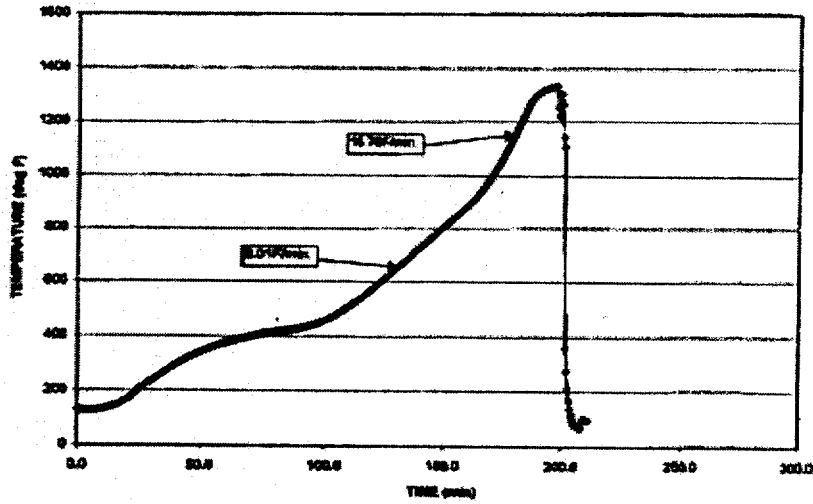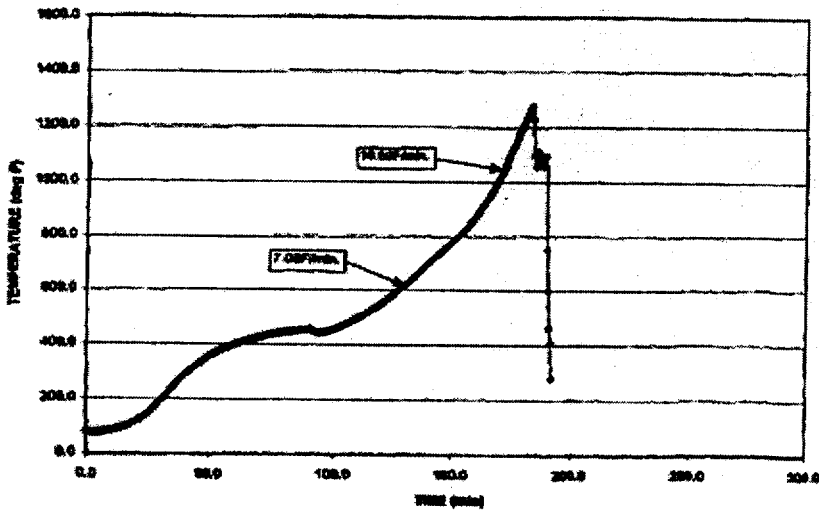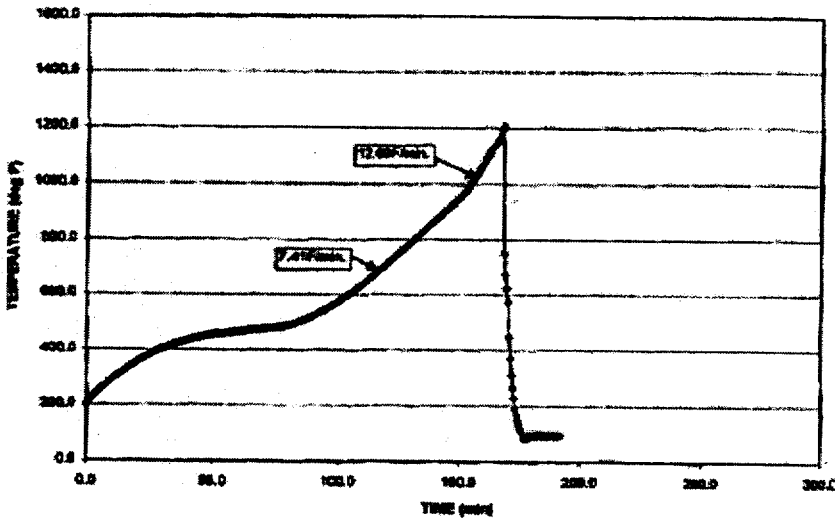
Fig. 4.102.
Temperature ramps used in FTI
tests on Electrosleeved speci-
mens (a) BTF-23, (b) BTF-25,
and (c) R.5.2

(c)

Table 4.6. *Observed and initial predictions of failure temperatures for the FTI severe-accident tests on unsleeved and Electrosleeved tubes.*

| Failure Temperature (°C) | Electrosleeved Alloy 600 tube | | | Unsleeved Alloy 600 tube | | |
	13 mm 100%TW	25 mm 100%TW	51 mm 100%TW	51 mm 50% TW	50% Uniform Thinning	Un-degraded
Observed	731	69i	611	727	724	82 min[a]
Predicted	766	728	682	738	726	164 min[b]

[a]Test was held at 764°C until it failed after 82 min.
[b]Predicted by creep rupture model of Ref. 18.

Table 4.7. *Summary of simulated severe accident tests conducted at ANL and FTI on notched Electrosleeved tubes.*

Test No.	Notch length, mm (in.)	Notch depth, mm (in.)	Tube wall thickness, mm (in.)	Electrosleeve thickness, mm (in.)	Failure temperature, (°C)
BTF-21	13 (0.5)	1.24 (0.0490)	1.24 (0.0490)	1.04 (0.0410)	807
BTF-13	13 (0.5)	1.25 (0.0492)	1.30 (0.051)	1.02 (0.0400)	806
BTF-4	25 (1.0)	1.22 (0.0482)	1.30 (0.051)	0.99 (0.0390)	722
BTF-10	25 (1.0)	1.27 (0.0500)	1.32 (0.0520)	0.97 (0.0380)	724
BTF-14	25 (1.0)	1.24 (0.0490)	1.27 (0.0500)	0.99 (0.0390)	714
BTF-19	51 (2.0)	1.24 (0.0490)	1.30 (0.051)	1.02 (0.0400)	680
BTF-22	51 (2.0)	1.26 (0.0495)	1.27 (0.0500)	0.97 (0.0380)	653
BTF-20	51 (2.0)	1.24 (0.0490)	1.30 (0.051)	0.94 (0.0370)	653
BTF-18	76 (3.0)	1.28 (0.0503)	1.28 (0.0505)	1.00 (0.0395)	643
BTF-17	76 (3.0)	1.25 (0.0493)	1.30 (0.051)	0.89 (0.0350)	630
BTF-5[a]	76 (3.0)	1.24 (0.0490)	1.24 (0.0490)	1.12 (0.0440)	673
BTF-23[b]	13 (0.5)	1.24 (0.0490)	1.27 (0.0500)	0.89 (0.0350)	731
BTF-25[b]	25 (1.0)	1.30 (0.051)	1.30 (0.051)	0.91 (0.036)	691
R.5.2[b]	51 (2.0)	1.30 (0.051)	1.27 (0.0500)	0.91 (0.036)	611

[a]One tip of notch in this specimen was ≈2.5 mm (0.1 in.) from end of Electrosleeve.
[b]Conducted by FTI.

previously estimated flow stress curve (Fig. 4.92) in Fig. 4.104. Note that the revised curve has a different shape and falls below the earlier estimated curve. This revised flow stress curve is used for all failure predictions in the remainder of this paper.

Predicted Failure Temperatures

ANL Tests. An examination of Table 4.7 shows that the geometries of the Electrosleeved tubes have some variations. An upper bound to the predicted failure temperatures was obtained by using the following:

Tube thickness = 1.3 mm, sleeve thickness = 1.0 mm and notch depth = 1.2 mm,

and a lower bound was obtained by using the following:
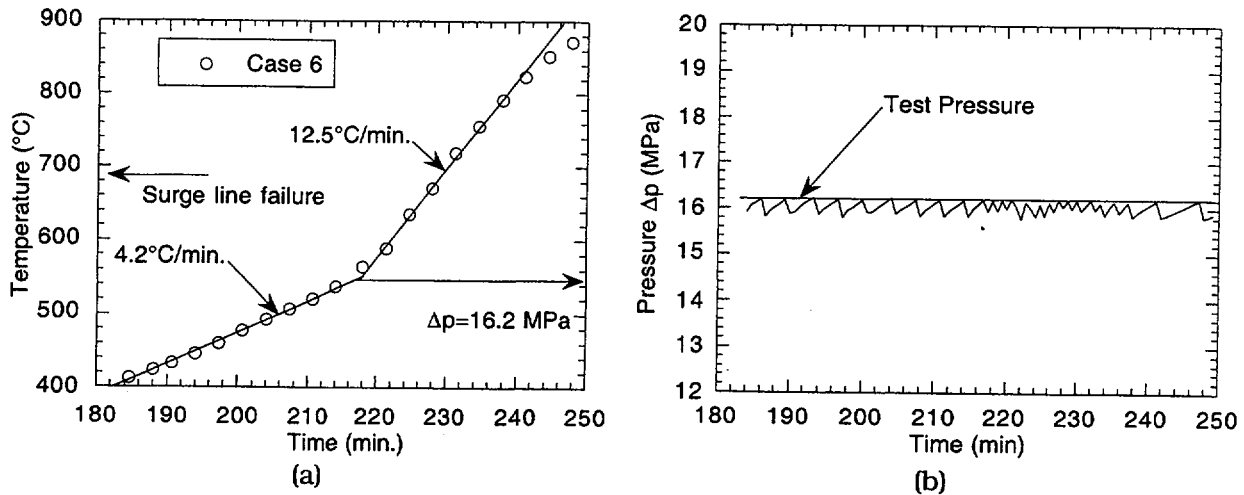
Fig. 4.103. *Calculated variation and ANL test simulation of (a) temperature and (b) pressure differential during SBO (case 6) severe accident transient.*

Table 4.8. *Summary of simulated severe accident tests conducted at ANL and FTI on part-TW notched Electrosleeved tube*

Test No.	Tube Wall Thickness mm (in.)	Electrosleeve Thickness mm (in.)	Crack Length mm (in.)	Crack Depth mm (in.)	Test Failure Temp (°C)	Predicted failure temp. (°C)
BTF-3[a]	1.27 (0.050)	0.99 (0.039)	44.7 (1.76)[b]	1.04 (0.041)[b]	689	692
BTF-7[a]	1.32 (0.052)	0.97 (0.038)	51 (2)[b]	1.09 (0.043)[b]	699	678
BTF-16	1.32 (0.052)	0.97 (0.038)	51 (2)	1.14 (0.045)	675	678

[a]Tests were conducted by FTI.
[b]Equivalent crack length and depth of trapezoidal flaws.

Tube thickness =1.2 mm, sleeve thickness = 0.89 mm and notch depth = 1.2 mm.

In cases where the notch depth was less than the full thickness of the parent tube wall, an effective flow stress for the ligament (average flow stress weighted by thickness) was used. The two bounds together with the test data are plotted in Fig. 4.105. Both the test data and the model indicate that the decrease in failure temperature with flaw length saturates at a notch length of ≈ 76 mm (3 in.) and no significant additional decrease of failure temperature should occur at longer flaw lengths. The tube-to tube variations in geometry give rise to a significant difference between the two bounds, and a much better correlation between the predicted and the observed failure temperatures is obtained if the actual geometry for each specimen is used in calculating the predicted failure temperatures (Fig. 4.106).
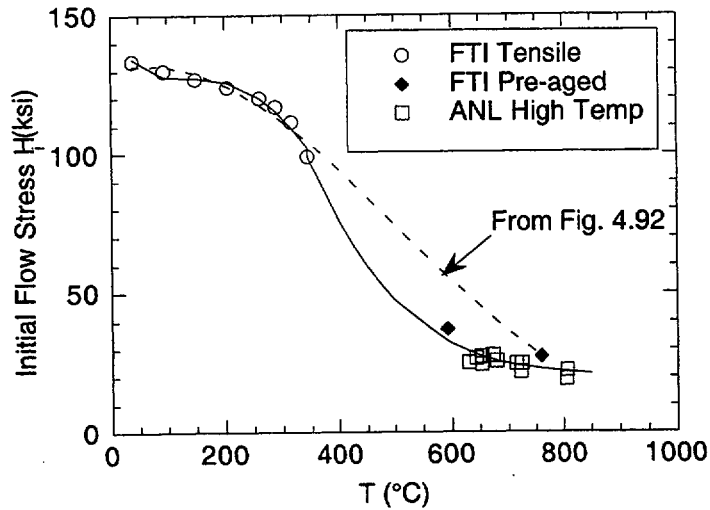
Fig. 4.104. *Original unaged flow stress curve (dashed line) of Electrosleeve estimated from FTI tensile data before ANL tests were conducted, and revised unaged flow stress curve (solid line) of Electrosleeve calculated using ANL tests.*
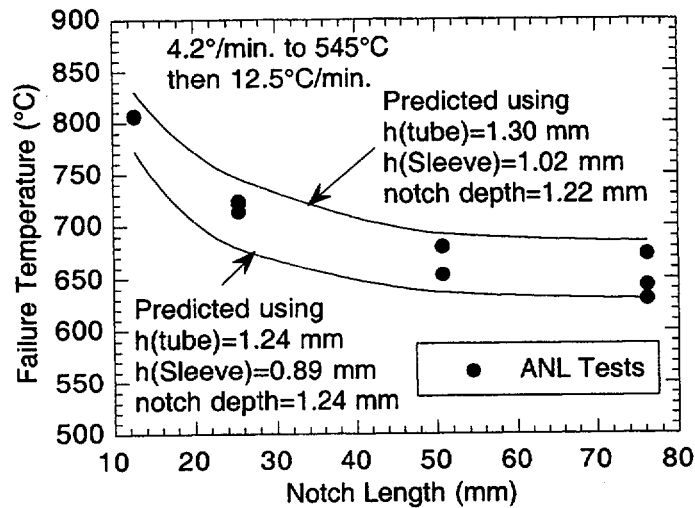
Fig. 4.105. *Variation of ANL test failure temperatures and predicted upper and lower bounds to failure temperatures with notch length.*

Confirmation of predictions by FEA. Finite-element analyses were conducted for an Electrosleeved tube (Reference geometry, Fig. 4.86) with 13, 25, and 51 mm (0.5, 1, and 2 in.) cracks that were 100% TW and subjected to the Case 6 temperature ramp at a constant pressure Δp = 16.2 MPa (2.35 ksi). The grain-growth model discussed in Section 4.8.4 was used to estimate the flow stress curve of the Electrosleeve as a function of temperature during the Case 6 ramp. The INEL flow stress curve was used for the Alloy 600 tube. Stress-strain curves for both materials were approximated by bilinear curves (Figs. 4.107a–b) with low tangent modulus (strain hardening). The tangent moduli were determined by a linear fit between the yield and ultimate tensile strengths.

158
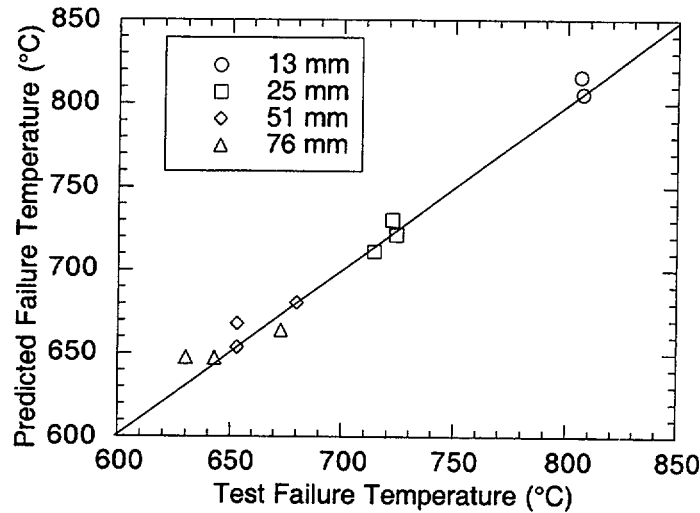
Fig. 4.106. Predicted vs. observed failure temperatures of tests.

(a)

(b)
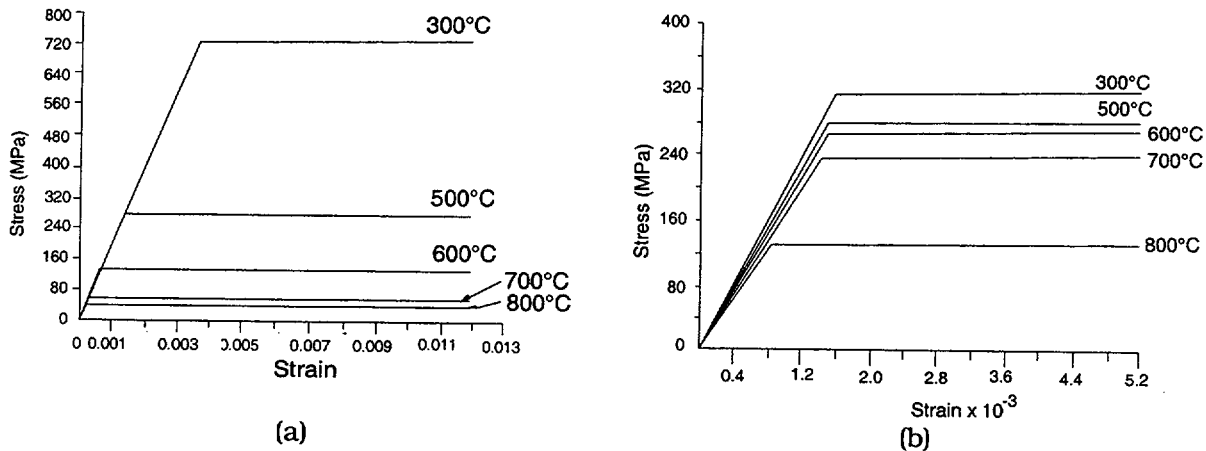
Fig. 4.107. Stress-strain curves used for (a) Electrosleeve (Case 6 ramp) and (b) Alloy 600.

Figures 4.108a-c show the calculated variations of the average ligament hoop stress and average ligament plastic strain with temperature during the ramp for a specimen with a 13 mm (0.5 in.), 25 mm (1 in.), and 51 mm (2 in.) 100% TW cracks. Also shown are variations of yield stress and flow stress of the Electrosleeve during the transient. In each case, the FEA predicts a rapid rise in the Electrosleeve ligament plastic strain after the average ligament stress exceeds the yield stress of the Electrosleeve. The temperatures needed to accumulate 2% average creep strain in the ligament of the 13, 25, and 51 mm cracks are 780, 720, and 675°C (1436, 1328, and 1247°F), respectively. These temperature agree fairly well with the test failure temperatures, which ranged from 806 to 807°C (1483 to 1485°F), 714 to 722°C (1317 to 1332°F), and 650 to 680°C (1202 to 1256°F) for the 13, 25, and 51 mm notches, respectively.
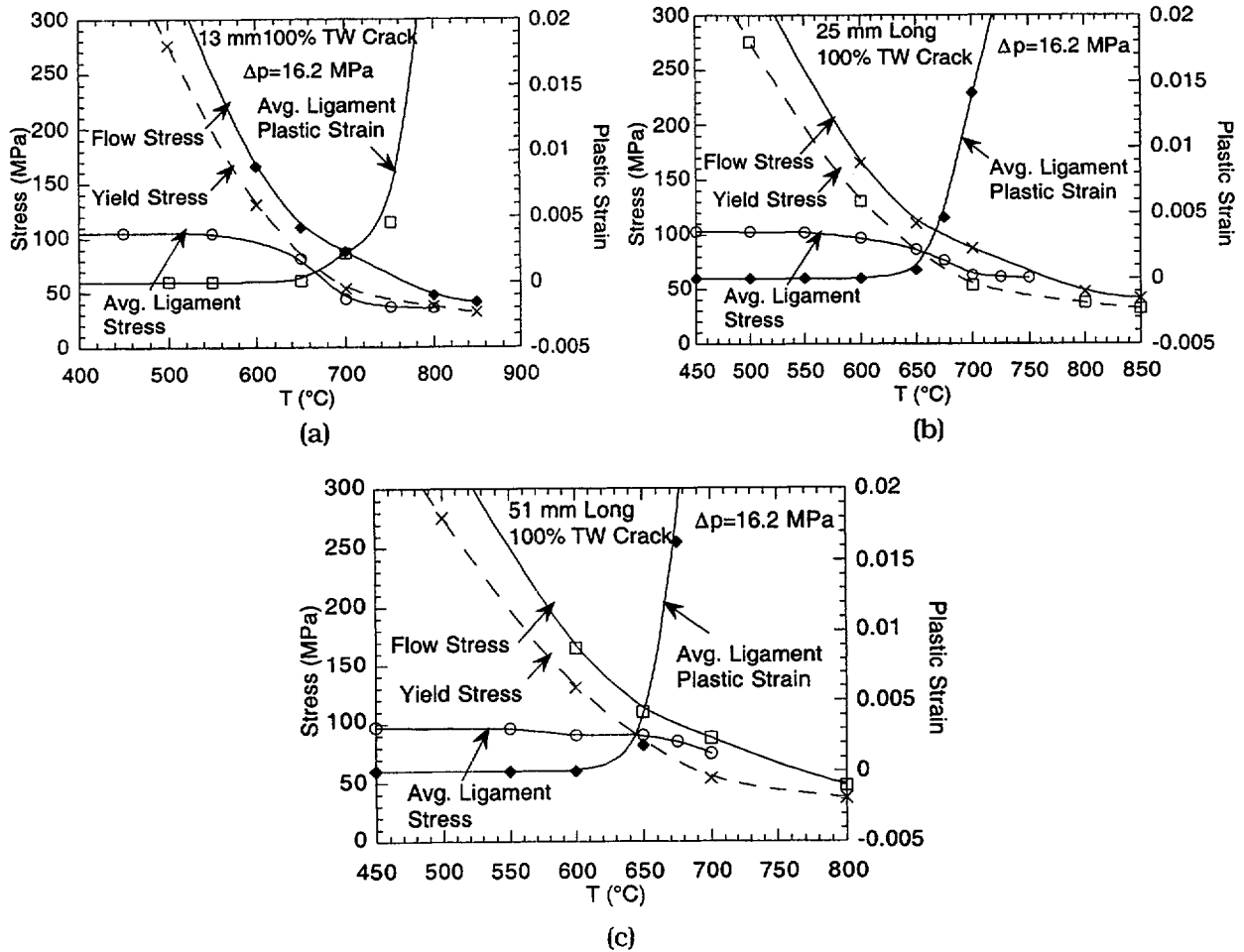
Fig. 4.108. Calculated variations of average ligament stress, average ligament plastic strain, yield stress and flow stress of Electrosleeve with temperature under Case 6 loading on tube with (a) 13-mm (0.5-in.), (b) 25-mm (1-in.), and (c) 51-mm (2-in.) long, 100% TW crack.

Calculated Failure Temperatures, FTI tests.

Figure 4.109 compares the failure temperatures as reported by FTI and the two bounds based on the same geometrical assumptions as in Fig. 4.105. All of the test results tend to fall near the lower-bound curve, which is not surprising because the thicknesses of the Electrosleeve were close to the lower-bound thickness assumed for the curve. The predicted failure temperatures (using actual geometry and actual temperature ramp) are within 15°C of the observed values. Failure temperatures of the Electrosleeved tubes with TW notches appear to vary almost linearly with notch length (the curve is actually slightly concave downward), as shown in Fig. 4.109, which is quite different from the predicted concave-upward shape of the bounds.

Figure 4.110 shows typical failure temperature data for Alloy 600 tubes with part-TW notches reported in Ref. 17, together with predicted values using a flow stress model. For the
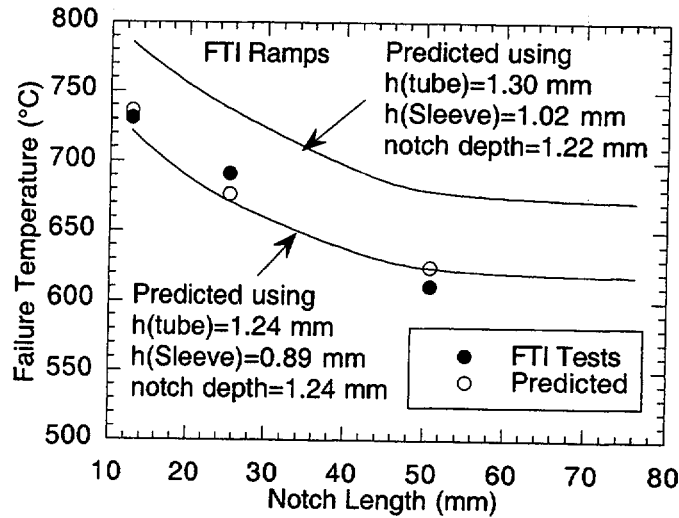
Fig. 4.109. Predicted vs. observed failure temperatures of FTI tests. Predicted points are based on actual geometry and actual temperature ramp for each specimen.
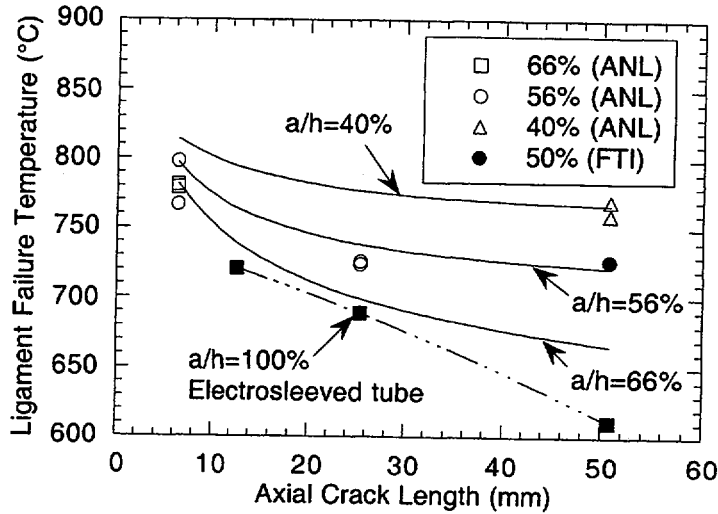
Fig. 4.110. Comparison of experimental ligament failure temperatures (open symbols from Ref. 18) with predicted values (solid lines using flow stress model) for unsleeved Alloy 600 tube with part-TW axial notches under EPRI ramp. Also shown are FTI data (filled circle) for unsleeved tube with 51 mm (2 in.)/50% TW notch and Electrosleeved tubes (filled squares) with TW notches in the parent tubes.

notch depths chosen, the predicted failure temperatures by the flow stress model are close to those predicted by the creep rupture model, which was shown to be the more accurate of the two in Ref. 17. In all cases, the predicted curves, which have been validated with many high-temperature tests at ANL, are concave upward, which is the shape predicted by all other available correlations also. However, as mentioned earlier, the FTI test failure temperatures of the Electrosleeved tubes appear to vary almost linearly with notch length. The difference can be traced to the fact that specimen BTF-23 (13 mm [0.5 in.] notch) had a slower temperature ramp at high temperature (>705°C [1301°F]) while the other two specimens did not. Also, the notch in specimen R.5.2 (51 mm [2 in.] notch) penetrated into the Electrosleeve. The test

failure temperatures were adjusted by using the flow stress model so that all specimens had identical (as those of BTF-25) tube wall thickness, Electrosleeve thickness, and notch depth and were subjected to the same temperature ramp used for specimen BTF-25. The adjusted failure temperature curve is concave upwards, as shown in Fig. 4.111. Note that the upward shift of the adjusted failure temperature for the specimen with the 13-mm (0.5-in.)-long notch (primarily due to adjusting the ramp rate) is much greater than that for the specimen with the 51-mm (2.0-in.)-long notch.

Part-TW Cracks

Initially, the failure temperatures of part-TW cracks were calculated by using the same approach as that for 100% TW cracks by replacing the ligament stress and flow stress by their thickness-averaged values. Since then, FTI has reported results from tests conducted on specimens with nominally 80% deep, 51-mm (2-in.)-long notches. The above approach overestimated the failure temperatures of these tests significantly. Therefore, a series of FEA was conducted on part-TW cracks (with the same reference tube wall and Electrosleeve thicknesses shown in Fig. 4.86 subjected to the Case 6 ramp).

Figures 4.112a-c show the calculated variations of the ligament-averaged hoop stress and plastic strain with temperature during the ramp for specimens with 13 mm (0.5 in.), 25 mm (1 in.), and 51 mm (2 in.) 80% TW cracks. Also shown are the variations of the ligament-averaged yield stress and flow stress during the transient. In contrast to the 100% deep cracks, the FEA-predicted rapid rise in the ligament-averaged plastic strain for the 80% deep cracks does not correlate with the ligament-averaged stress exceeding the ligament-averaged yield stress or flow stress. Figures 4.113a-c shows the variations of the ligament-averaged plastic strains with temperature for 80, 90 and 100% deep, and 13, 25, and 51 mm cracks under Case 6 loading. The increases in failure temperature compared to those of a tube with 100% deep, 13, 25, and 51 mm cracks are 10, 25 and 30°C for 90% deep cracks and 40, 60, and 80°C for 80% deep cracks, respectively. These incremental temperatures were added to the predicted failure temperatures for the 100% deep cracks to obtain the failure temperatures of the Electrosleeved tubes with part-throughwall cracks (Fig. 4.114).

Simplified Prediction Model for Shallow Flaws.

Figure 115a compares the accumulation of plastic strain with temperature in the ligament of a 100% TW crack with that in the Alloy 600 portion of the ligaments of 80% and 90% part-TW, 13-mm (0.5-in.)-long cracks. Similar plots for 25 and 51 mm (1 and 2 in.) cracks are shown in Figs. 4.115b-c. It is possible that because of the relatively high ductility of the Electrosleeve at high temperatures relative to that of Alloy 600, the Alloy 600 portions of the ligaments of the part-TW cracks may run out of ductility and fail first. Under this scenario, since the failure temperatures of the ligament of 100% TW cracks are less than or equal to those of the Alloy 600 ligaments of the part-TW cracks, the Electrosleeve ligaments will fail immediately after the collapse of the Alloy 600 portion of the ligaments. Such a two-step failure process would imply that the increases in failure temperature compared to those of a tube with 100% deep, 13-, 25-, and 51-mm-long cracks are 0, 10, and 25°C for 90% deep cracks and 30, 45, and 75°C for 80% deep cracks, respectively. These increases are somewhat smaller than those estimated earlier on the basis of sudden collapse of the full ligament.
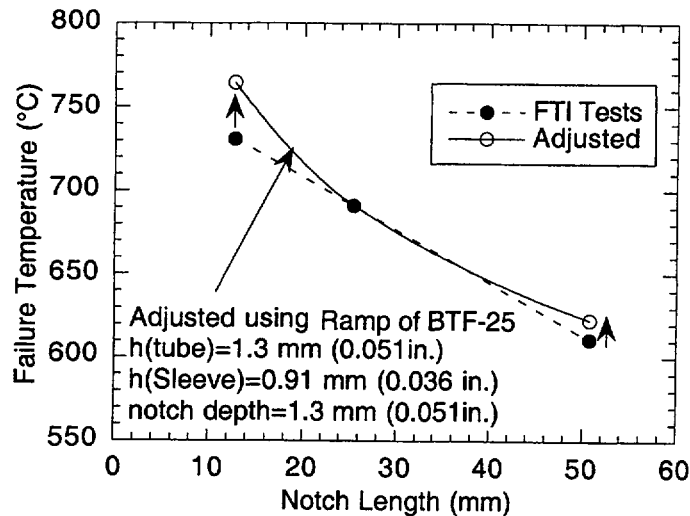
Fig. 4.111. Comparison of FTI test failure temperatures for Electrosleeved tubes with adjusted values obtained by using flow stress model so that all specimens have identical geometry (that of BTF-25) except notch length and are subjected to the same temperature ramp as BTF-25 (Fig. 4.102b).

As the Alloy 600 portion of the ligament becomes larger compared to the Electrosleeve thickness (i.e., as the crack depth decreases), the hoop load carried by the Alloy 600 ligament begins to dominate that carried by the Electrosleeve ligament, particularly at high temperatures. Figure 4.116a shows the calculated variation of the m_p for the Alloy 600 ligament at the tip of a 13-mm (0.5-in.)-long, 80 and 90% deep crack. Similar plots for 25- and 51-mm (1- and 2-in.)-long cracks are shown in Figs. 4.116b-c. Note that the values of m_p at the failure temperatures are much closer to those of the same cracks in an unsleeved tube [i.e., m_p (ANL)] for the 80% deep cracks than the 90% deep cracks. This is consistent with the fact that the hoop stress generated by the pressure loading in the ligament is carried mostly by the Alloy 600 tube ligament at high temperatures.

For the simplified model, the following two-step procedure is used to calculate the failure temperature of the ligament of the Electrosleeved tube with a part-TW crack. First, the failure temperature of the Alloy 600 ligament is calculated, ignoring the contribution of the Electrosleeve ligament and using the m_p for the same crack in an unsleeved tube. After the failure of the Alloy 600 ligament, the crack becomes 100% TW. If the failure temperature of an initially 100% TW crack is less than the failure temperature of the Alloy 600 ligament, the full ligament of the initially 80% TW crack will fail immediately upon failure of the Alloy 600 ligament. On the other hand, if the failure temperature of an initially 100% TW crack is greater than the failure temperature of the Alloy 600 ligament, the full ligament of the initially 80% TW crack will fail at the same temperature as the initially 100% TW crack. The predicted failure temperatures for Case 6 loading are shown in Fig. 4.117. Note that the simplified model predicts no increases in failure temperatures for 90% deep cracks from those of 100% TW cracks. The predicted failure temperatures for 80% deep, 25-51 mm (1-2 in.) long cracks are about 10-20°C lower than those predicted by FEA (Fig. 4.114).

163
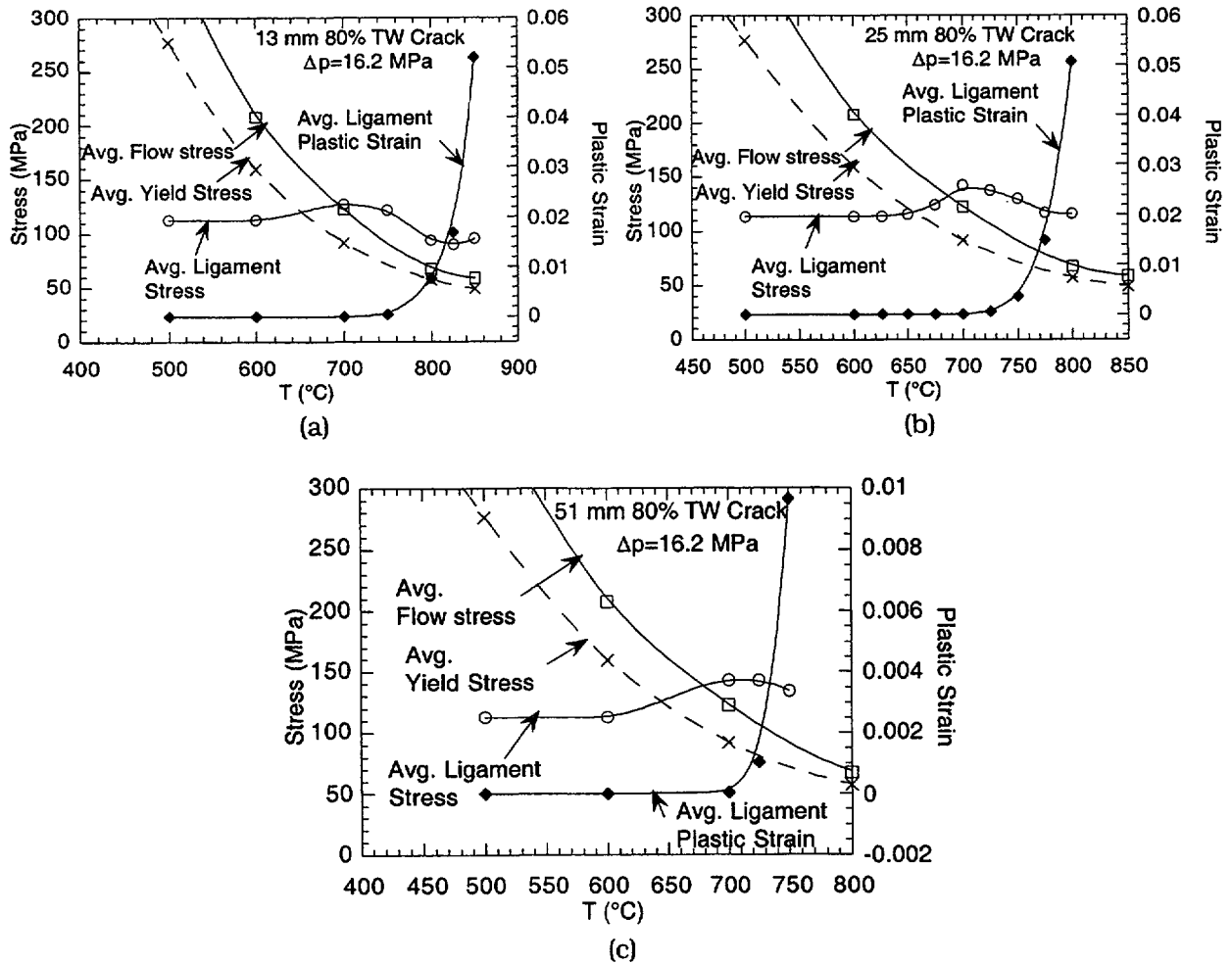
Fig. 4.112. *Calculated variations of ligament-averaged stress, plastic strain, yield stress and flow stress with temperature under Case 6 loading of tube with (a) 13-mm (0.5-in.), (b) 25-mm (1-in.), and (c) 51-mm (2-in.)-long, 80% part-TW crack.*

Tests on Part-throughwall Notched Specimens. A summary of the ANL and FTI tests on Electrosleeved specimens with part-TW notches are given in Table 4.8. The notches in the FTI test were trapezoidal (Figs. 4.118a-b). As before, the FTI tests were conducted with different temperature ramps than ANL tests (Figs. 4.119a-b). The predicted failure temperatures for all the tests are given in the last column of Table 4.8. The predicted failure temperature for the test conducted at ANL was based on the FEA analysis of part-TW cracks and is also shown in Fig. 4.114. Because FEA results for the FTI specimens subjected to the FTI ramps were not available, the simplified model was used to estimate the failure temperatures, which, as mentioned earlier, tend to be ≈10–20°C lower than the FEA results. The predicted failure temperatures are within 10-15°C of the experimentally observed values.
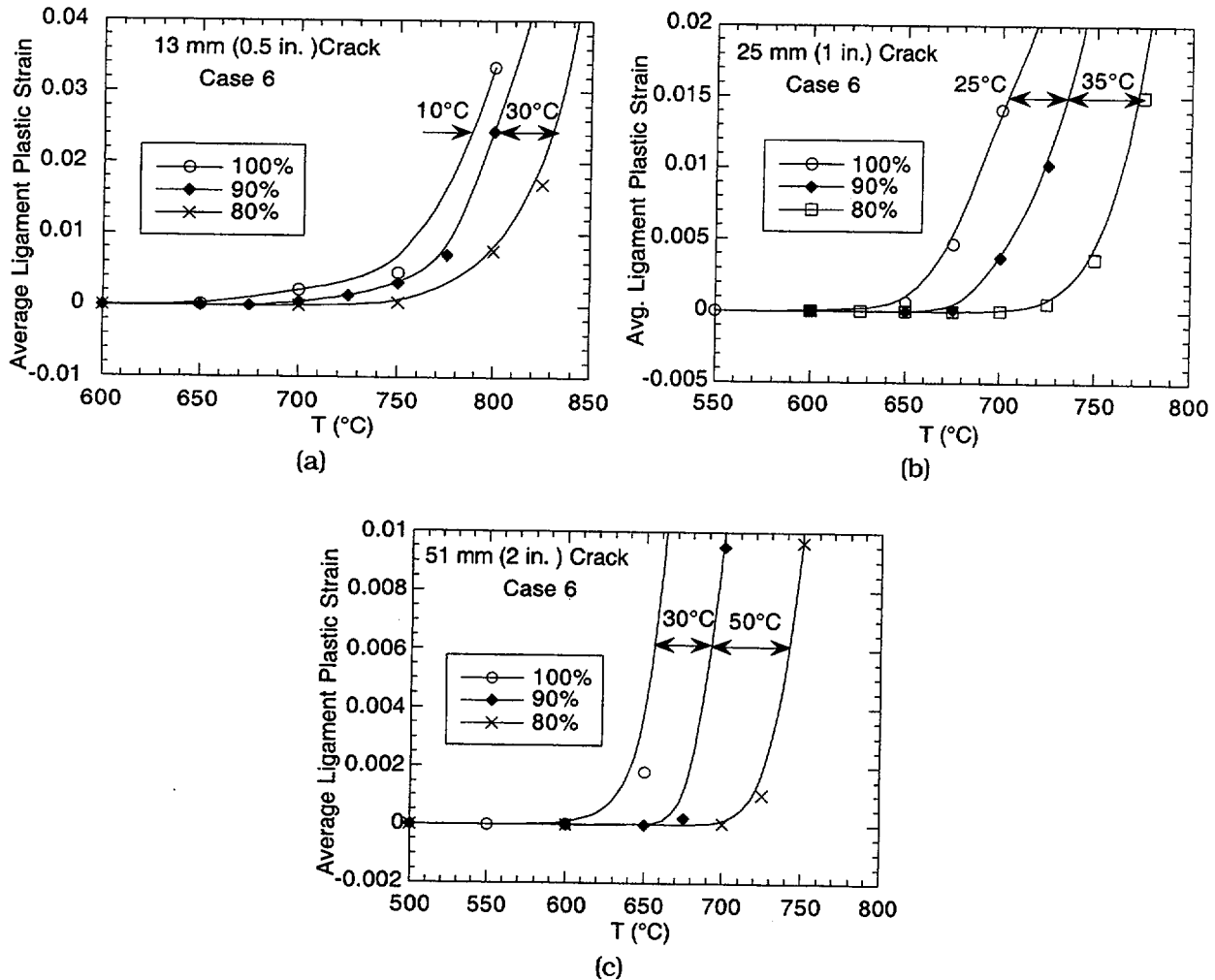
Fig. 4.113. *Calculated variations of ligament-averaged plastic strain with temperature under Case 6 loading of tube with (a) 13-mm (0.5-in.), (b) 25-mm (1-in.), and (c) 51-mm (2-in.)-long, 80, 90, and 100% deep part-TW crack.*

4.6.7 Predicted Failure Temperatures for Postulated SBO Severe Accidents

Case 6 (SBO severe accident)

As mentioned earlier, calculations were done for the temperature and pressure histories shown in Figs. 4.103a-b that closely simulate Case 6RU of Ref. 18. Failure calculations were performed for the reference 22.2-mm (7/8-in.)-diameter tube (wall thickness = 1.27 mm [0.050 in.] and Electrosleeve thickness = 0.97 mm [0.038 in.]) with 90% and 100% TW cracks of various lengths in the parent tube. The results, plotted in Fig. 4.114, show that failure temperatures for 100% TW 76-, 51-, 25- and 13-mm (3-, 2-, 1-, and 0.5-in.)-long cracks are 640, 650, 700 and 795°C (1180, 1200, and 1460°F), respectively. Because the surge line failure occurs when the tube temperature = 684°C, cracks ≤ 25 mm long are predicted to survive the Case 6 transient. If the cracks were 90% rather than 100% TW, cracks ≤ 40 mm long are predicted to survive the Case 6 SBO severe accident. All cracks ≤ 80% deep are predicted to survive the Case 6 transient.

165
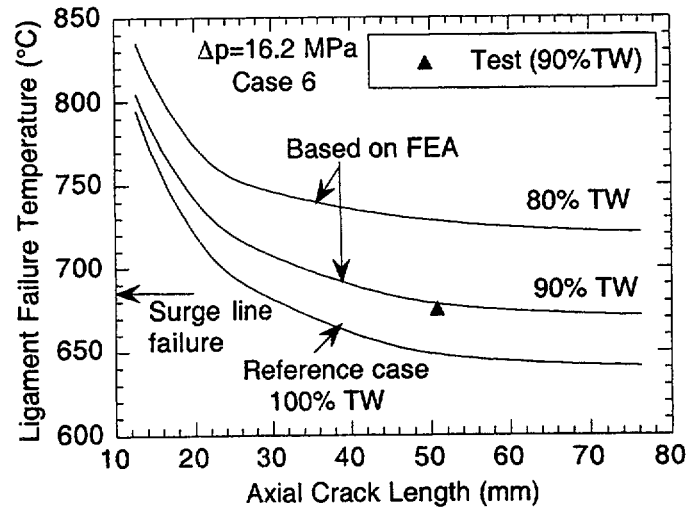
Fig. 4.114. Predicted ligament failure temperatures for 80%, 90%, and 100% TW cracks due to Case 6 loading. Symbol represents failure temperature of test (BTF-16) conducted at ANL on specimen with 90% part-TW, 51-mm (2-in.)-long EDM notch.

Case 20C (SBO with pump seal leakage)

The variation of temperature and pressure during an SBO severe accident with pump seal leakage (Case 20C) is shown in Fig. 4.120. The variations of temperature, ligament flow stress and ligament stresses for various crack lengths with time are plotted in Fig. 4.121 for the reference 22-mm (7/8-in.)-diameter tube (wall thickness = 1.3 mm [0.50 in.] and Electrosleeve thickness = 0.97 mm [0.38 in.]) with 100% TW cracks. Because none of the ligament stresses exceed the flow stress before surge line failure, tubes with 13-, 25-, and 51-mm (0.5-, 1.0-, and 2.0-in.)-long cracks are predicted to survive this transient.

4.6.8 Sensitivity Analyses

Creep Effect

In this report, a flow stress model was exclusively used to predict failure under severe accident transients. However, as was concluded in Ref. 17, a creep rupture model can predict the failure temperatures under severe accident transients more accurately than a flow stress model. A comparison between the predicted failure temperatures by the two models is shown in Table 4.9 for the case of an unsleeved tube with a $3\Delta p_{NO}$ crack, i.e., a 13 mm by 76.6% or a 25 mm by 67.1% or a 51 mm by 62% crack or a 80% deep 360° circumferential crack.

Note that the failure temperature predicted by the flow stress model agrees well with that by the creep rupture model for the 1°C/min ramp, but is conservative for the other three ramps. In particular, the faster the ramp rate the more conservative the prediction is. Since the unaged flow stress of the Electrosleeve was calculated from tests conducted with a temperature ramp of 12.5°C/min, it is expected that the flow stress model will overestimate the failure temperatures for tests at slower ramp rates unless grain growth effects predominate
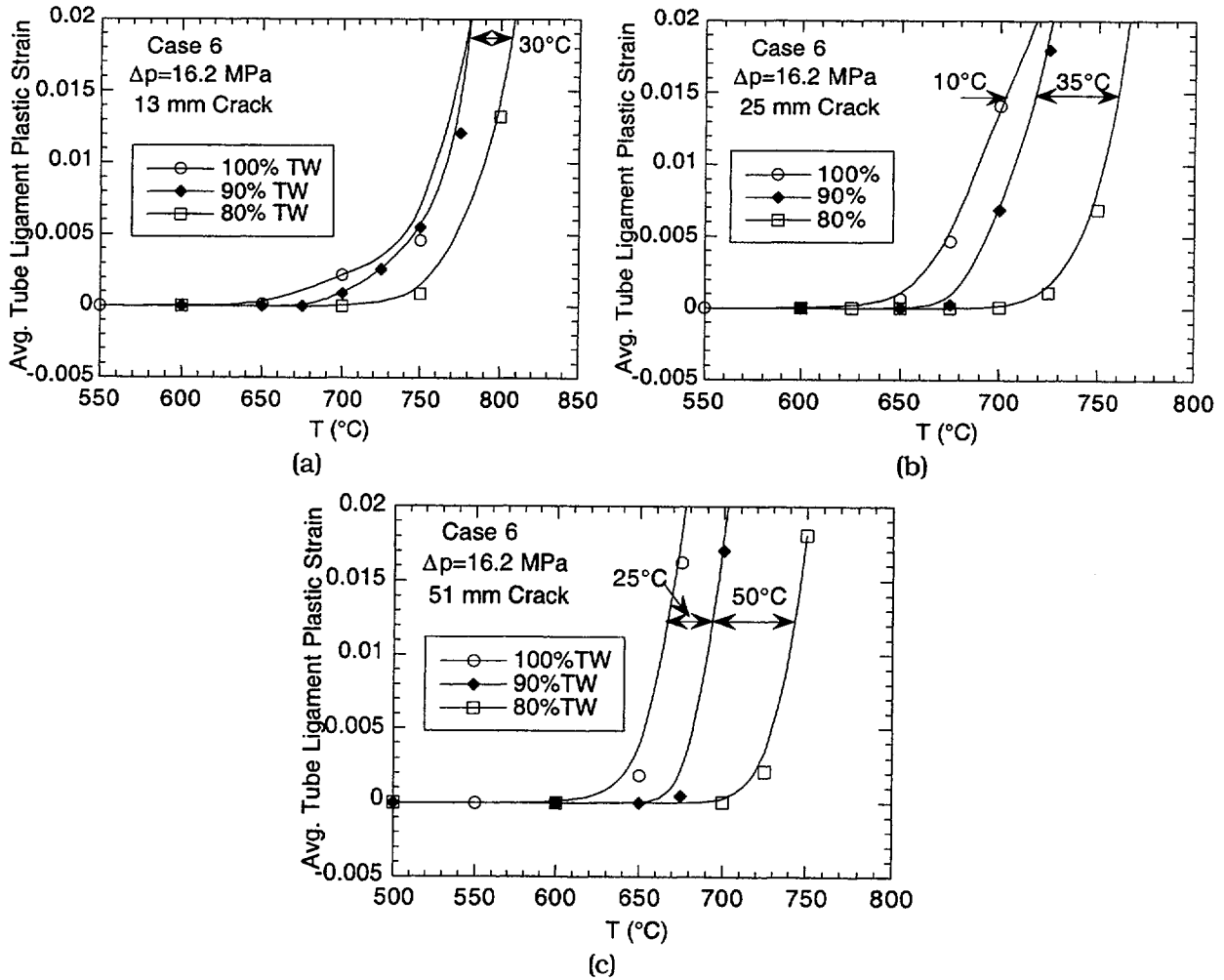
Fig. 4.115. *Calculated variations of average plastic strain in Alloy 600 tube ligament with temperature under Case 6 loading of tube with (a) 13-mm (0.5-in.), (b) 25-mm (1-in.), and (c) 51-mm (2-in.)-long, 80 and 90% TW cracks. Also shown are average ligament plastic strains for 100% TW cracks.*

over creep effects. Also, it should be noted that the failure times under constant temperature holds cannot be calculated with the flow stress models presented in this report unless grain growth effects predominate over creep effects. To accurately predict failure of Electrosleeved tubes under an arbitrarily varying temperature history including constant temperature holds, a creep rupture model analogous to that presented in Ref. 17, coupled with a grain growth model, must be developed.

Thickness of Electrosleeve

The effect of an increase of Electrosleeve thickness from 0.97 to 1.09 mm on the ligament failure temperature under the reference Case 6 SBO ramp is shown in Fig. 4.122. There is a ≈20°C increase in the failure temperature for all crack lengths.
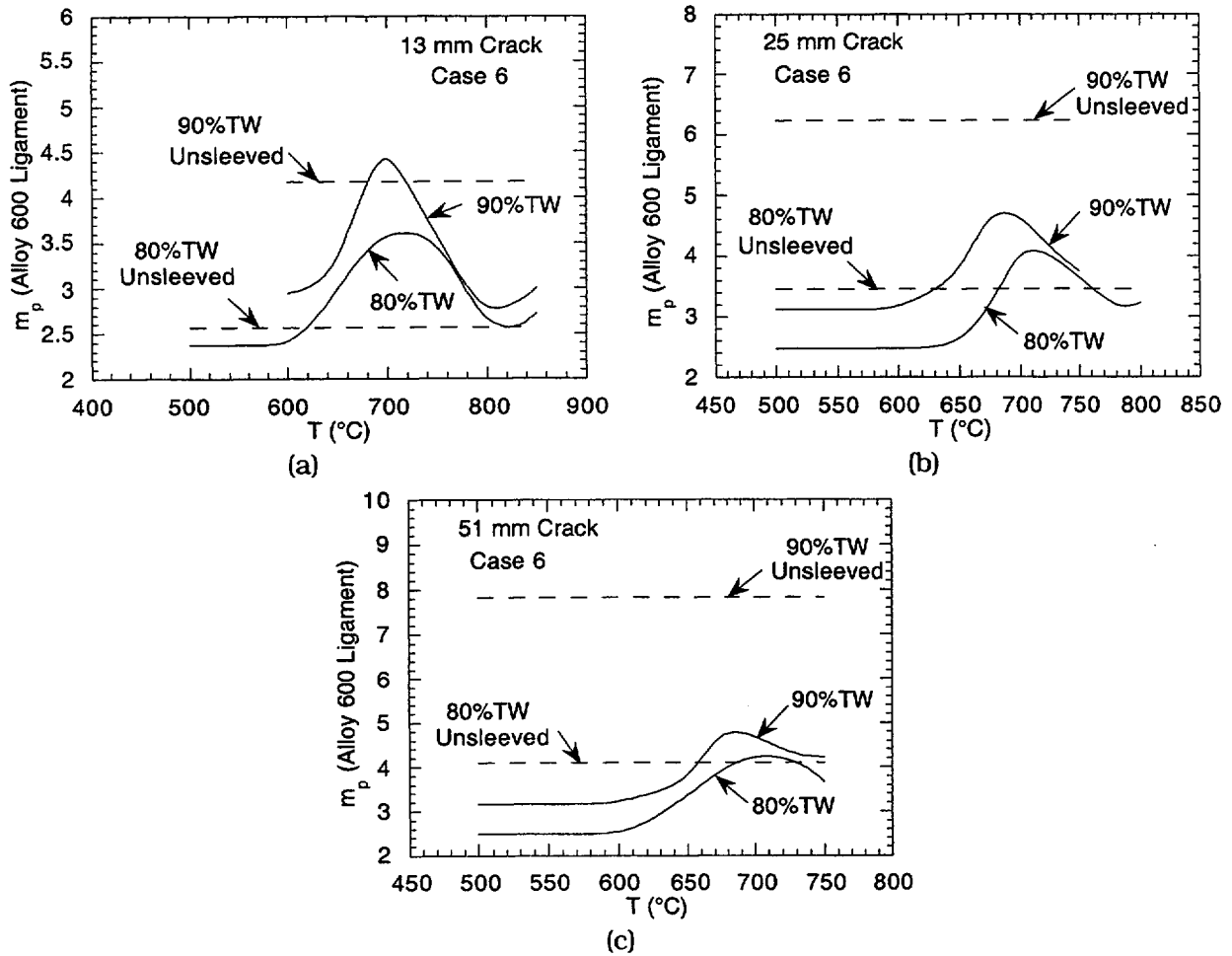
Fig. 4.116. Calculated variation of m_p for Alloy 600 tube ligament with temperature under Case 6 loading of tube with a (a) 13-mm (0.5-in.), (b) 25-mm (1-in.), and (c) 51-mm (2-in.)-long, 80 and 90% TW cracks. Also shown are m_p (ANL) values for unsleeved tubes with 80 and 90% TW cracks.

Crack Depth

In most of the analyses to date, the crack depths were assumed to be 100% of the parent tube wall. This is a major conservatism in the analysis, since the crack depth will typically be less than this. Limited analyses were carried out for Electrosleeved tubes with part-throughwall cracks, as discussed in Section 4.6.4. The predicted failure temperatures, plotted in Fig. 4.105 (which also includes a test data point), show that the increase in ligament failure temperature from that for a 100% deep crack ranges between 10-30°C for a 90% deep crack and 40-80°C for a 80% deep crack, with the larger increases occurring for longer cracks. The stress intensity factor for the preexisting crack would also be greatly reduced by the addition of the overlay which should substantially reduce, if not arrest, subsequent crack growth by fatigue or by stress corrosion. Additional tests with part-TW cracks are needed to verify the predicted failure temperatures.
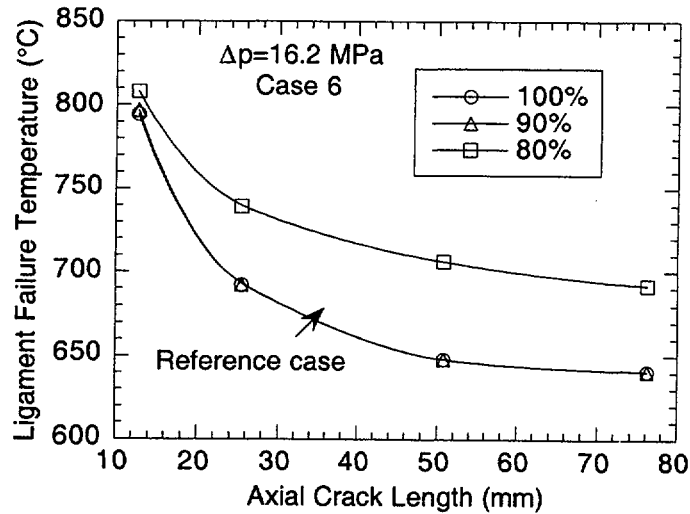
Fig. 4.117. Predicted ligament failure temperatures by simplified model for 80, 90, and 100% TW cracks due to Case 6 loading.
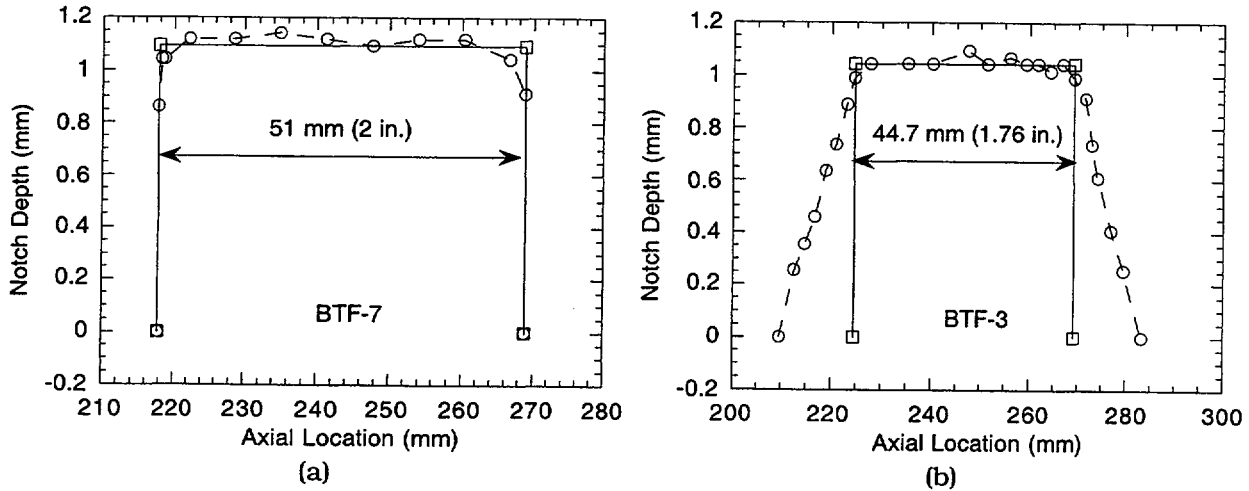
Fig. 4.118. Part-TW crack depth profiles reported by FTI for specimen (a) BTF-7 and (b) BTF-3. Also shown are equivalent crack lengths and depths.

Crack Length

In all the calculations and tests to date, the maximum crack length considered was 76 mm (3 in.) The test data shown in Fig. 4.115 clearly suggest a leveling-off of the failure temperature with increasing crack length beyond 76 mm (3 in.). However, a question arises as to whether there could be a significant reduction in failure temperature if the crack length were much longer. This is of particular concern because although the m_p values calculated by the ANL correlation and by FEA agree remarkably well for crack lengths ≤ 25 mm, there is some discrepancy between the two for crack lengths > 25 mm (Fig. 4.88). In Fig. 4.88, it is evident that for a flow stress ratio of 1, although the ANL correlation shows a slight increase of m_p from 2.0 to 2.1 as the crack length is increased from 51 to 76 mm, the FEA shows virtually no change in m_p from 1.85. In a similar fashion, for a flow stress ratio of 2, the FEA shows no

169
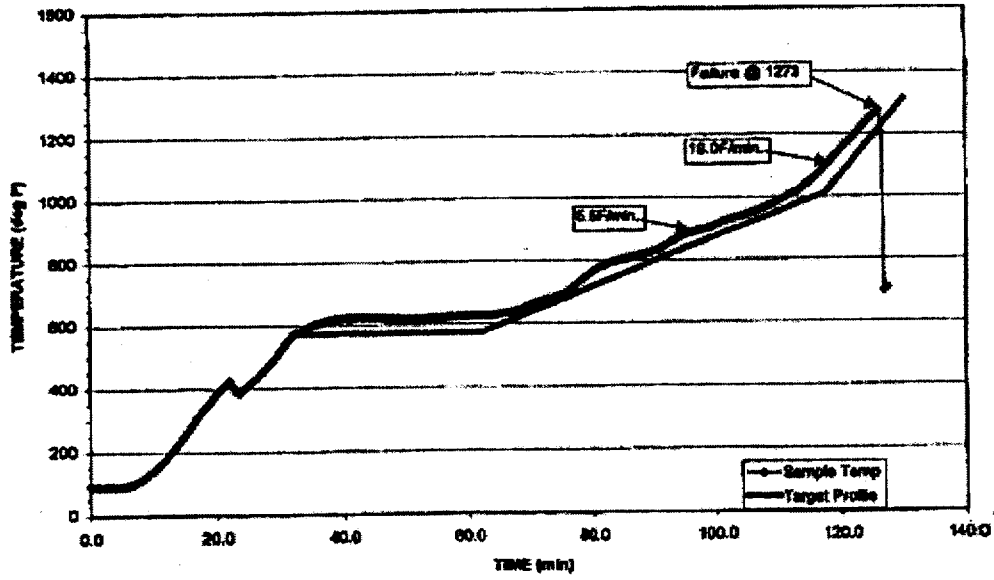
(a)
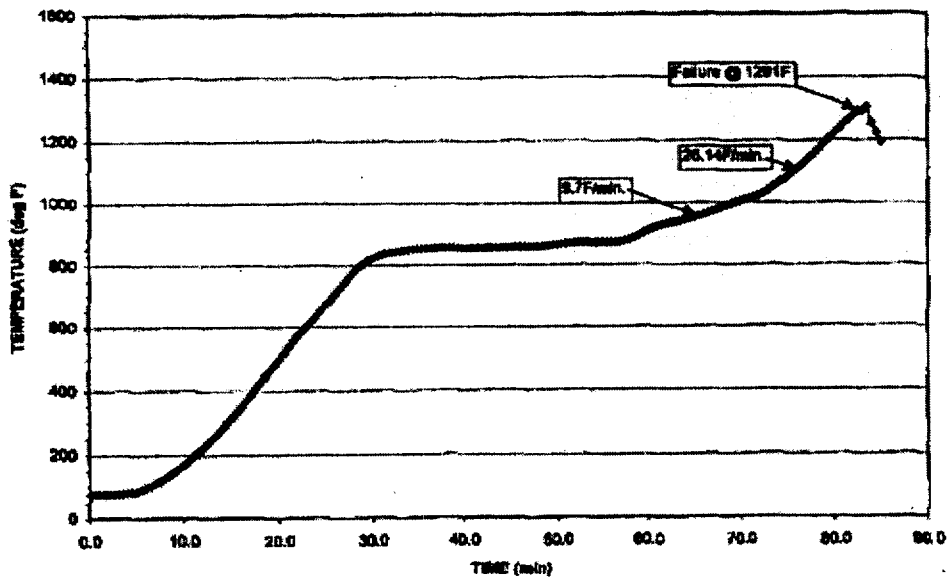
(b)

Fig. 4.119. Temperature ramps used in FTI tests on Electrosleeved specimens with part-TW notches (a) BTF-3 and (b) BTF-7

170
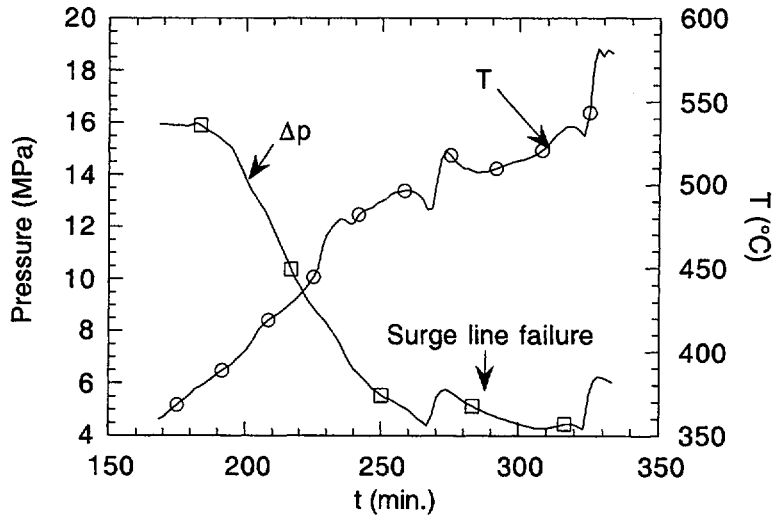
Fig. 4.120. *Variation of temperature and pressure during SBO with pump seal leak (case 20C) severe accident transient.*
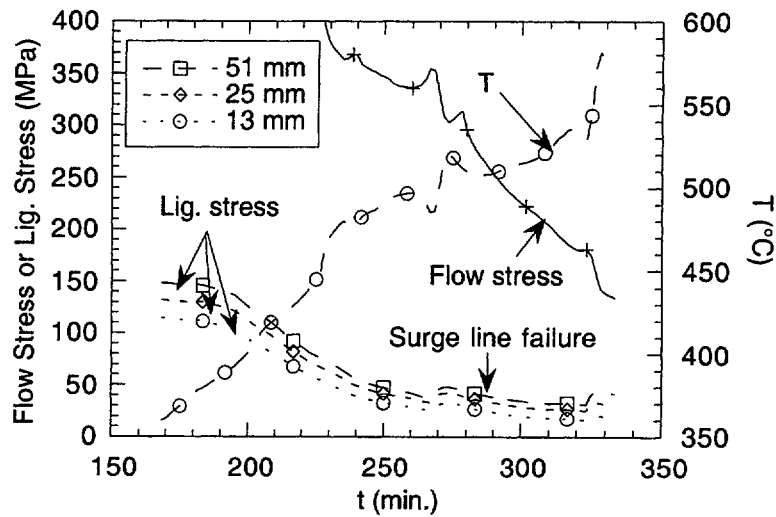
Fig. 4.121. *Time variations of temperature, flow stress of Electrosleeve, and average ligament stresses predicted for 100% TW cracks of length 13 mm (0.5 in.), 25 mm (1 in.), and 51 mm (2 in.) in parent tube during severe accident Case 20C (SBO with pump seal leak). Flow stresses for times less than ≈228 min are >400 MPa. Ligament stresses are well below flow stress up to time of surge line failure*

increase in m_p from 1.6 when the crack length is increased from 51 to 76 mm. The FEA results suggest that there should be no change in failure temperature beyond a crack length of 51 mm, and the test data in Fig. 4.105 may be interpreted to support this. On the other hand, ANL correlation implies a further decrease in failure temperature with crack length. To be conservative, the ANL correlation for m_p modified by flow stress correction factors derived from FEA was used. To estimate the magnitude of reduction in failure temperature with crack

Table 4.9. *Predicted failure temperatures by flow stress model and creep rupture model for unsleeved tube with 3Δp_{NO} crack subjected to various temperature transients and constant internal pressure of 16.2 MPa (2.35 ksi).*

Ramp Rate	Flow Stress Model (°C)	Creep Rupture Model (°C)
1°C/min	681	683
5°C/min	681	728
5°C/min to 670°C, then 2°C/min	681	707
4.2°c/min to 545°C, then 12.5°C/min	681	756
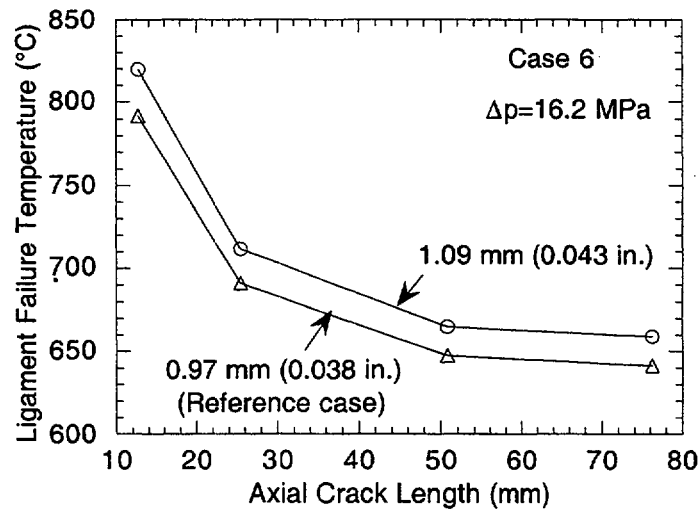
Fig. 4.122. *Effect of Electrosleeve thickness on predicted ligament failure temperature of tube with TW axial cracks.*

length, a plot of the ligament failure temperature with crack length up to 152 mm (6 in.) is shown in Fig. 4.123. Note that the reduction is 5°C in failure temperature when going from a crack length of 51 to 76 mm and an additional 5°C from 76 to 152 mm. Thus although the ANL correlation suggests that the failure temperature continuously decreases with increasing crack length, from a practical standpoint the additional decrease beyond a crack length of 76 mm is negligible.

172
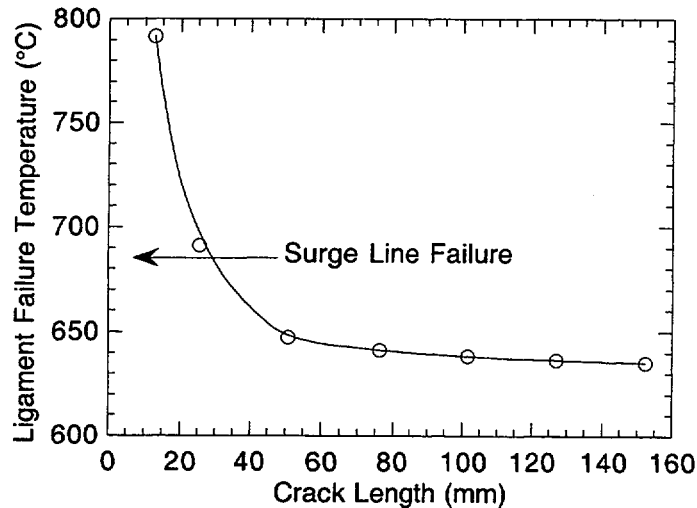
Fig. 4.123. *Effect of crack length on predicted ligament failure temperature of reference Electrosleeved tube with TW axial cracks in parent tube during Case 6 SBO severe accident ramp.*

Variation of Activation Energy with Temperature

For all analyses in this report, the variation of the activation energy with temperature has been idealized by a step function, as shown in Fig. 4.91. To check the sensitivity of the calculated flow stress on the shape of the activation energy curve, the step function was replaced by the following: i.e, plateaus at high and low temperature connected by a ramp. Figure 4.124 shows that while the choice of Q does affect the shape of the transition of the flow stress, it seems to have little real effect on the predicted behavior in severe accidents at high temperatures.

Failure Criterion

The failure criterion Eq. 4.35a was originally developed for cracks in homogeneous single layer shells and has been shown to be valid for a wide variety of ductile materials at low temperatures. FEA calculations for various ligament averaged stresses and plastic strain with pressure in a homogeneous tube with a 2.24 mm wall thickness containing a 76-mm-long, 1.27-mm (0.050-in.)-deep crack are shown in Fig. 4.125. This geometry corresponds to a crack in an Electrosleeved tube with a flow stress ratio = 1. Because the flow stress for the tube was assumed to be 414 MPa (60 ksi), Eq. 4.35a-b would predict a failure pressure of $\approx$55 MPa (8 ksi), which is close to the failure pressure (48 MPa [7 ksi]) predicted by the ANL correlation for m_p. Note that the failure pressure correlates better with the average hoop stress rather than with either the average von-Mises effective stress or the average plastic strain in the ligament. In fact, the failure pressure corresponds to a calculated average ligament plastic strain of only $\approx$3%, much less than the uniaxial ductility of Alloy 600. However, Fig. 4.125 shows that the average ligament plastic strain is rising steeply with pressure. This rapid rise of plastic strain with pressure, together with the high average hydrostatic stress (which generally reduces ductility) in the ligament. Is probably the reason for the success of the criterion. Although different materials may have different uniaxial strains to failure, they would cause only modest changes in the failure pressure.

173
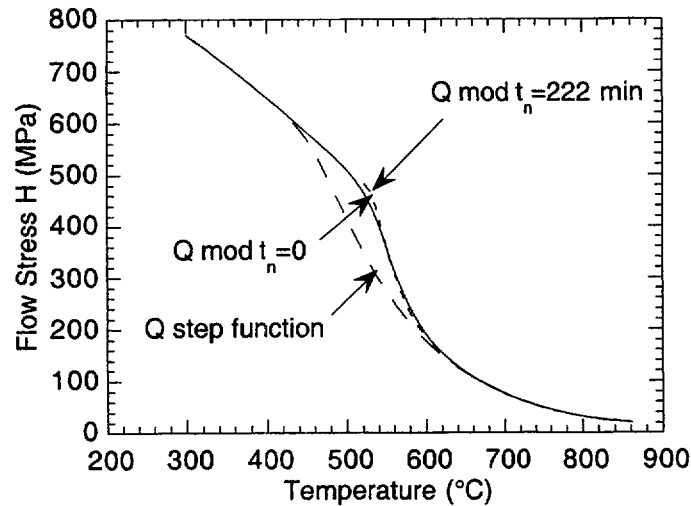
Fig. 4.124.   Effect of shape of variation of activation energy with temperature on calculated loss of flow stress for 1°C min ramp. Nucleation time t_n has little effect on flow stress at temperatures of interest.

The corresponding case of a bi–layer tube (simulating an Electrosleeved tube at high temperature) with a flow stress ratio = 2 is shown in Fig. 4.126. Since the flow stress of the softer inner layer (simulating the Electrosleeve) is 207 MPa (30 ksi), the current procedure with Fig. 4.126 would predict a failure pressure of 33 MPa (4.8 ksi), which again corresponds to an average ligament plastic strain of ≈3%. As before, the average plastic strain in the ligament is rising rapidly with pressure at this load level. Figure 4.126 shows results (using infinitesimal strain and displacement theory) up to a ligament plastic strain of 25%. A more appropriate finite deformation analysis would have indicated an even more rapidly rising plastic strain with pressure. Thus, even if the ductility of the inner layer (Electrosleeve) is greater than that of the outer layer (Alloy 600), the additional pressure capability of the tube beyond that corresponding to an average ligament plastic strain of 3% would be small. At room temperature where failure is controlled by time-independent plastic deformation, the FEA results suggest that Eq. 4.35a would be a reasonable failure criterion for Electrosleeved tubes. At high temperatures, tests on notched Alloy 600 tubes have shown that the flow stress criterion is less successful and that failure is better described by a creep damage criterion, particularly for deep notches (≥80%). But the flow stress model was still reasonably successful for shallower notches (≤66%), and it might be expected that the relative estimates of strength provided by the model are accurate even if the absolute failure temperatures are somewhat less so. Failure temperatures for tests on notched unsleeved and notched Electrosleeved tubes conducted by ANL and FTI have been predicted with reasonable success with the flow stress model except for a single test on an unnotched Alloy 600 tube which was subjected to a constant-temperature hold. It is expected that the current flow stress model will overestimate the failure temperatures if the temperature ramp rates are significantly slower than those used in the tests at ANL and if creep effects were to predominate over grain growth effects.

174
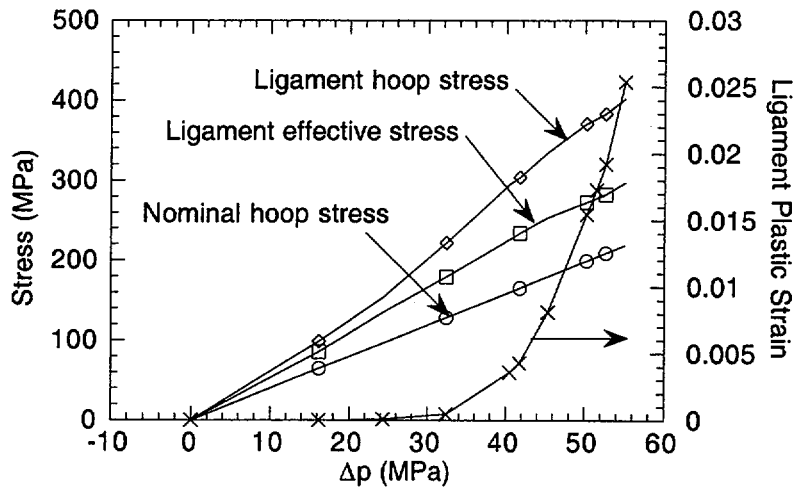
Fig. 4.125. Variations of average hoop stress, average effective stress, and average hoop plastic strain in ligament with pressure as calculated from FEA results for homogeneous tube of wall thickness 2.24 mm (0.088 in.) that contains a 76-mm (3-in.)-long, 1.27-mm (0.050-in.)-deep part-TW axial crack. Also shown is variation of nominal hoop stress in unflawed tube with pressure.
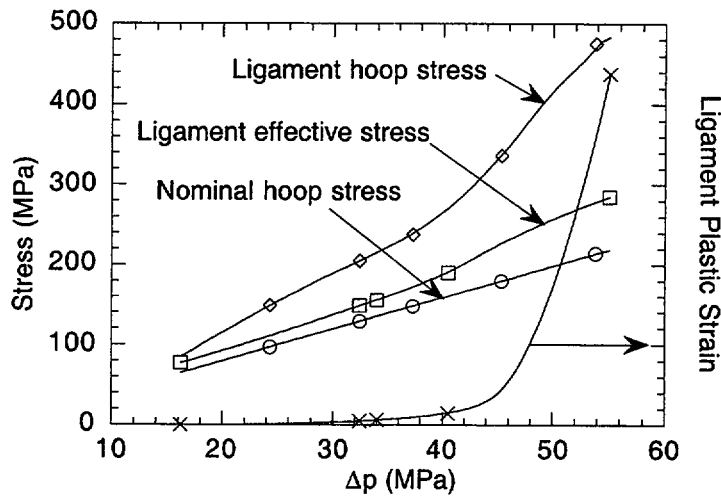
Fig. 4.126. Variations of average hoop stress, average effective stress, and average hoop plastic strain in ligament with pressure as calculated from FEA results for bilayer tube (simulating an Electrosleeved tube at high temperature) with 0.97-mm (0.038-in.) thick inner layer and 1.27-mm (0.050-in.)-thick outer layer containing a 76-mm (3-in.)-long, 100% TW axial crack. Flow stress ratio between outer and inner layer = 2. Also shown is variation of nominal hoop stress in unflawed tube with pressure.

175

In this report, aging has been simulated by using a grain growth model together with hardness data supplied by FTI on Electrosleeve specimens aged at high temperatures. Thus, there is reason to expect some uncertainty in the calculated loss of flow stress with aging. FTI has suggested that the flow stress of Ni-200 at high temperature should provide a reasonable estimate for the flow stress of Electrosleeve after grain growth. A comparison of flow stress data of Ni-200 and Ni-201 with the calculated flow stress of the Electrosleeve for the Case 6 ramp rate (including the effect of aging) is shown in Fig. 4.127. The data for Ni-201 extend only to 649°C. The two FTI data points at 593°C and 760°C on aged Electrosleeves fall quite close to the Ni-200 curve. In the temperature range of interest for severe accidents, i.e., >650°C, the calculated aged flow stress curve is close to but a little below the Ni-200 flow stress curve. Note that the FTI data at 760°C on aged Electrosleeves fall below the Ni-200 curve and are closer to the calculated flow stress curve. Thus, the present estimates for loss of flow stress with aging are consistent with the FTI assumption for the severe accident transient.

4.6.9   Discussion of Results on Behavior of Electrosleeved Tubes at High Temperatures

Two flow-stress-based models have been developed for predicting failure of Electrosleeved tubes under expected severe accident transients. Both models account for the loss of flow stress of the Electrosleeve with aging and predict comparable failure temperatures for both axial and circumferential cracks during a postulated SBO transient. The predicted flow stresses after accounting for aging agree reasonably well with those of Ni-200 at high temperatures. The Hall-Petch model, which is the more mechanistic of the two approaches, was adopted for calculating the failure temperatures of Electrosleeved Alloy 600 tubes with axial and circumferential TW cracks subjected to two severe accident transients: (a) SBO (Case 6) and (b) SBO with pump seal leakage (Case 20C).

Finite-element analyses were conducted to validate the m_p factor used in the model for calculating average ligament stress in single layer shells with part-TW axial cracks. The same model showed that the m_p factor for the Electrosleeve ligament in a 100% TW axial crack is reduced when the flow stress of the Electrosleeve is reduced compared to that of the parent tube. The reduction is greater for shorter cracks. Therefore, a flow-stress and crack-length-dependent correction factor was applied to the m_p factor calculated with the ANL correlation that was developed originally for single layer shells.

Eleven high-temperature tests simulating an SBO (Case 6) pressure and temperature ramp have been conducted on notched Electrosleeved tubes supplied by FTI. The test results indicate a leveling-off of failure temperature with notch length beyond 51–76 mm, which is consistent with the FEA results. The flow stress data supplied by FTI, together with the ANL test results, were used to derive an unaged flow stress curve of the Electrosleeve from room temperature to high temperatures. The unaged flow stress curve was used in the model for predicting failure. All the test data fall within the upper and lower bounds calculated on the basis of limiting geometrical parameters observed in the specimens. Also, high temperature test data on notched unsleeved, as well as on notched Electrosleeved tubes reported by FTI, can be predicted reasonably well by the flow stress model.
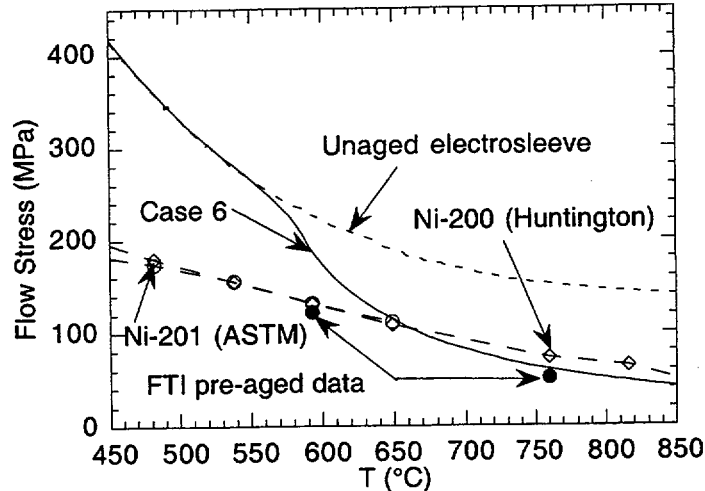
Fig. 4.127.   Comparison of calculated flow stresses (including aging) of Electrosleeve (solid line)
with flow stress data (open symbols) of Ni 200 (Huntington) and Ni-201 (ASTM).
Also shown are flow stress of unaged Electrosleeve (short dashed line) and two FTI
flow stress data (filled circle) on 30-min-aged specimens.

Based on model prediction and on four tests on two different heats of Alloy 600 tubes, undegraded virgin tubes are predicted to survive both severe accident transients. Tubes with the deepest axial and 360° circumferential cracks that meet the $3\Delta p_{NO}$ criterion are predicted to fail during the postulated SBO (case 6) transient at 681°C, which is close to the 684°C that corresponds to surge line failure. The same cracked tubes are predicted to easily survive the severe accident transient Case 20C until surge line failure.

Electrosleeved tubes with TW axial cracks ≤25 mm and TW 360° circumferential crack in the parent tube are predicted to survive the postulated SBO (Case 6) transient until surge line failure. Tubes with any ≤ 90% TW axial cracks in the parent tubes are predicted to survive the same transient until surge line failure. Electrosleeved tubes with TW axial and circumferential cracks are predicted to survive the severe accident transient Case 20C until surge line failure.

A sensitivity analysis showed that the predicted failure temperatures are increased significantly if the depth of the crack in the parent tube is ≤90% TW. They will also increase if the thickness of the Electrosleeve is increased. FEA calculations and ANL tests suggest that the adverse crack length effect should level off at 51-76 mm (2-3 in.). The model predicts a continuing reduction of failure temperature with increasing crack length. However, the additional reduction in predicted failure temperature from a crack length of 76 to 152 mm (3 to 6 in.) is only 5°C (9°F).

The proposed model with the unaged flow stress curve of the Electrosleeve reported here are valid for temperature ramps that are not significantly different from the ramp rate (12.5°C/min) used in the ANL tests because creep effects are neglected in the model. The rate effect that is predicted by the model is due to grain growth only. Predicted failure temperatures at ramp rates significantly different from 12.5°C/min will be accurate if grain growth effects predominate over creep effects.

177

The ligament rupture criterion based on flow stress of the ligament used in the present report was developed from analyses and tests on part-TW cracks in single-layer shells. Application of the flow stress criterion to a composite structure using the flow stress of the weaker Electrosleeve without any credit given to the stronger parent tube may be conservative, particularly for a highly ductile material like the Electrosleeve. However, all of the ANL and FTI tests, which did not include constant temperature holds, are consistent with the flow stress failure criterion. If prediction of failure under an arbitrarily varying temperature history is of interest, a creep-rupture-based model coupled with a grain growth model may be needed.

5 Integration of Results, Methodology, and Technical Assessments for Current and Emerging Regulatory Issues

5.1 NDE of Electrosleeved Tubes

Several tube sections with cracks grown at ANL have been Electrosleeved by FTI. Results of EC (+Point probe at 300 kHz) and ultrasonic (UT) examinations of two test sections are presented in this report. Figure 5.1 shows the EC isometric plot of a 90% TW CODSCC in a 22.2-mm (7/8-in.)-diameter Alloy 600 test section before Electrosleeving. The wall thickness is 1.25 mm (0.050 in.). Figure 5.2 shows a degraded EC isometric plot of the 90% TW CODSCC after Electrosleeving. The total wall thickness of the Electrosleeved test section is ≈2.1 mm (0.085 in.). Figure 5.3 is an EC isometric plot of a 360° CIDSCC, ≈40% TW, in a 22.2-mm (7/8-in.)-diameter Alloy 600 test section before Electrosleeving. The wall thickness is 1.25 mm (0.050 in.). Figure 5.4 is an EC isometric plot of the CIDSCC after the test section was Electrosleeved. The total wall thickness is ≈2.1 mm (0.085 in.). Although significant deterioration of the EC signal is evident after Electrosleeving, detection through the Electrosleeve of relatively deep cracks (>40% TW) is still possible, at least under laboratory conditions.

The two test sections examined by EC were also examined with UT 65° shear waves launched in the Electrosleeve by means of a 3.5 MHz, 6-mm (0.25-in.)-diameter PZT crystal on a wedge curved to fit the ID surface of the Electrosleeved test section. This configuration results in the propagation of essentially guided waves in the test section wall. Figure 5.5 shows the ultrasonic echo (center of trace) from a 90% TW CODSCC present in an Electrosleeved 22.2-mm (7/8-in.)-diameter Alloy 600 parent tube. The echo from the crack can be distinguished from spurious signals by its movement to shorter transit times as the probe approaches the crack. Crack echoes are recorded in a 12-15 μs window. Figure 5.6 shows the ultrasonic echo expanded from the center of the trace in Fig. 5.5.

Figure 5.7 shows a UT echo from the 40% TW (0.5-mm-deep) CIDSCC in the parent tube of the second Electrosleeved test section. The total tube wall thickness with sleeve is again ≈2.1 mm (0.085 in.). The echo from the crack can be distinguished from spurious signals by its movement to shorter transit times as the probe approaches the crack. Again, the crack echo is recorded in a 12-15 μs window. This crack does not intersect either the ID or the OD of the Electrosleeved tube, and thus no corner reflector is present to provide a strong ultrasonic echo. The echo is the result of backscattered UT waves from the crack surface.

Figure 5.8 shows an UT reference echo from a 1.0-mm (0.040-in.)-deep COD-EDM notch in a 2.5-mm (0.10-in.)-thick wall of a 22.2-mm (7/8-in.)-diameter test section. The echoes are also recorded in a 12-15 μs window. This reference test section has been very useful for setting up the UT system and setting system parameters.

For the CODSCC, CIDSCC, and EDM notches, the UT echoes have a very good S/N ratio. By using a frequency of ≈3-4 MHz, distortion of the UT signal from the rough ID surface of the Electrosleeve is minimized. Propagation of waves nearly parallel to the tube axis allows echoes to be generated from cracks that do not intersect either the ID or OD without the need for a corner reflector to provide a strong echo for crack detection.
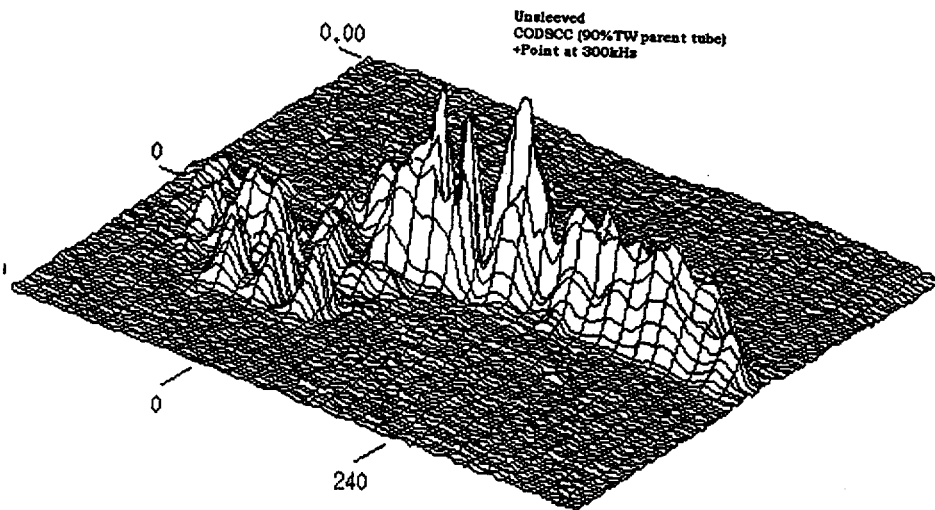
Fig. 5.1. *Eddy current isometric plot of 90% TW CODSCC in 22.2-mm (7/8-in.)-diameter Alloy 600 tube before Electrosleeving. Scan was generated with +Point probe at 300 kHz. Wall thickness is 1.25 mm (0.050 in.).*
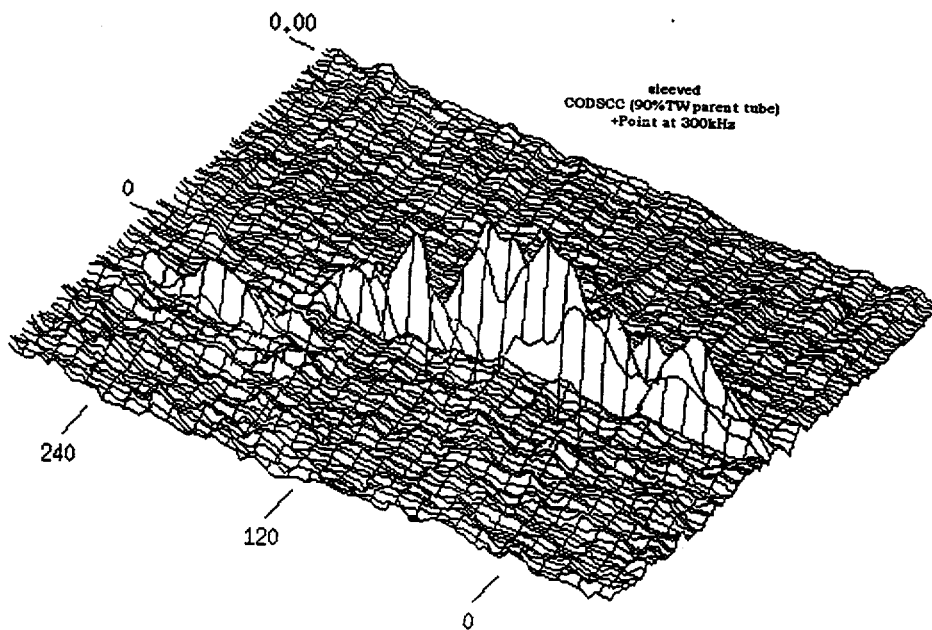
Fig. 5.2. *Eddy current isometric plot of 90% TW CODSCC in 22.2-mm (7/8-in.)-diameter Alloy 600 Electrosleeved parent tube (courtesy of FTI). Scan was generated with +Point probe at 300 kHz. Total wall thickness is ≈2.1 mm (0.085 in.).*

180
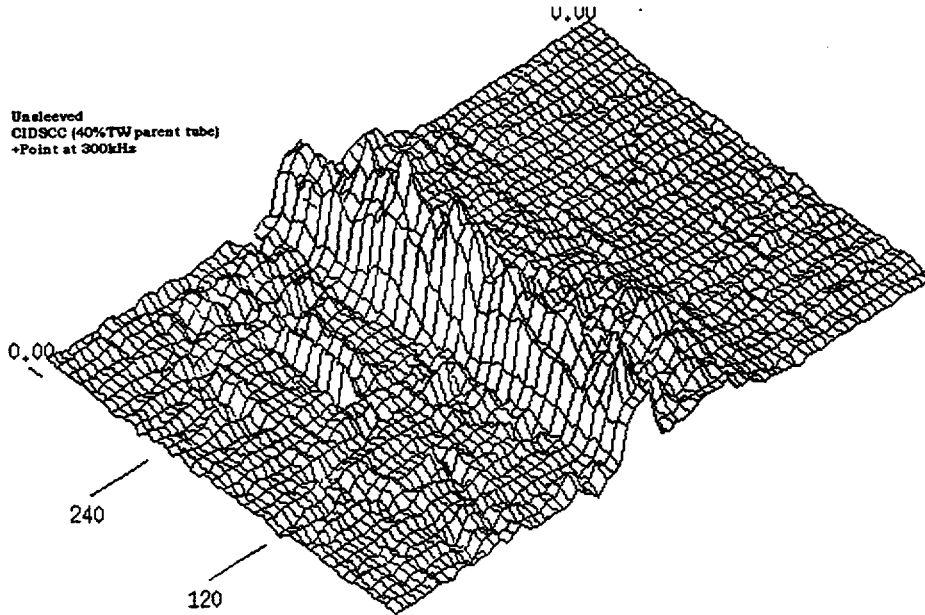
Fig. 5.3. *Eddy current isometric plot of ≈ 40% TW CIDSCC in a 22.2-mm (7/8-in.)-diameter Alloy 600 tube before Electrosleeving. Scan was generated with +Point probe at 300 kHz. Wall thickness is 1.25 mm (0.050 in.).*
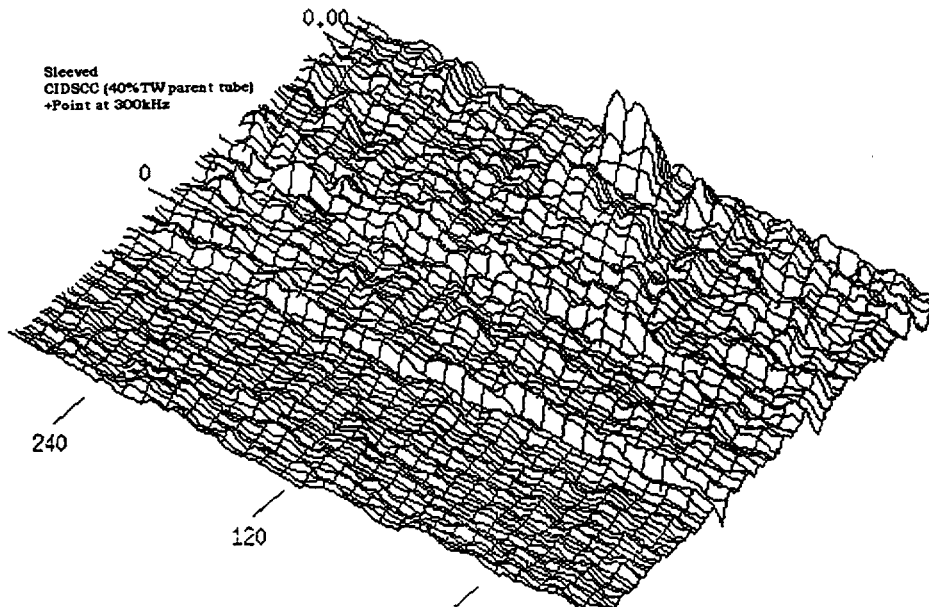
Fig. 5.4. *Eddy current isometric plot of ≈40% TW CIDSCC in a 22.2-mm (7/8-in.)-diameter Alloy 600 Electrosleeved parent tube (courtesy of FTI). Scan was generated with +Point probe at 300 kHz. Total wall thickness is ≈2.1 mm (0.085 in.).*
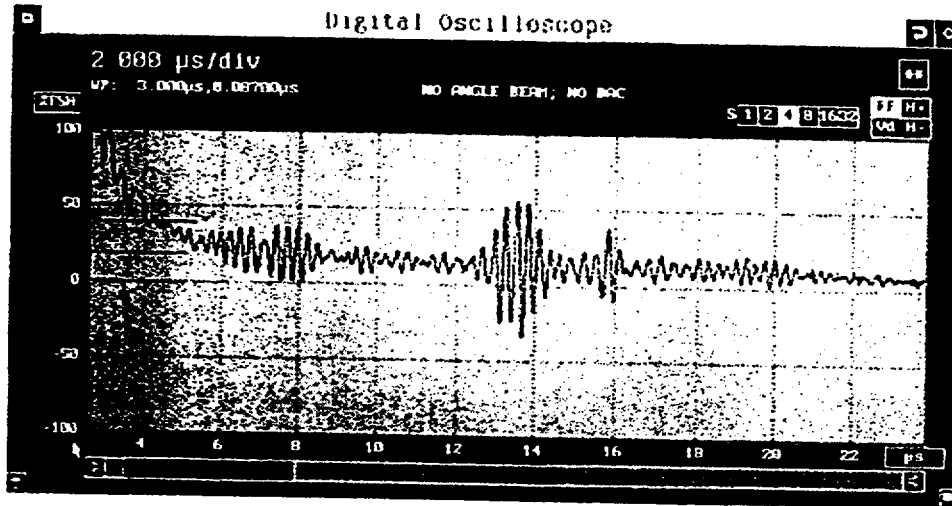
Fig. 5.5. Ultrasonic echo (center of trace) from 90% TW CODSCC in 1.25-mm (0.050-in.)-wall-thickness Electrosleeved 22.2-mm (7/8-in.)-diameter Alloy 600 parent tube. Total tube wall thickness is ≈2.1 mm (0.085 in.). A 3.5 MHz, 6-mm (0.25-in.)-diameter PZT crystal on wedge launches 65° shear waves from ID into Electrosleeve, effectively generating guided waves in tube wall. Echo from crack can be distinguished from spurious signals by its movement to shorter transit times as the probe approaches the crack. Crack echoes are recorded in 12-15 μs window.
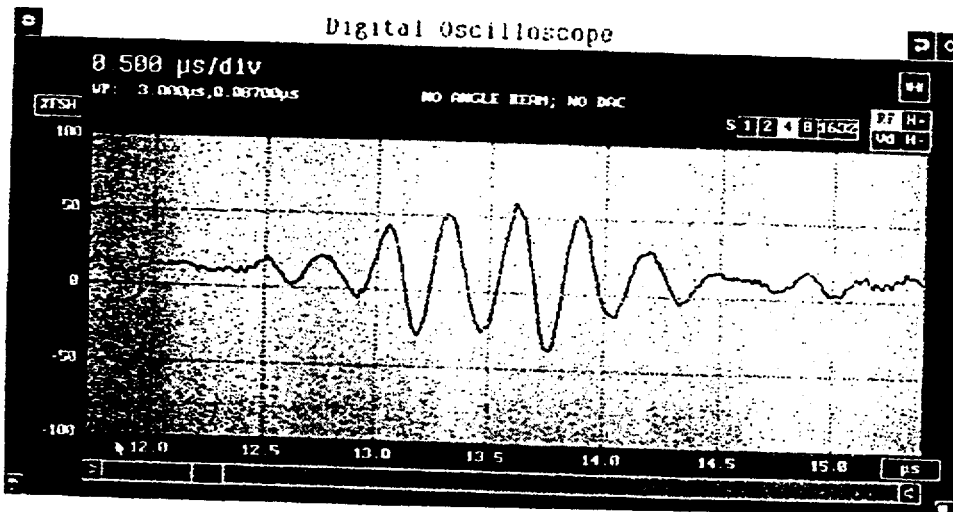
Fig. 5.6 UT echo expanded from center of trace in Fig 5.5. Echo is from CODSCC, 90% TW in 1.25-mm (0.050-in.)-wall-thickness Electrosleeved 22.2-mm (7/8-in.)-diameter Alloy 600 parent tube. Total tube wall thickness Is ≈2.1 mm (0.085 in.).

182
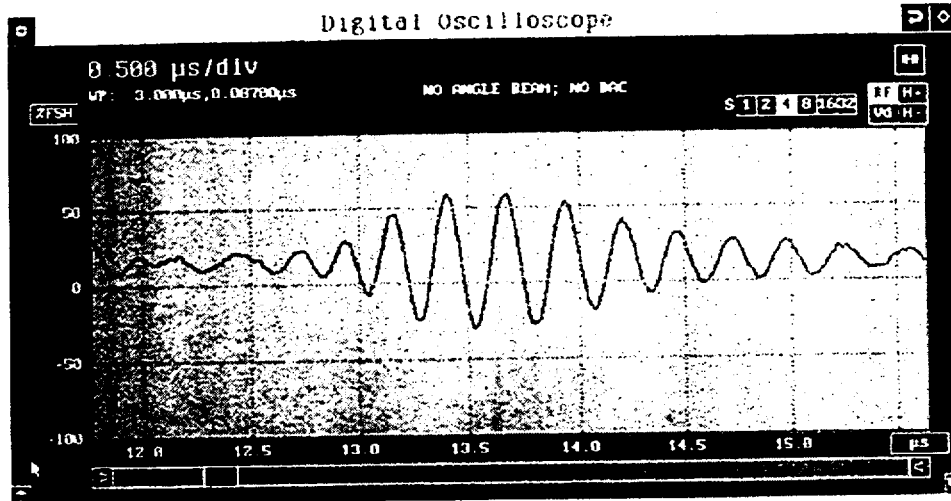
Fig. 5.7. Ultrasonic echo from 40% TW (0.5-mm-deep) CIDSCC in a 1.25-mm [0.050-in.]-wall-thickness Electrosleeved 22.2-mm (7/8-in.)-diameter Alloy 600 parent tube. Total tube wall thickness with sleeve is ≈2.1 mm (0.085 in.). Crack does not intersect either ID or OD of Electrosleeved tube and thus no corner reflector is present to provide a strong ultrasonic echo. Echo is result of backscattered waves from crack surface.
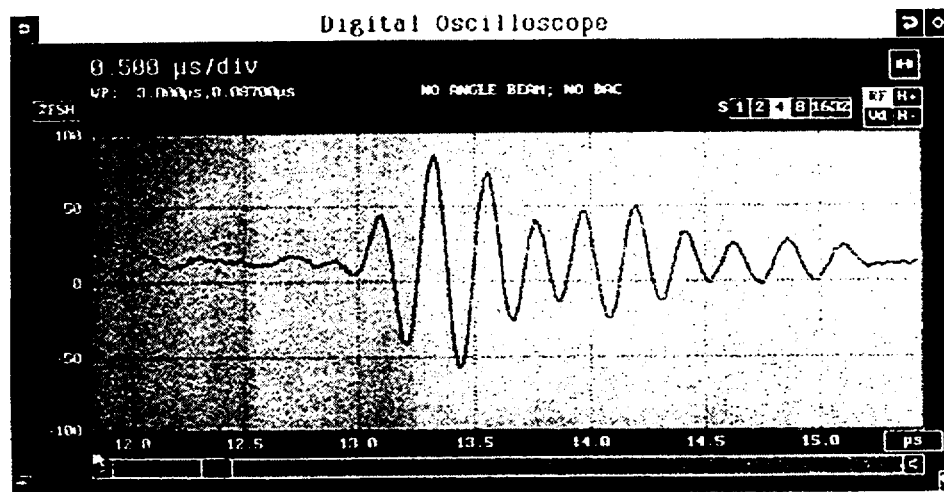
Fig. 5.8. Ultrasonic reference echo from 1.0-mm (0.040-in.)-deep COD EDM notch in the 2.5-mm (0.010-in.)-thick wall of 22.2-mm (7/8-in.)-diameter tube. Notch echoes are recorded in 12-14 μs window.

183

References

1. D. R. Diercks, S. Bakhtiari, K. E. Kasza, D. S. Kupperman, J. Y. Park, and W. J. Shack, Steam Generator Tube Integrity Program, Annual Report, October 1996-September 1997, NUREG/CR-6511, Vol. 4, ANL-98/15, U.S. Nuclear Regulatory Commission, Washington, DC (Jan. 1999).

2. D. R. Diercks, S. Bakhtiari, K. E. Kasza, D. S. Kupperman, J. Y. Park, and W. J. Shack, Steam Generator Tube Integrity Program, Semiannual Report, October 1999 - March 1999, NUREG/CR-6511, Vol. 7, ANL-98/15, U.S. Nuclear Regulatory Commission, Washington, DC (September 2000).

3. K. E. Kasza, S. Majumdar, and J. Muscara, "Steam Generator Tube Integrity/Analysis," Paper #D4-A5-US, SmiRT-15 International Conference on Structural Mechanics in Reactor Technology, Seoul, Korea, Aug. 15-20, 1999.

4. S. Ranganath and H. S. Mehta, "Engineering methods for the assessment of ductile fracture margin in nuclear power plant piping," Fracture Resistance Curves and Engineering Applications, ASTM STP 803, Philadelphia, 1983.

5. P. Hernalsteen, "Structural and leakage integrity of tubes affected by circumferential cracking," presented at NEA/CNRA/CSNI Workshop on Steam Generator Integrity in Nuclear Power Plants, Oak Brook, IL, Oct. 30- Nov. 2, 1995.

6. G. M. Wilkowski et al., "Degraded-Piping Program – Phase II," Semiannual Report, NUREG/CR-4082, Vols. 1-8, USNRC, Washington, DC, 1984-1989.

7. G. M. Wilkowski et al., "Short Cracks in Piping and Piping Welds," Semiannual Report, NUREG/CR-4599, Vols. 1-3, USNRC, Washington, DC, 1991-1994.

8. H. Tada, P. C. Paris and R. M. Gamble, "A stability analysis of circumferential cracks for reactor piping systems," Fracture Mechanics, ASTM STP 700, Philadelphia, 1980.

9. E. Smith, "The effect of axial forces on the conservatism of the net-section stress criterion for the failure of cracked stainless steel piping," SmiRT-12, Vol. G, pp. 57-62, 1993.

10. E. Smith, "Leakage via a through-wall circumferential crack in a piping or tubing system under accidental loading conditions," Int. J. Pressure Vessels and Piping, Vol. 75, pp. 121-124, 1998.

11. E. Smith, "Factors influencing the crack-system compliance of a piping system," Int. J. Pressure Vessels and Piping, Vol. 75, pp. 125 -129, 1998.

12. G. M. Wilkowski et al., "Degraded Piping Program—Phase II Progress," Proc. 13th Water Reactor Safety Information Meeting, Oct. 22-25, 1985, Gaithersburg, MD, U.S. Nuclear Regulatory Commission, Washington, DC 1986.

13. P. C. Paris and H. Tada, "The application of fracture proof design methods using tearing instability theory to nuclear piping postulating circumferential throughwall cracks," NUREG/CR-3464, USNRC, Washington, DC, 1983.

14. A. Zahoor, *Ductile Fracture Handbook*, Electric Power Research Institute, Palo Alto, 1989.

15. J. L. Rempe, S. A. Chavez, G. L. Thinnes, C. M. Allison, G. E. Korth, R. J. Witt, J. J. Sienicki, S. K. Wang, L. A. Stickler, C. H. Heath, and S. D. Snow, "*Light Water Reactor Lower Head Failure Analysis,*" NUREG/CR-5642, EGG-2618, Idaho National Engineering Laboratory, Oct. 1993.

16. D. R. Diercks, S. Bakhtiari, K. E. Kasza, D. S. Kupperman, J. Y. Park, and W. J. Shack, Steam Generator Tube Integrity Program, Annual Report, October 1997-September 1998, NUREG/CR-6511, Vol. 6, ANL-99/8, U.S. Nuclear Regulatory Commission, Washington, DC, Jan. 1999.

17. S. Majumdar, W. J. Shack, D.R. Diercks, K. Mruk, J. Franklin, and L. Knoblich, "Failure Behavior of Internally Pressurized Flawed and Unflawed Steam Generator Tubing at High Temperatures – Experiments and Comparison with Model Predictions," NUREG/CR–6575, ANL–97/17, 1998.

18. SGTR Severe Accident Working Group, "Risk Assessment of Severe Accident-Induced Steam Generator Tube Rupture," NUREG-1570, U.S. Nuclear Regulatory Commission, Washington, DC, 1998.

U.S. NUCLEAR REGULATORY COMMISSION

BIBLIOGRAPHIC DATA SHEET

(See instructions on the reverse)

1. REPORT NUMBER (Assigned by NRC, Add Vol., Supp., Rev., and Addendum Numbers, if any.)
NUREG/CR-6511, Vol. 8

2. TITLE AND SUBTITLE

Steam Generator Tube Integrity Program, Annual Report: October 1998-September 1999

3. DATE REPORT PUBLISHED	
MONTH	YEAR
July	2002

4. FIN OR GRANT NUMBER

W6487

5. AUTHOR(S)

D. R. Diercks, S. Bakhtiari, K. E. Kasza, D. S. Kupperman, S. Majumdar, J. Y. Park, and W. J. Shack

6. TYPE OF REPORT

Technical

7. PERIOD COVERED *(Inclusive Dates)*

10/98 to 9/99

8. PERFORMING ORGANIZATION - NAME AND ADDRESS *(If NRC, provide Division, Office or Region, U.S. Nuclear Regulatory Commission, and mailing address; if contractor, provide name and mailing address.)*

Argonne National Labortory
9700 S. Cass Ave.
Argonne, IL 60439

9. SPONSORING ORGANIZATION - NAME AND ADDRESS *(If NRC, type "Same as above"; if contractor, provide NRC Division, Office or Region, U.S. Nuclear Regulatory Commission, and mailing address.)*

Division of Engineering Technology
Office of Nuclear Regulatory Research
U.S. Nuclear Regulatory Commission
Washington, D.C. 20555-0001

10. SUPPLEMENTARY NOTES

J. Muscara, NRC Project Manager

11. ABSTRACT *(200 words or less)*

This report summarizes work performed by Argonne National Laboratory on the Steam Generator Tube Integrity Program during the period of October 1998 through September 1999. The program is divided into five tasks: (1) Assessment of Inspection Reliability; (2) Research on Inservice Inspection Technology; (3) Research on Degradation Modes and Integrity; (4) Integration of Results, Methodology, and Technical Assessments for Current and Emerging Regulatory Issues; and (5) Program Management. Under Task 1, progress is reported on the assembly of the steam generator tube mock-up, the collection of data for the round robin exercise, and the review of these data. In addition, the effect of a corrosion product on the eddy current signal from a stress corrosion crack is being evaluated, and a technique for profiling cracks based on phase analysis is being developed. Under task 2, research efforts were associated primarily with multiparameter analysis of eddy current NDE results. Two separate multifrequency mixing procedures are being evaluated, and the application of a signal restoration technique to enhance the spatial resolution of rotating probes is being studied. Under Task 3, laboratory-induced cracking has been produced in a total of ~450 Alloy 600 tubes. Additional tests have been conducted using the Pressure and Leak-Rate Test Facility on EDM axial notch OD flaws of several different lengths and flaw depth, and the High-Pressure Test Facility has been completed and utilized in initial tests on tubes with OD axial EDM throughwall and part-throughwall notches. Models for predicting the onset of crack growth and for calculating crack opening area and leak rate from a throughwall circumferential crack in a steam generator tube have been developed. In addition, models for predicting the failure of Electrosleeved tubes have been developed. Under Task 4, eddy current and ultrasonic examinations were conducted on test sections with cracks grown at Argonne.

12. KEY WORDS/DESCRIPTORS *(List words or phrases that will assist researchers in locating the report.)*

Steam generator tubes, inservice inspection, stress corrosion cracking, eddy current, ultrasonics, crack growth

13. AVAILABILITY STATEMENT

unlimited

14. SECURITY CLASSIFICATION

(This Page)

unclassified

(This Report)

unclassified

15. NUMBER OF PAGES

16. PRICE
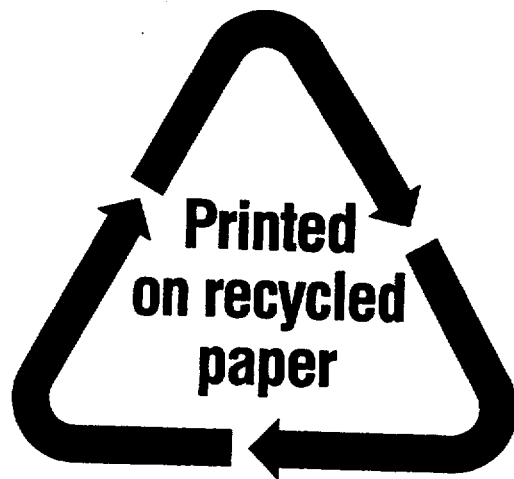
UNITED STATES
NUCLEAR REGULATORY COMMISSION
WASHINGTON, DC 20555-0001

OFFICIAL BUSINESS
PENALTY FOR PRIVATE USE, $300